Fall 1-16-2014

Testing and Analysis of a Post-Tensioned Coupled Wall System monitored with Multiple Digital Image Correlation Systems

Michelle Holloman

TESTING AND ANALYSIS OF A POST-TENSIONED COUPLED WALL SYSTEM MONITORED WITH MULTIPLE DIGITAL IMAGE CORRELATION SYSTEMS

by

MICHELLE HOLLOMAN

A thesis submitted in partial fulfillment
of the requirements for the degree of
Master of Science in Civil Engineering
Department of Civil Engineering

Michael McGinnis, Ph.D., Committee Chair

College of Engineering and Computer Science

The University of Texas at Tyler
May 2013

The University of Texas at Tyler
Tyler, Texas

This is to certify that the Master's Thesis of

MICHELLE HOLLOMAN

has been approved for the thesis requirement on
May 6, 2013
for the Master of Science in Civil Engineering

Approvals:

Thesis Chair: Michael McGinnis, Ph.D.

Member: Michael Gangone, Ph.D.

Member: Sara McCaslin, Ph.D.

Member: Yahya Kurama, Ph.D.

Chair, Department of Civil Engineering

Dean, College of Engineering and Computer Science

Acknowledgments

Funding for this research was provided for by the National Science Foundation through the Network for Earthquake Engineering Simulation (NEES) under Grant No. CMMI 10-41598. Also the technical assistance of MKA is thankfully recognized. Thanks to Suncoast prestress and Lenton interlock for their generous donations.

I also acknowledge the technical support provided by Dr. Michael McGinnis on the design, modeling and analysis of the data presented in this thesis. I would like to thank Dr. Michael Gangone, Dr. Sara McCaslin, and Dr. Yahya Kurama comprised the thesis committee and were an integral part of the completion of this document. The hard work and assistance on Steve Barbachyn of the University of Notre Dame is gratefully acknowledged.

I would like to acknowledge the love and patience always given to me by my parents, especially when I did not deserve it. They have always supported me throughout the course of my life. They have been the best parents to me.

Finally, I would like to thank my soon to be husband. He has pushed me to succeed when my rope has been cut and quitting would be easy. He has loved me through my impatience and demanding, and I will be proud to repay him for the rest of my life.

Table of Contents

List of Tables

List of Figures

Abstract

TESTING AND ANALYSIS OF A POST-TENSIONED COUPLED WALL SYSTEM MONITORED WITH MULTIPLE DIGITAL IMAGE CORRELATION SYSTEMS

Michelle Holloman

Thesis Chair: Michael McGinnis, Ph.D.

The University of Texas at Tyler
May 2013

This thesis discusses the design and experimental evaluation of a novel seismic-resistant reinforced concrete (RC) coupled shear wall system. In this system, the widely-used unbonded post-tensioned floor slab construction method is adapted to couple (i.e., link) two RC wall piers, providing significant performance and construction benefits over conventional RC coupling beams in high seismic regions. Previous experiments of post-tensioned coupled wall structures are limited to floor-level coupling beam subassemblies. The current study extends the available research to multi-story structures by construction and testing of a 15% scale eight story prototype specimen. This test is monitored by four digital image correlation systems simultaneously in order to gather data from all necessary areas of the specimen. The experimental specimen includes the foundation, the first three floors of the shear walls, and the associated coupling beams. The upper stories of the building are simulated with hydraulic jacks that supply the appropriate bending moment, shear, and axial forces at the top of the laboratory structure. This thesis compares the measured displacements and derived

parameters of the laboratory structure measured by the digital image correlation systems with predictions from design models. Experimental and design predictions of several key behavior parameters are shown to match well. Several design parameters that are unable to be measured from the specimen are able to be predicted using the validated models. Coordination of the four simultaneous digital image correlation systems presented some challenges – recommendations for future deployment are discussed. Future work involves the construction and testing of large scale (40%) specimens to validate the approach.

CHAPTER 1: INTRODUCTION

1.1 Project Motivation

Reinforced concrete coupled shear walls are a commonly used lateral load system in high-rise condominium, hotel, and office towers in the U.S. These structures are constructed by placing coupling (i.e., link) beams at the floor and roof levels to transfer forces between the wall piers and also dissipate energy during an earthquake. The resulting system is stronger than the sum of the wall piers, allowing for efficiency in design; however, the detailing and construction of the coupling beams pose significant challenges due to the presence of large reversed cyclic rotation demands under large shear forces.

To achieve ductile behavior, the most common practice for RC coupling beams in seismic regions is the diagonally reinforced system (Barney et al. 1978; Tassios et al. 1996; Bristowe 2000; Galano and Vignoli 2000; Canbolat et al. 2005). As shown in Fig. 1.1(a), the placement of two intersecting groups of diagonal reinforcing bars through the beam and into the wall piers is a major challenge in practice. More recently a new type of hybrid coupled wall system using steel beams that are not embedded in the walls has been investigated (Shen and Kurama 2000, 2022a, b; Kurama and Shen 2004; Kurama et al.2004, 2005; Shen et al. 2005a, b). Instead of traditional embedding, the beams and wall piers are post-tensioned together to create coupling in the system. Post-tensioned coupling beams offer significant advantages over the conventional coupling systems made with monolithic concrete and embedded steel beams: simpler and less costly

construction details, a reduction in the damage in the structure, and a self-centering capability of the structure. The research conducted by Shen and Kurama 2000 utilized steel coupling beams, while the research discussed here uses post-tensioned reinforced concrete beams for coupling (Fig. 1.1b). Concrete coupling beams are advantageous because of the consistency in materials used, less complex beam to wall joints, as well as an increase of fire and environmental protection for the post-tensioning tendons. The new system eliminates the diagonal reinforcement by using a combination of high-strength unbonded post-tensioning (PT) steel with top and bottom horizontal mild steel (U.S. Grade 60) reinforcing bars to develop the coupling forces. The PT force is provided by multi-strand tendons placed inside ungrouted ducts (to prevent bond between the steel and concrete) through the center of each coupling beam and the wall piers. The mild steel bars at the beam ends are designed to yield and dissipate energy while the PT tendon gives the system self-centering capability, thus creating an efficient structure.

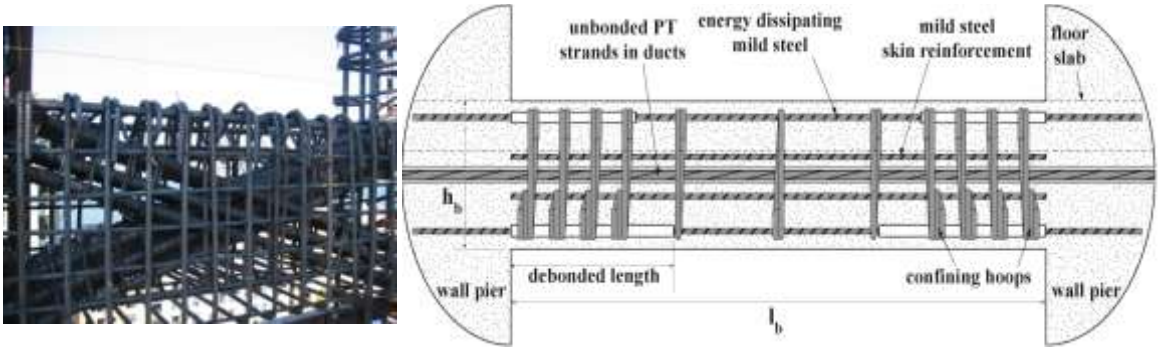

(a) (b)

Figure 1.1: RC coupling beams: (a) diagonally reinforced beam (courtesy, Magnusson Klemencic Associates); (b) proposed post-tensioned beam

1.2 Research Relationships

The University of Texas at Tyler, the University of Notre Dame and Lehigh University have been funded by NEESR in a joint effort to conduct system-level experimental and analytical research on unbonded post-tensioned coupled shear wall systems. This research is conducted because of the potential of these structures to provide significant construction and performance benefits and the potential of the structures to survive severe earthquakes with little structural damage. As a part of the study, analytical and numerical work has been conducted, supported by large scale testing involving novel data collection methods. The culmination of the NEESR work will be design, construction and testing of 40% scale structures, with construction and testing taking place at the Lehigh NEES site. UT Tyler's main responsibility in the project is the deployment of multiple DIC systems to enhance understanding of coupled shear wall systems and to aid in validating the structural behavior of models. This thesis describes the testing of a 15% scale multi-story structure at UT Tyler. Previous experiments on the use of unbonded post-tensioning to couple RC walls are limited to isolated floor level

subassembly studies (Weldon and Kurama 2007, 2009, 2010). The UT Tyler test is the first known test of a multi-story post-tensioned coupled wall system.

1.3 Research Significance and Scope

The project requires four 3D-DIC systems to be deployed simultaneously during testing; this is a new concept as simultaneous deployment has not been utilized in structural testing of buildings to date. This thesis covers the design, construction and analysis of a 15% scale prototype coupled wall system, and its testing under simulated earthquake loading while being monitored by multiple 3D-DIC systems. Some Specific Tasks to be achieved by this thesis are given below:

- Design and Construct a 15% Scale prototype coupled wall system using post-tensioning.
- Test the prototype under earthquake simulation in order to determine the structural behavior of the specimen.
- Monitor the specimen during testing with multiple DIC systems to collect the greatest data possible from every iteration of the test.
- Analyze the data collected from DIC systems and traditional data collection systems, compare and validate the data sets.
- Compare collected data with analytical analysis using finite element analysis to corroborate results and structural behavior.

Some Specific Goals of this thesis are given below:

- Perform the first ever physical model testing of a multi-story reinforced concrete coupled wall system.
- Provide data to validate the novel deployment of multiple DIC systems

simultaneously.

- Validate the analysis technique used here for testing coupled wall systems.
- Establish actual structural behavior of reinforced concrete coupled wall systems.
- Recommend improvements on data collection procedure using this technology, and conclude whether the coupled wall system is a valid system for actual construction.

1.4 Summary of Findings

A 15% scale prototype coupled wall system using post-tensioning was designed and constructed. The prototype was then tested to determine the structural behavior of the specimen. During testing, four DIC systems were simultaneously deployed to monitor the specimen, collecting the greatest amount of data possible from every iteration of the test. It is believed that this test represents the first instance of four DIC systems being deployed simultaneously as part of a building structure test. The data collected from the DIC systems and other traditional data collection systems (digital pressure gages, load cells and string potentiometers) were compared to validate the data. Furthermore, the data was further validated using finite element analysis, corroborating results and structural behavior. This thesis presents the first ever physical model testing of a multi-story reinforced concrete coupled wall system.

The following major conclusions are made based on the results presented herein:

- The 15% scaled model behaved as expected and showed some of the anticipated benefits of a coupled wall system.
- It is possible to coordinate multiple digital image correlation systems simultaneously, and use data collected from multiple systems interactively.

- The relatively simple modeling tools that were employed appear to capture the system behavior well.
- There are several limitations of the current experimental setup, the three major being:

  (1) Scaling the specimen meant that C-shaped walls became rectangular shaped, the slabs at the floor levels and energy dissipation steel in the coupling beams could not be included;

  (2) The forces in the beam post-tensioning cables were less than as designed, and

  (3) The tension reinforcement necessary to resist the base moment in each of the piers pulled out of the structural couplers in the foundation at lower than the design load.
- A detailed data set characterizing the deformations of all the elements of a multi-story coupled wall system has been presented and is available for use in calibrating more complex models.

In each of these areas, the following additional conclusions are noted:

SYSTEM BEHAVIOR

- The design procedure for the post-tensioned coupled wall system yielded a structure that performed as expected, and the analytical models yielded predictions in good agreement with measured behavior.
- As expected, the neutral axis depth decreased as the drift of the system increased. However, the measured results indicate that the tension pier does not necessarily have a smaller neutral axis depth for the duration of the test. This is believed to be

caused by the rebar pull-out at the foundation-pier joint which could have occurred unequally or at different loads in the two wall piers.

- The curvature in the piers due to axial elongation in the beams is illustrated through the deflected shape profile.
- The strain maps generated by the DIC showed that for phases I and II tension cracking occurred in the tension (West) pier while shear cracking was shown in the compression (East) pier. For phase III, the strain maps showed tension cracking in both piers due to existing cracks in the tension pier (West) from the previous testing phase.
- The strain maps generated by the DIC were also able to validate the use of the 2D-DIC systems at the bases of the piers by establishing small out-of-plane movements.
- When considering drift, the results for gap openings correlate well with the numerical model generated by ABAQUS.
- The deflected shape of the beams at all stories show little curvature; the system is dominated by rigid body movement.
- In the experiments, the axial elongation of the beams was similar in phase I and phase II for all three stories. In phase III, the 3rd story beam elongated significantly less than the other stories.
- The foundation did not contribute to rotation, slip or uplift during the test.

MULTIPLE DIGITAL IMAGE CORRELATION

- The use of multiple DIC systems provides a much larger supply of information about the specimen and helps to better establish its overall behavior.

- Because the data was collected the same time for each system, the information from more than one system can be used to calculate a single parameter.
- This data could not have been captured so easily or at all with traditional measurement techniques. A single DIC system could not have captured enough data to establish the behavior of the specimen. This test could only realistically have been conducted using multiple DIC systems.

ANALYTICAL MODELING

- The simple ABAQUS model created appears to provide reasonable results as it matches the experimental deformation data well; it also matches the more complex DRAIN-2DX model reasonably.
- The amount of angular gap opening at the beam ends was consistent with the predicted angular openings produced by the ABAQUS model.
- The deformations presented in Chapter 7 correlate well between the measured DIC data and the ABAQUS model results.
- The ABAQUS model and DRAIN-2DX model response quantities (pier base moment, base shear, and axial forces, beam end moment, end shear, and axial forces) match reasonably well, given the simplicity of the ABAQUS model, especially considering the elastic-plastic behavior of the concrete material properties.
- The ABAQUS model appears to provide a reasonable alternative for preliminary design and behavior characterization, given its relative simplicity. This data set is now available for calibrating more complex coupled wall system models.
- The ABAQUS deflected shape of the beams at all stories also show little

curvature; the center lines of the deflected shapes are essentially straight. As with the pier deflections, the values did not correlate well with the ABAQUS model at similar applied lateral loads, but when compared according to drift, the behaviors were comparable.

SYSTEM LIMITATIONS

- Because of the limitations, the specimen did not reach the expected design load of coupled wall system. Notwithstanding, the structure was scaled appropriately.
- When considering the rotations of the pier bases during the test, it is clear that the expected rotations, even when comparing drift, are much smaller than the measured rotations. This is potentially due to the rebar in the base of the piers pulling out of the foundation during testing.
- Error in the pretensioning of the gravity cables and the beam story cables likely had very little effect on the structure's response.
- The effectiveness of the moment steel crossing the foundation pier joint greatly affects the behavior of the coupled wall system. This is the greatest contributing factor to the difference between measured and expected results.
- The issue of rebar pull-out can be avoided completely by casting the entire system at the same time rather than casting separately and grouting the wall piers into place.
- While post-tensioning the cables in the system, the cables in the beams were post-tensioned consecutively and therefore the force in the cables that were post-tensioned first decreased as the others were put into tension. To address the first problem, depending on the type of machine used for post-tensioning, it is

recommended that a pressure measurement device be applied to the machine so that the tension applied can be monitored during application.

1.5 Organization of the Thesis

The remainder of this thesis is organized as follows:

Chapter 2 – Background: This chapter provides a review of the technologies used in this research as well as a brief review of past research conducted on reinforced concrete coupled wall systems. The impact of previous research on the current project is also discussed.

Chapter 3 – Apparatus and Instrumentation: This chapter provides general information for all apparatuses and instrumentation used for testing. A review is provided of the layout, design and capacity of the structure supporting the forces being applied to the specimen, hereafter to be called the load frame. Information regarding the implementation and use of digital image correlation systems as well as the specifications of the systems used is provided. Information pertaining to the iNET data collection system and associated parts and load cells is also given in this chapter.

Chapter 4 – Specimen Design: A description of the target model, 15% UT Tyler model, and the decisions that created the final design are given in this chapter, as well as the strong floor anchorage system, also called tie-downs.

Chapter 5 – Construction and Materials: This chapter describes the methods of construction for the 15% model used in this project, the materials used in construction, and their properties.

Chapter 6 – Test Protocol: This chapter describes how the test was completed and how the multiple digital image correlation systems were coordinated during testing.

Chapter 7 – Experimental Results: This chapter covers the results interpreted from the data collected during experimental testing. These results are based on the measured data from the iNET system and the digital image correlation systems.

Chapter 8 – Finite Element Analysis: This chapter provides the descriptions of both ABAQUS and DRAIN models. Additionally, a parametric study based on the ABAQUS model, and a comparison of the results from ABAQUS and DRAIN-2DX is presented.

Chapter 9 – Conclusions and Recommendations: The last chapter of this thesis provides a verification that the purpose of the thesis has been fulfilled, a brief look into the future work of the NEES project, recommendations for the future experimental and analytical research, and conclusions made about this project.

CHAPTER 2: BACKGROUND

This chapter provides a brief review of past research conducted on coupling wall systems that have led to the current research conducted for this thesis, specifically the research of traditional coupling beam systems, embedded steel beam coupling systems, non-embedded steel beam systems, unbonded post-tensioned precast coupling beam systems, and multistory post-tensioned reinforced concrete coupled wall systems. The impact of previous research on the current project is discussed. The basic theory of digital image correlation systems is highlighted to include any weaknesses of the method and any previous applications of the system. This portion validates the ability of the digital image correlation systems to accurately and efficiently collect the pertinent data for this test.

2.1 Previous Research

Reinforced concrete coupled shear wall structures are commonly used in the United States as the primary lateral load resistance system in multistory buildings. The lateral stiffness and strength of concrete walls can be significantly increased by coupling the walls. The typical coupled wall system consists of two or more vertical shear wall piers connected by coupling beams which are placed at floor and roof levels to disperse shear and dissipate energy over the height of the structure. Traditionally, researchers focus on cast in place reinforced concrete coupling beams that are embedded into the wall structure (e.g., Harries et al. 2000; Harries 2001). To achieve ductile behavior, the most

common practice for RC coupling beams in seismic regions is the diagonally reinforced system (Barney et al. 1978; Tassios et al. 1996; Bristowe 2000; Galano and Vignoli 2000; Canbolat et al. 2005). As shown in Fig. 1(a), the placement of two intersecting groups of diagonal reinforcing bars through the beam and into the wall piers is a major challenge in practice. For seismic conditions, ACI 318 (2011) entails extensive requirements for the design and detailing of coupling beams. The primary reinforcement in these types of beams is two groups of diagonal bars from one corner to the other diagonal corner of the beam. These diagonal bars are confined by transverse reinforcement across the span of the beam and anchored into the walls.

Because of the difficulty in constructing this type of coupling beam, different types of coupling beams have been investigated. The first progression into coupling wall systems was the embedded steel coupling beam. Previous researchers (Shahrooz et al. 1993; Harries et al. 1993, 2000; El-Tawil et al. 2002) have shown that the lateral stiffness and strength of concrete walls can be significantly increased by coupling the walls using these embedded steel beams. Because of the difficulty in properly embedding steel into concrete walls, whether a steel beam or diagonal rebar reinforcement, without causing damage to the walls, a new type of coupled wall system using steel beams that are not embedded in the walls has been investigated (Shen and Kurama 2002; Kurama and Shen 2004), with the use of post-tensioning cables, previously used for post-tensioned mat foundations, to support non-embedded steel coupling beams. Post-tensioned coupling beams offer critical advantages over the conventional coupling systems made with monolithic concrete and embedded steel beams, such as simpler, and therefore less costly, construction details, a reduction in the damage in the structure, and a self-centering

capability of the structure.

The research conducted by Shen and Kurama 2000 utilized steel coupling beams, while the research discussed here uses precast reinforced concrete beams for coupling. Concrete coupling beams are advantageous because of the consistency in materials used, less complex beam to wall joints, as well as an increase of fire and environmental protection for the post-tensioning tendons. Previous experiments on the use of unbonded post-tensioning to couple RC walls are limited to isolated floor level subassembly studies (Weldon and Kurama 2007, 2009, 2010). The research presented here is the first known physical experimental evaluation of a multi-story post-tensioned coupled wall system. This section represents an overview of previous research conducted on coupling wall systems.

2.1.1 Traditional Coupling Beam Studies

Traditionally, researchers focus on coupling beams that are cast in place reinforced concrete coupling beams that are embedded into the wall structure (e.g., Harries et al. 2000; Harries 2001). To achieve ductile behavior, the most common practice for RC coupling beams in seismic regions is the diagonally reinforced system (Barney et al. 1980; Bristowe 2000; Galano and Vignoli 2000; Canbolat et al. 2005).

2.1.1.1 Barney et al. 1980

The current ACI 318 shear strength limit for RC coupling beams was adopted based on experimental testing presented in Barney et al. (1980). A total of 8 beam specimens were tested under reversed-cyclic loading to failure; two of these beams were diagonally-reinforced. The testing conducted was approximately one third scale and tested a coupled wall system consisting of two coupling beams embedded in abutment

walls. Figure 2.1 shows the layout use in Specimen C6 of Barney's testing which included diagonal reinforcement. The results of the tests indicated relative influence of different reinforcement details on the hysteretic response of coupling beams, but they do not indicate a system that is better overall for all situations. For very short beams under severe earthquake loads, the diagonal reinforcement may be the best solution, but for other situations, conventionally reinforced beams might be adequate.

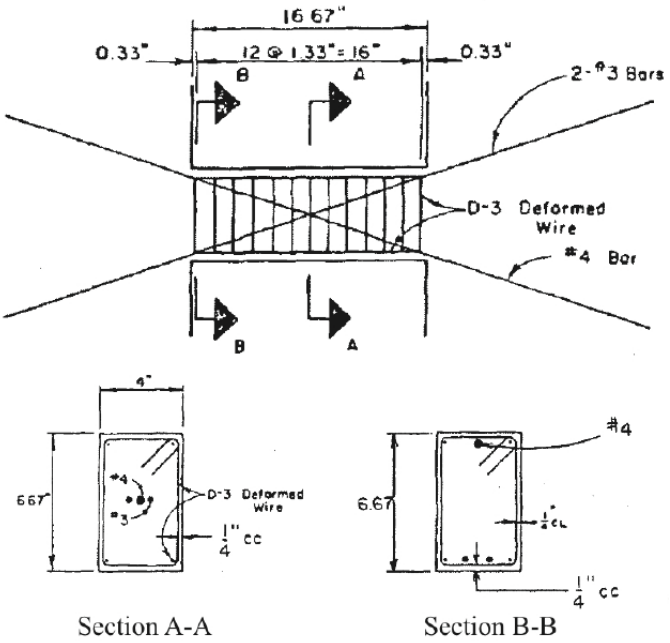

Figure 2.1: Barney et al. Specimen C6 (adopted from Barney et al. 1980)

2.1.1.2 Bristowe 2000

Bristowe explored the possibilities of different arrangements of reinforcement for reinforced concrete coupling beams using high-strength concrete. Six specimens were constructed using normal and high-strength concrete and contained varying amounts of transverse reinforcement consistent with both beam and column detailing requirements for different ductility levels. His tests examined the influence of several parameters, including the effect of confinement, bar buckling and concrete strength. Bristowe's beam

(N1 and H1) reinforcement layout (Figure 2.2) did not use diagonal reinforcement. Beam N1 was constructed using normal strength concrete while beam H1 used high-strength concrete, their reinforcement was identical. Each beam was subjected to reverse cyclic loading in an isolated beam simulation of seismic activity. These beams experienced buckling in the lateral reinforcement which caused spalling and decreased performance. This is to be expected at such severe seismic loading. These tests concluded that the large side cover on the beams caused the spalling to be a major event in the performance of the beams, and that the specimens constructed with high-strength concrete performed as well or better that the normal strength concrete beams.

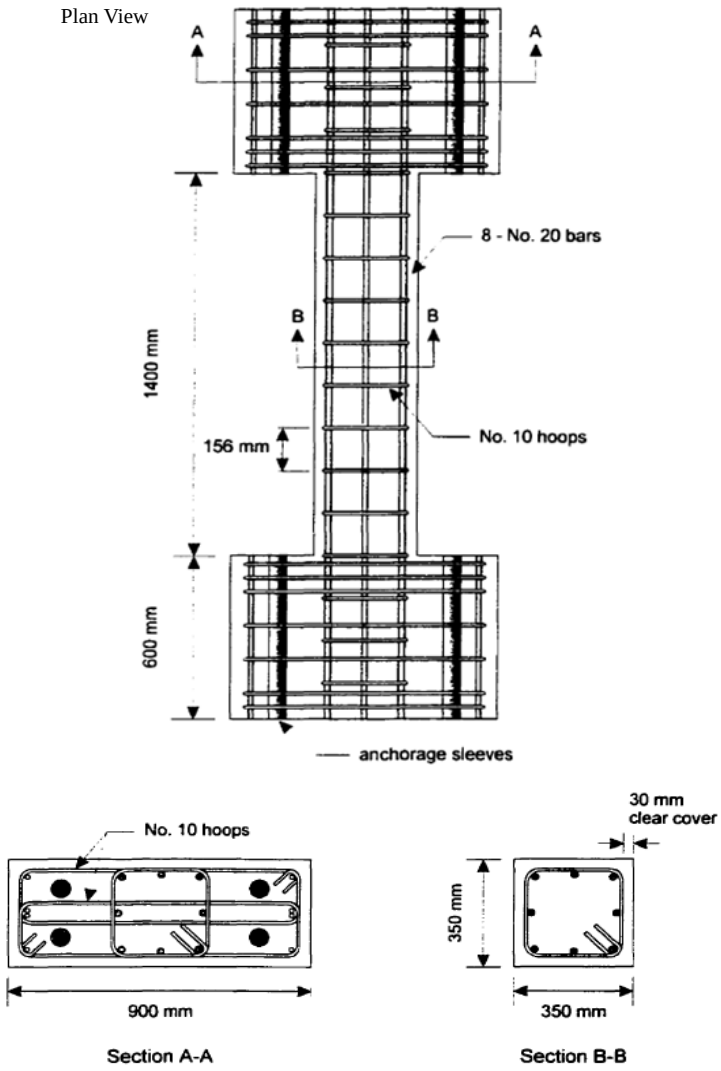

Figure 2.2: Bristowe (2000) Specimen N1 and H1 Reinforcing Details (adopted from Bristowe 2000)

2.1.1.3 Galano and Vignoli 2000

Galano and Vignoli (2000) tested two diagonally-reinforced coupling beams with the same dimensions, but each beam had different reinforcement details (Figure 2.3), b1 and b2 respectively, and material properties. The primary difference between the two beams was the transverse ties that confined the diagonal bar groups in layout b2. A different beam type was also constructed to evaluate the value of the new “rhombic”,

layout c, reinforcement design (Figure 2.3). The three beams were tested as isolated beam structures under reversed cyclic loading. The beams constructed using layout c showed improved ductility and dissipated energy during testing. The authors concluded that the rhombic layout of the main reinforcements gave the highest ductility values, but produced lower values of strength with the same geometrical percentage of steel area as its diagonally-reinforced counterparts.

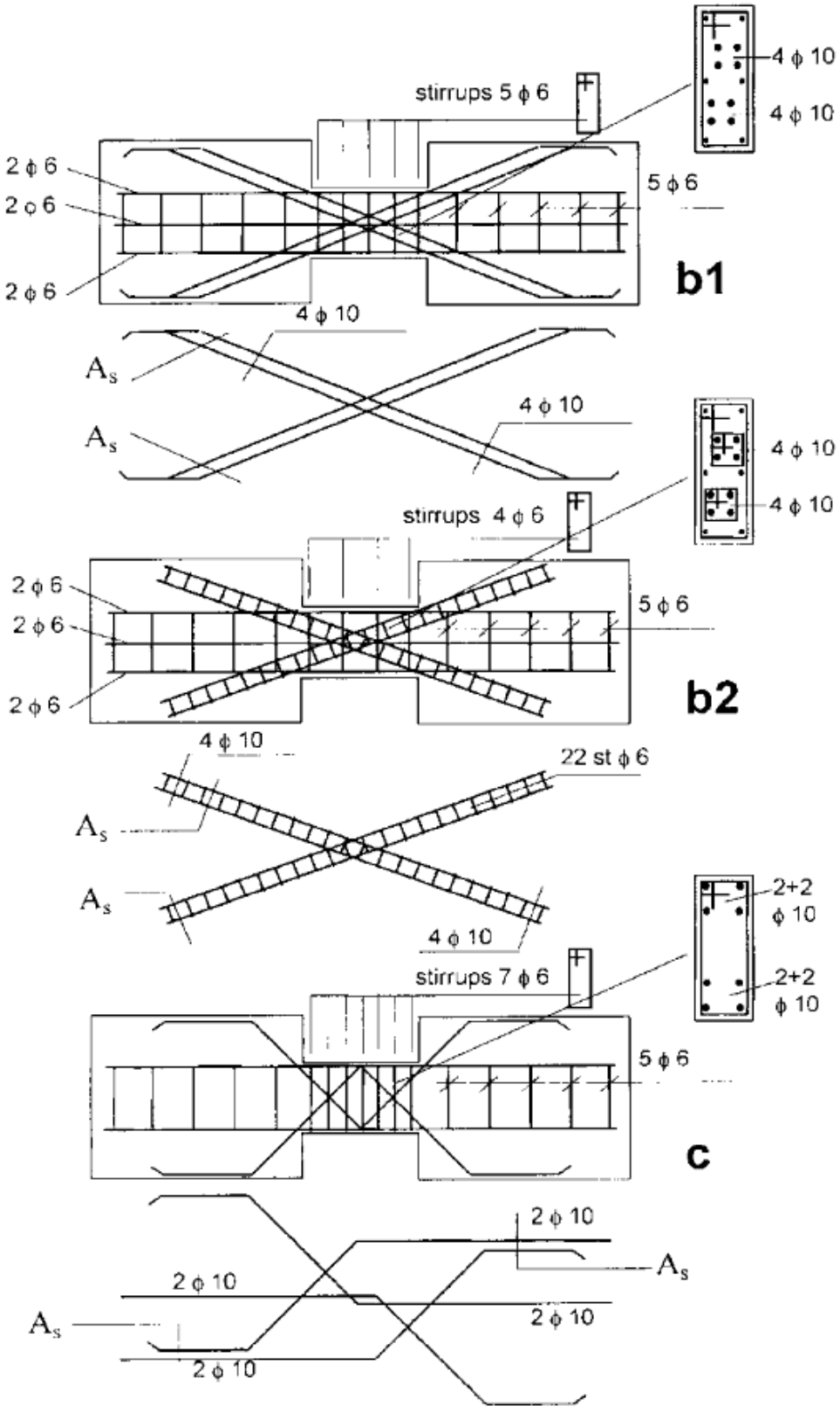

Figure 2.3: Galano and Vignoli (adopted from Galano and Vignoli): includes design layouts b1, b2 and c respectively

2.1.1.4 Canbolat et al. 2005

Canbolat et al. (2005) describes the testing of an isolated short diagonally-reinforced coupling beam. Similar to Galano and Vagnoli (2000), the diagonal bars were confined by transverse hoops. The conclusion of the testing was that the coupling beam provided efficient energy dissipation even at larger drifts based on the lack of buckling and anchorage problems in the diagonal reinforcement. The reinforcement layout is provided below in Figure 2.4.

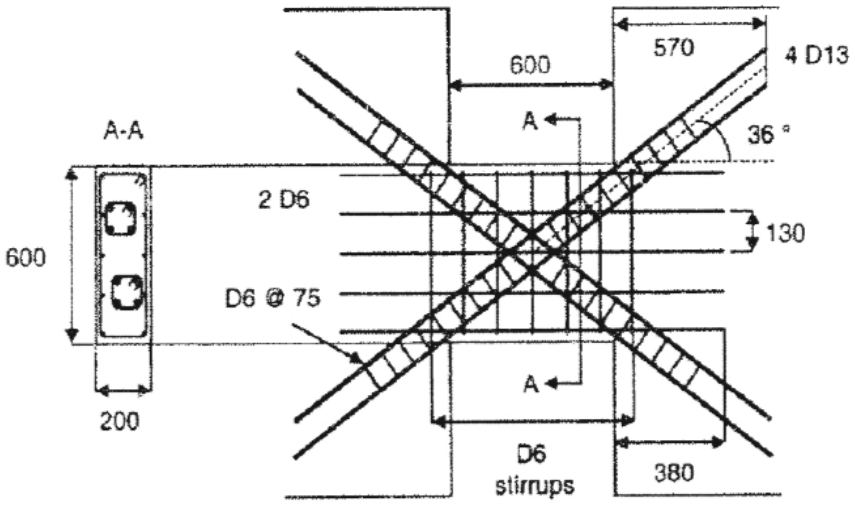

Figure 2.4: Canbolat et al. (adopted from Canbolat et al. 2005) Reinforcement Details for Coupling Beam

2.1.2 Embedded Steel Coupling Beam Studies

Previous researchers (e.g., Shahrooz et al. 1993; Harries et al. 1993, 2000; El-Tawil et al. 2002) have shown that the lateral stiffness and strength of concrete walls can be significantly increased by coupling the walls using embedded steel beams. These systems are often referred to as ‘‘hybrid’’ coupled wall systems. The term hybrid has come to have many meanings in engineering; in this case it refers to the use of steel instead of reinforced concrete for the coupling beam.

2.1.2.1 Shahrooz et al. 1993

To investigate the fundamental cyclic response of this hybrid structural system using embedded steel coupling beams, three half-scale subassemblies were designed, constructed, and tested by Shahrooz et al. 1993. Each specimen consisted of a wall pier and a stub beam embedded in the wall to represent one-half of a coupling beam. The steel coupling beams were found to perform satisfactorily for energy dissipation, but the level of coupling between the steel beams and reinforced concrete walls is limited. The reinforcement details for the wall and beam interface is given in Figure 2.5.

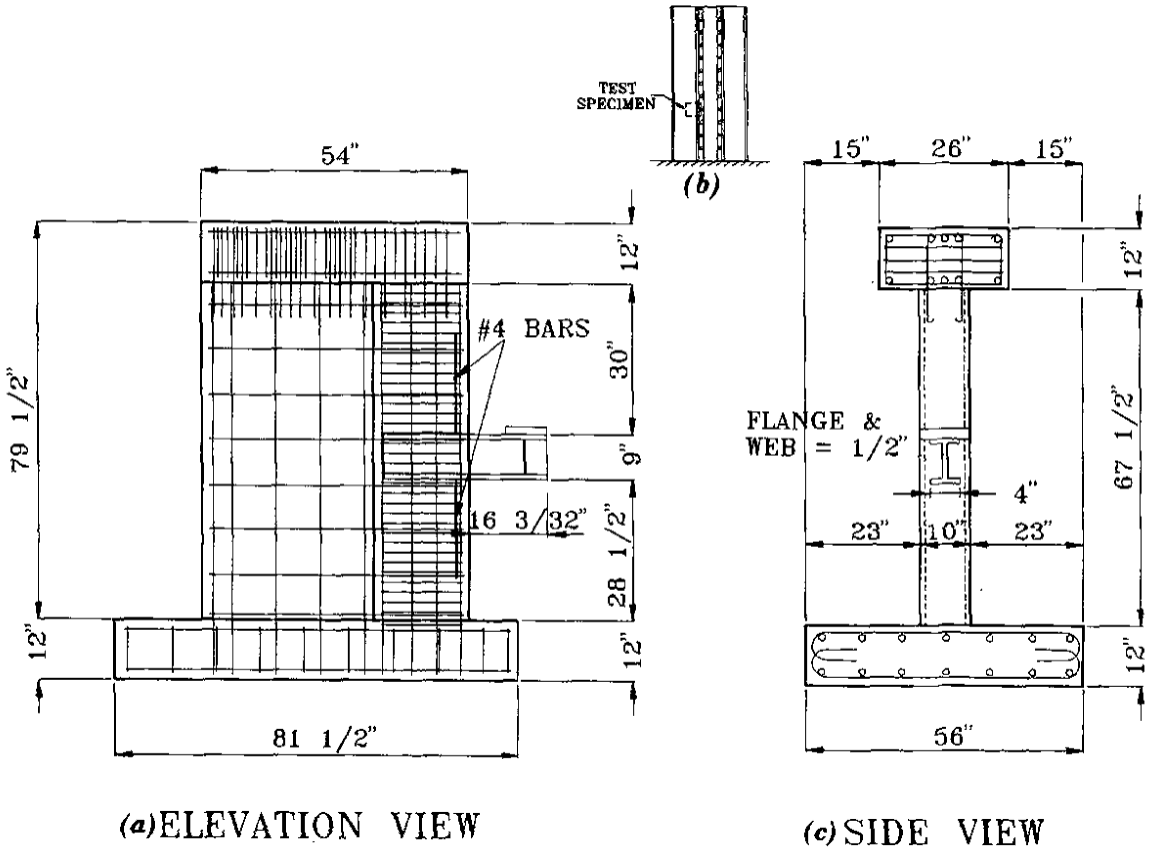

Figure 2.5: Shahrooz et al. 1993 (adopted from Shahrooz et al. 1993): a) Elevation View, b) Beam Location (Global Perspective) and c) Side View (Wall and Beam Details)

2.1.2.2 Harries et al. 1993, 2000

Harries et al. 1993 conducted tests similar to those by Shahrooz et al. 1993 except

that the steel coupling beams in Harries et al. 1993 were designed with stiffeners in order to increase the stiffness at the beam to wall interface. In these tests it was concluded that the stiffeners were useful in dissipating energy and feasible because although they experience severe damage, they can be easily replaced after seismic activity.

Harries et al. 2000 compares the common reinforced concrete reinforcement styles, longitudinally reinforced and diagonally reinforced. This paper reviewed the current state of the art for the design of conventional reinforced concrete, diagonally reinforced concrete, steel and composite steel-concrete coupling beams. The steel coupling beam concept presented here is slightly different than that of Harries et al. 1993 because the steel beams are also presented in a composite form, encased in concrete for better wall to beam coupling. This is not an experimental program, but a review of other research and their differences.

2.1.2.3 El-Tawil et al. 2002

El-Tawil et al. 2002 provided the testing of the hybrid steel coupling wall 12 story system with a static cyclic pushover loading of an analytical model. In the first portion of the publication, the setup, manner of loading, and experimental results for the tests are presented. In the second portion of the publication, the finite element analysis is provided and discussed. The conclusion of this project was that although steel coupling beams are well suited for moderately coupled hybrid wall systems, overcoupling of the system can lead to cracking due to higher shear and compressive axial loads.

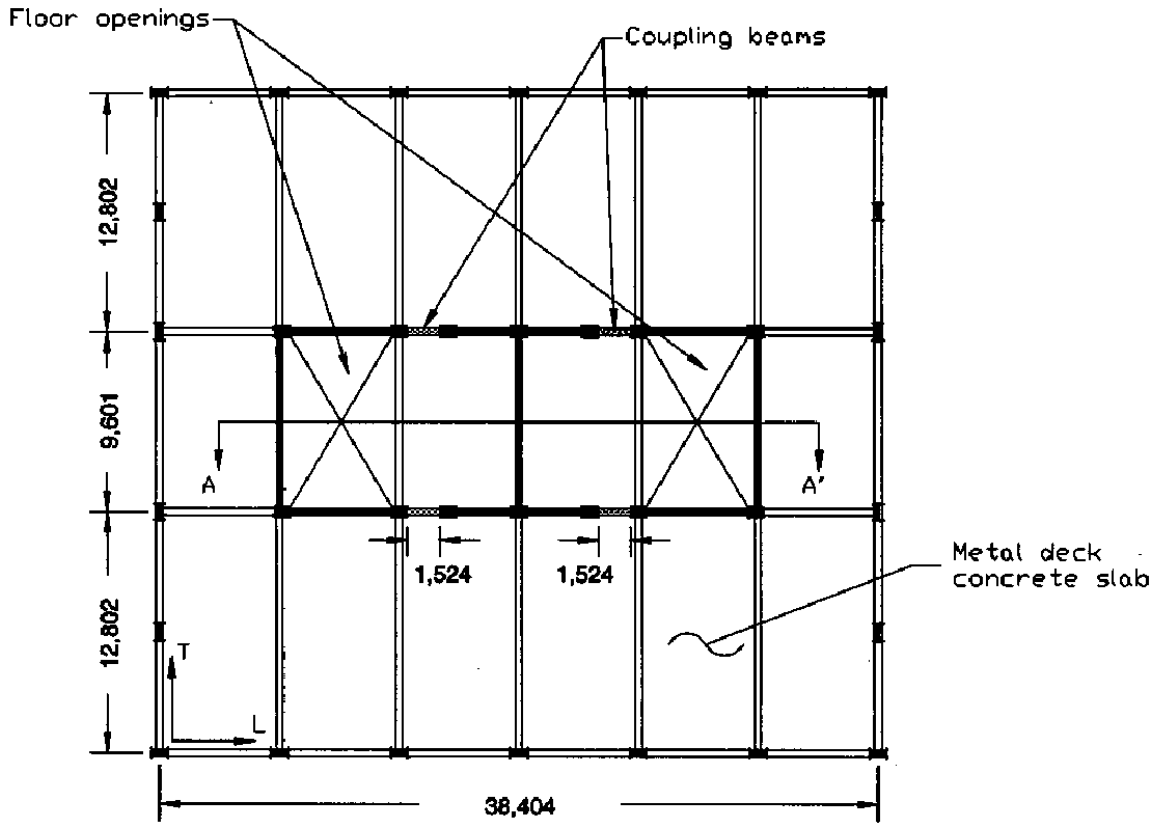

Figure 2.6: El-Tawil et al. 2002 (adopted from El-Tawil et al. 2002) Plan View of U.S.-Japan Theme Structure (all dimensions in millimeters)

2.1.3 Non-embedded Steel Coupling Beam Studies

Because of the difficulty in properly embedding steel into concrete walls, whether a steel beam or diagonal rebar reinforcement, a new type of hybrid coupled wall system using steel beams that are not embedded in the walls has been investigated (Shen and Kurama 2002; Kurama and Shen 2004).

2.1.3.1 Shen and Kurama 2002

Shen and Kurama 2002 investigates a different method of coupling beams than previously discussed. This new method uses unbonded post-tensioning to couple steel beams into concrete walls to achieve coupling without embedding the steel beams into the concrete walls. Based on their analytical modeling, the possibilities of the

effectiveness of this type of hybrid coupling wall system are substantial. First, the steel coupling beam could be added to existing shear walls because this method does not require embedding into the concrete walls. Second, because the steel beam does not behave in a monolithic manner with the shear walls, most of the damage can be contained to the angles that support the steel beam at the wall to beam interface. Also, the post-tensioning force provides a restoring force that pulls the walls and the beams back toward their undisplaced position, providing a large self-centering capability. This is all done without the loss of initial stiffness of the original system or performance during loading.

2.1.3.2 Shen and Kurama 2004

Shen and Kurama 2004 discusses the same method of coupling concrete walls using unbounded post-tensioned steel beams without embedding the beams into the walls. In this publication the method is analytically evaluated both in the nonlinear behavior of a floor level coupled wall subassemblage as well as multi-story coupled wall structures under lateral loads. The experimental investigation of Shen and Kurama 2004 was conducted on half scale coupled wall subassemblies. The conclusion of the extensive research conducted there was that unbounded post-tensioned steel beams provide an effective and feasible system to couple reinforced concrete wall piers in seismic regions. It is important to note that Shen and Kurama 2004 established that the kinking of the post-tensioning strands at the beam to wall interfaces during loading does not have adverse effects on the performance of the post-tensioned cables.

2.1.4 Unbonded Post-tensioned Precast Coupling Beam Studies

Although the research conducted by Shen and Kurama 2004 concluded that non-embedded steel coupling beams were an effective tool for coupling wall systems,

research for post-tensioned coupling systems has been extended to precast concrete beams (Weldon and Kurama 2005, 2007, 2010). These tests are the most directly applicable to the current research.

2.1.4.1 Weldon and Kurama 2005

Weldon and Kurama 2005 evaluated the behavior of unbounded post-tensioned precast coupling systems through analytical modeling. Unbonded post-tensioned coupling beams offer many advantages including reduced damage to the overall structure, significant self-centering capability, and simpler design and construction for the beams and the wall piers. These advantages are similar to those experienced through the use of their steel counterparts.

2.1.4.2 Weldon and Kurama 2007

Weldon and Kurama 2007 provides a description of the nonlinear reversed cyclic behavior of precast concrete coupling beam subassemblies. This publication shows the results for experiments conducted on a half scale wall assembly including a coupling beam and the adjacent concrete wall regions at a floor level. Weldon and Kurama 2007 concluded that although the strength, stiffness, and self-centering capability of the test beam were limited by the deterioration of the patched concrete at one end of the beam and the premature fracture of beam post-tensioning strand wires inside the performance in these categories of the precast concrete beam was better than any monolithic concrete coupling beam, including systems with diagonal reinforcement. The experimental findings here corroborated the conclusions based on analytical data from Weldon and Kurama 2005.

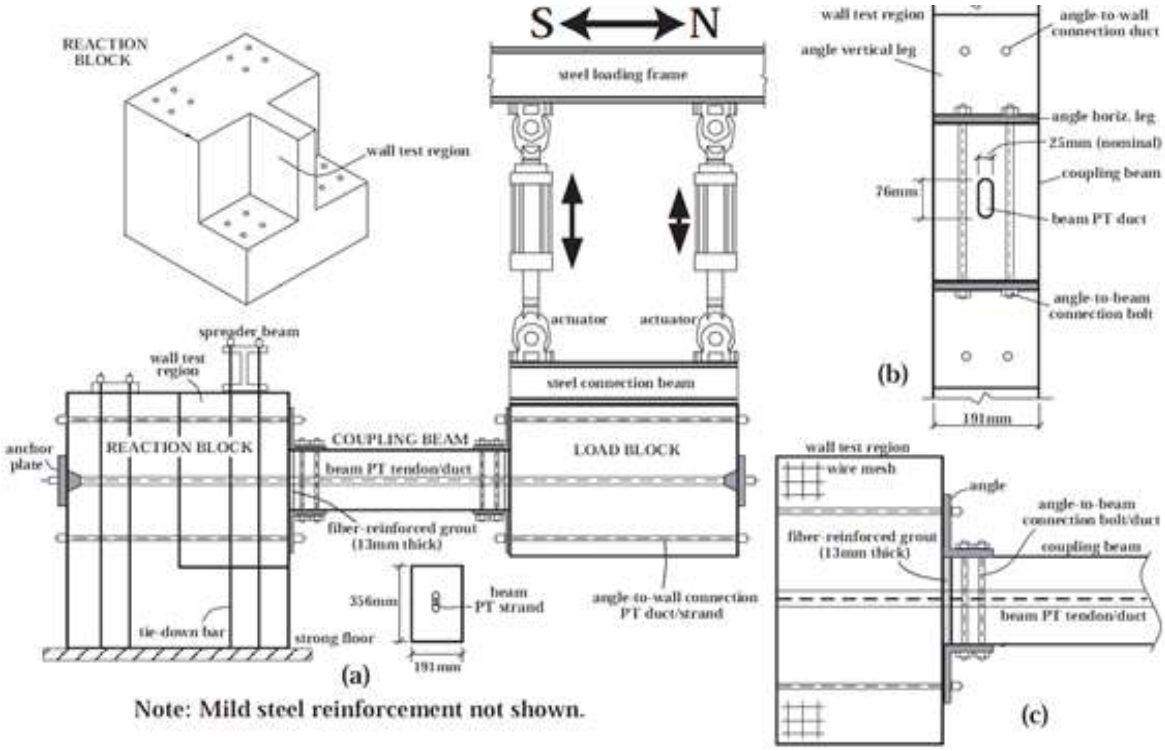

Figure 2.7: Weldon and Kurama 2007 (adopted from Weldon and Kurama 2007) Test set-up: a) Elevation View; b) Beam End View; c) Beam-to-Wall Connection

2.1.4.3 Weldon and Kurama 2010

This publication builds on the earlier work conducted by Weldon and Kurama (2005, 2007) by presenting the results from a subsequent experimental program which conducted experimental testing on four half scale precast concrete coupling beams. This is essentially an extension of the work conducted for Weldon and Kurama 2007, verifying the earlier conclusions with more testing.

2.1.5 Multistory Post-Tensioned Reinforced Concrete Studies

Previous experiments on the use of unbonded post-tensioning to couple RC walls are limited to isolated floor level subassembly studies (Weldon and Kurama 2007, 2009, 2010). Analytical models have been created to simulate a multi-story system, but the test represented in this thesis is the first known physical experimental evaluation of a multi-story post-tensioned coupled wall system.

2.2 Digital Image Correlation Systems

The section presents the important background information pertaining to digital image correlation systems which were used to record data during testing including the history of the method, basic theory, common sources of error, weaknesses of the method, and previous application of the method.

2.2.1 History of Digital Image Correlation Systems

Digital image correlation refers to the type of non-contacting methods that acquire images of an object, store those images in digital form and perform image analysis to extract full field of measurements for patterned objects in the images. The image analysis that calculates the displacements from the digital images is based on the basic principle called photogrammetry.

With the invention of photographic methods, photogrammetry has developed into four major phases (Sutton et al. 2009): (1) plane photogrammetry (1850-1900), (2) analog photogrammetry (1900-1950), (3) analytical photogrammetry (1950-1985) and (4) digital photogrammetry (1985-Present). Although only digital photogrammetry is directly used, the three prior phases contributed greatly in the mathematical developments they established. The most important of these being the relationship between projective geometry and perspective imaging (Sturms and Haick 1883), the fundamental geometry of photogrammetry (Finsterwald 1899), the projective equations and their differentials for stereo-imaging (Otto von Gruber 1924), simplified analytical solutions to the equations of photogrammetry (Church 1945) and the development of the principles of modern multi-station analytical photogrammetry using matrix notation (Schmid 1953).

As digitized images became available in the 1960s and 1970s, researchers began

to develop methods for digitally recording images containing measurement data, to generate algorithms to analyze the digital images and extract measurement data, and to create approaches for automating the entire process. 2D digital image correlation (2D-DIC) was the first progression from photogrammetry principles to correlation systems. This system allows the displacements in plane to be measured from collected digital images. 2D-DIC was used extensively, and continues to be used today, for fracture mechanics: studying the propagation of cracks that cannot be seen on the surface by tracking the deformations and calculating the stresses and strains for measured areas. 2D-DIC is not limited to this field; it is capable of measuring in plane displacements for most any material or object. Since 2D-DIC requires predominantly in-plane displacements and strains, relatively small out-of-plane motion will change the magnification and introduce errors in the measured in-plane displacements (further discussion can be seen in Section 2.3.2).

3D digital image correlation (3D-DIC) is similar to the 2D-DIC in that it also measures displacements; it is different in that 3D-DIC is capable of measuring the out-of-plane displacements and also account for them in the in-plane displacements. Morimoto and Fuligaki were the first to discuss the use of multiple cameras with images of a deforming rectangular grid and Fast Fourier transform methods for image analysis and surface motion estimates in 1993. Chao et al. (1994) successfully developed, automated and applied a two-camera stereo vision system for the measurement of three dimensional crack tip deformations. Because of the nature of the data collections process, from recording images to extracting information, processing any full field of measured data efficiently could only be done with advent of the high-speed computer. These are various

examples of 3D-DIC research that encompass progress of the application and feasibility of the system. As a result of the developments which have occurred in recent years, 3D-DIC is now being used for a wide range of applications on both large and small structures (further discussion can be seen in Section 2.3.5).

2.2.2 Basic Theory

Digital Image correlation was first conceived for measuring deformations incurred by a nominally planar object that is subjected to loading resulting in predominantly in-plane motions. This method has been designated 2D digital image correlation (2D-DIC). This method is limited to monitoring the in-plane motions. Once the motions within the sensor's plane are determined through subset matching, scale factors are used to convert the data into object measurements. The two dimensional (2D) surface strains on the object are extracted using continuum mechanics principles and estimated gradients in the surface displacement components. In order to measure the out-of-plane displacements, another system was developed: three dimensional digital image correlation (3D-DIC).

In 3D-DIC, the measured object is photographed with a pair of digital cameras (Figure 2.8) before, during and after a load event and a stochastic pattern marked on the object is tracked from one set of images to the next such that a full field of displacements is derived. The experimental set-up at UT Tyler is designed to develop a protocol for deploying multiple DIC sensors simultaneously during the same structural test. For the locations and calibration details of the DIC systems used during testing see Chapter 3. The experiment is designed to allow four camera pairs to capture the deformations of key structural components of a coupled post-tensioned shear wall system.

Figure 2.8: 3D-DIC Physical Setup

3D-DIC (Tyson et al. 2002) combines techniques of image correlation with photogrammetric location principles. In photogrammetry, multiple photographs (from different orientations) of a series of targets are captured in order to determine the 3D coordinates of the targets. Three major analytical functions that must be performed to analyze photogrammetric data are: (1) triangulation; (2) resection (the process of determining the camera's position and orientation); and (3) self-calibration of the camera to eliminate errors such as those due to lens and camera imperfections, temperature and humidity effects, etc. Accuracy and precision in industrial photogrammetry are related to the size of the measured object and numerous other factors, including the resolution of

the captured images, camera calibration, angles between captured photos, redundancy in the appearance of targets appearing in multiple images, and the placement of the targets.

For DIC, sample preparation consists of applying a regular or random pattern with good contrast to the surface of the measured object. The pattern will then deform with the object under load. For 3D-DIC, the object is captured in a stereo pair of high quality cameras while it is loaded. Typically, these two cameras are mounted at either end of a base bar such that their relative position and orientation with respect to one another is fixed and known (Figure 2.8).

Thousands of unique correlation areas known as facets are defined across the entire imaging area of the measured object. The center of each facet is a measurement point that is tracked in each successive pair of images by employing a similarity measure such as the normalized cross correlation. An image correlation algorithm, as for example, the iterative spatial domain cross correlation algorithm, tracks facets by maximizing this similarity measure. Three-dimensional locations of these facets are calculated before and after each load step, yielding displacements. Tracking the dense cloud of points within the applied pattern provides displacement information that is full field.

2.2.3 Common Sources of Error

The basic sources of error for this system are the error in calculated initial position of the cameras, error in triangulation, and the error in correlation of facets. Most of these can be minimized based on other aspects of testing.

One of the simplest ways to control noise in data collection is to make a pattern that is appropriate to the field of view (FOV). Although the only requirement for functionality of the pattern is that it is of high contrast, for best results, the pattern must

fit with the FOV. As the FOV decreases, the size of each facet also decreases. Because of this, the pattern must also become smaller in order for each facet to contain both colors.

Because this technology is camera based, two other seemingly obvious adjustments are necessary for the application of 3D-DIC: appropriate lighting and elimination of obstructions. The lighting is crucial to the clarity of this form of data acquisition. If the images that are captured are too dark, often the software is unable to track the facets for lack of clarity. It is similar to looking at a candid photo that was taken at night without a flash; sometimes it is difficult to see the object of the image. Also, when using an image based technology, the object must be seen clearly in order for the data to yield results. As with any camera, if the view of the object of interest is obstructed, then no information about the object can be gathered from the image.

Most importantly, the quality of the calibration for the FOV is directly related to the quality of the data collected from the image series. After a calibration is completed, a chart of resulting parameters is given by the program. This chart lists important bounds such as the calibrated volume, deviation of facets and similar limits. If the FOV used is larger than the area that the system is calibrated for, the data outside that area is typically very noisy. Also, if the deviation found from the calibration is very large, then the error in the data calculated also is increased.

A simple test can be conducted to ascertain the amount of noise or error that exists in the images before testing begins. Take two successive images, one immediately after the other, while the specimen is still unloaded. Then, by processing the two images, the first as a baseline and the second as a test, the amount of noise and its location in the FOV will be clear. Because the specimen is still not loaded, the displacements, and

FOV will be clear. Because the specimen is still not loaded, the displacements, and therefore the stresses, should be equal to zero. Any place within the FOV that has some displacement other than zero is where error has occurred. By conducting this test prior to collecting data with the system, errors can be recognized and addressed before wasting effort in the data collection.

2.2.4 Weaknesses of the Method

In a 2D-DIC system designed for in-plane displacement measurement of an object, an out-of-plane displacement will cause a change of magnification of the imaging system, and thus introduce an apparent in-plane displacement. The apparent in-plane displacement causes measurement error in the collected data. Because of this, the object of interest must move a minimal amount in order for the 2D data collected to be accurate.

Some key limitations to the use of 3D-DIC systems are the relatively complicated optical system, mismatch in triangulation of corresponding points, a defocus problem when the magnification is high or the physical system is moved and a laborious calibration process.

In addition both DIC systems require constant attention to prevent alteration to the position of the cameras, the full physical setup, and the constant sightline to the specimen during data collection, any of which would result in error in data collection. If these alterations are not prevented, not only does this result in data error, but can result in the decalibration of the system. After data collection is complete, the post-processing can be very laborious and requires specific training on the software.

2.2.5 Examples of Application

Both 2D and 3D-DIC systems have been used for various purposes, from large to

small. The DIC systems are not limited to only simple static concrete or steel specimens, the following case studies show how the technology has enhanced understanding of structural behavior in applications as far ranging as fracture analysis, material characterization, geotechnical studies, infrastructure analysis, and even extensive studies in biomechanics.

2.2.5.1 Fracture Analysis

A very common use for digital image correlation is that of fracture analysis. Because of the system's ability to recognize tension in the surface of an object before a visible crack appears, the DIC is the optimal tool to predict and analyze cracking and fracture in materials.

Lin and Labuz (2012) used DIC to monitor the locations of sandstone fracture during testing. The different Brazilian testing methods for sandstone were evaluated using DIC by Stirling et al. (2012). Perdomo et al (2012) used DIC to corroborate predictions about fracture behavior in reinforced concrete elements. Carloni and Subramaniam (2012) monitored fatigue crack growth at an interface using DIC. The damage within a fiber reinforced mortar wall was monitored by Rouchier et al. (2012) using DIC. Erdem and Blackson (2012) used DIC for fracture analysis of impact-fractured surfaces. Hamad et al. (2013) monitored the flexural cracking behavior of concrete prisms using DIC.

2.2.5.2 Material Characterization

Unlike traditional methods of data collection such as strain gages and linear variable differential transformers (LVDT), DIC camera system can be easily transported, adapted and reused. Because of the flexible nature of DIC, it is an efficient method for

defining the material characteristics of many types of materials. Giancane et al. (2010) used DIC to define the fatigue evolution of fiber reinforced composites, while Laurin et al. (2012) defined properties of composite materials using DIC.

2.2.5.3 Geotechnical Studies

The behavior and properties of soil are difficult to gather because of its granular nature. Soil, although a solid material is often not considered a solid as an object. Its ability to separate and move easily makes collected data problematic. Because DIC does not need to be attached to an object of interest, it is able to track the deformations in the challenging material. Peth et al. (2012) used DIC to monitor the deformation of soil under mechanical and hydraulic stresses. McGinnis et al. (2012) explored the use of DIC in collecting the stresses from the compression testing of rammed earth. DIC was used by Helm and Suleiman (2012) to determine the surface soil structure interaction of laterally loaded piles.

2.2.5.4 Infrastructure Analysis

The ability of the DIC to view an area, rather than collect data from many isolated points, makes it extremely useful for monitoring several parts of an infrastructure at one time. Its non-contact nature also allows it to be used in the testing of previously challenging practices such as dynamic and fire testing. McGinnis et al (2012) discusses several case studies of DIC application. Among these the dynamic testing of a multistory non-linear frame as well as monitoring the stresses of a fire tested load bearing wall. Kim and Kim (2011) monitored the displacement response of infrastructures using DIC.

2.2.5.5 Biomechanics

Biomechanics is a field in which an enormous amount of testing is required in

order to establish a standard for design because of the extreme variance from person to person. Collecting data on tissues and bone has proven particularly problematic. The limited supply of materials for study produces a need to get the most data out of a test possible. Also, in order to collect accurate data, the material that is tested must be undamaged by the data collection system. DIC's non-contact nature makes it the perfect candidate for biomechanic testing.

Lin et al. (2012) used DIC to monitor testing conducted on a bone-periodontal ligament-tooth fibrous joint. Similarly Yachouch et al. (2012) studies the biomechanics of a weakened mandible using DIC. Moermand et al. (2009) and Gao and Desai (2009) both studied the mechanical properties of human tissues using DIC. The mechanical properties of articular cartilage were studied by Wang et al. (2011) using DIC. A method to measure dynamic dorsal foot surface shape and deformation during linear running was created, using DIC, by Blenkinsopp et al. (2012).

2.2.5.6 Deploying Multiple Sensors

There have been a few successful deployments of multiple DIC sensors. McGinnis et al. (2012) deployed two DIC sensors simultaneously in several of the concrete shear wall tests described previously. The experiment presented in this thesis is the first known instance of deploying as many as four DIC systems simultaneously.

CHAPTER 3: APPARATUS AND INSTRUMENTATION

3.1 Load Frame

The section will cover the basic information on the load frame that was used to support the actuators which applied load to the specimen during testing. This includes the basic layout of the load frame: the simple beam and column arrangement in which members were designed as beam columns, including moment connections which were designed to take moments and shear forces produced by the systems as well as to resist lateral forces and small struts located at the base of the columns to resist out of plane forces. This system was secured to the strong floor beneath using a floor anchor system through the small struts. This section also includes the Load and Resistance Factor Design (LRFD) methodology that was used for the load frame and the final capacity of the frame based on individual portions of the design, as well as the later addition of the strut to add lateral resistance because of large unexpected deformations that prevented progress during testing.

3.1.1 Layout

The layout of the load frame is a simple beam and column arrangement (Figure 3.1) including moment connections to resist lateral forces and small struts at the base of the columns for out of plane resistance. The left column is a W24x117 and the right column is a W18x119. The beam used as the top cross bar was created from two HSS 18x6x⅜ spaced 4 inches apart. The beam used as the bottom cross bar, considered in

some load case scenarios, was created from two HSS 14x6x⅜. The frame is connected to the strong floor beneath using anchors through the small struts located at the base on the columns. The connection details of the load frame can be seen in Figure 3.2.

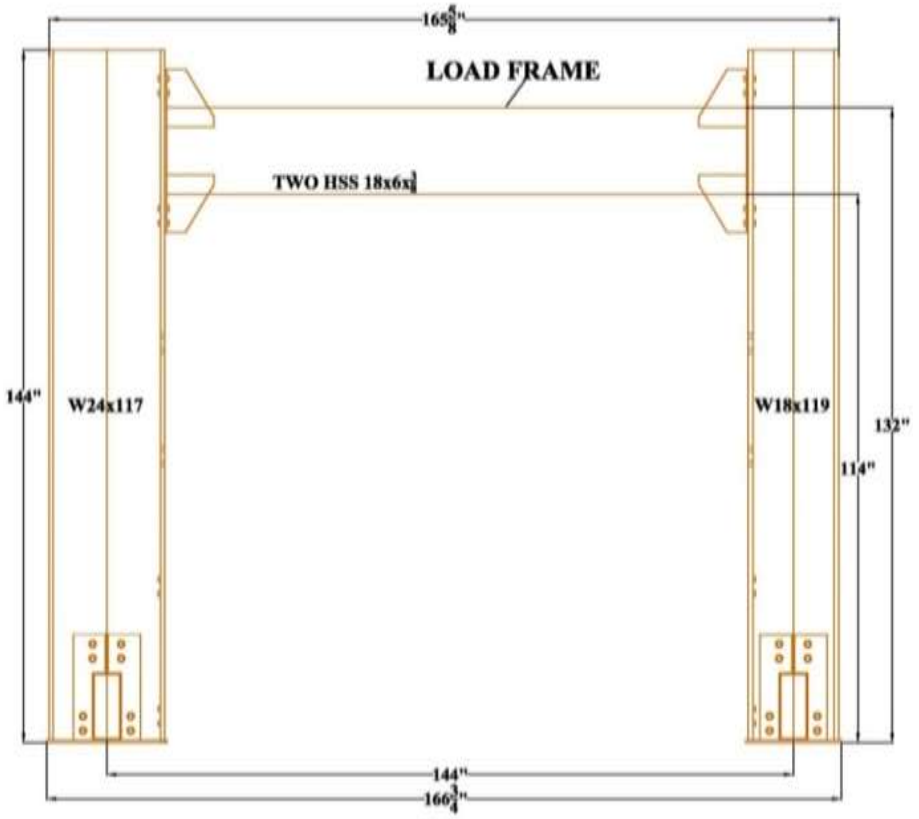

(a)

(b)

Figure 3.1: Load Frame: (a) Schematic; (b) Photograph

3.1.1.1 Connection Details

A basic bolt pattern was used to connect the cross beam to the columns and the columns to the small struts. The first connection plate in Figure 3.2 is from the connection between the cross beam and that columns. The second connection plate in Figure 3.2 is from the connection between the small floor struts and the base of the columns. The third portion of Figure 3.2 is a detailed view of the small struts that resist out of plane deformations. All bolt holes are 1 inch in diameter. Beam end plates (image 1 in Figure 3.2a) are ⅜ inch thick and all other plates are ½ inch thick. The steel tubes used for the small struts are HSS 14x6x⅜.

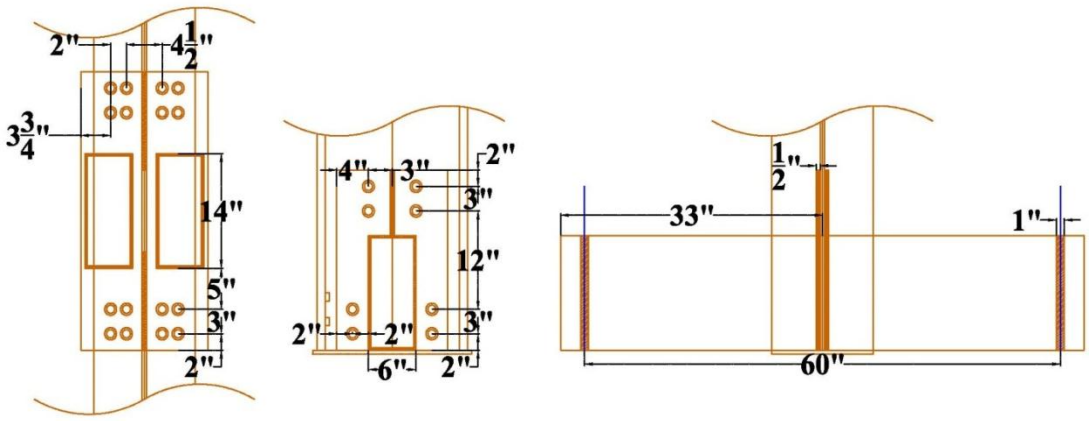

(a)

(b)

Figure 3.2: Connection Details: (a) Schematics; (b) Photographs

3.1.1.2 Strut Details

A later addition of a strut was necessary because of the large lateral deflections experienced during the first phase of testing. With the addition of the strut to the system, the geometry of the strut was determined, as well as the connection detail and anchorage system at the base connection of the strut. Figure 3.3 shows the strut attachment layout in association with the left column where it was connected. The details of the base connection and the column connection can be seen in Figure 3.4. The strut is a W8x31 and the base of the strut was constructed from a W12x65. All plates use 1 inch diameter holes and ½ inch thick steel.

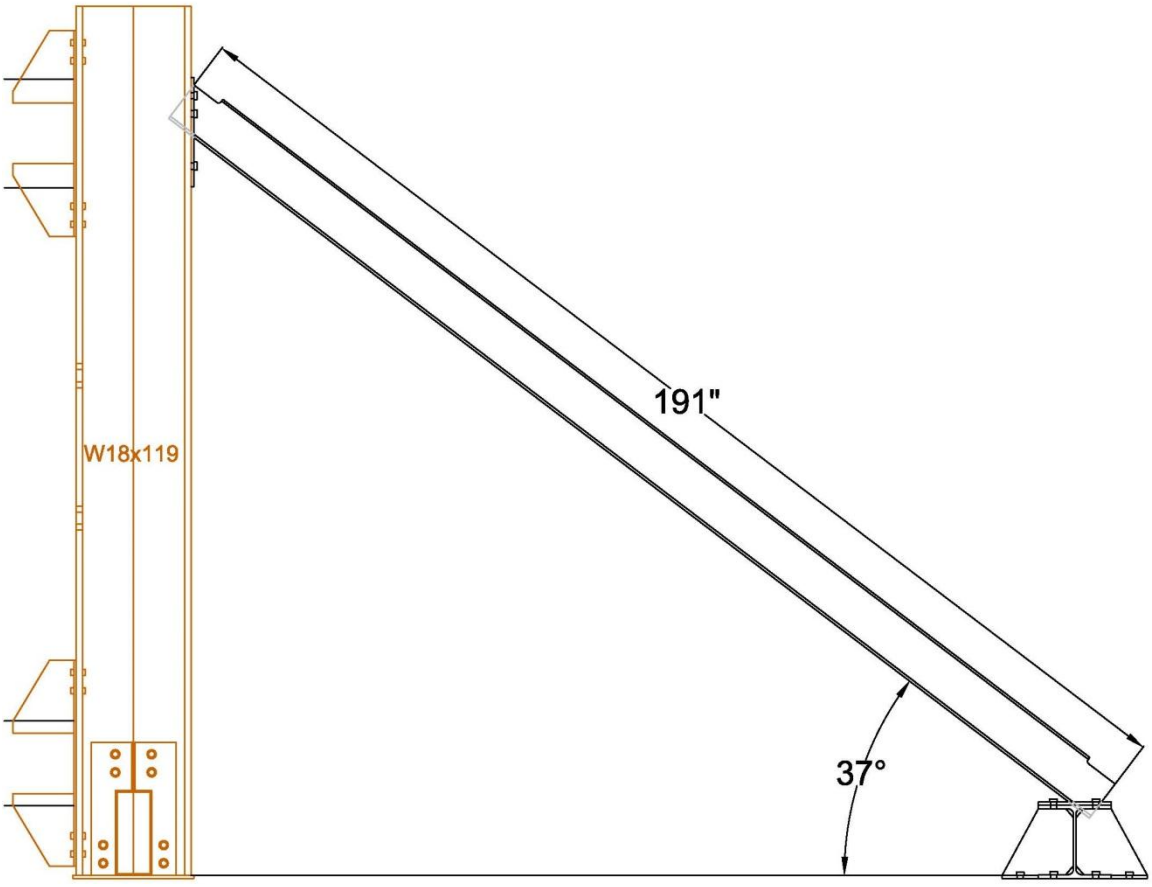

Figure 3.3: Strut Attachment to Left Column of Load Frame

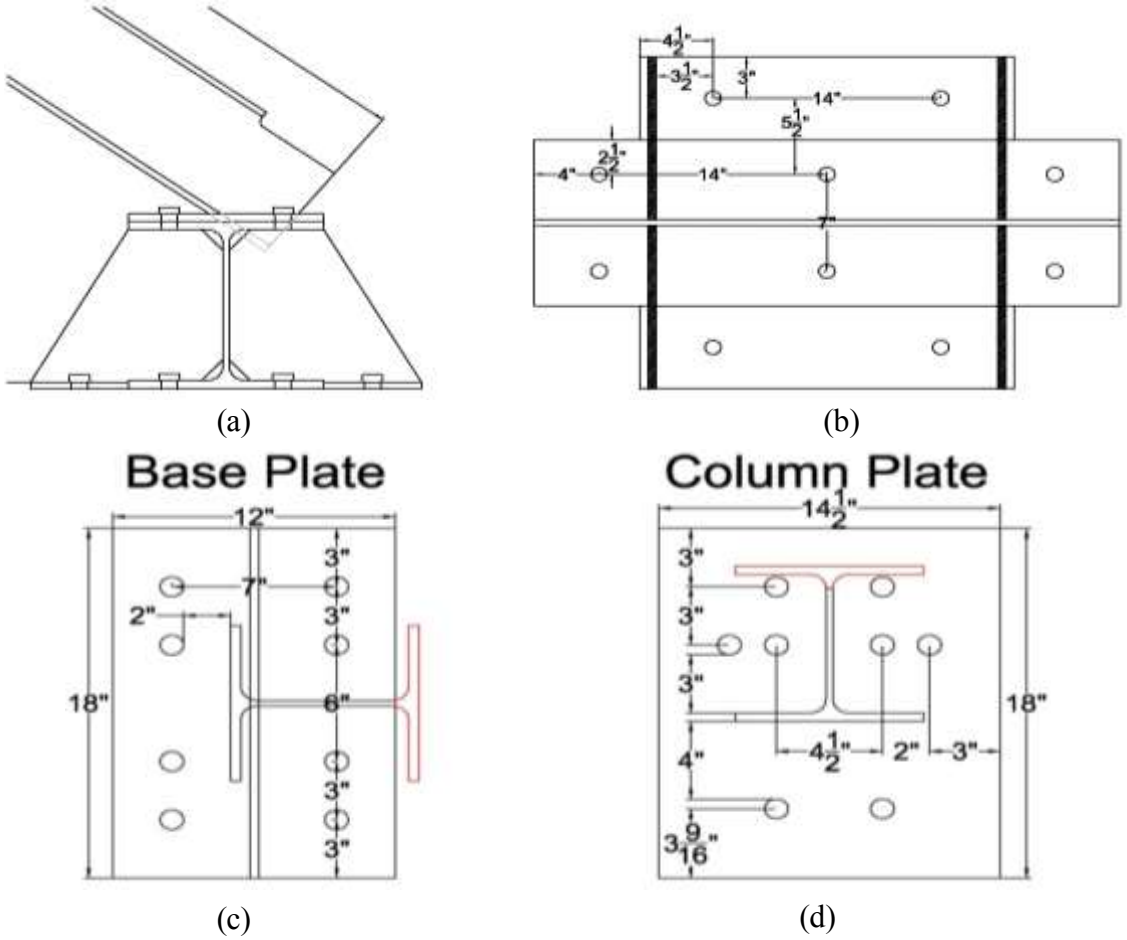

Figure 3.4: Strut Attachment: (a) Side View of for Strut Base Support; (b) Plan View of Strut Base Support; (c) Base Connection Plate; (d) Column Connection Plate

3.1.2 Load Capacity and Design

The capacity of the load frame depends on its configuration because of its ability to use different arrangements. This section will discuss the different configurations, their resulting moments, shear forces and axial forces, their final capacities based on the arrangement, as well as the LRFD methodology used for design. The beams used in all designs are labeled as single HSS tubes, but the effective areas and other structural parameters were doubled for calculations.

3.1.2.1 Design for Top Cross Member Only (without Strut Addition)

This load case employed one cross beam on the top at 10.25 feet from the ground

(based on the center line of the cross beam shown in Figure 3.1) with a single lateral force of 120 kips located 8 feet from the ground. Figure 3.5 shows the member sections and the location of the laterally applied load. The base of the columns were assumed to be pinned.

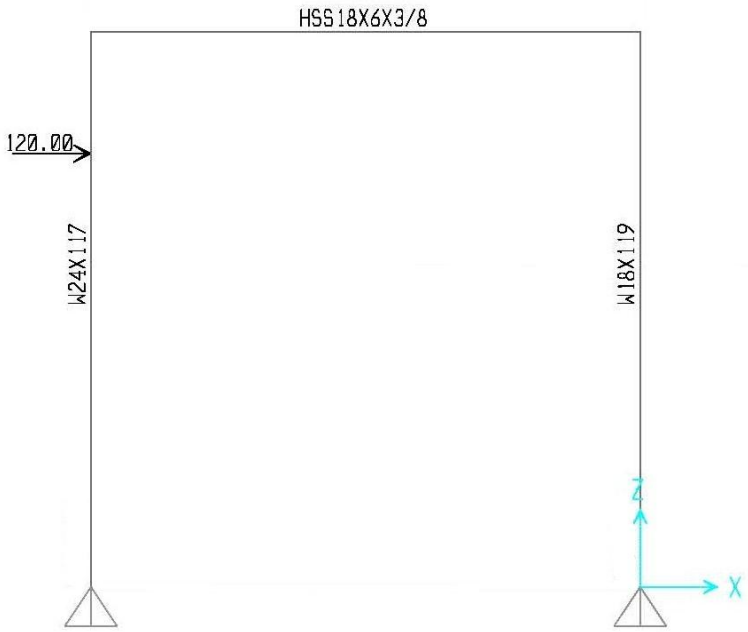

Figure 3.5: Load Frame Configuration (Top Cross Member Only)

3.1.2.1.1 SAP2000 Analysis

SAP2000 was used to model the behavior of the load frame in this configuration. Figure 3.6 gives the resulting in plane bending moment, shear, and axial force diagrams. These demands were used to check the sufficiency of the design capacities. The resultant forces at the base of the columns (shown in Figure 3.7) provided the demand on the base connection and the anchor system.

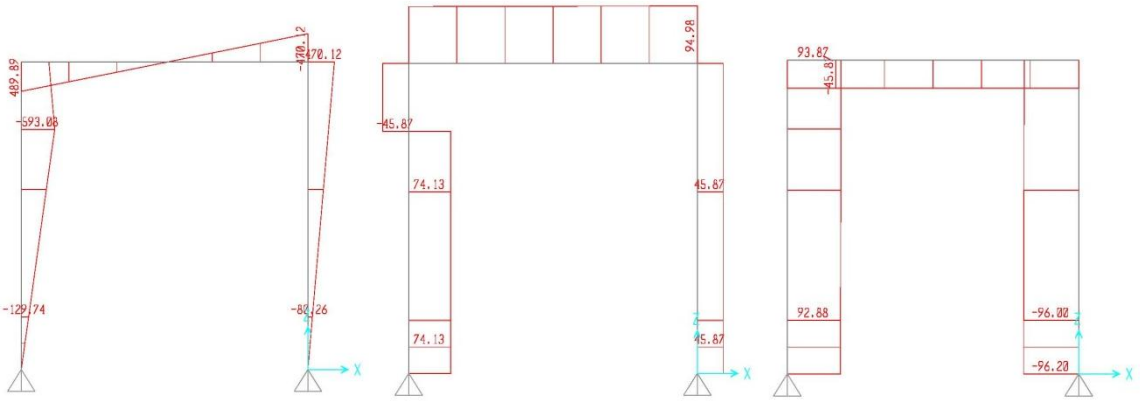

(a) (b) (c)

Figure 3.6: Resulting Diagrams for Top Cross Member Only (without Strut Addition) from SAP2000: (a) Moment; (b) Shear; (c) Axial

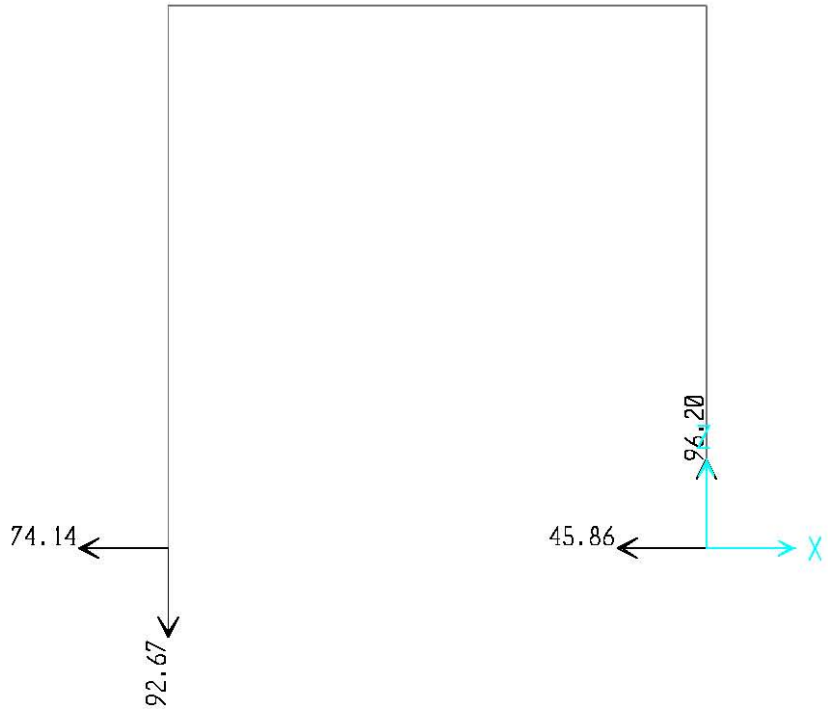

Figure 3.7: Column Base Resultant Forces for Top Cross Member Only

3.1.2.1.2 Demand and Capacity

The demands were taken from the SAP2000 results to determine the adequacy of the design by comparing them with the capacities of the design. The demand and capacity for each member and connection is given in Table 3.1; the ratio of capacity to demand

(i.e. factor of safety) is given in parentheses below each capacity. The demand loads considered are unfactored (γ_i = 1.0 for LRFD) and standard resistance factors were used for capacity design. Because of this, the capacity-demand ratio shown in Table 3.1 is especially conservative. The anchorage system is clearly inadequate for the uplift experienced for this load case, but with the addition of the strut, the system is more than acceptable.

Table 3.1: Demands and Capacities for Top Cross Member Only (without Strut Addition)

		Demand			Capacity			
Member Section	**Design Type**	**Moment (k-ft)**	**Shear (kips)**	**Axial (kips)**	**Moment (k-ft)**	**Shear (kips)**	**Axial (kips)**	**Interaction (Moment and Axial)**
Double HSS 18x6x3/8	Beam	490	95	94	596 (1.216)	588.16 (6.191)	640.51 (6.814)	0.8955
Beam/Column Joint	Moment Connection	28.44	95	--	111 (3.903)	194.4 (2.042)	--	--
W24x117	Column	594	75	93	1230 (2.071)	360.86 (4.811)	1482.3 (15.939)	0.4291
W18x119	Column	470	46	96	983 (2.091)	336.01 (7.305)	1471.4 (15.327)	0.5011
Anchorage System	Floor Connection	--	74.14	96.3	--	168.96 (2.279)	88 (0.913)	--

3.1.2.1.3 LRFD Design Methodology

Load and resistance factor design (LRFD) was used to calculate the capacities of the beams, columns and connections. Several tools from the American Institute of Steel Construction (AISC) steel construction manual such as tables and charts were utilized in order to simplify calculations. The capacities were computed by tracking the forces through the frame by following the load path from the applied loads, transferring the force to the top cross bar, which was treated as a beam, then to the moment connections at the beam to column interface, passed down into the columns, to the small struts and the anchor system in the strong floor beneath the system. For the beams, the limit states of

bending (moment), shear, axial and the interaction of axial and bending were considered.

The moment capacity of the beams was calculated using Table 3-12 of AISC (2011). Shear capacity of the beams was calculated using Section G, Equation G2-1, of AISC (2011). Axial capacity was calculated assuming compression using Section E, Equation E3-1, of AISC (2011). The interaction capacity of axial and bending for the beam was calculated using Section H1, Equation H1-1b, of AISC (2011).

The beam-column interface required a moment connection. The shear capacity was calculated by considering yield, fracture, and block shear for the plate and the column flanges using Section J4 of AISC (2011), Equations J4-1, J4-2, and J4-5, respectively. The shear capacity of the bolts was also considered using the values from Table J3.2 of AISC (2011). These capacities are in resistance of the shear force in the connection; the lowest shear capacity was used for the shear capacity of the connection. The moment capacity of the connection is governed by the capacity of the stiffener and the capacity of the bolts. The stiffener forms a T-shape with the connection plate shown in Figure 3.8. The moment capacity of the stiffener was calculated using plastic moment capacity. The moment capacity of the bolts was calculated using the tension capacities of the bolts, from Table J3.2 of AISC (2011), at distances based on the layout shown in Figure 3.9. The lowest moment capacity was used as the moment capacity of the connection. The capacity of the welds was checked using Section J3 of AISC (2011), Equation J3-2. Table 3.2 shows the capacities for each limit state of the moment connection at the beam-column interface. The yield, fracture, and block shear are not shown because the thickness of the I-beam is greater than the thickness of the plate, therefore the plate will govern. Furthermore, the shear and moment interaction was

investigated (Section J3, Equation J3-3a, of AISC 2011), but the shear load was such that it need not be considered.

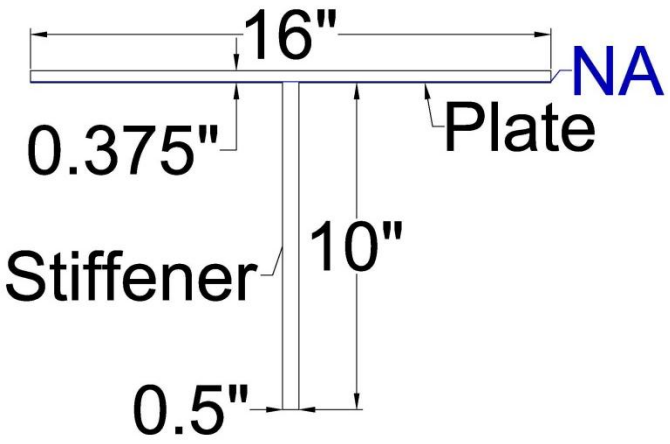

Figure 3.8: Moment Calculation T-Shape

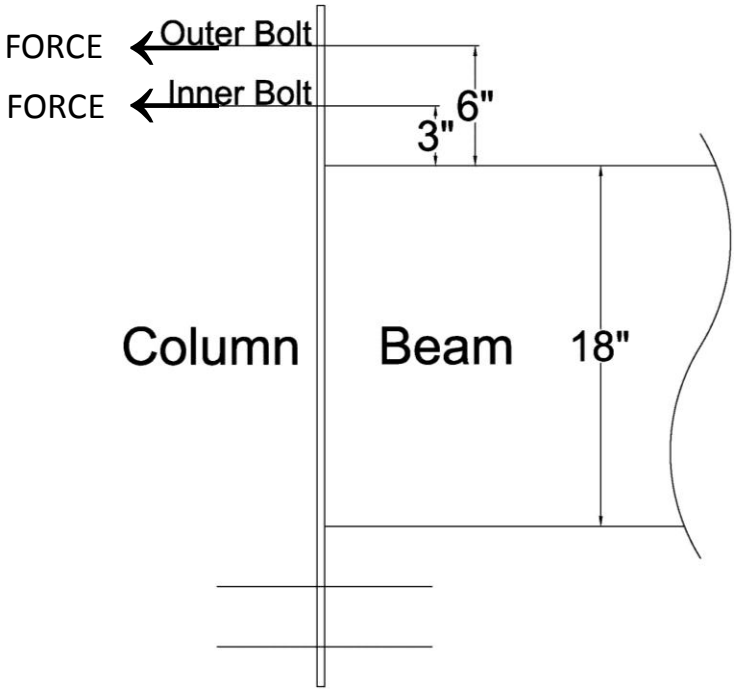

Figure 3.9: Moment Calculation Bolt Layout

Table 3.2: Beam End Connection Limit State Capacities

		Capacity		
		Moment (k-ft)	Shear (kips)	Equation Used
Connection Plate	Yield	--	194.4	J4-1
	Fracture	--	234.9	J4-2
	Block Shear	--	315.9	J4-5
Bolt	Shear	--	328.6	J3-1
	Moment	111	--	Fig. 3.8
Stiffener	Plastic Moment	126	--	Fig.3.7

The columns were then considered with capacities determined similarly to the beams using Table 3-12, Section G2, and Section E3 of AISC (2011) except for the interaction capacity which was calculated for the columns using Table 6-1 of AISC (2011); they were determined to not be slender and then the resulting bending, shear, axial and interaction capacities were considered.

The small struts were attached to the base of the columns using a base plate attached to the end of the small struts. The base of the columns were connected to the strong floor directly using anchors attached to the strong floor beneath; these anchors are used for anchor capacity, they provide little out of plane moment resistance. The small struts were then connected to the strong floor by attaching long anchors through the struts – see Section 3.1.1.1. The purpose of the small struts was to provide lateral load resistance for out of plane forces. The moment capacity for out-of-plane forces for the load frame based on the anchorage system is calculated using distances shown in the layout shown in Figure 3.10. The moment capacities of the bolts and stiffener were calculated in the same manner as the beam-column connection. The moment capacity based on the anchorage system is 290 k-ft, which will allow for up to a 24 kip out-of-

plane force when the lateral load is applied to the highest point on the load frame (12 ft). The moment capacity based on the bolt pattern is 713.2 k-ft, which will allow for up to a 59.4 kip out-of-plane force under the same loading position (12 ft). The moment capacity based on the plate stiffener is 156.64 k-ft, which will allow for up to a 13 kip out-of-plane force. The moment capacity of the stiffener governs the capacity of the out-of-plane moment capacity of the load frame.

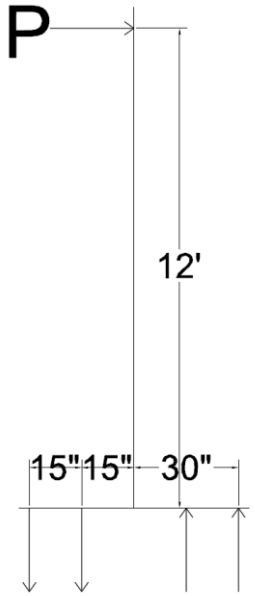

Figure 3.10: Moment Calculation Anchorage Layout

The lateral and vertical forces on the load frame cause a compression force in one column and uplift on the other. The lateral force also causes a shear force at both column bases. These forces must be resisted by the anchorage system. The shear force at the base of each column is resisted by the friction between the frame and the floor, based on the weight of the frame, and the shear strength of the anchors connecting to the floors based on ASTM A193. The compression force at one column base is easily resisted by the strong concrete floor beneath the load frame. The uplift force is resisted by the tension capacity (ASTM A193) of the anchors to the floor. The anchorage is found to be slightly

inadequate for the load cases that do not include the strut addition (see Tables 3.1, 3.3, 3.4, and 3.5). The strut addition will be necessary for all future testing.

Analysis was only conducted for a lateral force applied at the left side of the load frame although the lateral force may also be applied to the right side of the load frame. An in depth analysis of the load reversal was not investigated as the only difference in the two scenarios are the columns shapes; both columns were found to have adequate capacities which meet the applied demand.

3.1.2.2 Design for Two Cross Members (without Strut Addition)

This load case employed one cross beam on the top at 10.25 feet from the ground and one cross beam with the center line located 21 inches from the ground with a single lateral force of 120 kips located 8 feet up from the ground. See Figure 3.11 for member sections.

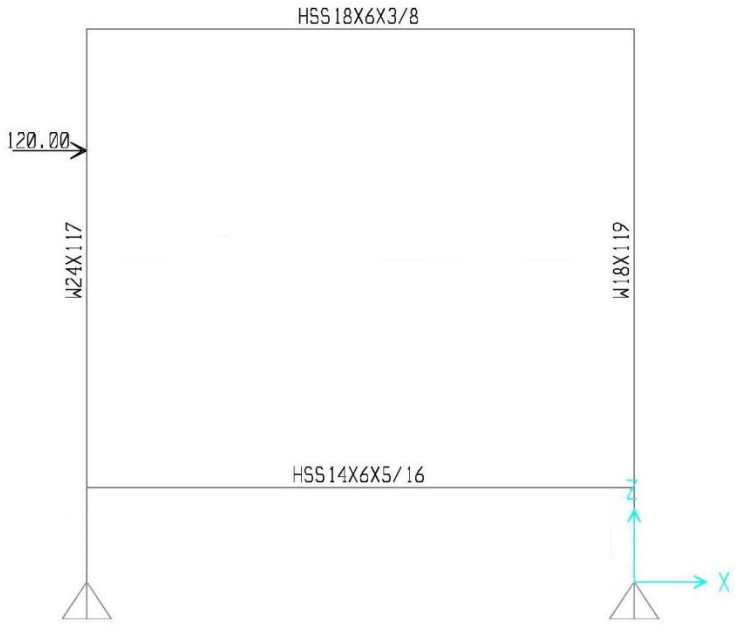

Figure 3.11: Load Frame Configuration (Two Cross Members)

3.1.2.2.1 SAP2000 Analysis

SAP2000 was used again to model the behavior of the load frame. Figure 3.12 gives the resulting bending moment, shear, and axial force diagrams. These demands were used to check the sufficiency of the design capacities. The resultant forces at the base of the columns provided the demand to the base connection and the anchor system. Figure 3.13 shows the resultant forces at the base of the columns.

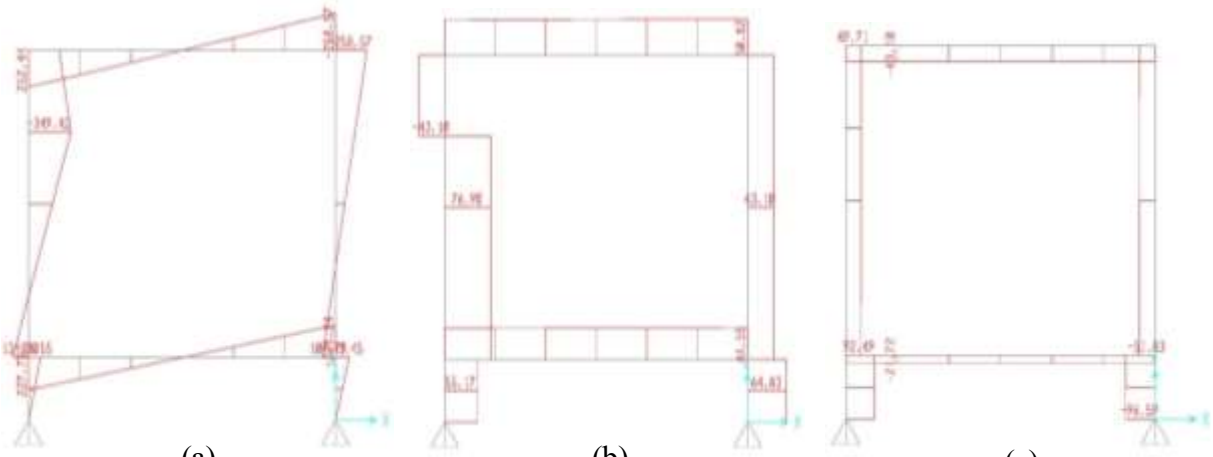

(a) (b) (c)

Figure 3.12: Resulting Diagrams for Two Cross Members (without Strut Addition) from SAP2000: (a) Moment; (b) Shear; (c) Axial

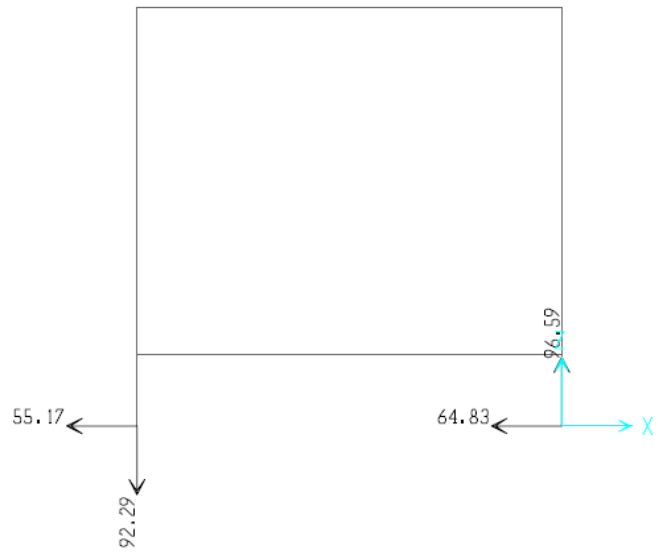

Figure 3.13: Column Base Resultant Forces for Two Cross Members

3.1.2.2.2 Demand and Capacity

The demands were taken from the SAP2000 results to determine the adequacy of the design by comparing them with the capacities of the design. The demand and capacity for each member and connection is given in Table 3.3; the ratio of capacity to demand is given below each capacity. The design capacities were determined similarly to Section 3.1.2.1.3. The anchorage system is clearly inadequate for the uplift experienced for this load case, but with the addition of the strut, the system is more than acceptable.

Table 3.3: Demand and Capacity of Load Case: Two Cross Members (without Strut)

		Demand			Capacity			
Member Section	**Design Type**	**Moment (k-ft)**	**Shear (kips)**	**Axial (kips)**	**Moment (k-ft)**	**Shear (kips)**	**Axial (kips)**	**Interaction (Moment and Axial)**
Double HSS 18x6x3/8	Beam	259	51	44	596 (2.301)	588.16 (11.532)	640.51 (14.557)	0.4689
Beam/Column Joint	Moment Connection	27.1	51	--	111 (4.096)	194.4 (3.812)	--	--
W24x117	Column	350	77	93	1230 (3.514)	360.86 (4.686)	1482.3 (15.939)	0.3258
W18x119	Column	259	65	97	983 (3.795)	336.01 (5.169)	1471.4 (15.169)	0.3087
Double HSS 14x6x5/16	Beam	228	45	22	335.4 (1.471)	379.4 (8.431)	777.87 (35.358)	0.6939
Anchorage System	Floor Connection	--	64.83	96.59	--	126 (1.944)	88 (0.911)	1.2122

3.1.2.2.3 LRFD Design Methodology

The LRFD design methodology for this load case is the same as the first load case, shown in Section 3.1.2.1.3.

3.1.2.3 Design for Phase I Testing (without Strut Addition)

This load case employed one cross beam on the top at 10.25 feet from the ground with a lateral force of 120 kips located 8 feet up from the ground and a downward vertical force of 50 kips located 2 feet in from the left side. See Figure 3.14 for member

sections and load case layout.

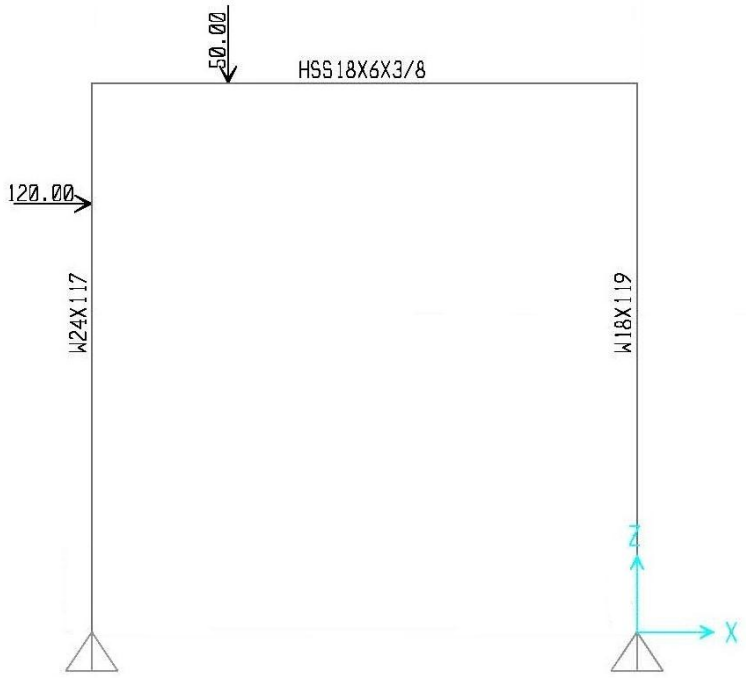

Figure 3.14: Load Frame Configuration (Phase I Testing)

3.1.2.3.1 SAP2000 Analysis

A simple SAP2000 model was used to model the behavior of the load frame in this configuration. Figure 3.15 gives the resulting diagrams for the moments, shear forces, and axial forces. These demands were used to check the sufficiency of the design capacities. The resultant forces at the base of the columns were used as the demand on the base connection and the anchor system. Figure 3.16 shows the resultant forces at the base of the columns.

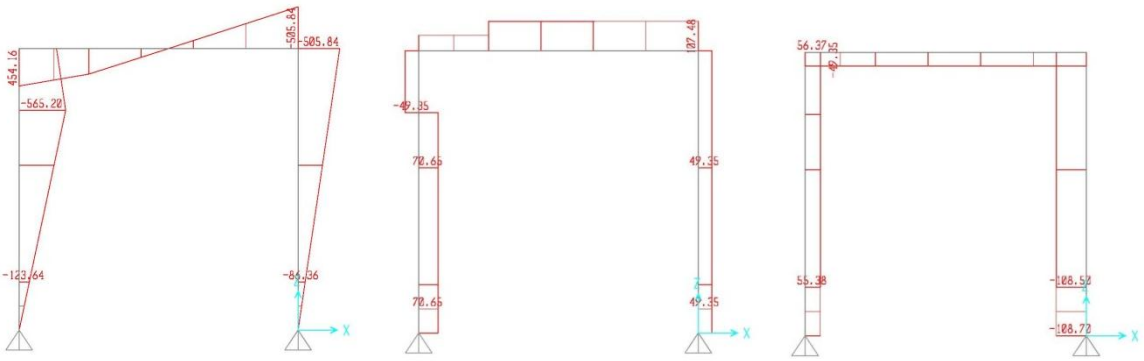

Figure 3.15: Resulting Diagrams for Phase I Testing (without Strut Addition) from SAP2000: (a) Moment; (b) Shear; (c) Axial

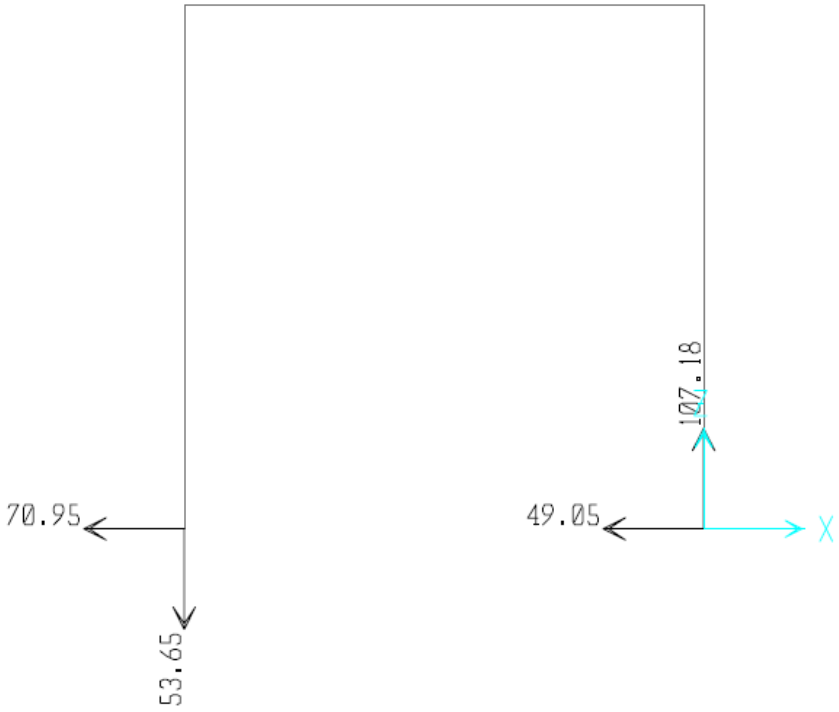

Figure 3.16: Column Base Resultant Forces for Phase I Testing

3.1.2.3.2 Demand and Capacity

The demands were taken from the SAP2000 results to determine the adequacy of the design by comparing them with each capacity of the design. The demand and capacity for each member and connection is given in Table 3.4; the capacity-demand ratio is given

below the capacities in the table. The design capacities were determined similarly to Section 3.1.2.1.3. The anchorage system is clearly inadequate for the uplift experienced for this load case, but with the addition of the strut, the system is more than acceptable.

Table 3.4: Demand and Capacity of Load Case: Phase I Testing (without Strut Addition)

		Demand			Capacity			
Member Section	**Design Type**	**Moment (k-ft)**	**Shear (kips)**	**Axial (kips)**	**Moment (k-ft)**	**Shear (kips)**	**Axial (kips)**	**Interaction (Moment and Axial)**
Double HSS 18x6x3/8	Beam	506	108	50	596 (1.178)	588.16 (5.446)	640.51 (12.810)	0.8880
Beam/Column Joint	Moment Connection	52.95	108	--	111 (2.096)	194.4 (1.800)	--	--
W24x117	Column	566	73	56	1230 (2.173)	360.86 (4.943)	1482.3 (26.470)	0.4564
W18x119	Column	506	50	109	983 (1.943)	336.01 (6.720)	1471.4 (13.499)	0.5437
Anchorage System	Floor Connection	--	70.95	107.18	--	126 (1.776)	88 (0.821)	1.342

3.1.2.3.3 LRFD Design Methodology

The LRFD design methodology for this load case is the same as the first load case. The methodology used in the first load case can be seen in Section 3.1.2.1.3.

3.1.2.4 Design for Phase II and III Testing (with Strut Addition)

For the tests that form the bulk of this thesis (see Chapter 6 and 7), the structural tests were completed in three Phases – I, II, and III. A full description of the loading in these phases is given in Section 6.1.

A strut addition was necessary based on the large lateral deflections from the one cross beam load case of 0.967 in prior to the addition of the strut. The new load case employed one cross beam on the top at 10.25 feet from the ground as well as a diagonal strut on the right side that provided additional lateral load resistance in the plane of the lateral load. A lateral force of 120 kips is applied 8 feet up from the ground and a

downward vertical force of 50 kips located 2 feet in from the left side. This load case with the strut addition allowed only 0.126 inches in lateral deflection. See Figure 3.17 for member sections and load case layout.

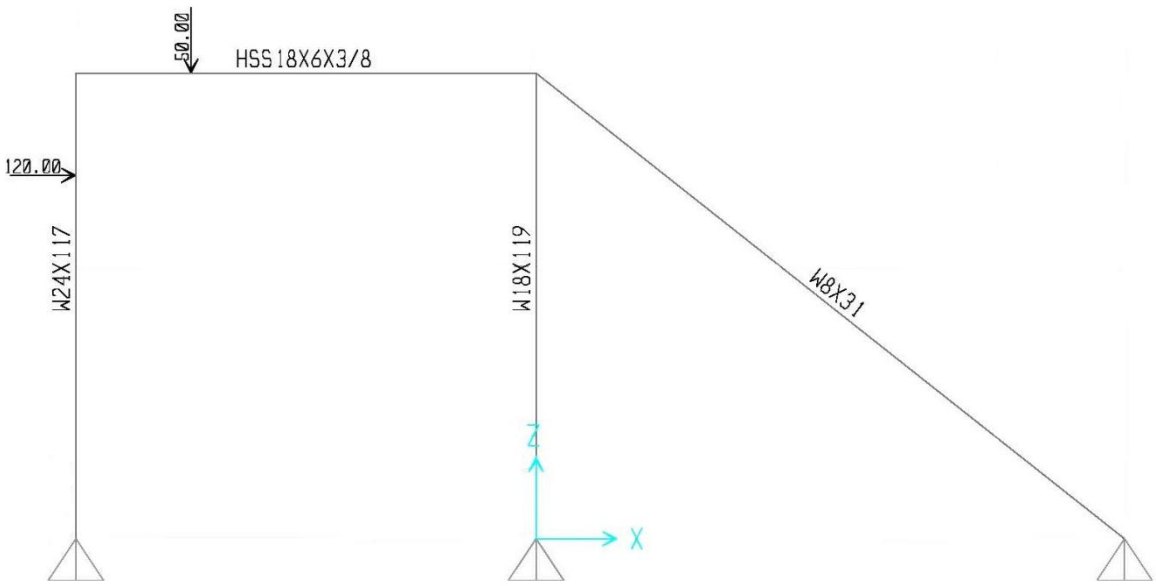

Figure 3.17: Load Frame Configuration (Phase II and III Testing)

3.1.2.4.1 SAP2000 Analysis

Again, SAP2000 was used to model the behavior of the load frame. Figure 3.18 gives the resulting bending moment, shear, and axial force diagrams. These demands were used to check the sufficiency of the design capacities. The resultant forces at the base of the columns provided the demand on the base connection and the anchor system. Figure 3.19 shows the resultant forces at the base of the columns.

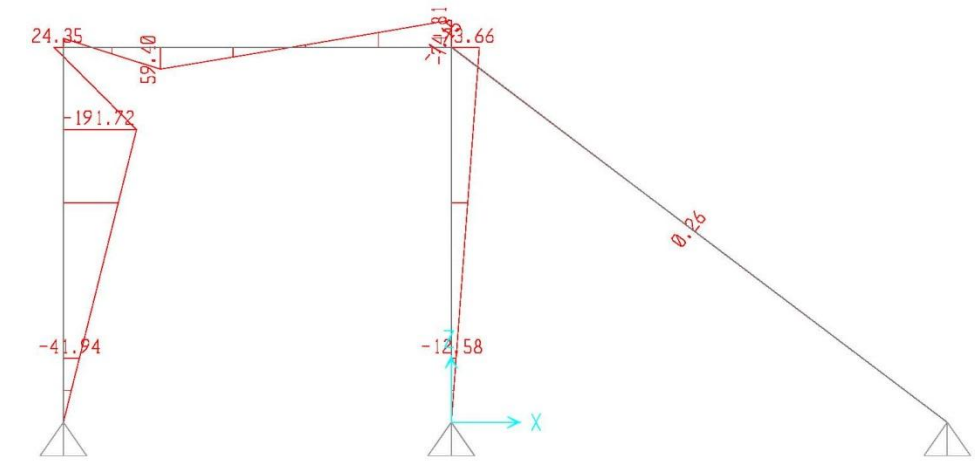

(a)

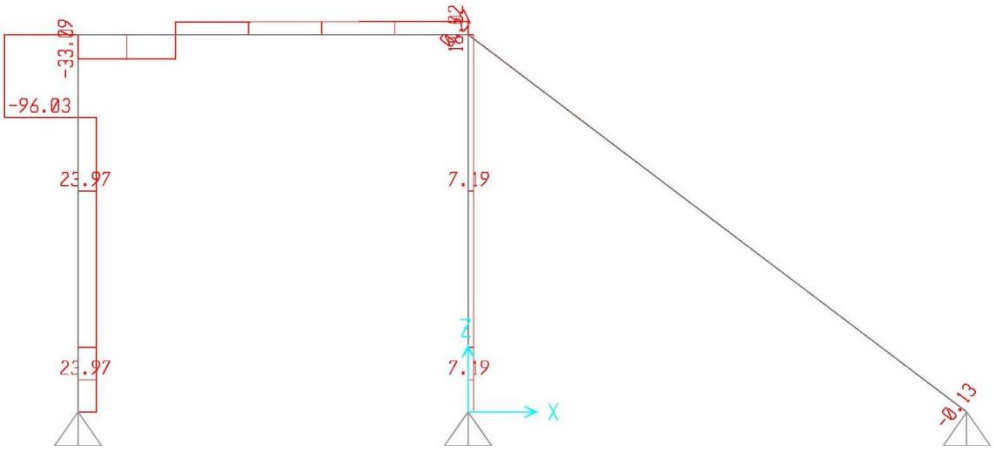

(b)

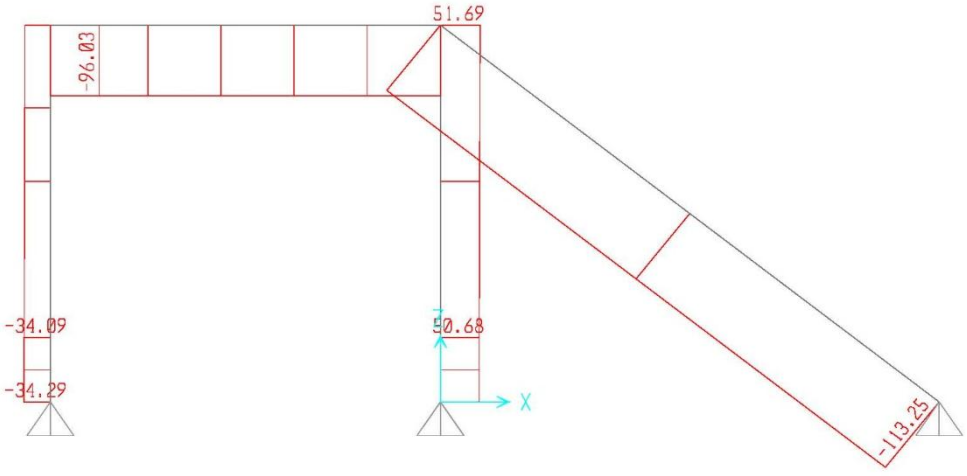

(c)

Figure 3.18: Resulting Diagrams for Phase II and III Testing (with Strut Addition) from SAP2000: (a) Moment; (b) Shear; (c) Axial

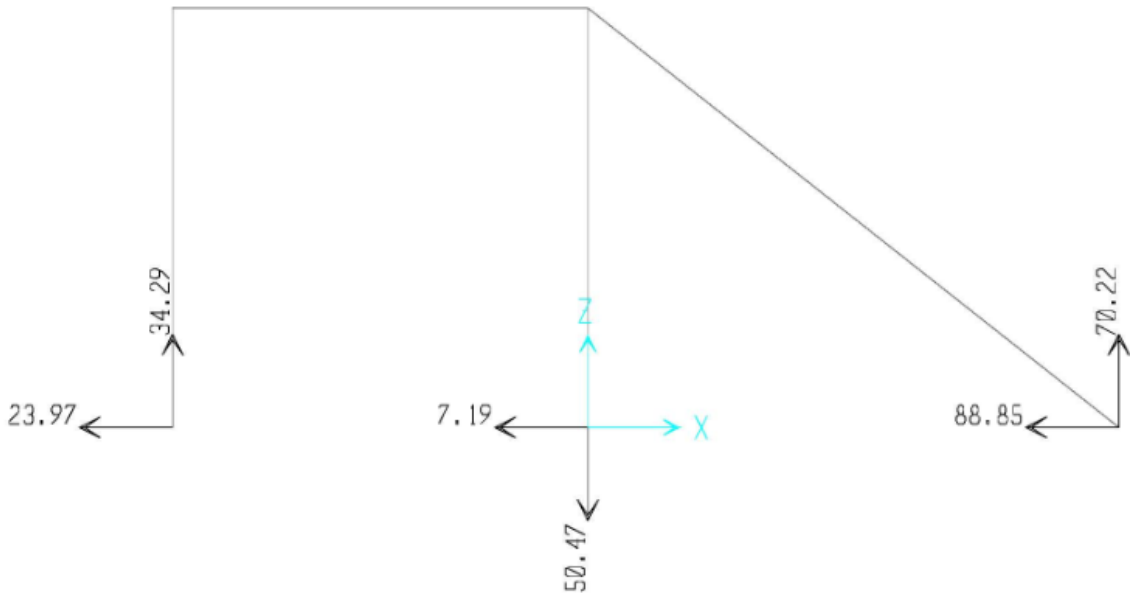

Figure 3.19: Column Base Resultant Forces Phase II and III Testing

3.1.2.4.2 Demand and Capacity

The demands were taken from the SAP2000 results to determine the adequacy of the design by comparing them with the capacities of the design. The demand and capacity for each member and connection is given in Table 3.5. The design capacities were determined similarly to Section 3.1.2.1.3. Strut axial capacity is calculated for compression; the axial forces shown for the strut are in compression. The anchorage system is clearly adequate for the uplift experienced for this load case because of the addition of the strut.

Table 3.5: Demand and Capacity of Load Case: Phase II and III Testing (with Strut Addition)

		Demand			Capacity			
Member Section	**Design Type**	**Moment (k-ft)**	**Shear (kips)**	**Axial (kips)**	**Moment (k-ft)**	**Shear (kips)**	**Axial (kips)**	**Interaction (Moment and Axial)**
Double HSS 18x6x3/8	Beam	75	34	96	596 (7.947)	588.16 (17.29)	640.51 (6.672)	0.2008
Beam/Column Joint	Moment Connection	7.85	96	--	111 (14.140)	194.4 (2.025)	--	--
W24x117	Column	192	96	34	1230 (6.406)	360.86 (3.759)	1482.3 (43.597)	0.1676
W18x119	Column	74	8	52	983 (13.466)	336.01 (42.00)	1471.4 (28.296)	0.0929
Anchorage System	Floor Connection	--	23.97	50.47	--	126 (5.257)	88 (1.744)	0.6043
Strut/Column Joint	Shear Connection	--	19	--	--	194.40 (10.23)	--	--
W8x31	Strut (Angled Column)	--	1	114	--	61.56 (61.56)	651.16 (5.712)	--
Strut/Base Joint	Shear Connection	--	88.85	70.22	--	156.60 (156.6)	234.4 (3.338)	--
Strut Anchorage	Floor Connection	--	88.85	70.22	--	157.5 (1.773)	98 (1.282)	0.9628

3.1.2.4.3 LRFD Design Methodology

The LRFD design methodology for this load case is the same as the first load case except for the strut addition whose capacity was calculated with the LRFD as the columns in the first case. The methodology used in the first load case can be seen in Section 3.1.2.1.3.

3.2 Data Acquisition Systems

This section describes the data acquisition systems used in the structural tests that form the bulk of this thesis (see Chapter 6 and 7). The tests involved the lateral loading of a coupled wall system that consists of wall piers and coupling beams supported by a foundation with reinforcement, and post-tensioning to connect the separate elements. Post-tensioning was also used to simulate gravity loading on the structure. Loading of the system was accomplished using hydraulic actuators. A full description of that testing is

provided in Section 6.2.

Twelve channels of data were collected during the test as follows: (1) load cells LC1-LC3 to measure the forces in the actuators as they applied load to the specimen, MH1-MH4 to monitor the gravity loads in the post-tensioning cables embedded in the foundation that run through top of the piers, and ND1-ND3 to monitor the stresses in the PT cables at the floor levels that coupled the wall system; (2) 2 string potentiometers were used to measure the displacements of the load frame and the specimen relative to the building housing the test; (3) 4 Digital Image Correlation systems were used to record the displacements of the specimen from 4 different fields of view simultaneously. The Digital Image Correlation (DIC) systems are monitored independent of the iNET acquisition system. More information is available for the channels monitored by the iNET system in Table 3.6 and the locations of each instrument can be seen in Figure 3.20. The DIC systems each have a different field of view (FOV); some are located on the front of the specimen and some on the back. Note that since some systems are looking North and some looking South, interpretation of results can be complex. East/West and North/South notation is used consistently throughout this thesis for clarity. The DIC locations can be seen in Figure 3.16.

Table 3.6: Instrumentation Information

Data Channel	Instrument Name	Instrument Type	Instrument Installation	Instrument Location (Figure 3.5)
1	LC1	Large Donut Load Cell	Placed in Line with Actuator	Location 1
2	LC2	Large Donut Load Cell	Placed in Line with Actuator	Location 2
3	LC3	Large Donut Load Cell	Placed in Line with Actuator	Location 3
4	ND1	Small Barrel Nut Load Cell	Post-Tensioned with Cable	Location 4
5	ND2	Small Barrel Nut Load Cell	Post-Tensioned with Cable	Location 5
6	ND3	Small Barrel Nut Load Cell	Post-Tensioned with Cable	Location 6
7	MH1	Small Barrel Nut Load Cell	Post-Tensioned with Cable	Location 7
8	MH2	Small Barrel Nut Load Cell	Post-Tensioned with Cable	Location 8
9	MH3	Small Barrel Nut Load Cell	Post-Tensioned with Cable	Location 9
10	MH4	Small Barrel Nut Load Cell	Post-Tensioned with Cable	Location 10
11	SP1	String Potentiometer	Attached to Stationary Wall	Location 11
12	SP2	String Potentiometer	Attached to Stationary Wall	Location 12

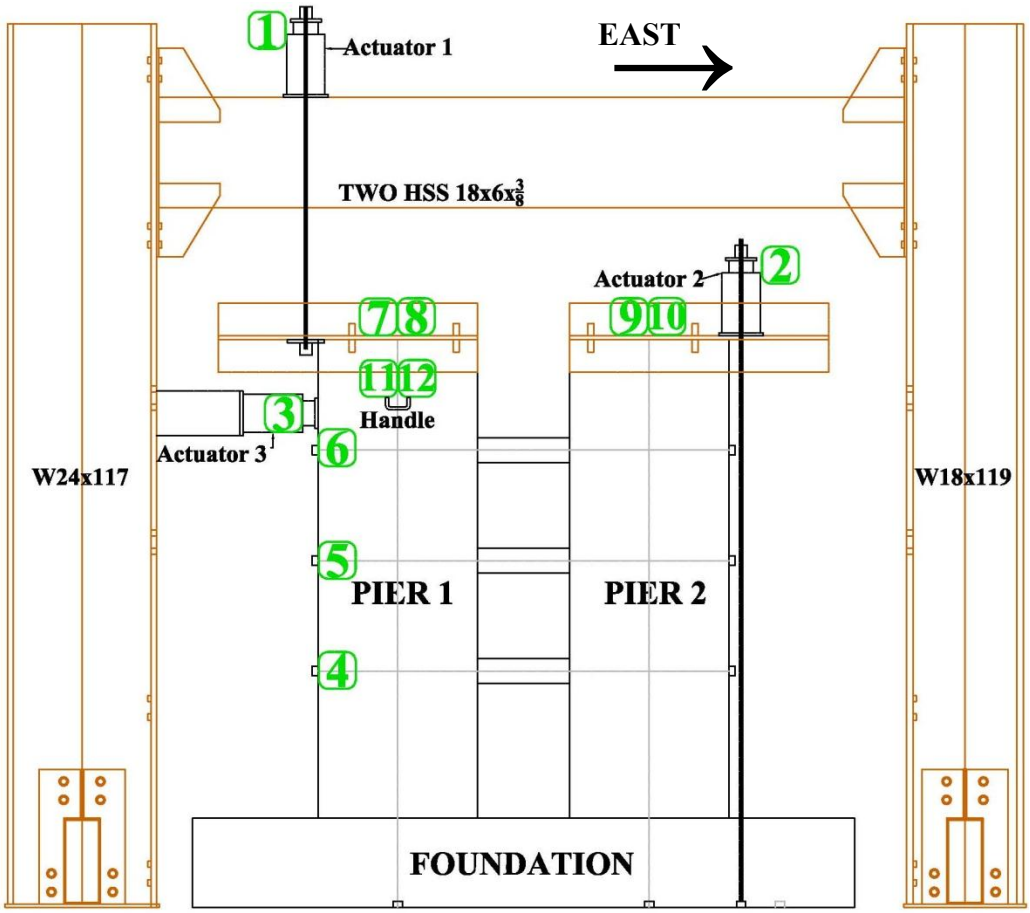

Figure 3.20: Instrumentation Placement (Looking North): Locations of Load Cells and String Potentiometers – See Table 3.6

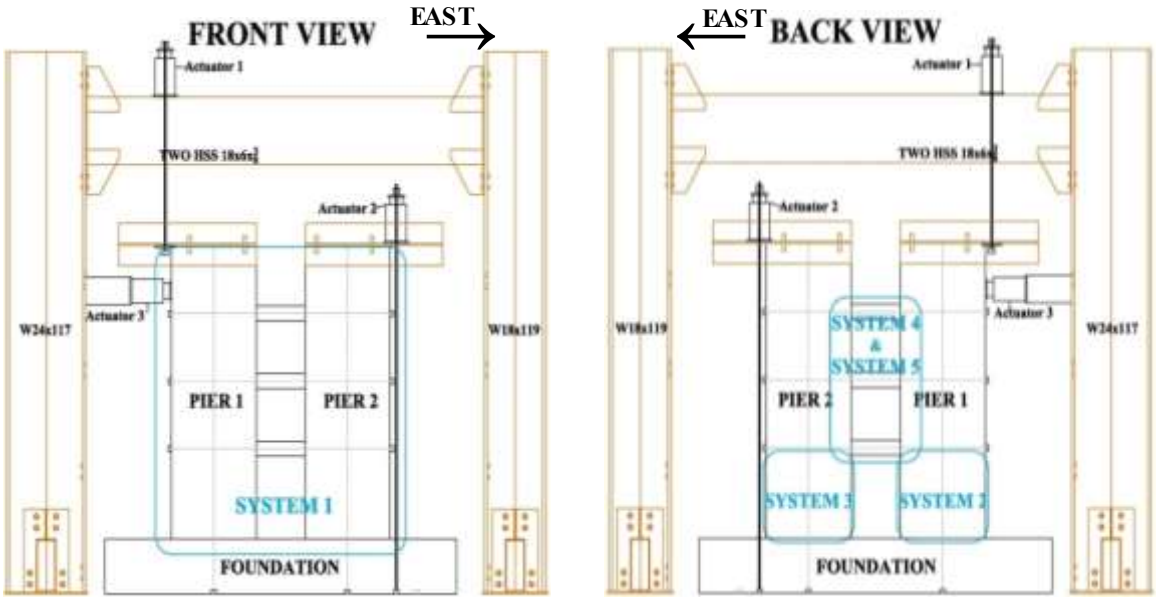

(a) (b)

Figure 3.21: DIC FOV Locations: (a) Front View (Looking North); (b) Back View (Looking South)

3.2.1 iNET Set Up

The iNET system used to monitor the instrumentation described above was made up of the i-240 iNET connector, a power supply cord, extension cables, an i-100 data port and cables. The organizational schematic of the iNET system is shown in Figure 3.22. The iNET software used was InstruNet World Plus including digitize Direct to Excel. This software only works with iNET hardware; the i-240 connector and i-100 data port all of which were used during testing. The iNET physical setup of hardware is shown in Figure 3.23.

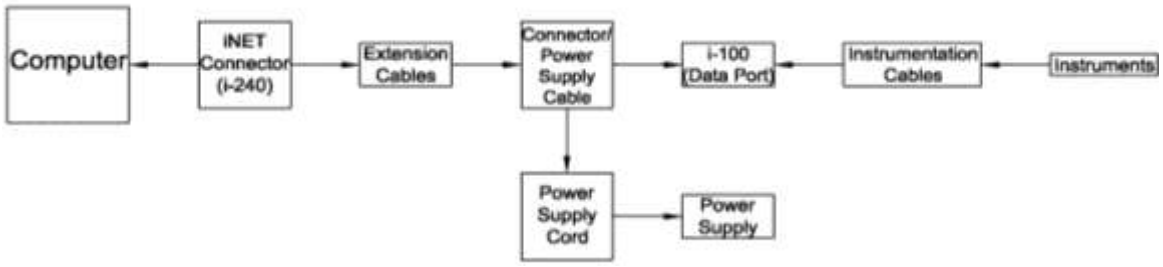

Figure 3.22: iNET Organizational Schematic

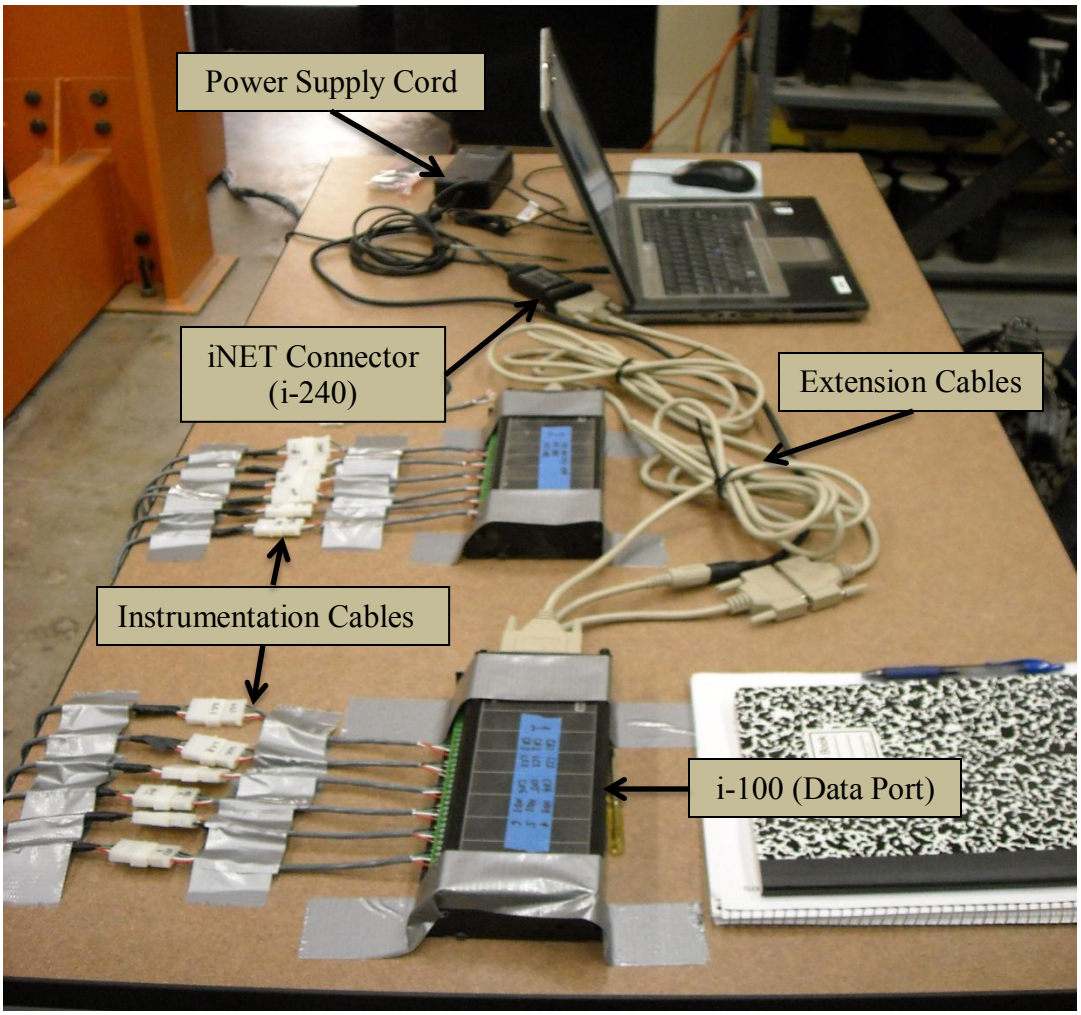

Figure 3.23: iNET System Physical Set Up

The instruments are plugged into the instrumentation cables and those cables are then plugged into the i-100 data port as shown in Figure 3.23. The connection between the end of the instrumentation cables and the i-100 data port is not a simple plug, it consists of four colored (green, white, red and blue) wires being tightened into four individual ports. The arrangement of the colored wires to their associated ports is shown in Figure 3.24.

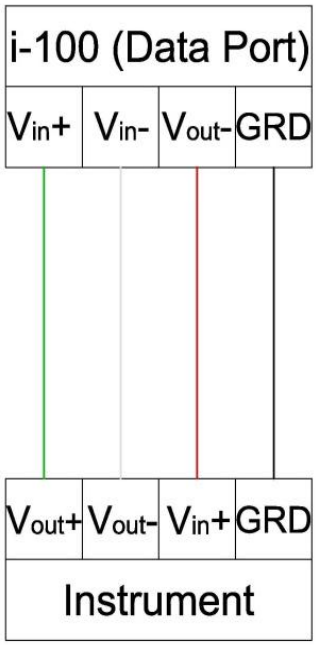

Figure 3.24: Instrument Cable Connection Details

3.2.2 Load Cell Calibrations

In order to calibrate the output values from the iNET system, some variables needed to be adjusted. By applying a compression force using a compression machine, the value of the force actually being applied was known. Because of this, the accuracy of the readings from the iNET system could be evaluated. First, a load cell was put through a pre-programed compression test and the values from the iNET system were compared with the actual force being applied. The first adjustment made was to alter the initial input voltage value until the unloaded value produced by the iNET system was close to zero, and then the load cell would be tested again. After this iteration was completed, the GF value (Gage Factor) was adjusted and the load cell tested again. The GF value could then be adjusted again if necessary until the iNET output values matched those of the pre-programed test. The settings for instruments used during testing are given in Table 3.7.

Table 3.7: Calibration Data for Instruments

Instrument	Resistance (Ω)	Voltage Out	Voltage In	Gage Factor	Multiplier
LC1	350	4.46484375	-2.50E-05	2.54E-08	2.639
LC2	350	-4.4648438	-8.50E-05	2.54E-08	2.606194
LC3	350	4.46484375	0.00026	2.54E-08	2.631449
ND1	120	-1.2979175	0.000675	1.00E-08	0.32
ND2	120	1.2979175	-0.00107	1.00E-08	0.3107
ND3	120	-1.2979175	0.00112	1.00E-08	0.3658
MH1	120	-1.2979175	0.0005	1.30E-08	29.74
MH2	120	1.2979175	0.00014	1.30E-08	68
MH3	120	-1.2979175	0.00105	1.30E-08	30
MH4	120	1.2979175	-0.00035	1.30E-08	32.73
SP1	360	4	1.27255	1.58E-08	11
SP2	360	-4	-2.51	1.58E-08	11

Three different types of load cells were used to monitor loads during testing; they can be seen in Figure 3.25. They are also denoted in Table 3.7. The LC load cells are large donut load cells with a lower variability than the other two types as they were purchased and not constructed. The ND load cells are small barrel nut load cells that were created and borrowed from Notre Dame's lab. The MH load cells are also small barrel nut load cells, but they were constructed in the UT Tyler lab for this project. Although both the ND and the MH load cells were constructed, the MH load cells had less variability based on the graphs given in Figures 3.26 through 3.35. All load cells were able to be calibrated to an acceptable level of accuracy.

(a)

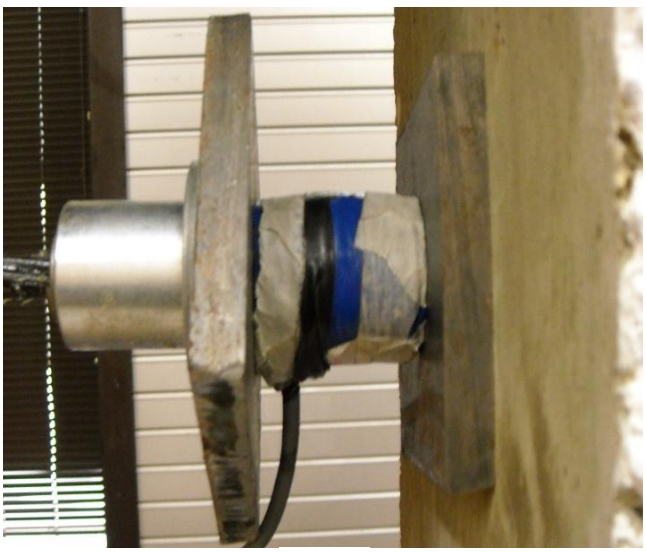

(b)

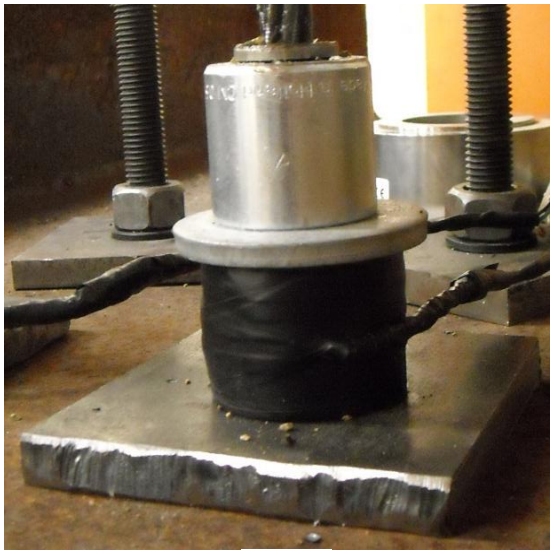

(c)

Figure 3.25: Load Cell Types: (a) LC; (b) ND; (c) MH

The calibration curves are shown in Figures 3.26 through 3.35 for the load cells used. The scatter plot shows the values read during different iterations and the linear curve represents the values used for the iNET calibrations.

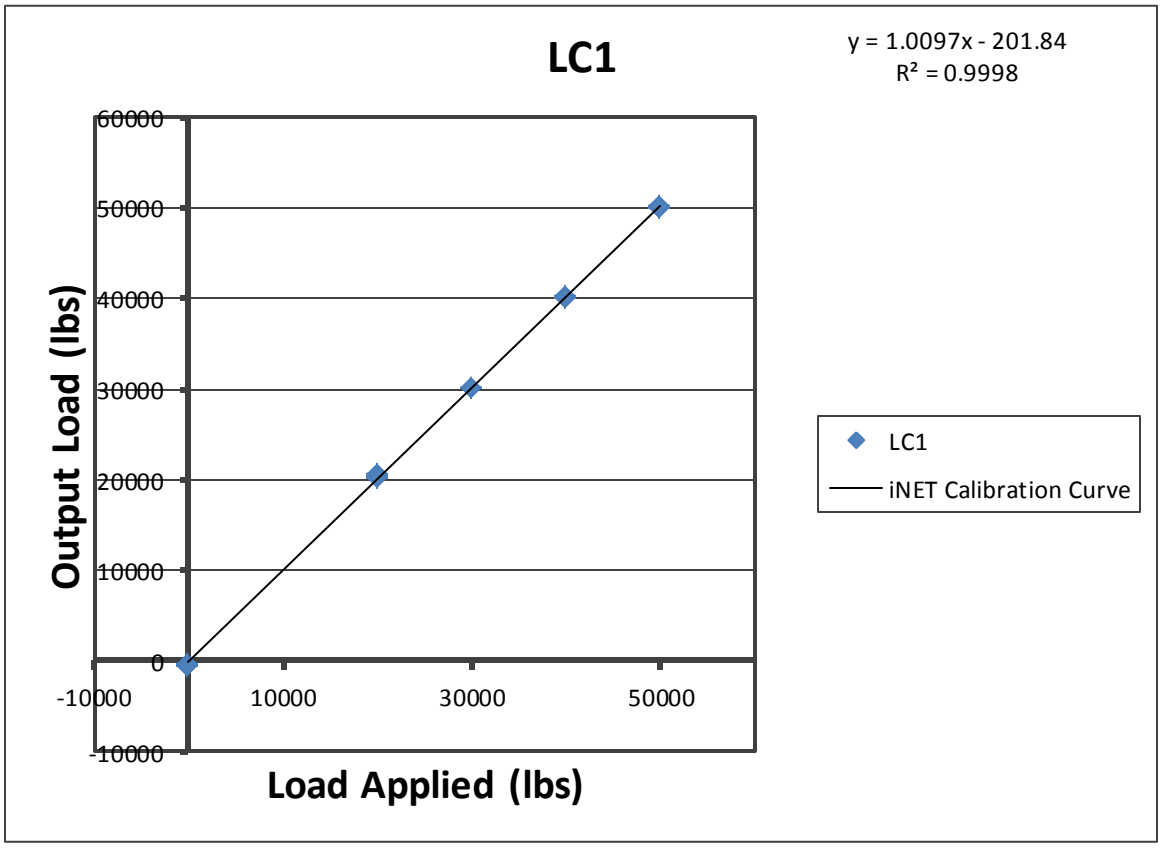

Figure 3.26: LC1 iNET Calibration Curve

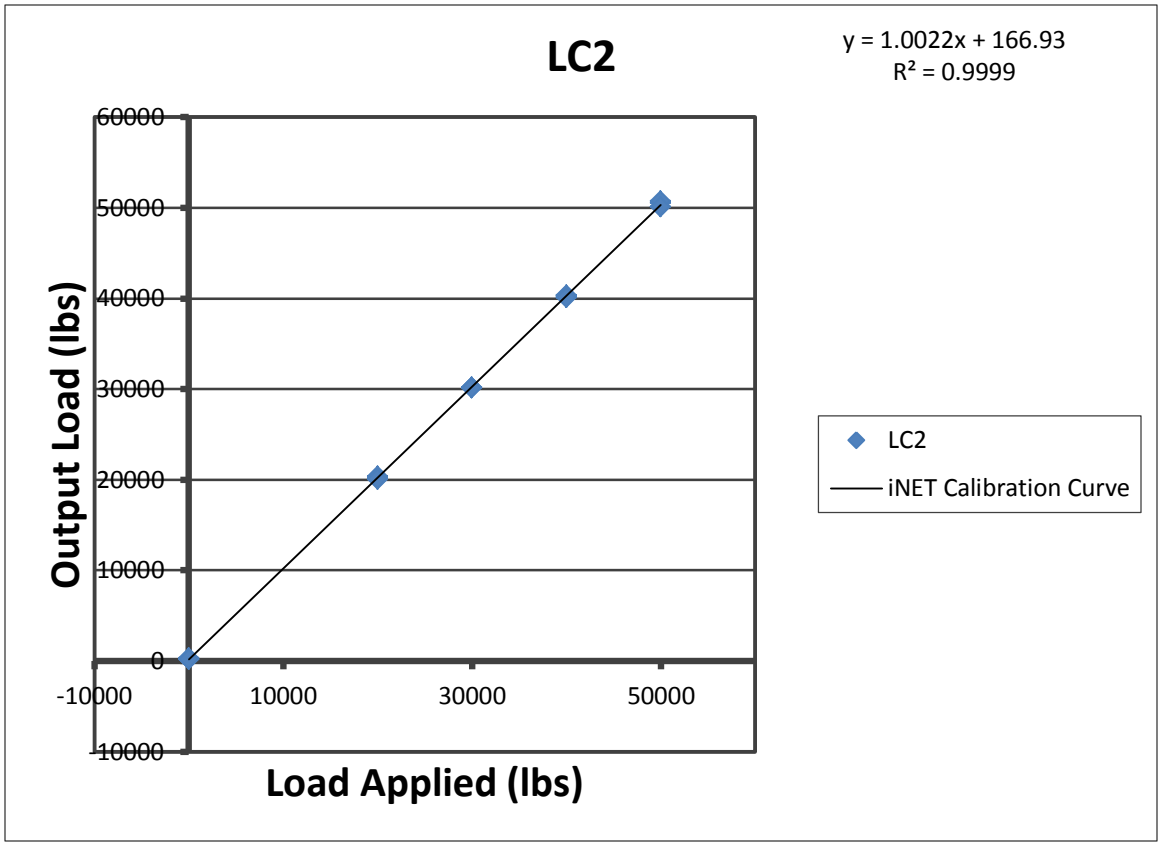

Figure 3.27: LC2 iNET Calibration Curve

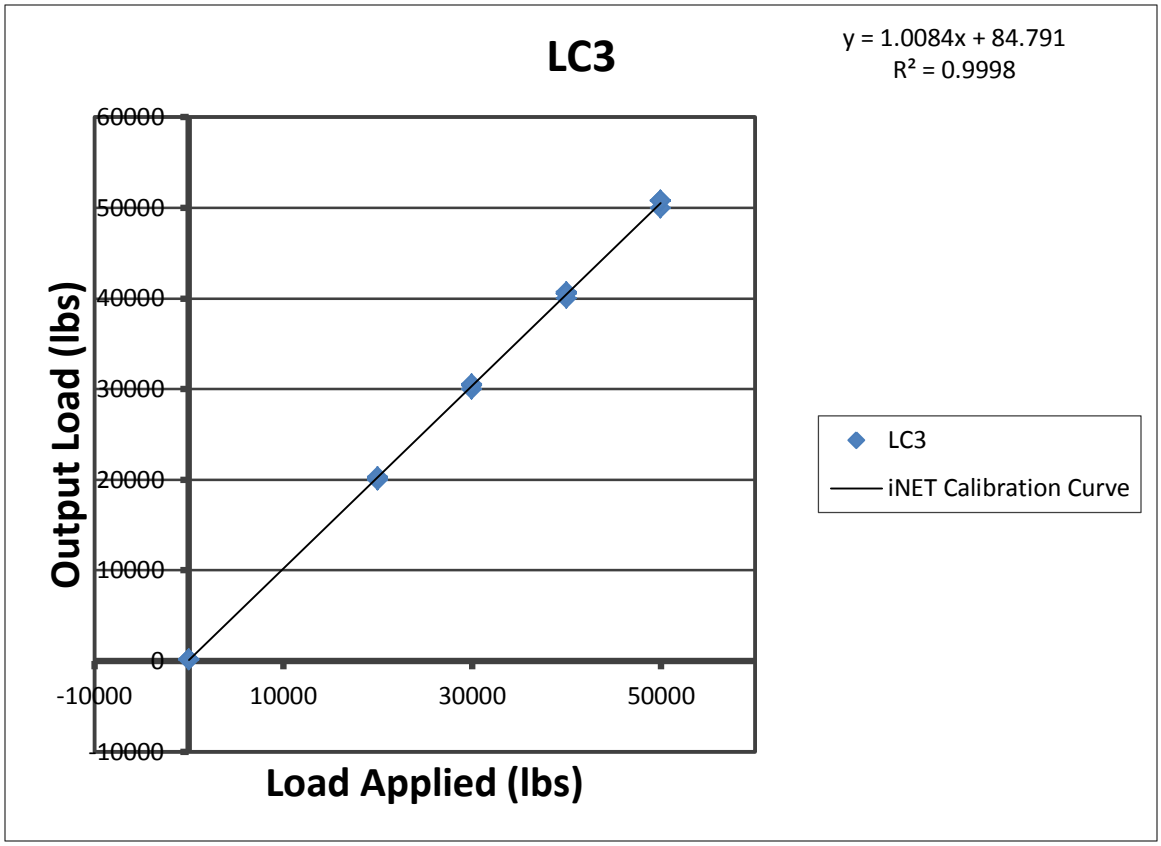

Figure 3.28: LC3 iNET Calibration Curve

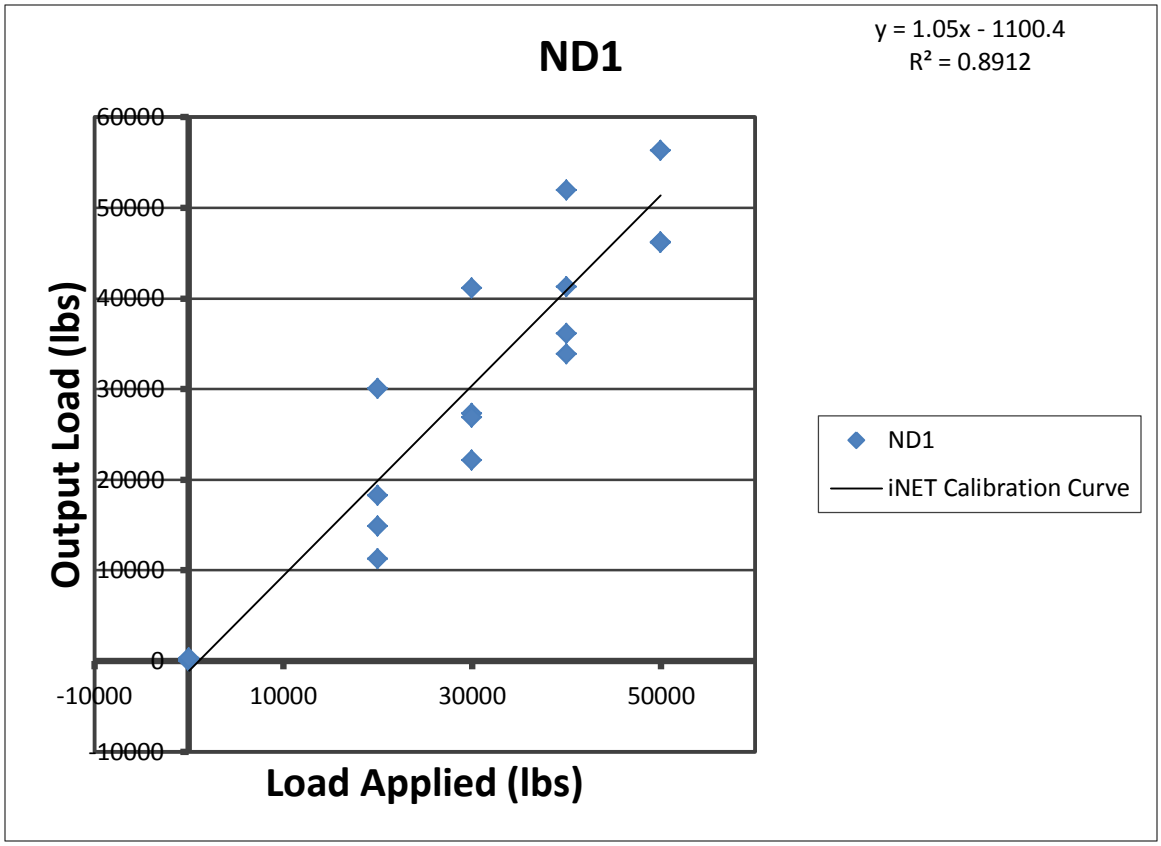

Figure 3.29: ND1 iNET Calibration Curve

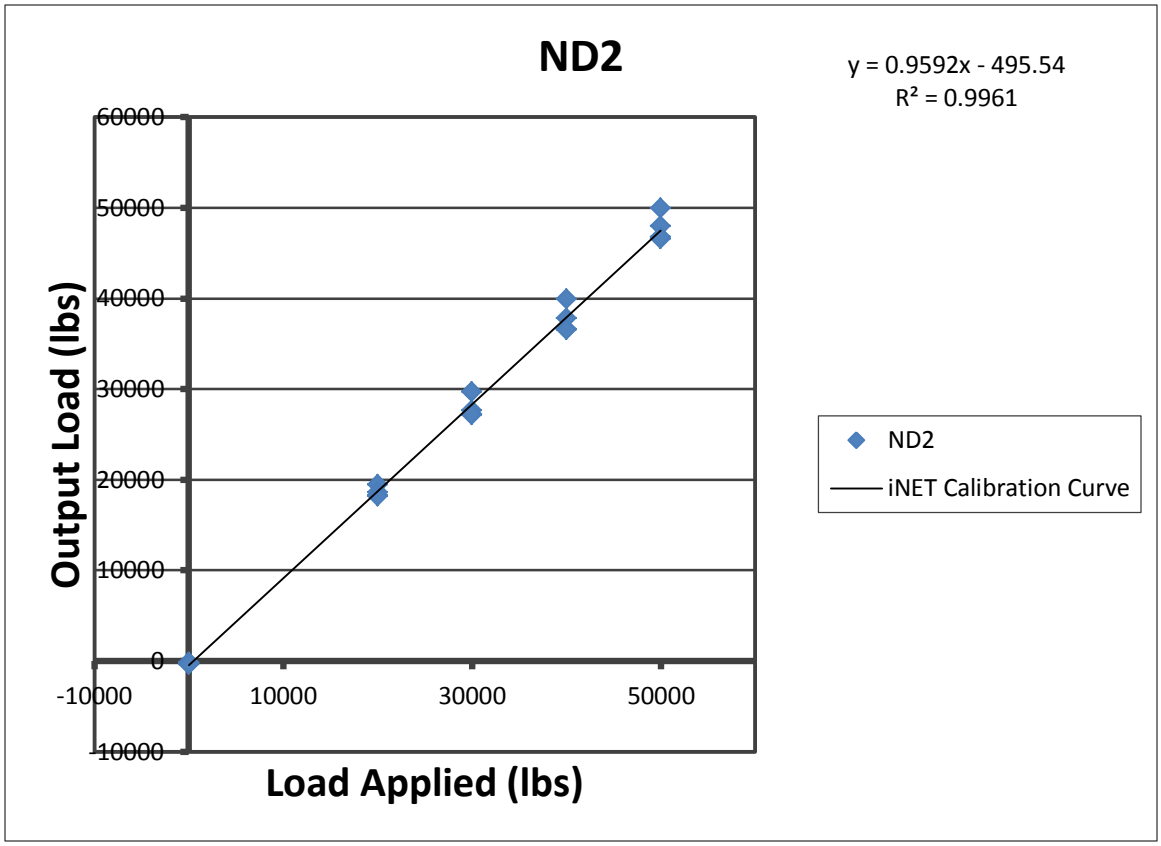

Figure 3.30: ND2 iNET Calibration Curve

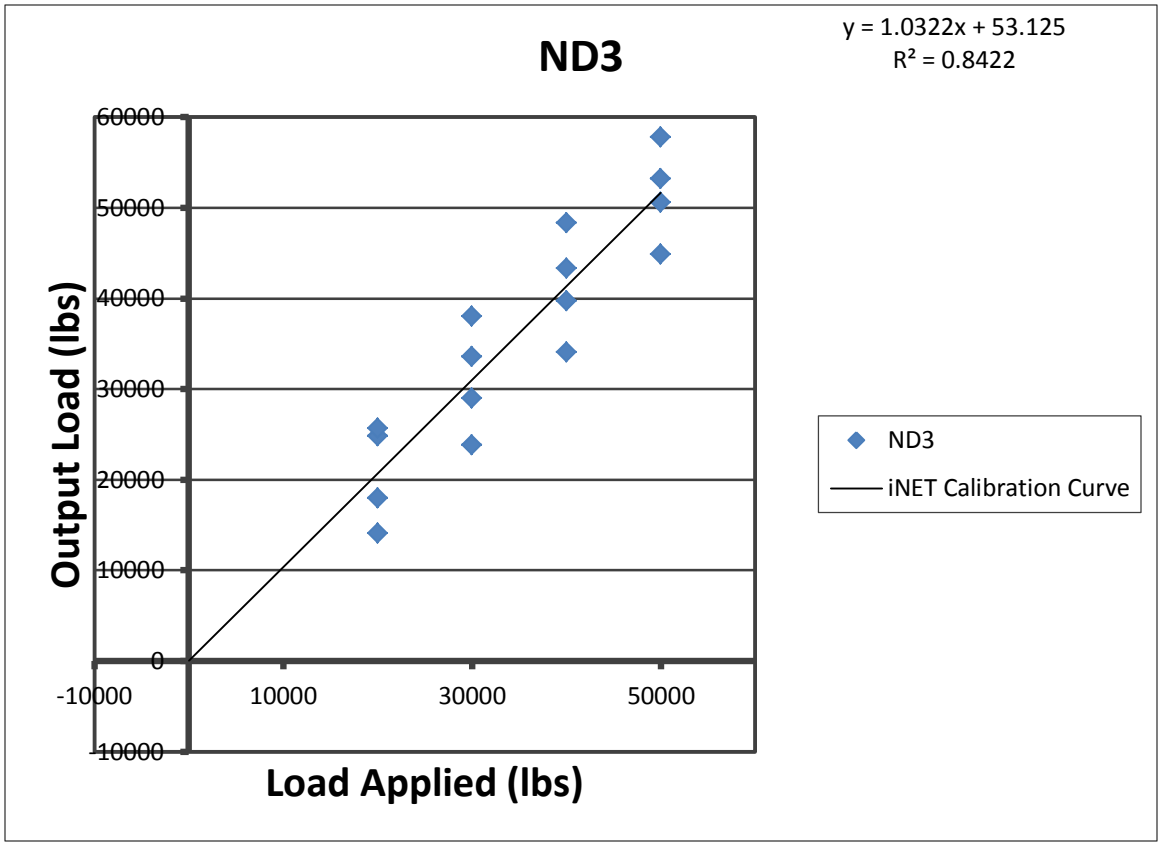

Figure 3.31: ND3 iNET Calibration Curve

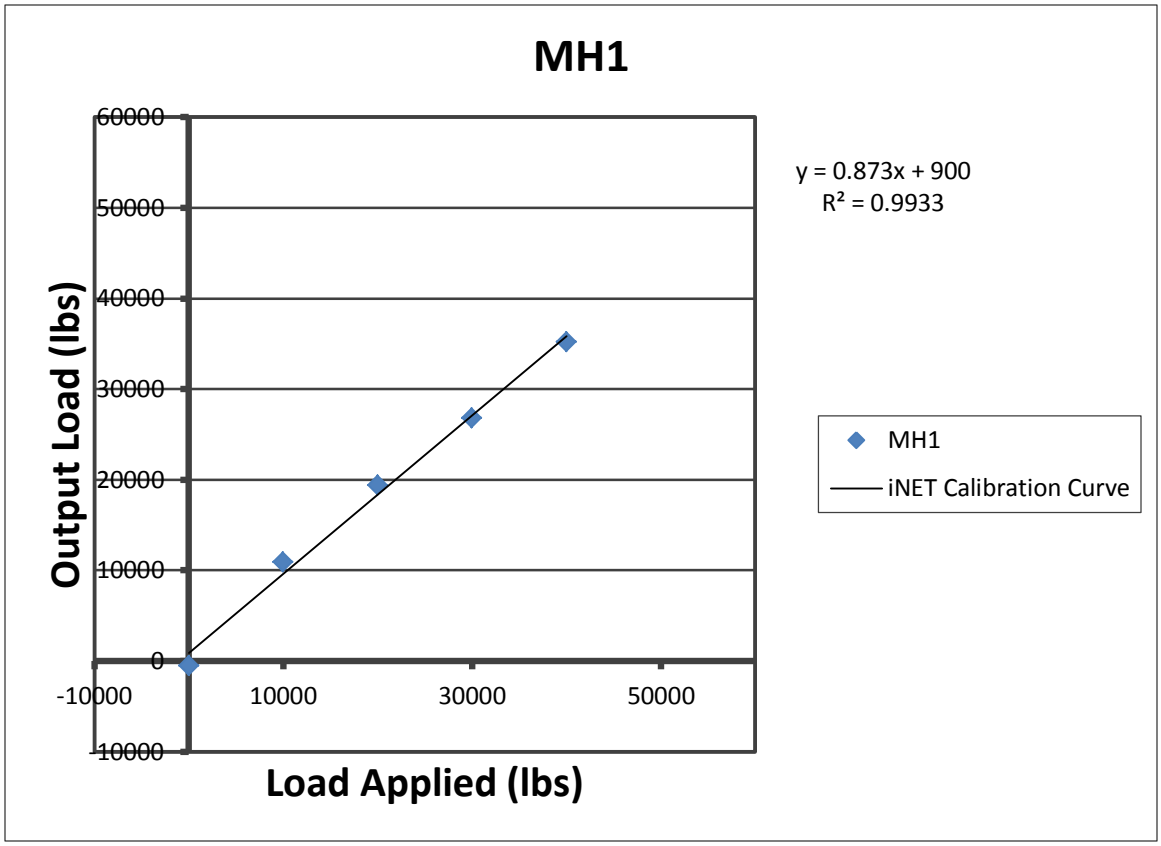

Figure 3.32: MH1 iNET Calibration Curve

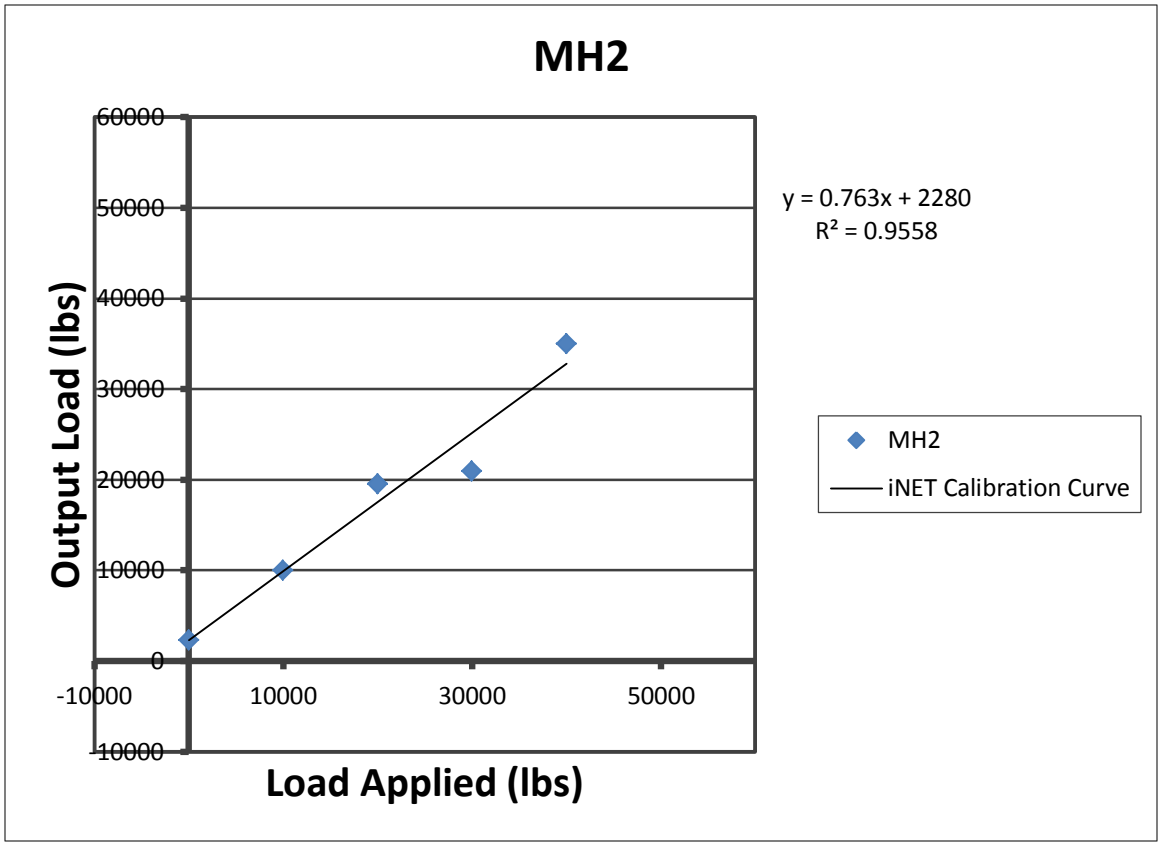

Figure 3.33: MH2 iNET Calibration Curve

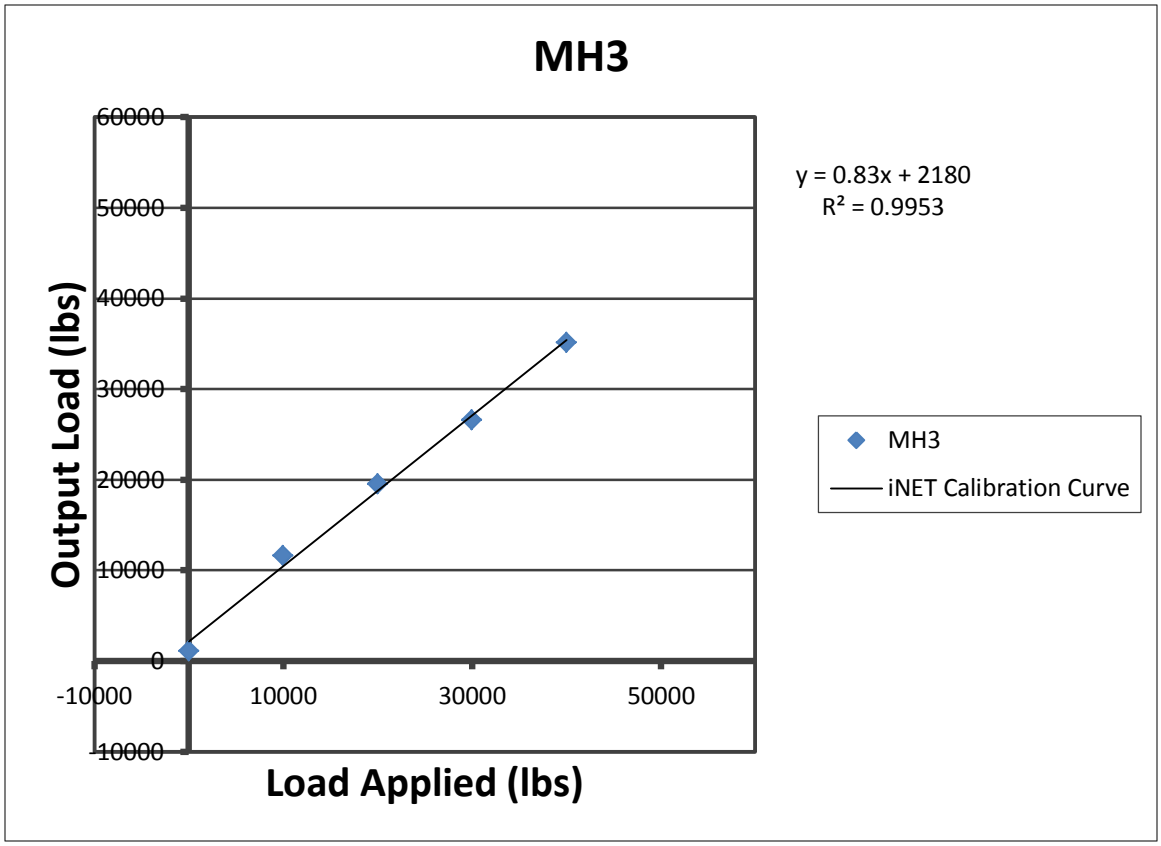

Figure 3.34: MH3 iNET Calibration Curve

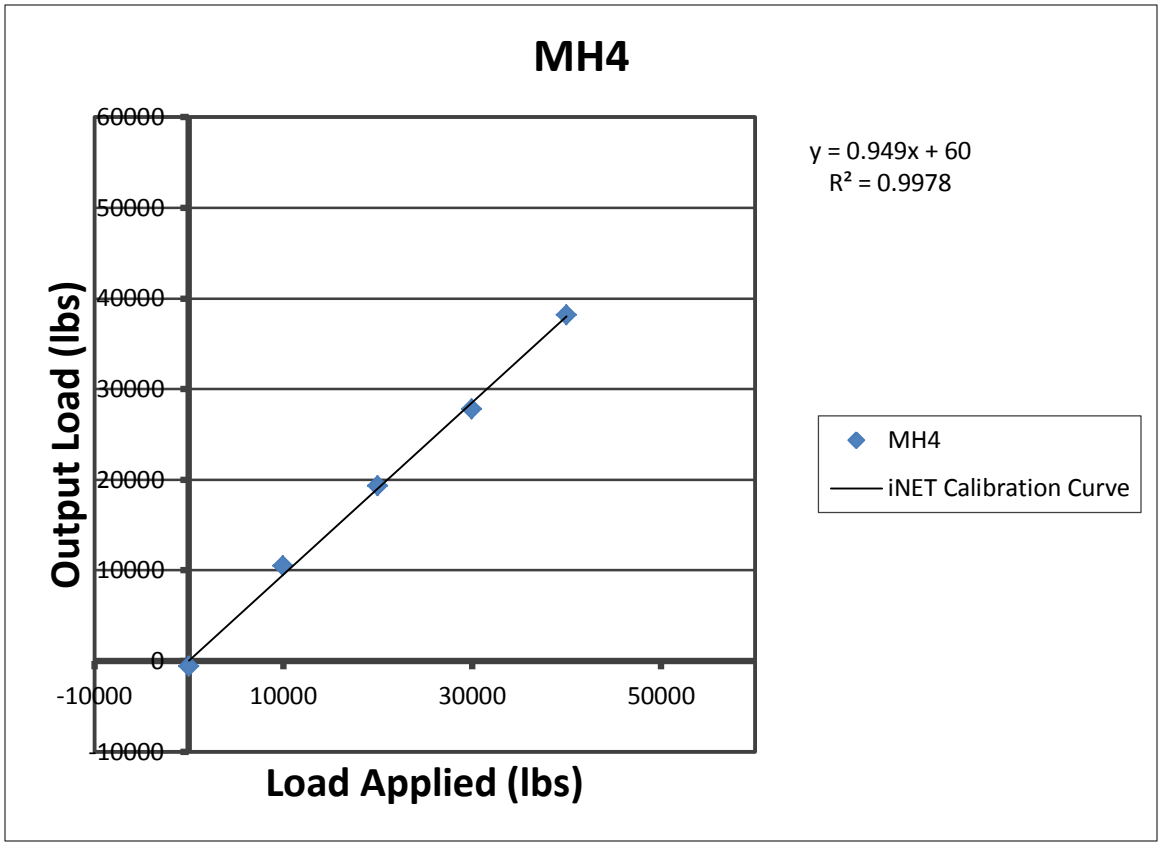

Figure 3.35: MH4 iNET Calibration Curve

3.3 Digital Image Correlation Systems

This section describes the actual DIC systems that were used during testing, the calibration procedure, actual calibrations used for each image series captured during testing, and the field of view for each system.

3.3.1 Systems Used

The following systems were used to capture the images during testing. See Figure 3.16 for FOV locations and Figures 3.31 through 3.34 for FOV images.

3.3.1.1 System 1: 3D system, used for FOV Global, Aramis 2M system: 1624 pixels by 1236 pixels, Measuring Area of 1000 mm by 750 mm, Utilized 12 mm lenses during testing.

3.3.1.2 System 2: 2D system, used for FOV Tension Base, Hispec 1 system: 1280 pixels by 1024 pixels, Measuring Area of 650 mm by 650 mm, Utilized 25 mm lenses during testing.

3.3.1.3 System 3: 2D system, used for FOV Compression Base, Hispec 1 system: 1280 pixels by 1024 pixels, Measuring Area of 650 mm by 650 mm, Utilized 25 mm lenses during testing.

3.3.1.4 System 4: 3D system, used for FOV Beams during Phase I, Aramis 5M system: 2448 pixels by 2050 pixels, Measuring Area of 1200 mm by 900 mm, Utilized 12 mm lenses during testing.

3.3.1.5 System 5: 2D system, used for FOV Beams during Phases II and III, Canon EOS Rebel T3i: 5184 pixels by 3456 pixels, Utilized 25 mm focal length during testing.

3.3.2 Camera Calibrations and Set Up

This section of Chapter 3 reviews the basics for calibration and set up procedure as well as the calibrations and specific FOVs used during testing.

3.3.2.1 Calibration and Set Up Procedure

In 3D-DIC, sample preparation consists of applying a regular or random pattern with good contrast to the surface of the measured object. The pattern will then deform with the object under load. The object is captured in a stereo pair of high quality cameras while it is loaded. Typically, these two cameras are mounted at either end of a base bar such that their relative position and orientation with respect to one another is fixed and known.

Before using the 3D-DIC system as described above, the system must be calibrated using NIST-traceable calibration panels for each field of view (FOV). A

sequence of pictures of the panel at different distances and orientations is captured and a bundle adjustment is used to establish the precise relationship between the two cameras, and to compensate for any distortions in the individual camera lenses. The fixed position of the two cameras with respect to one another greatly simplifies the photogrammetric calculations, but if the camera's position with respect to one another is altered (even accidentally) during testing, a new calibration sequence is required.

Once calibrated, thousands of unique correlation areas known as facets are defined across the entire imaging area of the measured object. The center of each facet is a measurement point that is tracked in each successive pair of images by employing a similarity measure such as the normalized cross correlation. Three-dimensional locations of these facets are calculated before and after each load step, yielding displacements. Tracking the dense cloud of points within the applied pattern provides displacement information that is 'near' full field.

The optimum angle between the cameras is 25 degrees. Lower angles reduce accuracy in triangulation, and thus reduce accuracy in the out-of-plane (z-axis) coordinates and displacements. Wider angles increase accuracy of the z coordinates, but the increased perspective reduces the useful FOV. Many researchers use 2D-DIC (which involves using only one camera and does not require triangulation) when the out-of-plane deformations of the problem are deemed unimportant. The 2D-DIC calibration procedure is similar to that of the 3D-DIC, but requires fewer photographs as it does not have to establish the relative position of another camera. In a 2D-DIC, the calibration produces an area instead of a volume that is calibrated and does not account for out of plane displacements. In order to use a distance calibration, two points must be clearly marked

in the FOV of the 2D system. After the image series is imported into the software, a line is created and the distance measured between the points is inputted and the system can be calibrated.

3.3.2.2 Calibration Specifications Used during Testing

After following the calibration procedure, the DIC software will produce calibration information including deviation, angle (for 3D systems), and calibrated volume (area for 2D systems). The calibration specifics used during testing are given in Table 3.8. System 5 used the distance calibration discussed above.

Table 3.8: DIC Calibration Specifics Used During Testing

System		Phase I	Phase II	Phase III
System 1 (3D)	Deviation (mm)	0.022	0.028	0.026
	Angle (^{0})	17.1	11.4	11.3
	Volume (mm/mm/mm)	2075/1630/1630	2200/1700/1700	2200/1700/1700
System 2 (2D)	Deviation (mm)	0.058	0.055	0.055
	Area (mm/mm)	638.2/635.3	640.9/636.6	640.9/636.6
System 3 (2D)	Deviation (mm)	0.061	0.068	0.068
	Area (mm/mm)	638.2/635.3	640.9/636.6	640.9/636.6
System 4 (3D)	Deviation (mm)	0.059	Was not used for this Phase	Was not used for this Phase
	Angle (^{0})	17.3		
	Volume (mm/mm/mm)	1240/1080/1080		
System 5 (2D)	Two points marked in FOV measured: input to Distance Calibration	Was not used for this Phase	Used Distance Calibration After The Fact	Used Distance Calibration After The Fact

3.3.2.3 Fields of View

A global perspective of the FOV for each DIC system can be seen in Figure 3.20. The images provided in Figures 3.36 through 3.39 are visuals to aid in the clarity of the established FOV for each DIC system. The FOV provided are the same for all three phases. The colors that appear on the specimen show the area for which data was recorded during testing.

Figure 3.36: FOV Global (Looking North): System 1 (3D)

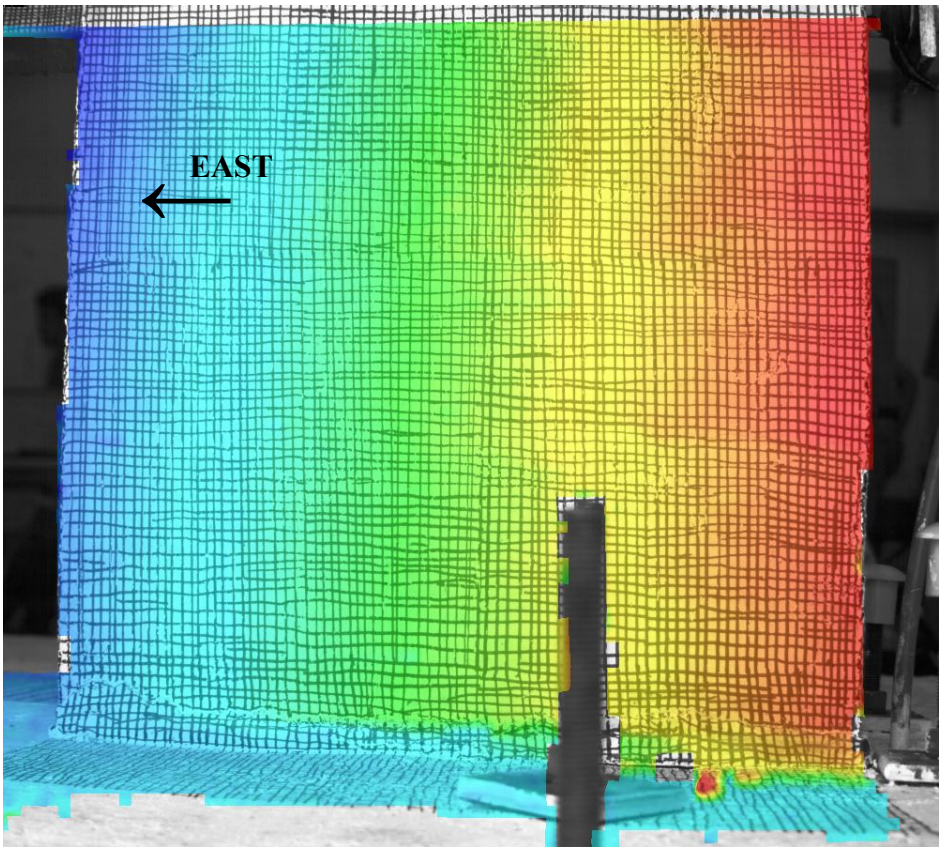

Figure 3.37: FOV Tension Pier Base (Looking South): System 2 (2D)

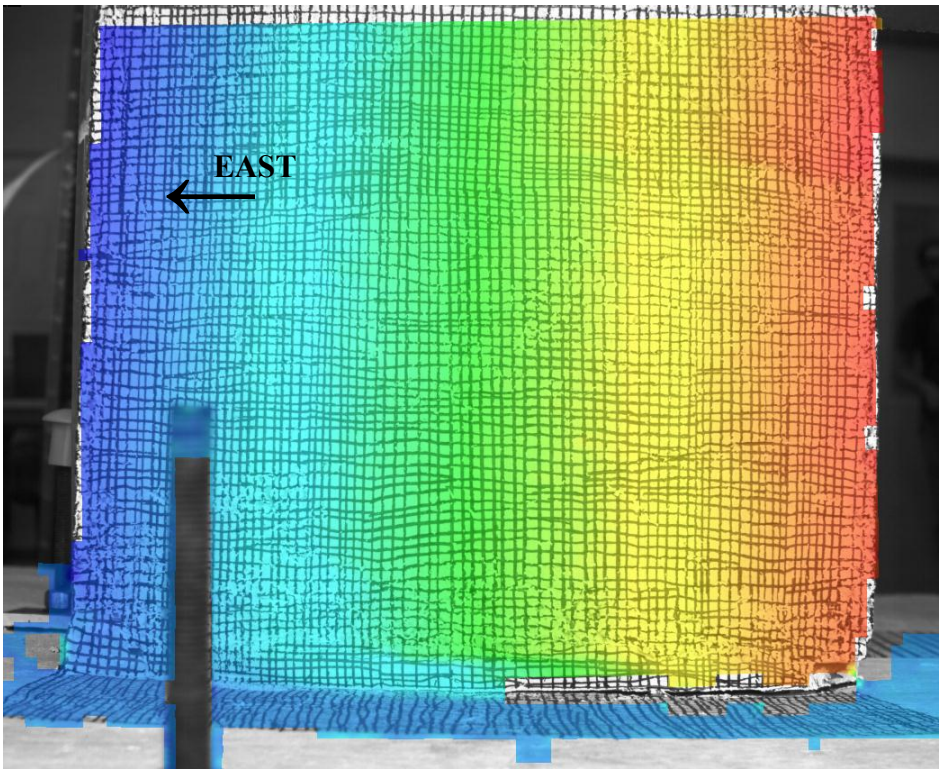

Figure 3.38: FOV Compression Pier Base (Looking South): System 3 (2D)

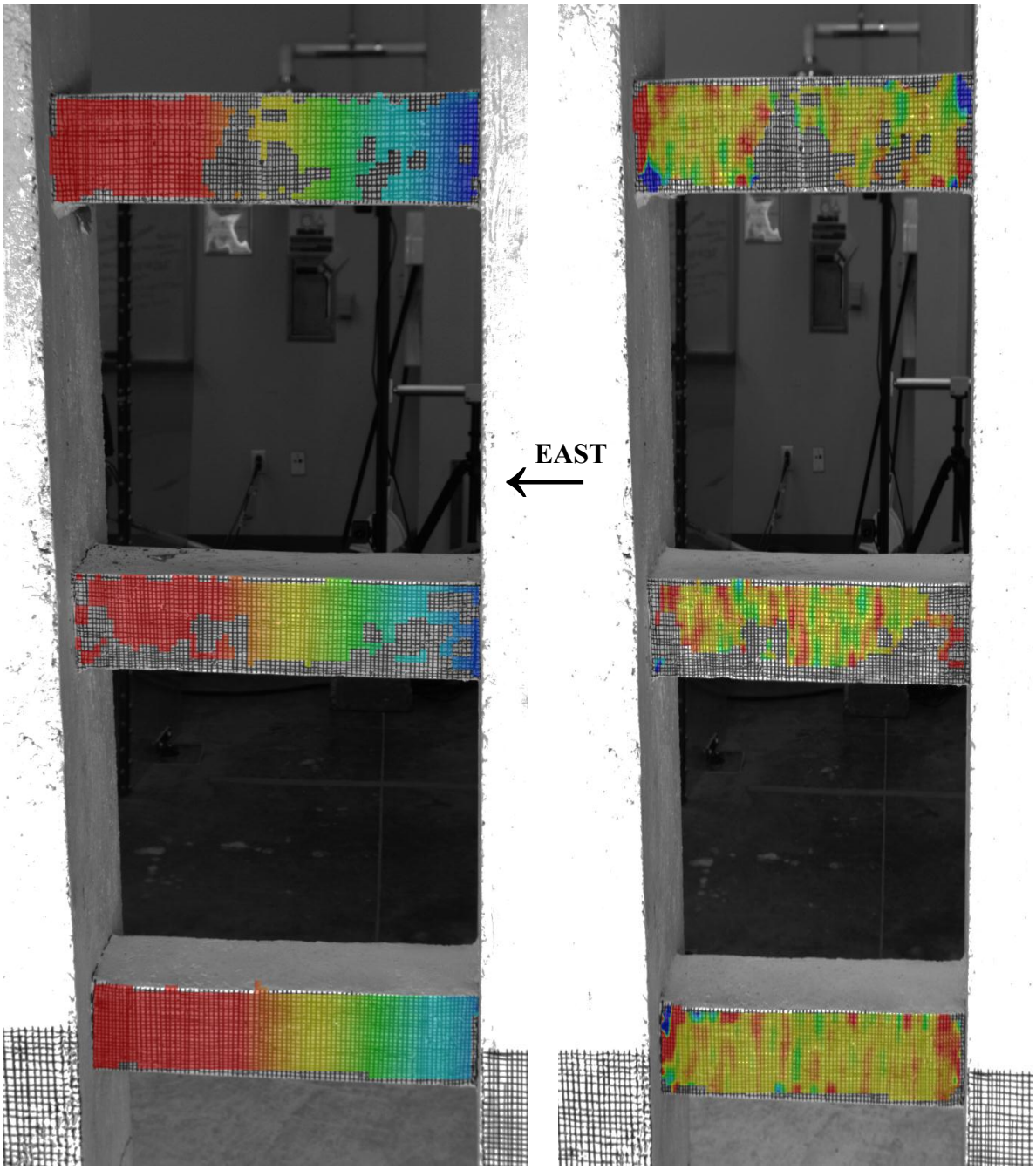

(a) (b)

Figure 3.39: FOV Beams Local (Looking South): (a) System 4 (3D); (b) System 5 (2D)

CHAPTER 4: SPECIMEN DESIGN

4.1 Prototype Specimen Design

To form a basis for the experimental investigation of the 40% and 15%-scale PT coupled shear wall structures, a full-scale 8-story prototype building was designed for a site in Los Angeles, California with a calculated seismic response coefficient of C_s=0.136g. The plan and elevation views of this structure are shown in Figures 4.1(a) and 4.1(b). The primary lateral load resistance is provided by the coupled core wall at the center of the building – two C-shaped shear walls connected by coupling beams at each floor level. This core includes two openings to simulate the location of elevator shafts and stairwells in a typical office building. These openings were centered inside the core in the north-south direction to help eliminate any asymmetric behavior under loading. The configuration, dimensions, and detailing of the prototype building were chosen with the assistance of Magnusson Klemencic Associates (MKA).

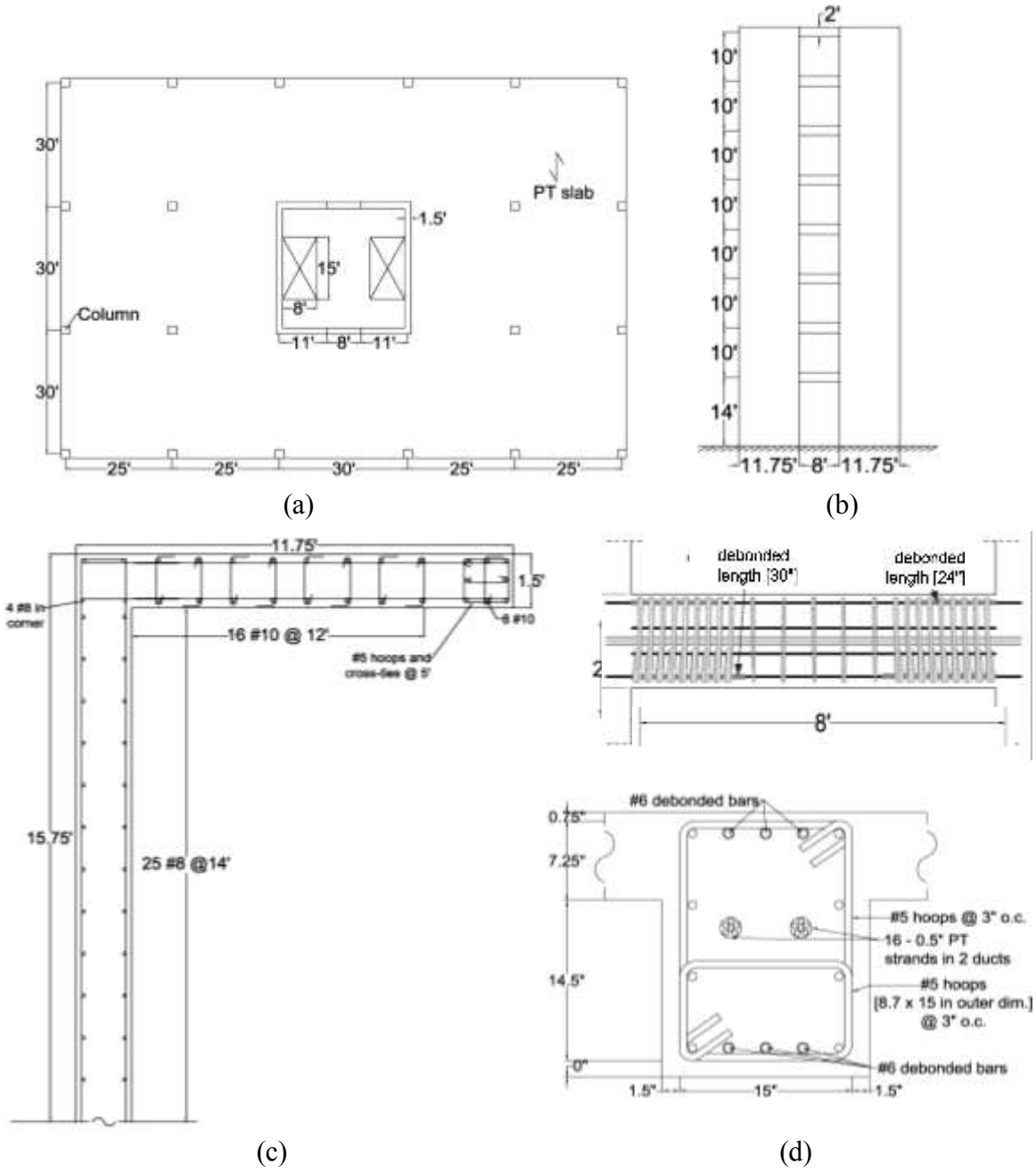

Figure 4.1: Prototype structure: (a) building plan; (b) building elevation; (c) wall base details; (d) coupling beam details

Figure 4.1(c) shows the wall pier reinforcement details at the base of the structure. The reinforcement plan was selected so that it was similar to the typical reinforcement used in a conventional coupled shear wall design. The post-tensioned coupling beam details are given in Figure 4.1(d). The post-tensioning force is provided by 16 - 0.5 in.

diameter PT strands, placed inside two ungrouted ducts to prevent bonding to the concrete. Energy dissipation in the structure is provided by 3 – U.S. No. 6 bars at the top and bottom of the beams. These bars are wrapped in plastic at the beam ends to prevent bond between the steel and concrete. The length of this wrapped section is selected to limit the maximum strains in the steel during reversed-cyclic loading.

To determine the design forces for the prototype structure, the Equivalent Lateral Force (ELF) procedure from ASCE 7 was used with an assigned R-factor of 6.0. The structure had a calculated period of T = 0.74 seconds. The period was estimated by Magnusson Klemencic Associates (MKA) based on computer simulations of the 100% prototype. This period is a more accurate estimation of the fundamental period than the equations found in ASCE 7. The ELF procedure resulted in a design total base moment and total base shear force, which were then distributed to the individual components of the coupled core wall structure by making a number of design selections. First, a coupling degree of 30% was chosen, meaning that 30% of the design base moment is to be carried by the coupling action between the two wall piers. The coupling moment is converted to an axial force at the bottom of each wall pier, using the distance between the centroids of the two wall piers to form a couple. The axial force is then distributed to the ends of each coupling beam as a shear force and the corresponding moments at the beam ends. Linear distribution of the moment is assumed along the beam length with zero moment at the centroid. The remaining base moment is distributed evenly between the two wall piers. The reinforcement details of the wall pier base and PT coupling beams were then selected to satisfy these design forces.

4.2 15% Scale Specimen Description

Several key decisions were made to create the 15% scale model of the prototype building within the capabilities of the laboratory. First, scaling the C-shaped wall piers directly would result in walls in the experimental specimen only 2.7 inches thick. Instead, the section modulus of the scaled C-shape was matched using a wall that was rectangular in shape, as shown in Figure 4.2 and Table 4.1. Rather than scaling the actual reinforcement from the prototype structure, the base moment of the prototype structure was scaled, and then the flexural steel of the laboratory walls was designed using basic reinforced concrete principles, resulting in the selection of the #6 and #7 bars shown in Figure 4.2, and the moment capacities shown in Table 4.1. Target base moments were derived from a DRAIN-2DX analytical model described in Chapter 7. Similarly, the base shear forces of the prototype structure wall piers were scaled, and design using traditional reinforced concrete principles resulted in the #4 hoops in the wall piers shown in Figure 4.2(c). The reinforcement layout shown in Figure 4.2(c) is specifically for the West pier; the East pier uses a mirror image of the layout with #7 bars on the East edge and #6 bars on the West edge.

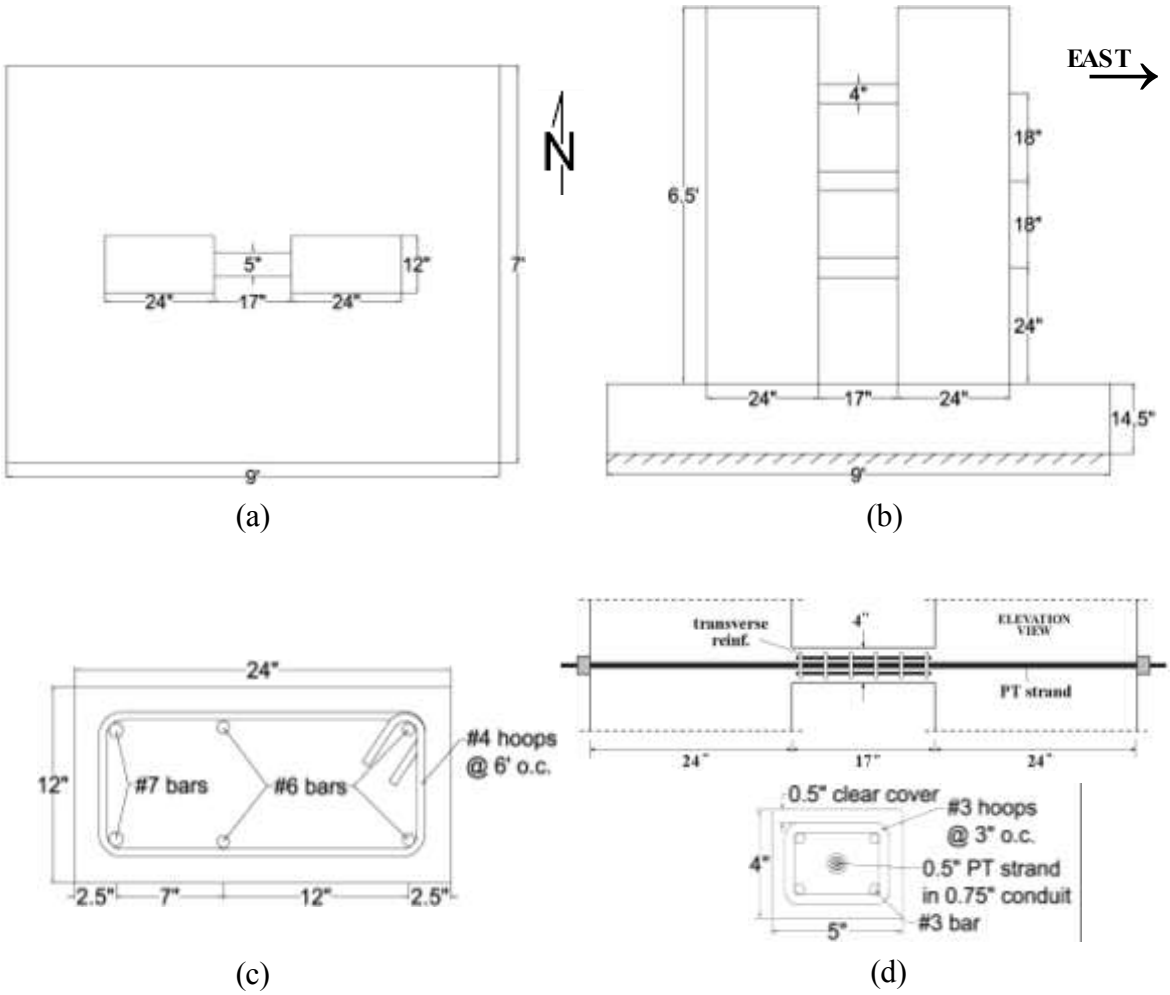

Figure 4.2: UT Tyler Specimen: (a) specimen plan; (b) specimen elevation (Looking North); (c) wall pier details; (d) coupling beam details

The prototype structure has two coupling beams per story – in the 15% structure these beams were combined, resulting in constructible beam geometry. The scaling of the beams was based on the directly scaled cross-section dimensions, and therefore the scaled cross-sectional area. Energy dissipation steel was not included in the beams. The moment and shear capacity design of the coupling beams followed a similar approach to the pier design – demands from the prototype structure were scaled, and basic prestressed and reinforced concrete design principles were used to select the steel for the 15% structure – see Figure 4.2 and Table 4.1.

Table 4.1: UT Tyler Scaling Details

		Section Modulus (in^3)	Moment of Inertia (in^4)	Base Moment (k-ft)	Base Shear (kips)	Area of Coupling Beams (in^2)	Moment of Coupling Beams (k-in)	Shear of Coupling Beams (kips)
Prototype Structure	(T) Pier	183231	19092676	46812	767	864	9442	196.6
	(C) Pier	518819		46812	1424			
Target (15% Scale)	(T) Pier	618.4	9666	158	17.3	19.44	31.9	4.42
	(C) Pier	1751		158	32			
UT Tyler Structure	(T) Pier	1152	13824	164.4	34.2	20	37.2	13.12
	(C) Pier	1152		83.8	34.2			

Figure 4.3 shows the 15% laboratory structure. Loading was accomplished using a lateral jack that supplied the story shears for all three stories constructed plus the resultant shear for the upper five stories. In an actual structure, lateral load from an earthquake would be applied to both piers independently – in the UT Tyler structure this load was lumped and applied through one jack only. The gravity load from the upper stories was applied using tensioned cables within ducts of the piers. The forces in the post-tensioned cables are shown in Table 4.2. The prototype and 15% target have two beams per story, while the UT Tyler Structure only has one per story. The scale of 15% caused this difference to be necessary as the beams would have been so small that the behavior of the system would not have matched that of the larger prototypes. In order to scale the design forces properly, the forces for a single scaled beam are multiplied by two to account for the combining of the beams made necessary by scaling. The PT forces in the beams are not equal in the 100% scale model, but for simplicity the target PT design forces for the UT Tyler Structure were made equal. However, this equality did not actually occur due to errors made in construction – see Section 5.2.4.

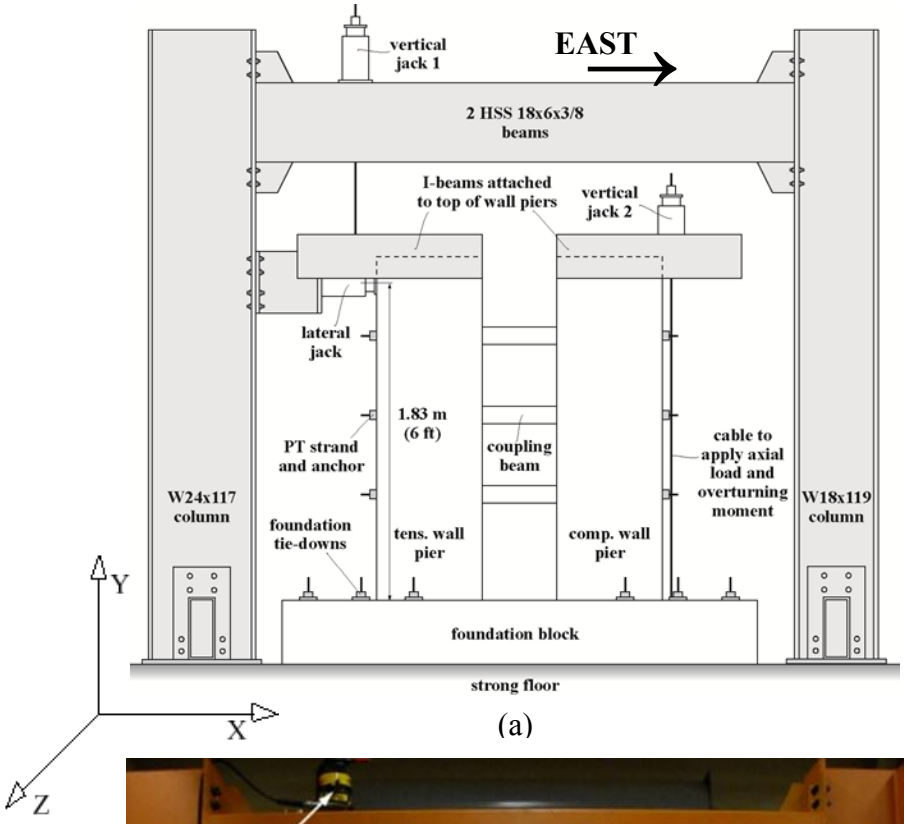

(a)

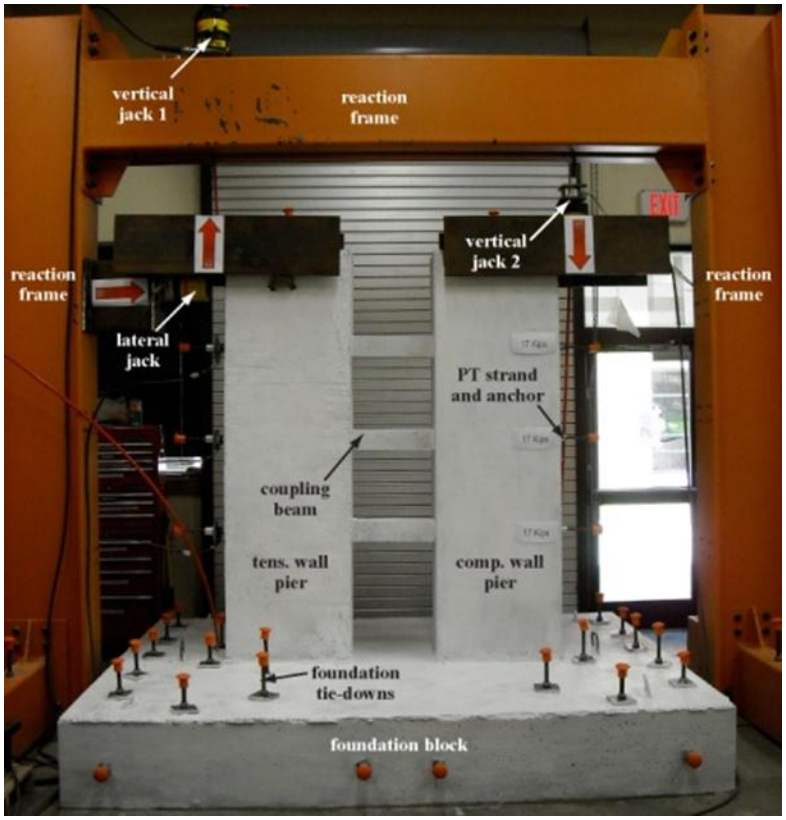

(b)

Figure 4.3: UT Tyler Experimental Specimen (Looking North): (a) schematic; (b) laboratory test setup

Additional axial force (both tensile and compressive) in the piers caused by coupling was provided by jacks attached to cables at the top of the wall piers that allowed both tension and compression to be applied. These cables were connected to steel beams attached to the tops of the walls. By attaching these cables at a distance from the centerline of the wall piers, the associated jacks were also used to provide the overturning moment at the top of each pier caused by the upper stories. Forces in all three hydraulic jacks were measured using calibrated load cells (see Section 3.2.2 for calibration details).

The foundation, wall piers, and coupling beams were all cast separately. The flexural reinforcement in the wall piers was cast with a 7 in. extension protruding from the base, and the base moment connection for each pier was created by grouting these bars into anchors embedded in the foundation.

The applied loads (lateral, overturning moment, and axial) in the experiment were scaled directly from those of the prototype building.

Table 4.2: Post-Tension Cable and Gravity Forces

	PT 1st Story Beam Force (kips)	PT 2nd Story Beam Force (kips)	PT 3rd Story Beam Force (kips)	Gravity Pier Force (kips)
Prototype Structure	404.6x2=809.2	285.3x2=570.6	285.3x2=570.6	2644.4
Target (15% Scale)	9.10x2=18.2	6.42x2=12.84	6.42x2=12.84	59.5
UT Tyler Structure	17	17	17	56.6

4.2.1 Foundation Design

The foundation was designed as three sections separated by sheet metal so that it could be dissembled simply – see Figure 4.4. In order for the system to function as a unit

during testing the three pieces were post-tensioned together. The capacity of each section was calculated assuming the system was singly reinforced. The area of steel provided in the middle block is 3.2 in^2 (four - #7 bars and four - #4 bars). This yields a moment capacity of 171 k-ft using reinforced concrete design principles (ACI 318). Similarly, the identical edge sections provide an area of steel of 0.6 in^2 (three - #4 bars) and a moment capacity of 38 k-ft each. This makes the total capacity of the foundation 297 k-ft.

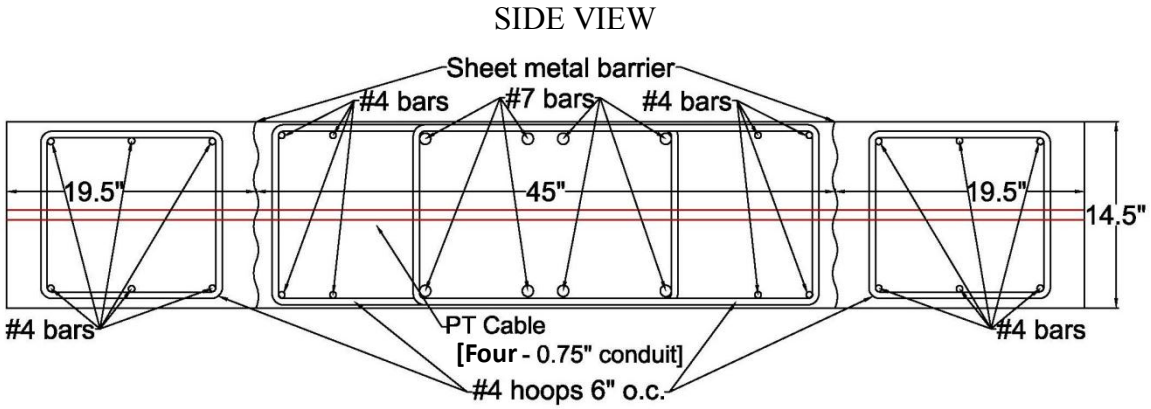

Figure 4.4: Schematic of Reinforcement Layout (Side View)

The moment demand for the foundation was calculated using the worst case moment within the foundation from the As-Built ABAQUS model (see Section 8.1.1 for model description). The worst case moment demand was calculated based on examining the extreme fiber stresses and with the assumption of elastic behavior. These stresses were localized to a small area, but for design purposes were assumed to encompass the entire width of the foundation. This produces a severely conservative moment demand of 142 k-ft for the foundation. In spite of the extremely conservative demand calculations, the middle portion of the foundation is capable of resisting the moment demand without the edge blocks.

4.3 Strong Floor Tie Down Design

The basic anchor design of the existing floor was insufficient for the loads that were required for this test. Drop in anchors (Simpson StrongTie coil-threaded drop-in carbon steel anchors) were used to strengthen the connection between the foundation of the specimen and the strong floor beneath. They were arranged as shown in Figure 4.5.

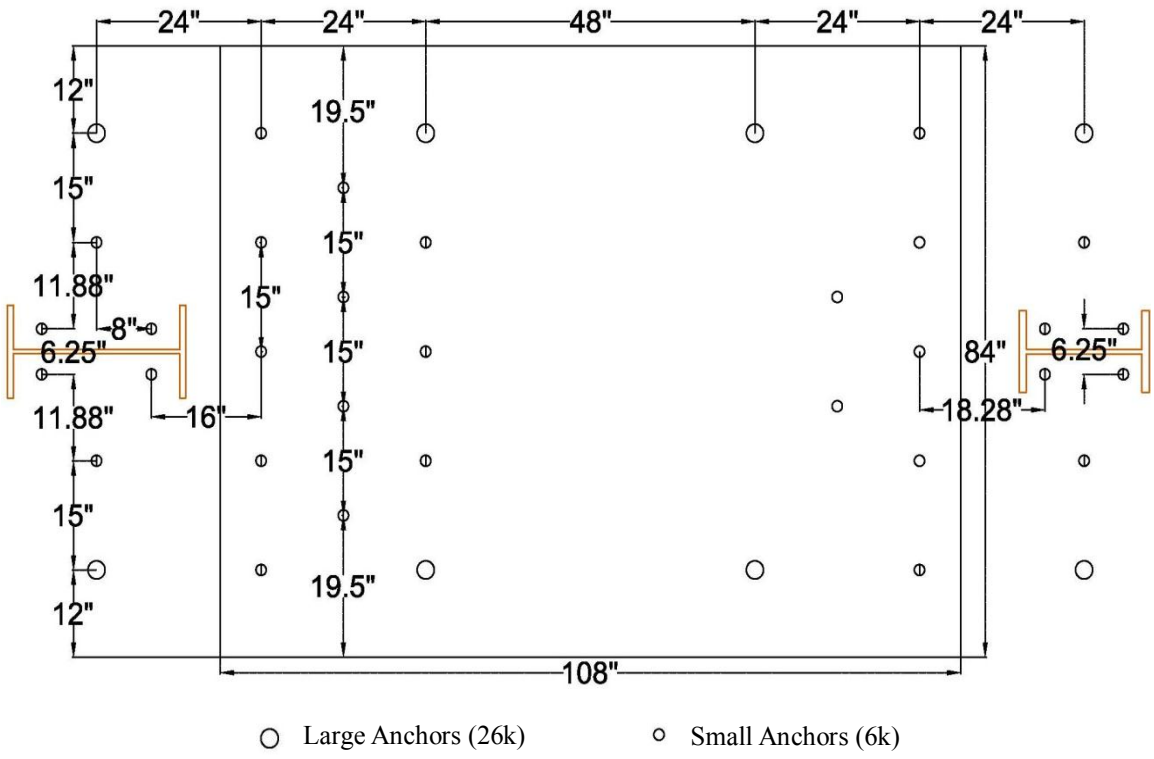

Figure 4.5: Strong Floor Anchor Layout

Based on this layout, the capacity of the strong floor anchor system was calculated. A force of 6 kips was assumed for the drop in anchors that were added to the larger existing anchors. For the larger existing anchors, a force of 26 kips was assumed. These forces were assumed based on the manufacturer's recommendation for the small anchor capacities and the larger existing anchors were assumed based on the tensile strength of the B7 threaded rod used as a connector into the anchors. The moments of

these forces were taken with respect to the center line of the foundation. The moment capacity of the anchor system was calculated to be 282 k-ft. The moment demand calculated in Section 4.2.1 is also the demand for the anchor system. The anchor system provides a moment capacity of 664 k-ft. The anchor system can withstand up to 92 kips at the applied lateral load height of 86.5 inches (pier height + foundation thickness).

CHAPTER 5: CONSTRUCTION AND MATERIALS

5.1 Construction Methods

This section describes the methods used to construct the test specimen. The specimen was a reinforced concrete structure which required formwork construction, bending of various sizes of rebar for cages, and concrete placement. After the separate portions of the specimen were cast and cured, the piers had to be grouted into the foundation and the beams had to be grouted into place to remove placement gaps. After the grout finished curing, the foundation was post-tensioned together through ungrouted conduits shown in Figure 5.1a, and the beams and walls were post-tensioned together to form the coupling wall system.

5.1.1 Formwork Construction

The formwork was constructed with the foundation in place, and both piers side by side next to the foundation formwork, as shown in Figure 5.1, in order to use the least amount of lumber and provide the most stability. For the foundation, a layer of plastic was placed on the floor to prevent bonding between the foundation and the strong floor beneath. Additionally, sheet metal was placed to divide the foundation into three parts for easier removal after testing. The three separate pieces were later post-tensioned together in order for the foundation to behave as one unit. Underneath the piers two pieces of plywood were placed so that the formwork walls could be constructed at equal height throughout. For the ends of the piers, which had protruding rebar for later embedding into the foundation and threaded rod for attaching the steel I-Beam lever (Figure 5.2), holes

were drilled into the ends of the formwork to allow the rebar to be placed correctly without allowing concrete to leak out of the form. The side of the plywood that would be directly exposed to concrete had vegetable oil applied immediately before placement of concrete to increase ease of removability.

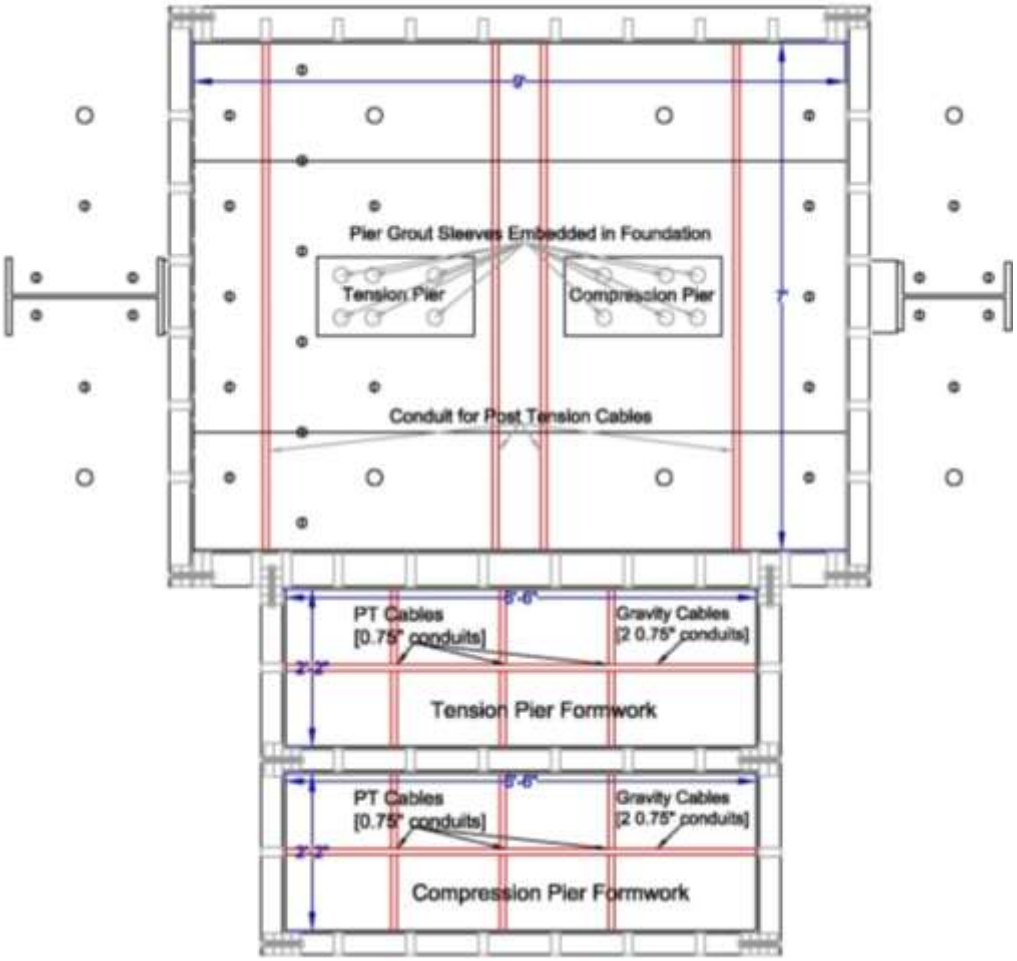

(a)

(b)

Figure 5.1: Formwork of Foundation and Piers: (a) Schematic Layout; (b) Photograph of Formwork

5.1.2 Rebar Construction

The rebar was bent using the jig in Figure 5.2. The bent rebar was then arranged into cages using the longitudinal reinforcement in the foundation and the piers (Figure 5.3). The smaller cages surrounding the anchors were created using the same rebar jig in Figure 5.2. The rebar for the beams had to be bent in a table mounted vice grip in order for the small dimensions to be achieved. Bend radii specified in ACI 318 were not satisfied due to small scale nature of the test. No adverse effects were observed. Longitudinal reinforcement in the piers protruded out of the base of the piers by 7 inches. The protruding rebar was later embedded into the foundation using grout sleeves described in Section 5.1.4. A lifting handle was added to the outward facing side of each pier to aid in the removal and later placement of the piers.

Figure 5.2: Steel Jig Used to Bend Rebar

Figure 5.3: Foundation Rebar: Rebar Cages Arranged in Foundation

In addition, ¾ inch threaded rod protruded out of the top of the piers. Four rods, 32 inches long, were embedded 20 inches into the top of the piers with 12 inches protruding. The details of the layout of threaded rods and how they attached to the steel I-Beam lever is discussed later in Section 6.2 (Figure 6.2). The embedded end of each rod had a nut attached to insure greater embedment strength. The detailed view of the protruding rebar and threaded rod can be seen in Figure 5.4.

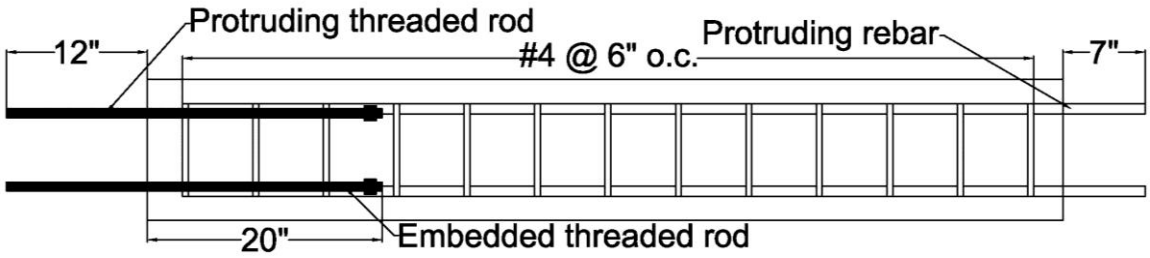

Figure 5.4: Protruding Threaded Rod and Rebar Details of a Pier

5.1.3 Concrete Placement and Curing

The placement of concrete was difficult as the distance from the truck to the farthest pier was 19 ft. The extensions provided by the concrete vendor allowed the center

of the closest pier to be easily reached. The remaining concrete had to be shoveled the extra 3 ft to the farthest pier. While placing the concrete, each section was vibrated to prevent air pockets in the concrete. The beams were placed separately by hand and were also vibrated to prevent air pockets. The concrete was then covered in 2 mm plastic and cured for 28 days, after which time the formwork was removed and the piers prepped for placement.

5.1.4 Pier Grouting

To connect the piers to the foundation as if they were cast as one object, grout sleeves (Figure 5.5) were used to grout in the 7 in of rebar that protruded from the bottom of the piers. The piers were lifted into place and held there by a two ton crane while small wooden blocks were placed at the corners to provide space between the top of the foundation and the bottom of the piers in which grout could be placed. The grout was then pushed into the grout sleeves and the space between the pier and foundation all while still supported by the two ton crane for safety. The piers remained on the blocks with the support of the crane for the recommended 28 days, after which time the blocks and crane support was removed.

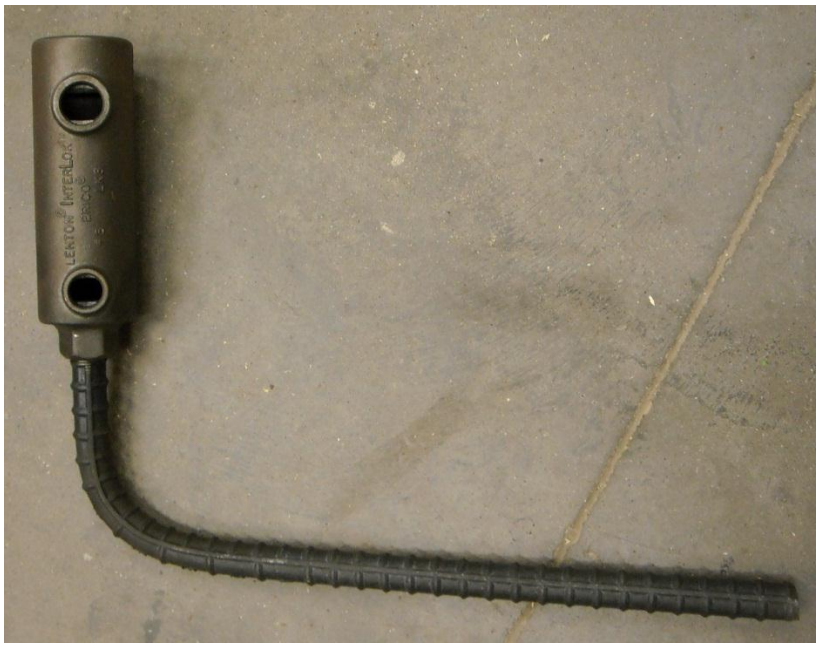

(a)

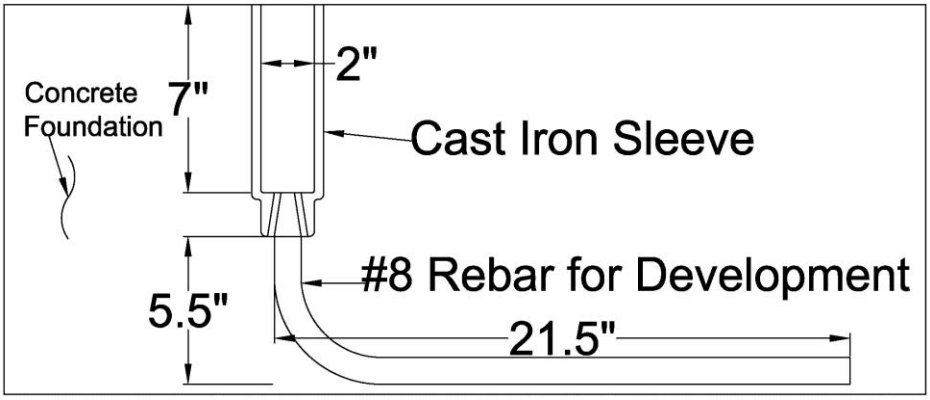

(b)

Figure 5.5: Lenton Interlock (LK8) Grout Sleeve: (a) Grout Sleeve; (b) Schematic of Placement in Foundation

5.1.5 Post-Tensioning Cables

After the grout supporting the pier-foundation connection had cured for the recommended 28 days, the specimen could be post-tensioned. The foundation was post-tensioned first to better understand the process because the post-tensioning force in the foundation was not critical. All of the other post-tension cables required a load cell on the

cable in order for the iNET system to monitor the forces within the cable throughout the tests. The ends that required load cells where arranged as shown below in Figure 5.6.

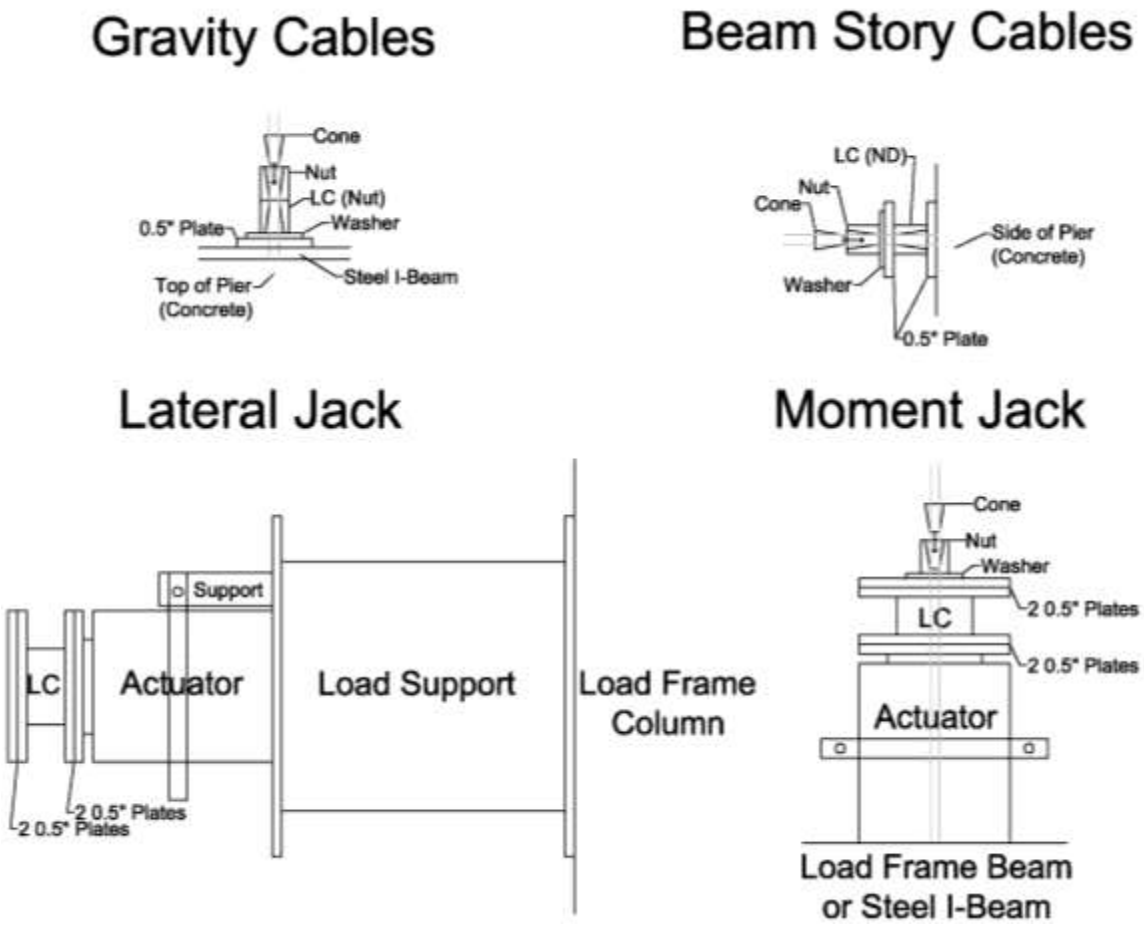

Figure 5.6: Load Cell Details Schematic

5.2 Specimen Materials

This section describes the material properties and sizes of the materials that were used to construct the specimen.

5.2.1 Concrete

The concrete was designed to the strength specifications needed for this project by Transit Mix Concrete, and was delivered to the project site. Pea gravel was elected as the

primary large aggregate to better simulate scaled standard size large aggregate.

5.2.1.1 Mix design

Table 5.1: Mix Design (provided by Transit Mix Concrete of Tyler, TX)

Material	Design Qty	Adj. Total	Required	Batched	% Var	% Moisture	Actual Water	Total Water
3/8" Pea Gravel	1894 lb	1919	11512 lb	11550 lb	0.0033	0.013%	18 gl	18
Sand	1065 lb	1113	6678 lb	6680 lb	0.0004	0.045%	35 gl	35
Cement	799 lb	799	4794 lb	4780 lb	-0.003			
Water	267 lb	176	1056 lb	1060 lb	0.0035		127 gl	127
Pozz 80	32 oz	32	192 oz	192 oz	0			
PS1466	32 oz	32	192 oz	192 oz	0			

Sand was ASTM C33 concrete sand; cement was ASTM C150 Type I-II with ASTM C618 class F fly ash. PS1466 is a mid-range water reducer meeting ASTM C494 Type F. Pozz 80 can be classified as a Type A, B, or D admixture under ASTM C494.

5.2.1.2 Concrete Strength

The concrete used in construction of the specimen was tested using a compressive testing machine over time in order to generate a time history of the compressive strength. Initially the curve generated in Figure 5.7 is used to estimate the full strength of the concrete based on the 28 day strength. Based on the 28 day strength, f'_c is estimated to be 7540 psi. Later tests were conducted to find the actual strength at the time of testing and beyond. The strength of the concrete during Phase I was measured at 8230 psi while the strength during Phase II and III, which were conducted only two days apart, was found to be 8680 psi. The original design specifies a strength of 6000 psi; therefore the concrete used in the actual construction was significantly stronger than designed.

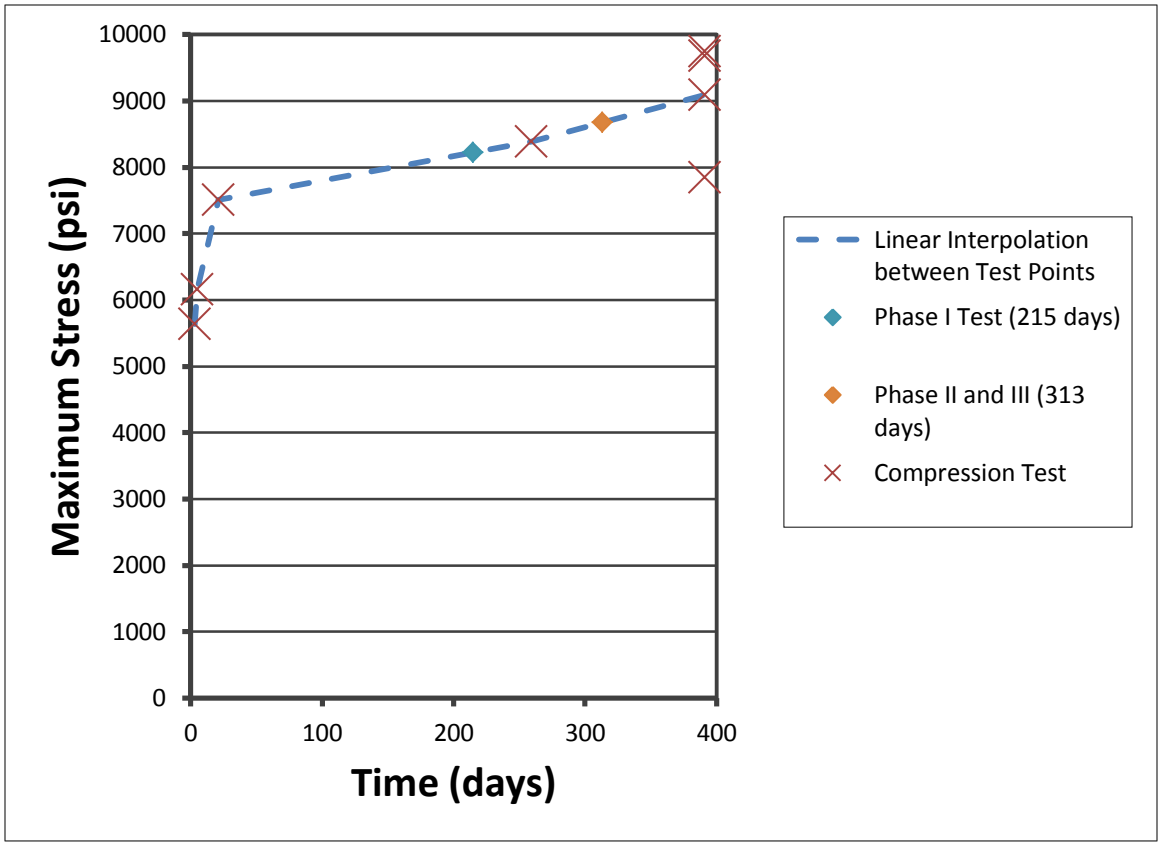

Figure 5.7: Time History Compressive Strength Curve for Concrete

5.2.2 Grout

Five Star® Grout was chosen to grout the piers into the foundation and the beams to the piers.

5.2.2.1 Grout Thermal Specifications

Five Star® Grout: When tested in accordance with ASTM C 827, Five Star® Grout exhibits positive thermal expansion and meets the performance requirements of ASTM C 1107-02 Grades A, B and C, ASTM C 1107-07, and CRD-C 621-93 specifications for non-shrink grout over a wide temperature range, 40°F - 90°F (4°C - 32°C).

5.2.2.2 Grout Mechanical Strength Specifications

Five Star® Grout was used because of its non-shrink formula and rated

compressive strength of 8 ksi and pull-out strength of 2.4 ksi. In order to determine the strength of the grout used to connect the piers to the foundation via grout sleeves, the grout was tested several times using a compressive testing machine. These values were then recorded and averaged to determine the best estimate for the strength of the grout (Table 5.2). Test 1 and 2 were conducted at the first time of testing, Phase I. Tests 3 through 7 were conducted 175 days later. Surprisingly, the values of the first two tests were higher than the values of the latter five. The reason for this loss of strength is unclear but may explain the unexpected pull out of the rebar from the embedded grout sleeves in the foundation.

Table 5.2: Grout Strength (psi) from Compression Testing

	Strength (psi)
Test 1	5780
Test 2	5900
Test 3	3130
Test 4	5390
Test 5	4260
Test 6	3780
Test 7	6630
Average	4981

5.2.3 Rebar

The rebar used in the construction of the specimen are listed by size and application in Table 5.3. No physical testing was conducted on the rebar; standard Grade 60 rebar was used. The general design for steel reinforcement for the foundation, piers and beams can be found in Section 4.2.

Table 5.3: Size and Application of Rebar Used

Application	Size
Pier Shear Stirrups	#4
Pier Tension	#6 and #7
Beam Shear Stirrups	#3
Beam Tension	#3
Foundation Stirrups	#4
Foundation Tension	#7 and #8

5.2.4 Post-Tension Cables

All post-tensioning cables were ½ inch diameter, and grade 270. The post-tension cables were run through ungrouted conduit; the layout of which can be seen in Figure 5.1a. An anchor was attached to one end and a tension machine (Figure 5.7) was used to tighten the cone and nut configuration similar to that seen in Figure 5.4. The post-tension cables that were not through the foundation required one end of the cable to have a load cell in the line to monitor forces during testing. The tension machine used a gage attachment to read the force that it applied to the cable in order to achieve a specific load. This gage, along with the load cells on each cable, was initially used to indicate when to stop applying pressure to the cables. During the post-tensioning of the cables, the force applied dropped substantially as soon as the tension machine was removed from the line. Because of this, the maximum force of the tension machine was applied to each of the cables. In spite of this apparent excess loading, the forces in the cables were significantly lower than designed – see Table 5.4. In addition, because the cables located through the center of the beams were not re-tensioned after all beam cables were tensioned, the cables that were first tightened retained less force.

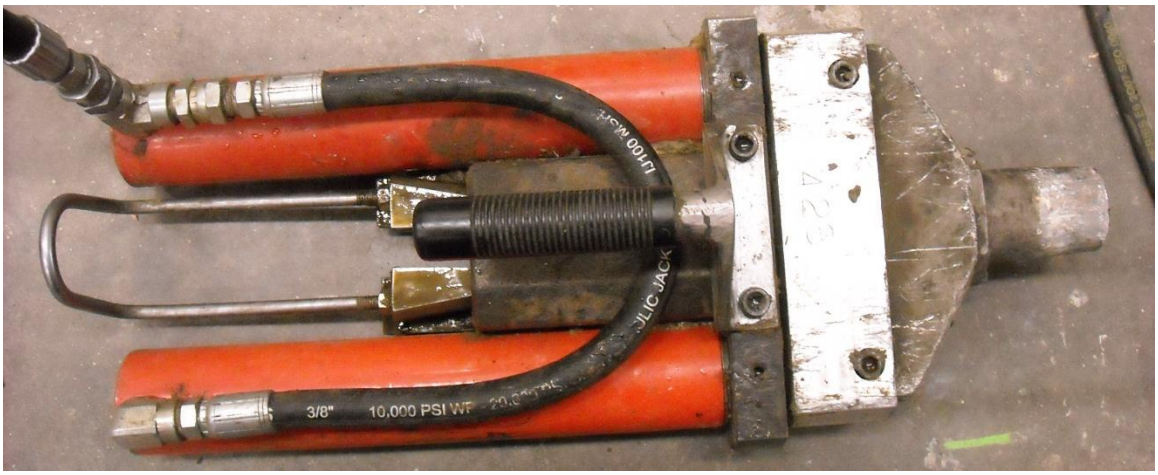

Figure 5.8: Post-Tension Machine

Table 5.4: As-Built Loads vs. Target Loads

	Target (lb)	As-Built (lb)
Tension Pier Gravity	56600	37700
Compression Pier Gravity	56600	44600
Beam Cable -- 1st Story	17000	454
Beam Cable -- 2nd Story	17000	3284
Beam Cable -- 3rd Story	17000	8338

CHAPTER 6: TEST PROTOCOL

6.1 Basic Structure Physical Set-up

After the UT Tyler specimen construction was completed, the load cells were assembled and calibrated as denoted in chapter 3. Several of the load cells were placed on PT cable lines in order to monitor the PT forces throughout loading.

Phase I of the project was set up as shown in Figure 6.1(a), with the lateral force being applied from the West side when looking North. Phase I ended because the lateral actuator ran out of stroke due to the large displacement in the load frame; the test had to be concluded until the issue with deformation of the load frame could be addressed. Several data points were taken during the unloading of the specimen. Phase II was conducted in the same manner as Phase I with an added support strut as indicated in Chapter 3. Phase II continued until the specimen failed in the direction of loading. Phase III was then conducted, as shown in Figure 6.1.1b, in the opposite direction, with the lateral force being applied to the East side when looking North. Phase III continued until the specimen began to fail in the second direction.

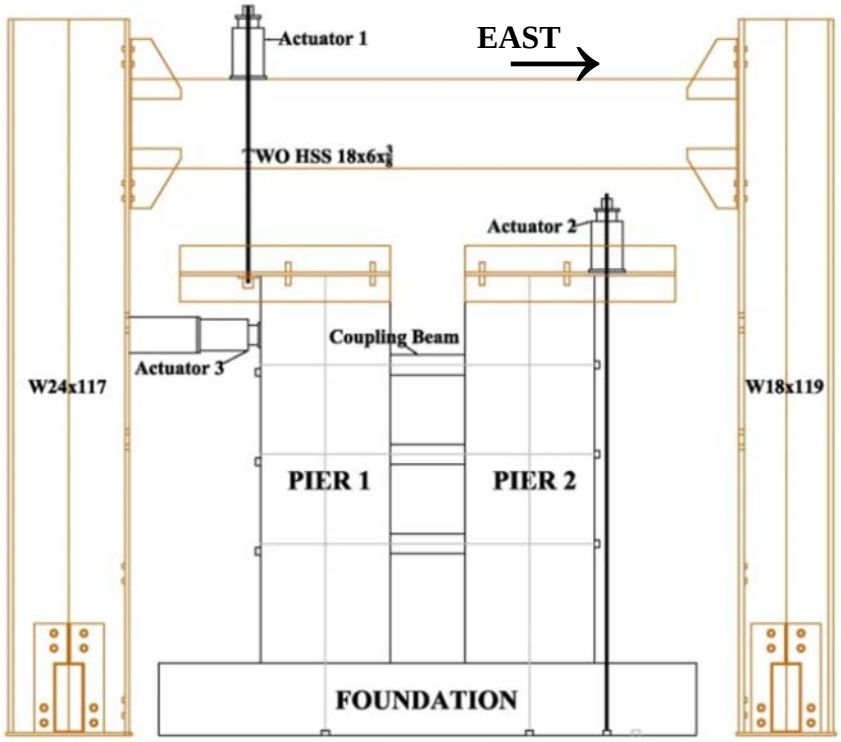

(a)

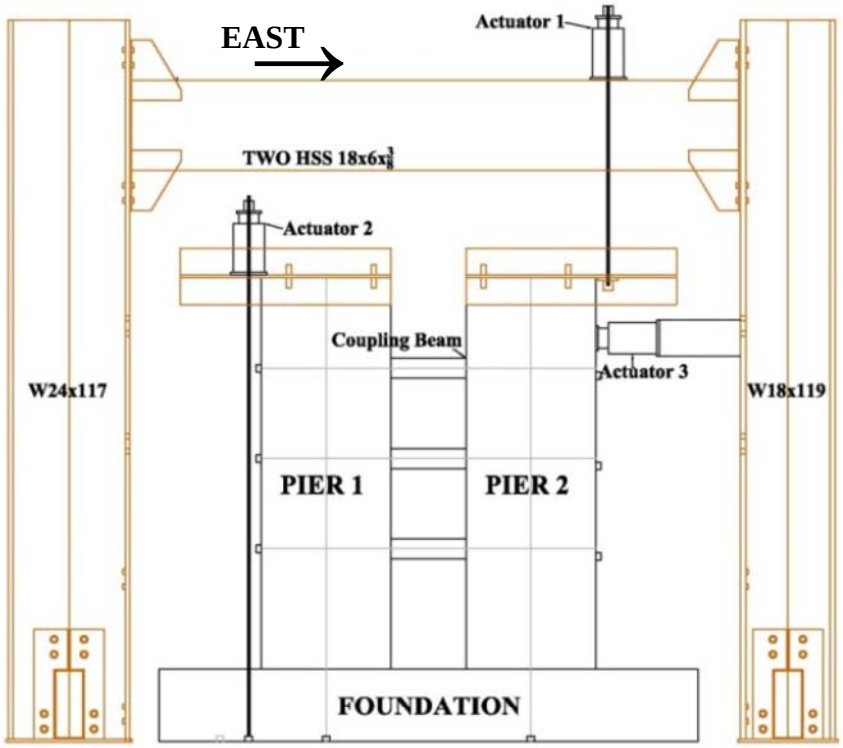

(b)

Figure 6.1: Actuator Set Up (Looking North): (a) Phase I and II; (b) Phase III

6.2 Loading Procedure

Before the test began, the iNET system was turned on and all the connections were checked. Then, the load cell readings were monitored to ensure that all wiring and constants for the iNET system were still correct. After the load cells were considered accurate, the lateral actuator had to be blocked up in order for the actuator to have the most stroke possible to be applied perpendicular to the tension pier. This was achieved by adding steel spacers and slightly activating the lateral actuator, until the friction force was great enough to suspend the steel spacers between the actuator and the tension pier. In order to support the lateral load, an actuator was hung from a lateral support which was attached to the load frame column.

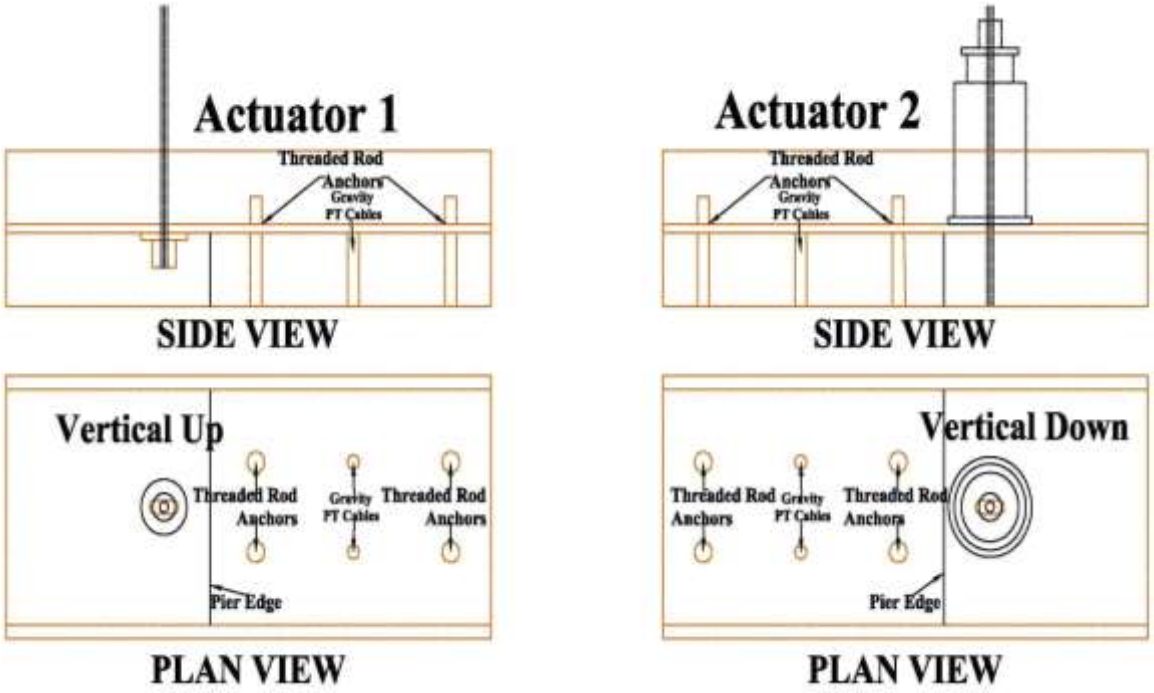

Figure 6.2: Load Application through I-Beam Attachments

Additional axial force (both tensile and compressive) in the piers caused by coupling was provided by jacks attached to cables at the top of the wall piers that allowed

both tension and compression to be applied. These cables were connected to steel beams attached to the tops of the walls. By attaching these cables at a distance from the centerline of the wall piers, the associated jacks were also used to provide the overturning moment at the top of each pier caused by the upper stories. The PT strands that were anchored to the base of the foundation were used to pull down on the piers and another PT cable was run through the load frame's upper support to pull up on the top of the piers as shown in Figure 6.2.

The load curve that was used for testing was derived from the results of the UT Tyler DRAIN analysis conducted by Notre Dame. Based on this continuous curve, a series of discrete points were taken for our force application. The actuator system was controlled by a single line hydro pump (Enterpac ZU4 class pump). The single line was broken up into a four line attachment, with one line locked closed. The Schematic of the pump manifold, including valves, gages and pumps, is shown in Figure 6.3. Each of the remaining three lines was given a digital pressure gage to monitor the force applied to each line as shown in Figure 6.4.

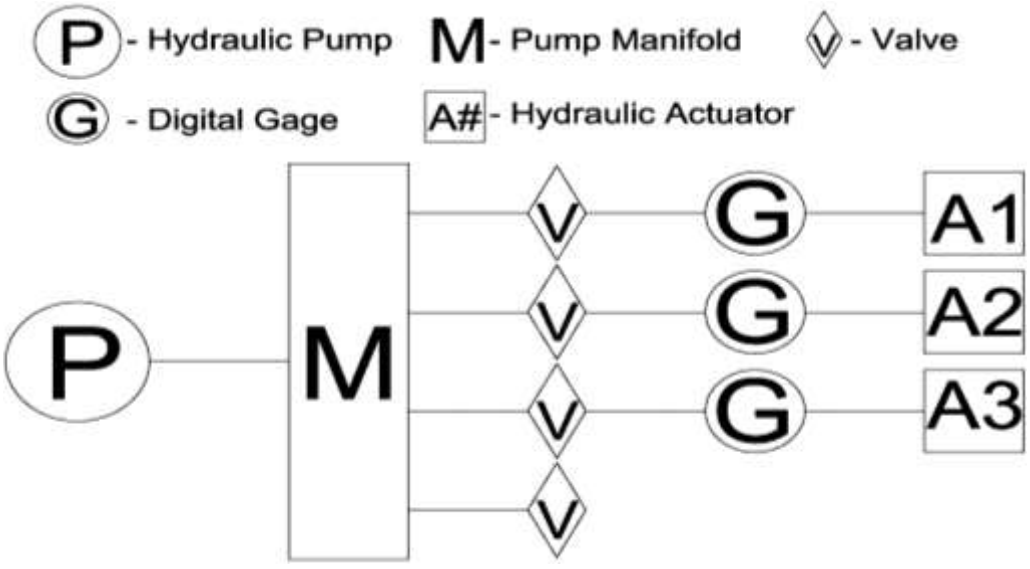

Figure 6.3: Schematic of the Pump Manifold

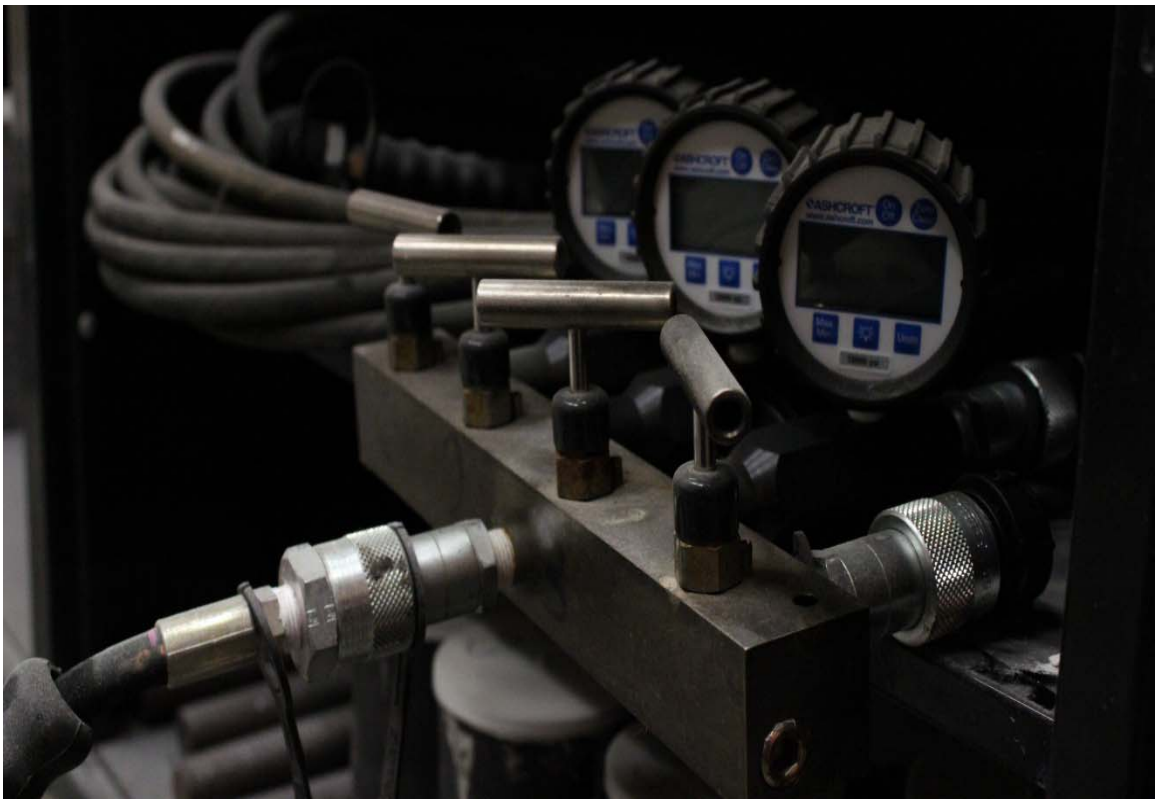

Figure 6.4: Photograph of Hydraulic Manifold with Digital Gages

In order to best control the pressure in each line, a system for application was derived. The highest force applied would be the lateral force; therefore that line would be opened. The vertical loads were lower and therefore were brought up to the required force, as read by the iNET system, one at a time. After each actuator was found to be applying the necessary load it was locked off to retain its pressure while the other actuators could be brought to their appropriate forces. Once all three actuators were brought to the forces designated by the curve described above, an image was taken by the DIC systems.

The calibration and set up for the DIC systems are provided in Chapter 3. Typically multiple DIC systems can be easily coordinated by simply placing them all on the same time interval between images and starting them simultaneously. For this test, it

was important to know the forces being applied during each of the images in order for the results to be useful. Since the exact timing of the force application was not known, a different approach was needed. Instead of setting a timer and walking away, as each point on the target curve was reached, an image was taken manually on all of the systems.

Table 6.1 shows the loads actually applied to the specimen during testing. The table shows the values based on the DIC stage, or image captured, and the phase in which the stages were captured. Each phase has a different number of stages as a different number of images where captured from each phase.

Table 6.1: Loads Applied During Testing Based on DIC Stage

	Phase I				Phase II				Phase III		
	Act. 1	Act. 2	Act. 3		Act. 1	Act. 2	Act. 3		Act. 1	Act. 2	Act. 3
Stage	LC1	LC2	LC3	Stage	LC1	LC2	LC3	Stage	LC1	LC2	LC3
0	-0.4	0.076	-0.12	0	-0.5	0.3	-0.4	0	0.1	0.2	-0.2
1	2.6	1.3	1.2	1	10.4	5.1	5.1	1	2.1	0.2	-0.05
2	5.1	2.8	2.9	2	20.1	10.9	10.3	2	4.9	2.7	2.4
3	10.5	5.5	5.7	3	30.9	18	17.2	3	9.8	4.9	3.6
4	15.1	9.7	8.8	4	40.2	26	22.7	4	15.2	7.3	6.3
5	20.3	11.1	11.1	5	49.8	27.5	27.3	5	20.3	9.6	10.5
6	25.5	13.7	13.8	6	55.2	28.9	29.3	6	25.3	14.4	13.9
7	30.6	16.6	16.8	7	59.7	30.7	31.6	7	30.1	16.3	17.1
8	35.2	19.8	19.7	8	64.7	31.7	32.3	8	35.4	18.2	18.3
9	40.6	22.5	22.2	9	62.3	28.1	31.6	9	40.9	21.1	21.2
10	42.54	23.9	23.7	10	58	21.7	31.4	10	44.8	25.3	24.3
11	44.9	25.6	25.9	11	57.5	21.6	30.9	11	50.7	26.6	26.7
12	47.2	26.7	26.8	12	56.9	21.4	31.3	12	55.6	27.4	28.7
13	47.5	28.2	26.5	13	56.5	21.4	31.1	13	60.9	29.7	29.5
14	50.1	28	27.8	14	56.5	21.6	30.9	14	42.6	22.9	22.3
15	52.8	28.4	28.4	15	56.4	21.5	31	15	22.7	10.8	10.9
16	55.1	30.4	30.3	16	56.5	21.3	31.2	16	0.15	-0.05	-0.2
17	57.1	30.1	30.1	17	-0.08	0.15	-0.2	17	4.1	0.3	-0.1
18	60.1	30.8	31.4	18	0.2	32.3	34.9	18	30.4	13.8	15.6
19	62.7	31.5	31.6	19	42.1	22.9	32.6	19	51.2	24.9	26.7
20	65.2	32.5	32.3	20	49.3	18.5	31.6	20	55.9	29.7	29.5
21	60	33.2	33.2	21	50.4	13.9	30.7	21	60.9	30	32.5
22	50.1	27.3	27.7	22	45.5	10.9	29.2	22	65.6	31.5	32.6
23	39.4	22.6	22.4	23	0	0	0	23	70.8	31.9	33.9
24	28.3	15.8	16.1					24	72.6	35.8	38.3
25	19.5	11.1	11					25	75.3	35.4	37.9
26	10.1	5.6	5.7					26	0.1	0.2	-0.2
27	-0.13	0.344	0.145								

CHAPTER 7: EXPERIMENTAL RESULTS

This section presents the results gathered from the experimental data collected during testing. First, the measurement and acquisition systems are validated using secondary measurement systems. The remainder of the chapter is spent establishing the behavior of the coupled wall system based on the behavior of critical areas and validating the developed ABAQUS model. The behaviors that are focused on include: the global behavior, foundation behavior, pier behavior and beam behavior. All four fields of view (FOV), as defined in Section 3.3.2.3, are used in order to define the system behavior. Strain maps generated by the DIC software are provided for each FOV for phases I, II, and III as visual aids. The post test condition of the test specimen and the conclusions made about the structural behavior is also presented.

7.1 Instrumentation Validation

The load displacement response of the string potentiometer and the digital image correlation systems are compared for all phases in Figure 7.1-3 in order to validate the data collection processes. The load displacement response of the recorded pump values will be compared with the iNET system outputs for the load cells (Figures 7.4-6) for all phases to validate the accuracy of the monitoring systems.

7.1.1 String Potentiometer vs. DIC

The string potentiometer measured the displacement of the specimen at one specific point: the handle located in the center of the tension pier. The precise location

and information on the string potentiometer can be found in Table 3.1 and Figure 3.5. In order to compare the displacements collected by the DIC System 1 to the string potentiometer results, a line at the height of the handle was generated and the displacement data from that line was averaged for each stage in each phase. Each stage had a load associated with it. Based on this data, the two methods of measuring displacement were compared. Figures 7.1, 7.2, and 7.3 show the graphical comparison for all phases. The initial displacement was removed from Phase II and III for simple comparison.

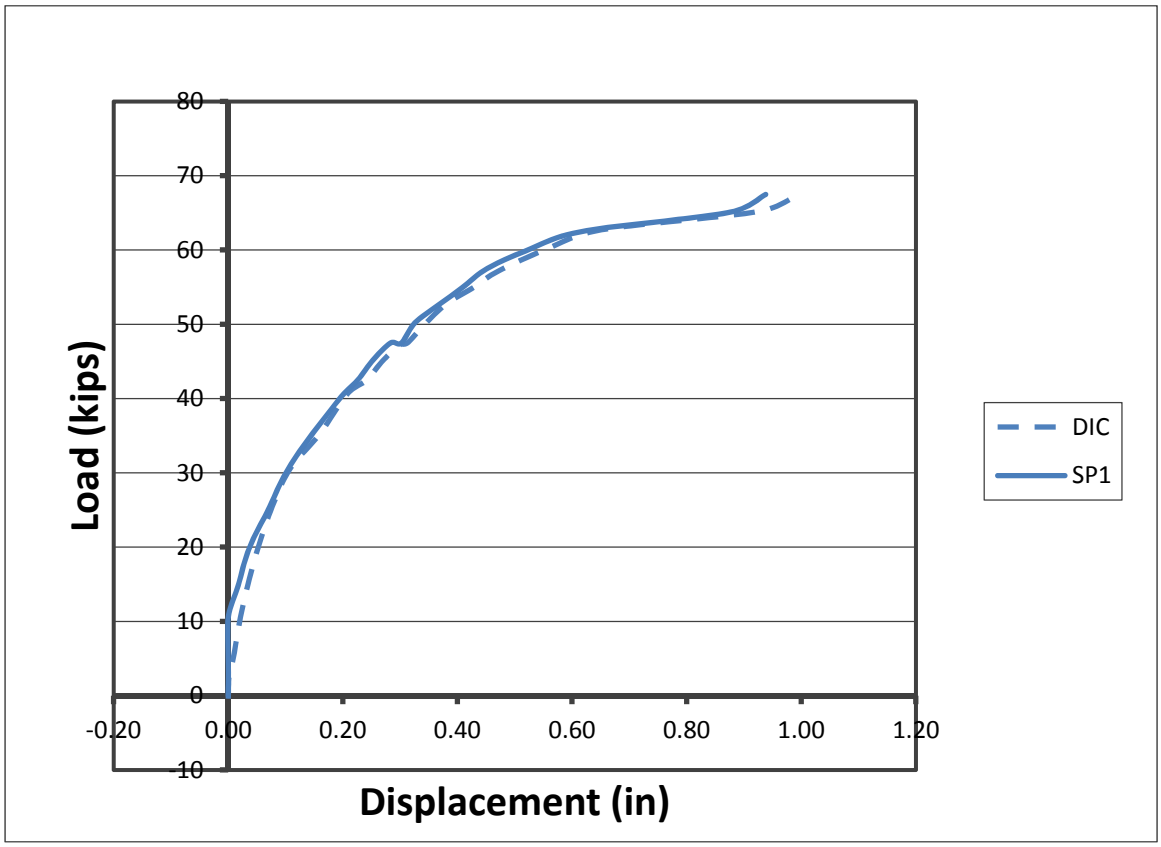

Figure 7.1: String Potentiometer vs. Digital Image Correlation System for Phase I

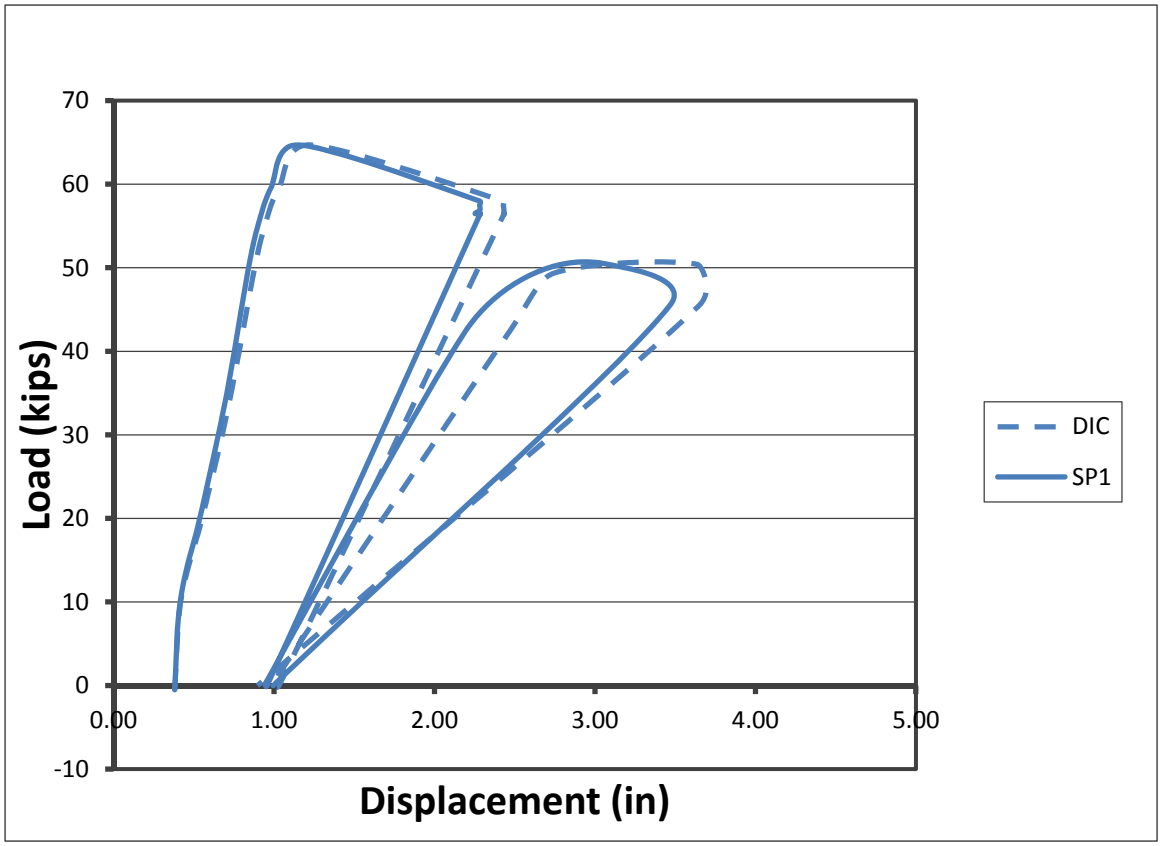

Figure 7.2: String Potentiometer vs. Digital Image Correlation System for Phase II

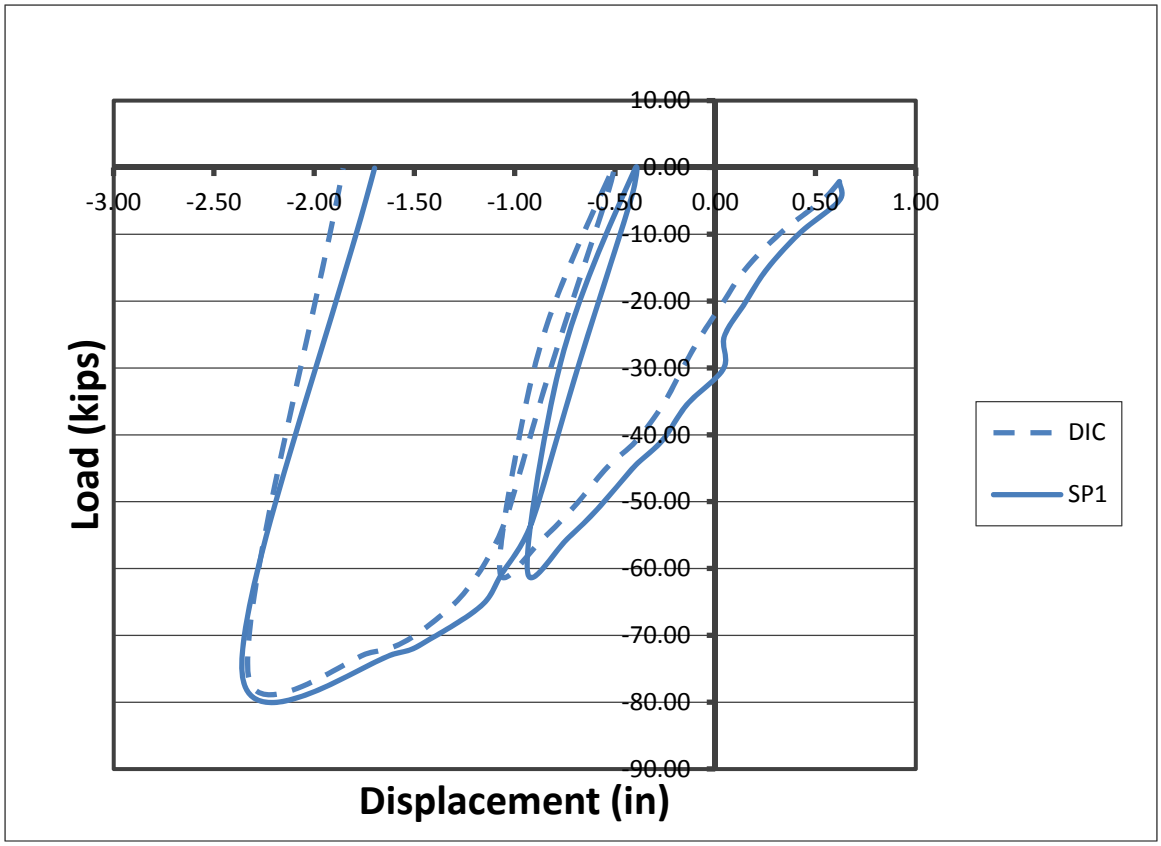

Figure 7.3: String Potentiometer vs. Digital Image Correlation System for Phase III

7.1.2 Pressure vs. Load Cells

The pressure in each actuator was monitored during testing and recorded for comparison to verify that the iNET outputs were accurate. This was done using the digital gages (Figure 6.4) to read the pressure in each line and then convert it to a force based on the effective area of the actuator head. The digital gages have an accuracy of ±0.5 % according to the manufacturer. The actuators used were Enterpac Model RCH-603 with an effective area of 12.73 square inches. During testing the digital gage turned off during one of the readings, therefore the graph for Phase I is missing a data point. The comparison was only conducted for the lateral actuator because of its critical nature. Figures 7.4, 7.5, and 7.6 show the comparison of the values. The values were plotted with the stage number, the number assigned to the image by the DIC software starting at stage

0, instead of lateral load for simplicity. Stage numbers are not necessarily associated with linearly applied forces.

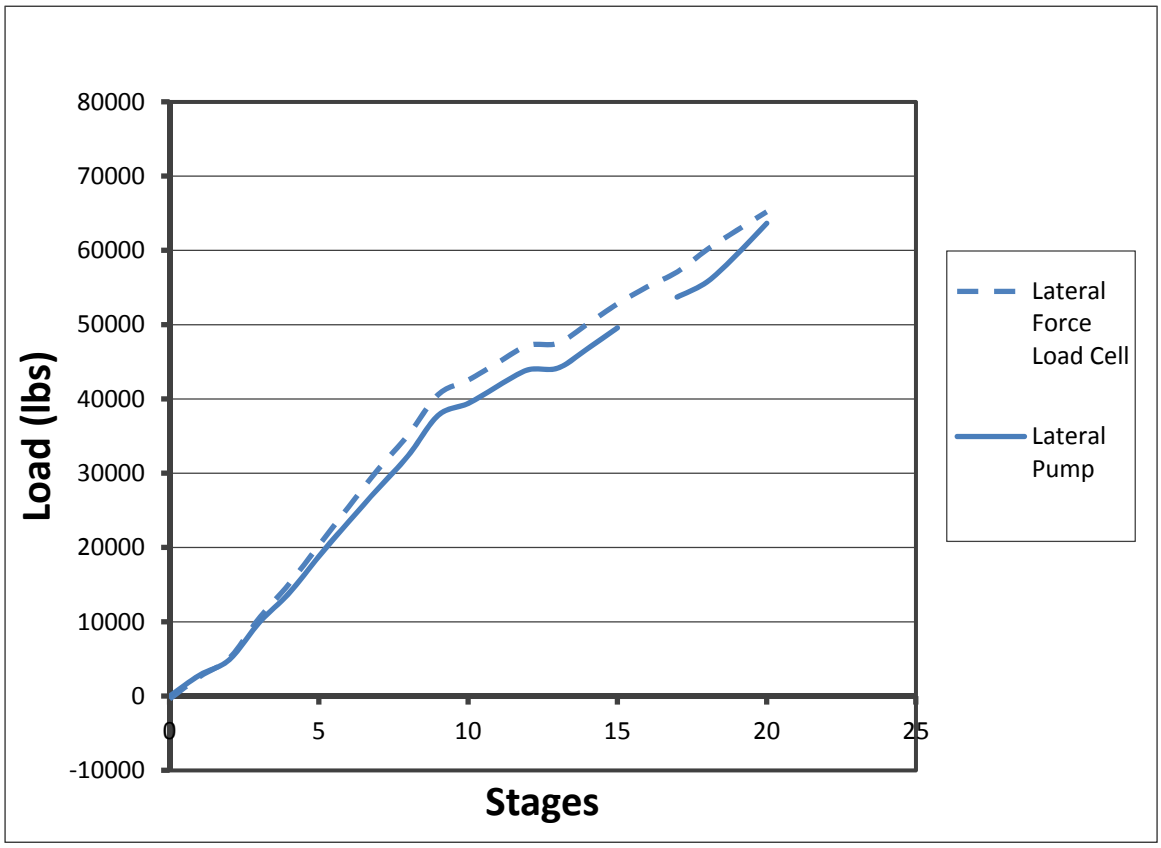

Figure 7.4: Actuator Pressure Gage vs. iNET Outputs for Load Cell for Phase I

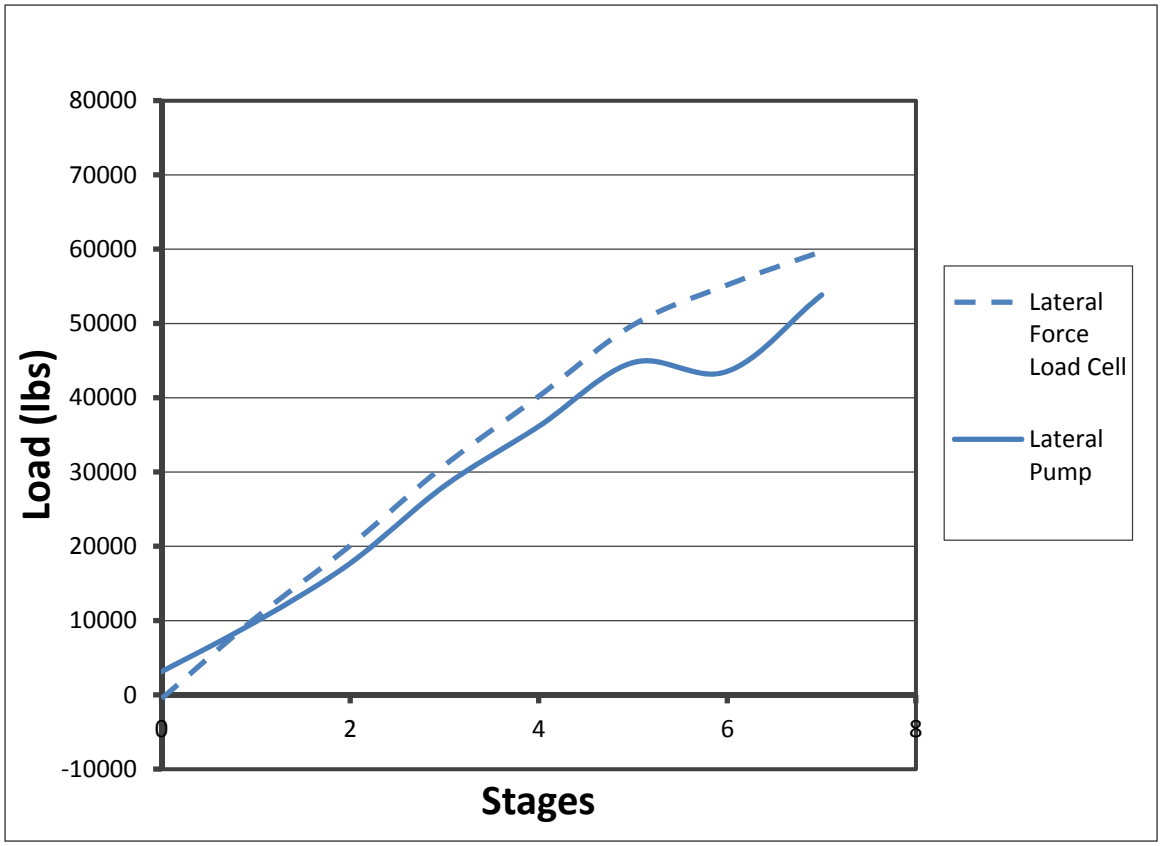

Figure 7.5: Actuator Pressure Gage vs. iNET Outputs for Load Cell for Phase II

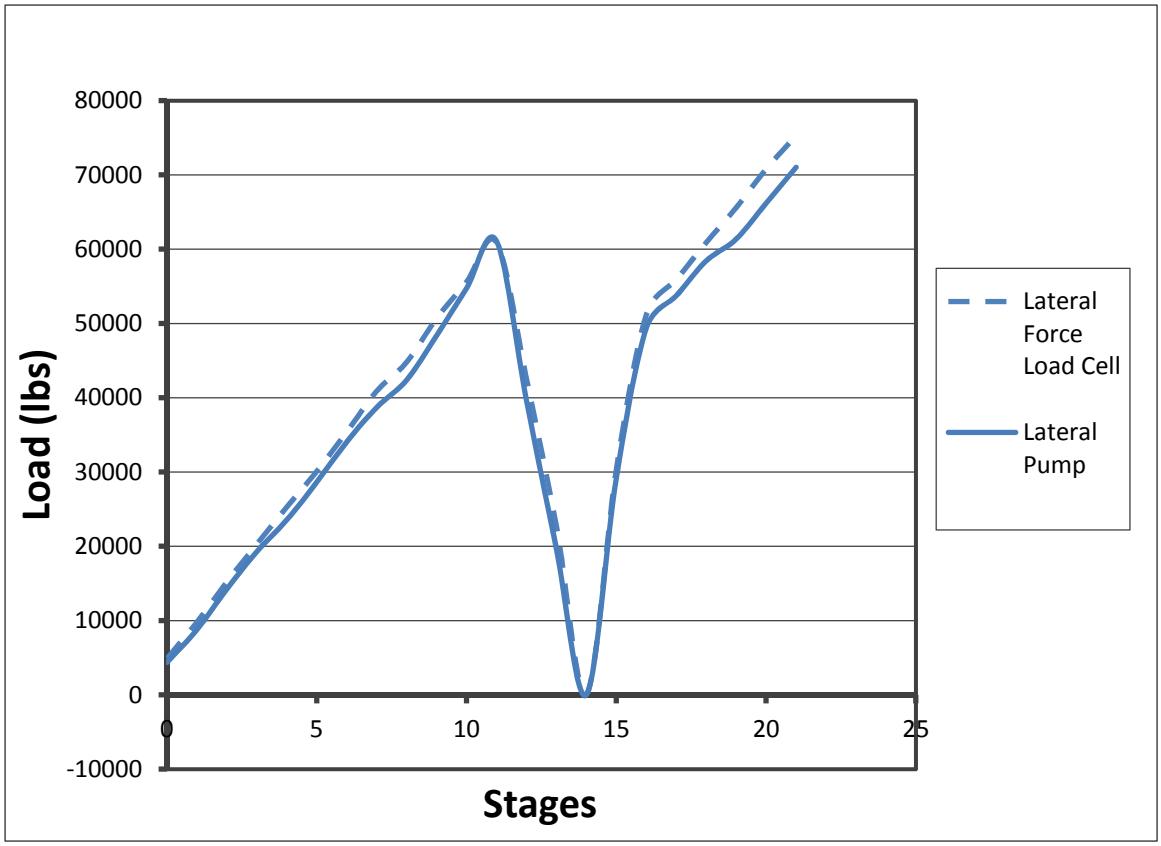

Figure 7.6: Actuator Pressure Gage vs. iNET Outputs for Load Cell for Phase III

7.1.3 Instrumentation Validity Conclusions

Based on the comparisons provided, it was determined that the measurement and acquisition system were functioning properly. For the remainder of this chapter, load is reported using LC1 which reflects the applied lateral load – see Section 3.2.2 for calibration information; displacements and drifts in all future plots are calculates using SP1 values – see Section 3.2.1 for information regarding string potentiometers used during testing.

7.2 Global Behavior

The remainder of this chapter will include comparisons between the measured DIC data and the results from the generated ABAQUS model. For a full model description and future work conducted using finite element analysis, see Chapter 8.

The 15% scale post-tension coupled wall system was tested in three phases as described in Section 6.2. Figure 7.7 shows the lateral load versus displacement history from SP1 for the experimental test. The difference in displacements between the end of each phase and the beginning of the next is attributed to the self-centering capability of the coupling wall system. One full load reversal was applied to the structure until failure in both directions. To achieve the full load reversal, the lateral jack and the two vertical jacks were moved from their initial positions shown in Figure 6.1(a) after failure in the first loading direction as discussed in Section 6.1 herein. During both Phase II and III the specimen was unloaded and reloaded; this is seen in Figure 7.7 where the force goes to zero and is then reapplied. Because Phase III was conducted in the opposite direction, the displacements are recorded as negative values. Locations where unloading is evident in the plot occurred when the displacement capacity of the lateral loading jack was exceeded, so the jack was depressurized while spacers were added to increase the total structure lateral travel; the second hysteresis of the phase II is not considered for comparisons seen in this Chapter. The hysteresis of the structure exhibited a smaller amount of re-centering capability than was expected, which was due to the relatively small PT forces that were achieved in the coupling beam strands as shown in Table 5.4. In order to limit confusion for interpretation of the data, a coordinate system, shown in Figure 4.3, will be used to describe directional information. Drift is a measure of lateral displacement – it is the lateral displacement divided by the height of the measurement. Drifts used in the comparisons given in this thesis were calculated using the heights at which the displacements were collected; a height of 72 inches (the location at which the highest displacement is measured on the specimen) was used for all measured data (DIC)

and 78 inches (the top left corner of the models) was used for data collected from analytical modeling. Drift here is relative to the distance of the monitored point from the base of the foundation, therefore the variation in measurement height does not affect the measurement. Also, the direction of East will be denoted and the direction of the view (i.e. North or South) will be identified on all pertinent figures.

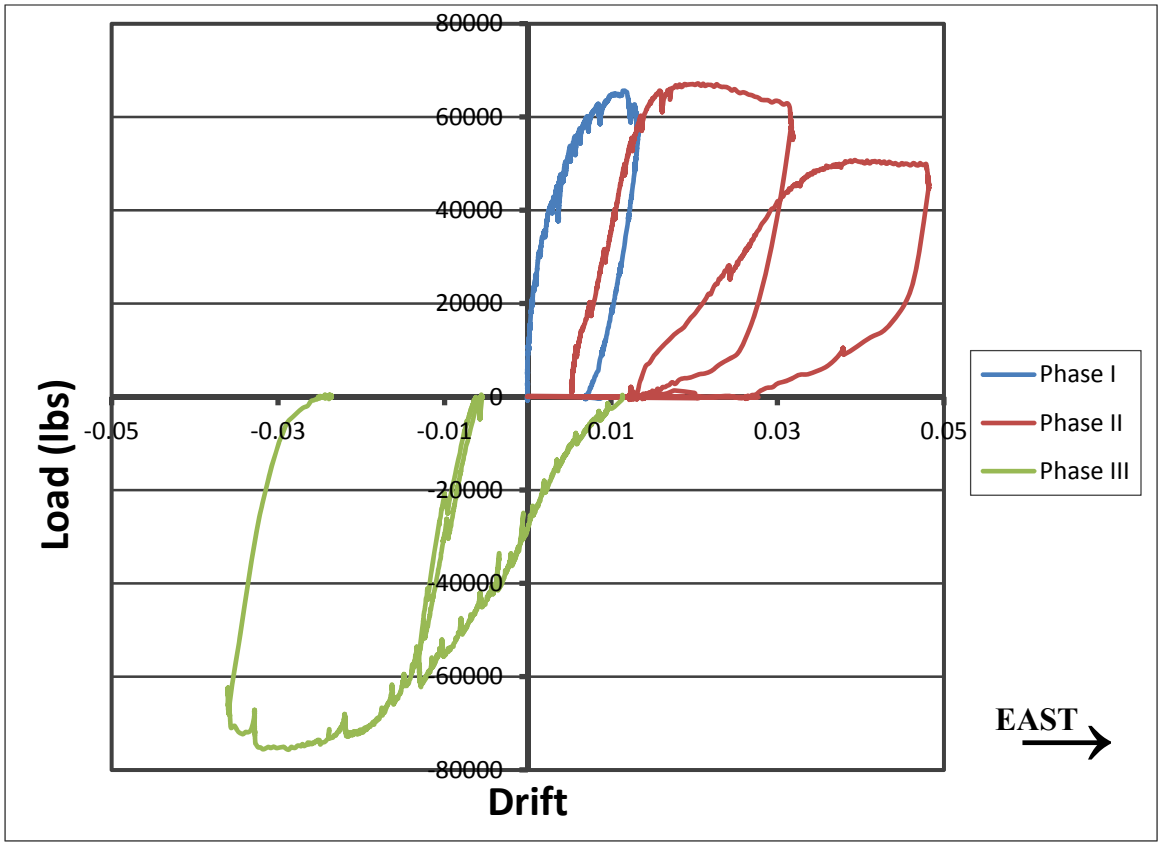

Figure 7.7: Lateral Drift (Looking North) vs. Applied Lateral Load

7.3 Foundation Behavior

It is necessary to establish that the foundation does not allow for any large amount of rotation, uplift, or slip. The rotation of the foundation can be seen in Section 7.4.2.4. Figure 7.8 shows the displacement in the *y* direction of the foundation (uplift) versus the drift measured during testing. This information was calculated using the average movement of the foundation across the two local FOV at the base of each pier, defined in

Figure 3.14 as System 3 and 4. The maximum uplift measured during testing was less than 5 mm. Based on this graph, it can be concluded that uplift in the foundation will not greatly alter the results collected during testing; therefore it will be neglected in further calculations.

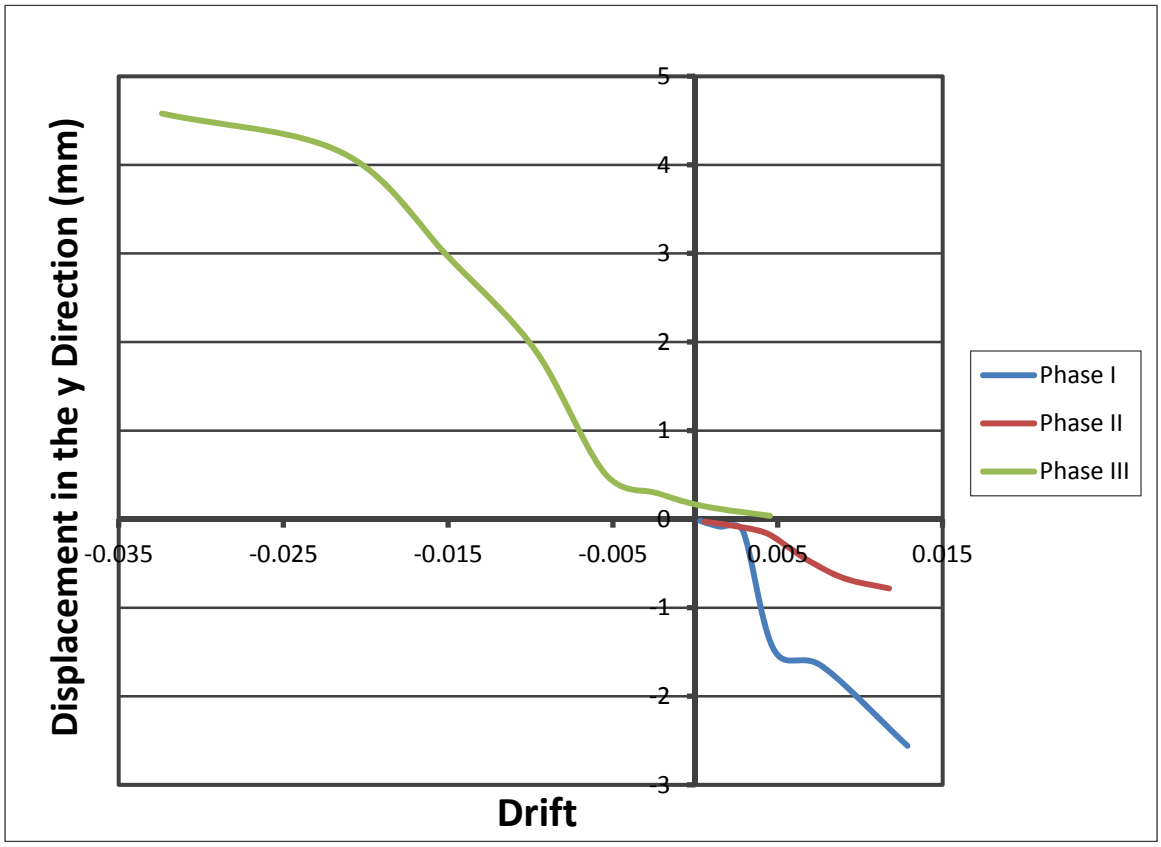

Figure 7.8: Foundation Movement in the *y* Direction vs. Drift

Figure 7.9 shows the displacement in the *x* direction of the foundation verses the drift measured during testing (slip). This information was calculated using the average movement of the foundation from the same FOV as above. The maximum slip measured during testing was less than 7 mm. Based on this graph, it can be concluded that slip of the foundation will not greatly alter the results collected during testing; therefore it will also be neglected in further calculations.

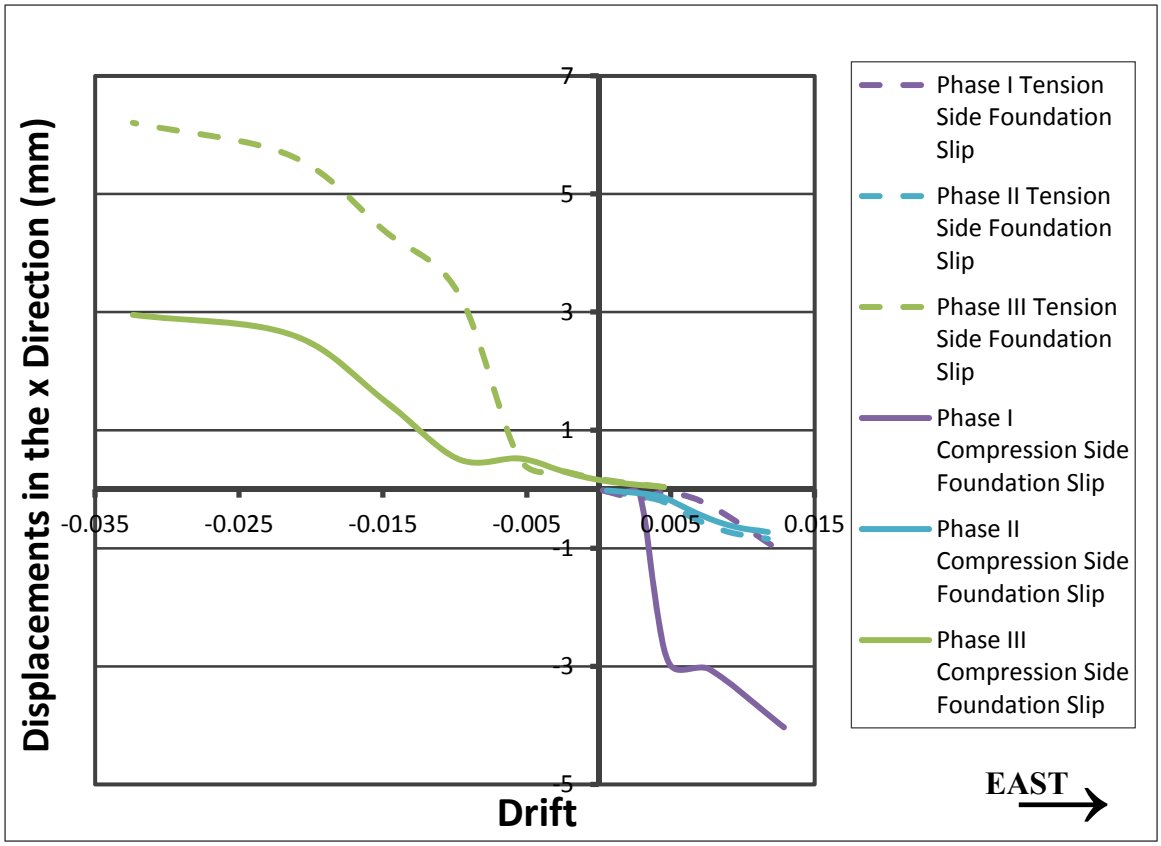

Figure 7.9: Foundation Movement in the *x* Direction (Looking North) vs. Drift

7.4 Pier Behavior

The behavior of the piers is a vital component in establishing the overall behavior and validity of the coupled wall system. This behavior will be established through the analysis of the center line deflections of the piers; cracking in the concrete and out of plane displacements will be presented in strain maps for visual aid and clarity.

7.4.1 Full Pier Behavior

The global behavior of the specimen is defined through analysis of the entire pier. In order to analyze information from both of the entire piers, the global FOV, defined in Figure 3.21, is utilized.

7.4.1.1 Deflected Shape

The center line deflections from the Aramis DIC system are shown in Figures

7.10, 7.11 and 7.12 for Phase I, II and III, respectively. These graphs show the deflections from the test at increments of 10k and the maximum load for each phase. The maximum deflections at each load are almost equal, while the deflections for the compression pier are greater through the rest of the height of the piers. This is due to the beams between the piers. As the load increases, the beams are pushed into an angle with the piers and a gap opens at each end of the beams; because of this, the distance between the piers is greater as the deformations of the piers increases. The beam gap opening is presented later in Section 7.5.1. Phase III was conducted in the opposite direction as Phase I and II (see Figure 6.1); therefore the DIC System 1, with FOV Global, recorded the displacements in the negative *x* direction. Because of this reversal, the pier that was the tension pier in Phase I and II is now called new compression and the previously named compression pier is called new tension.

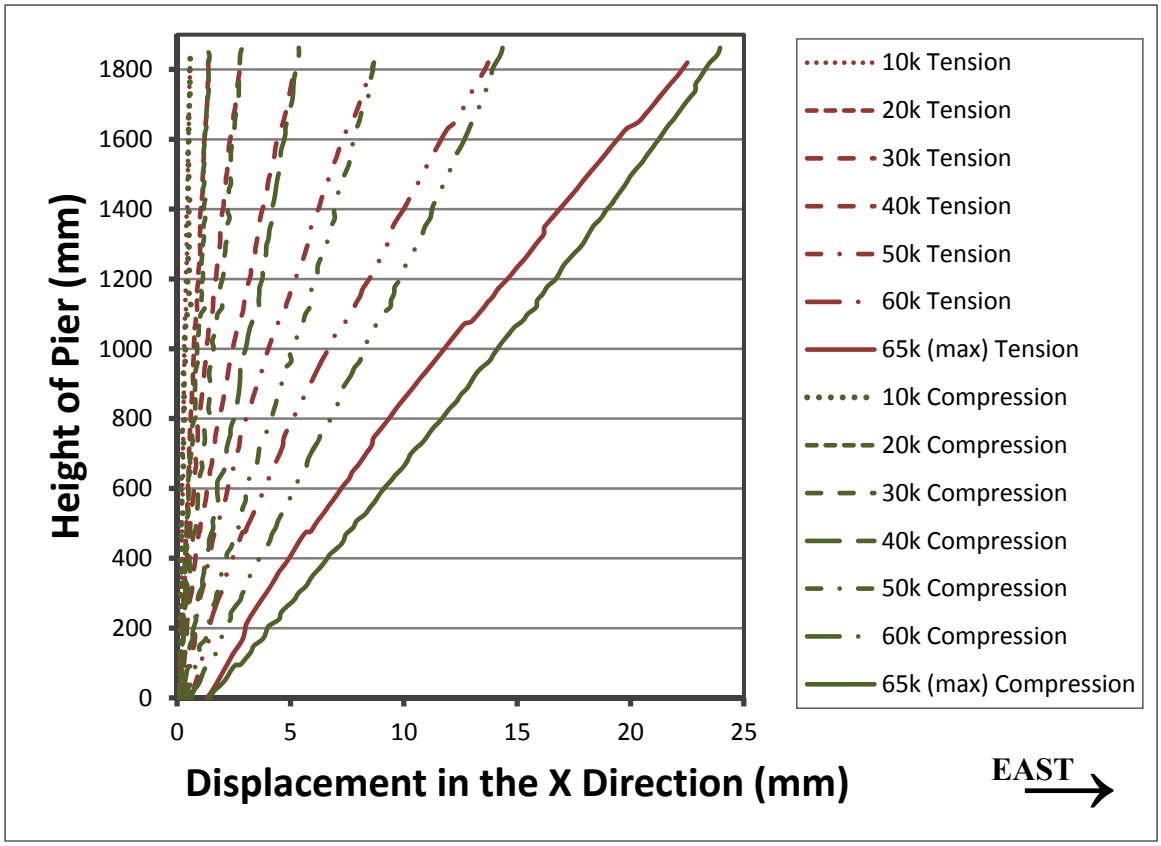

Figure 7.10: Phase I Tension and Compression Pier (Looking North) Deflections

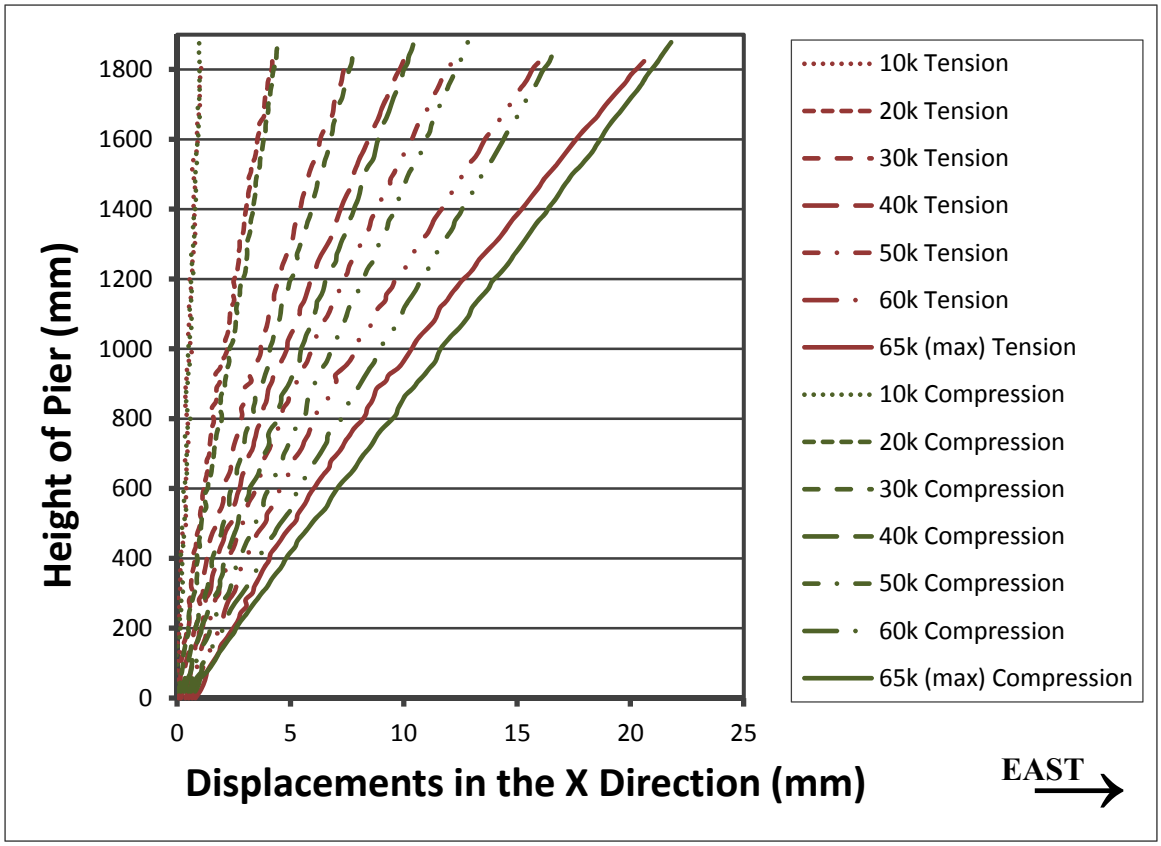

Figure 7.11: Phase II Tension and Compression Pier (Looking North) Deflections

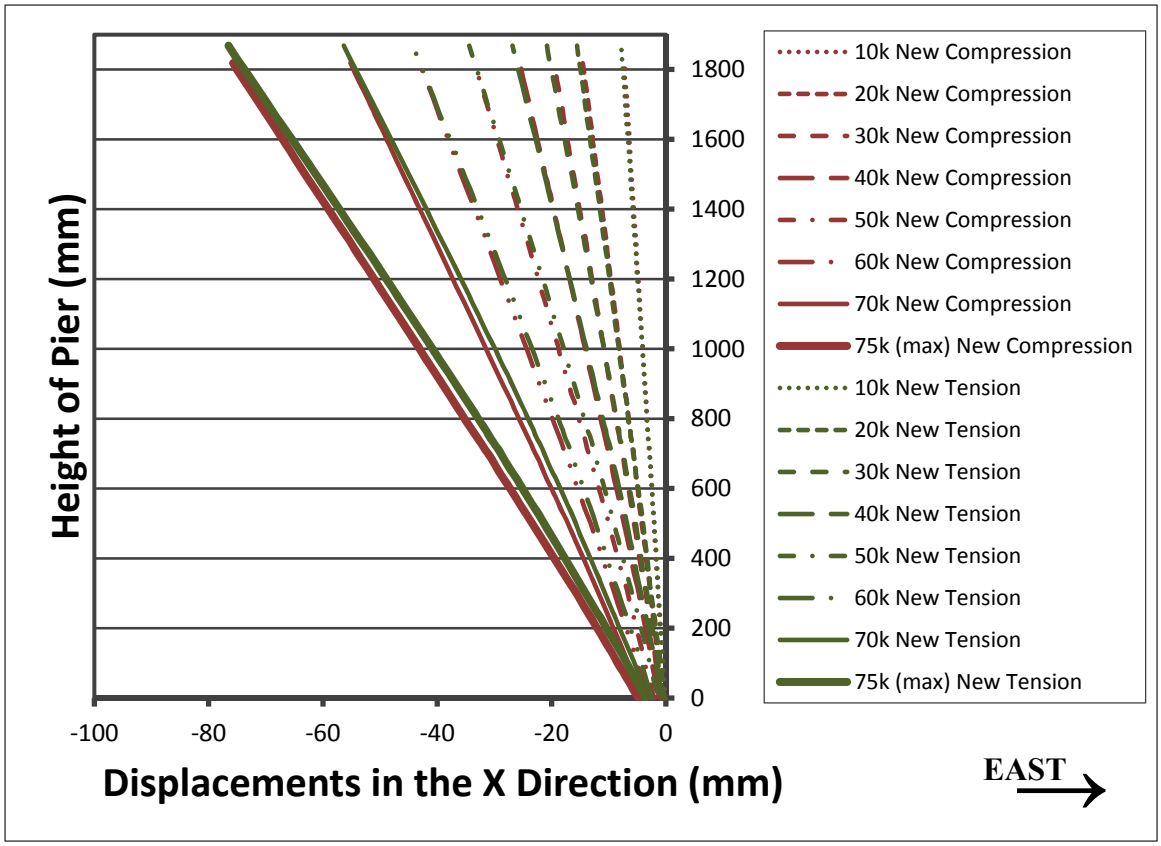

Figure 7.12: Phase III (Reversal) Tension and Compression Pier (Looking North) Deflections

A direct comparison of the deflected center line shape from the DIC system and ABAQUS models based on applied loads is given in Figure 7.13. A full description of these ABAQUS models is given in Chapter 8. Because of the poor performance of the pier-foundation joint, greater deflections were experienced during the test at lower applied loads that in the models.

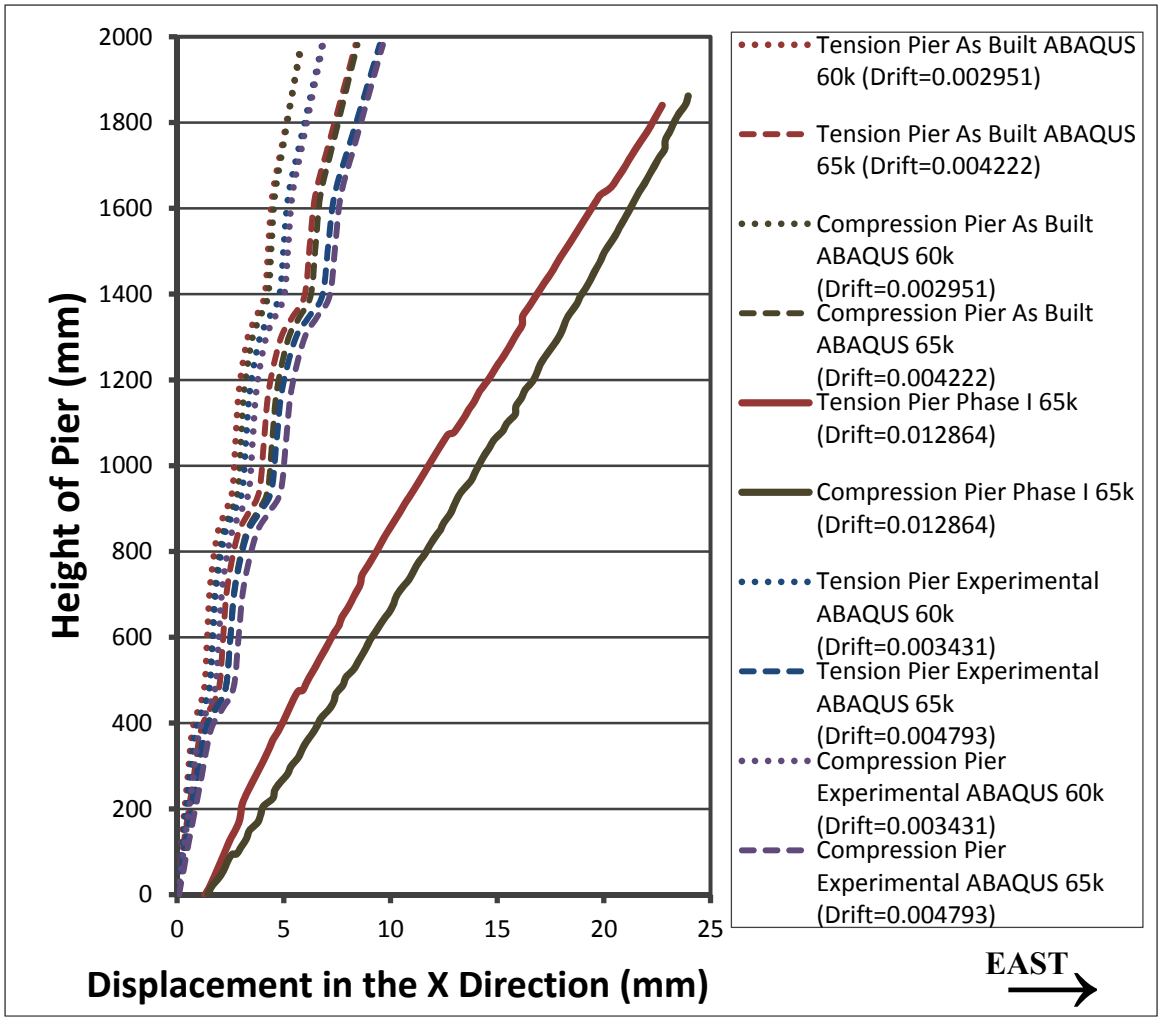

Figure 7.13: Deflected Shape, Applied Load Based Comparison (Looking North)

In order to compare the behavior more appropriately, the deflections are compared at different levels of drift, instead of applied loads. This drift based comparison is given in Figure 7.14. The behavior of the piers during testing is similar to those produced by the ABAQUS models when compared by levels of drift.

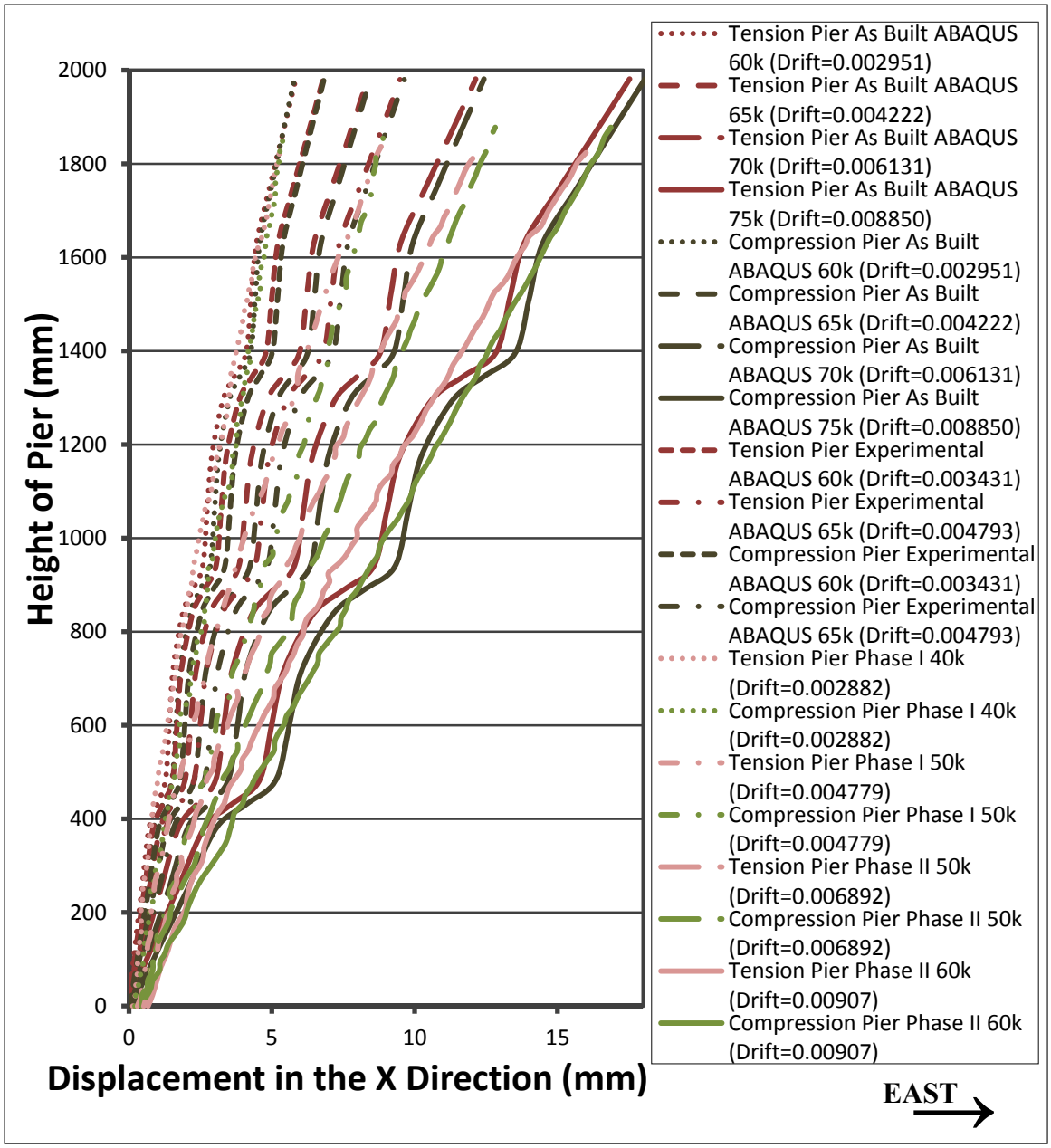

Figure 7.14: Deflected Shape, Drift Based Comparison (Looking North)

7.4.1.2 Global Strain Maps (ε_y)

Figures 7.15, 7.16, and 7.17 show images of the strain maps that are generated in the DIC software for phases I, II, and III, respectively. The red areas show high tension area where cracks will begin to open. The dark blue areas show the compression zones; at the higher applied loads, the compression toes begin to develop.

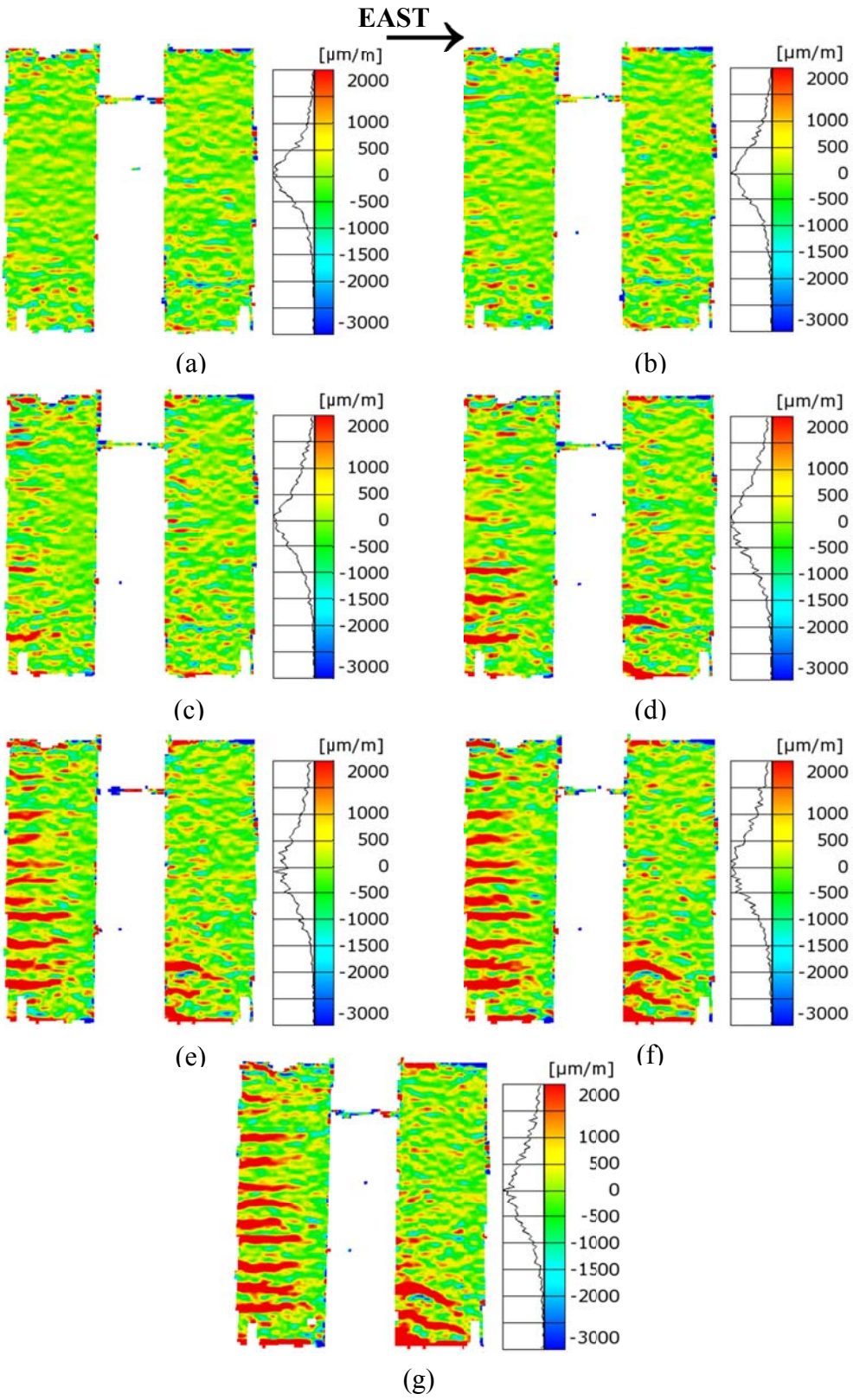

Figure 7.15: Phase I Strain Maps (Looking North): (a) 10k; (b) 20k; (c) 30k; (d) 40k; (e) 50k; (f) 60k; (g) 65k (max load)

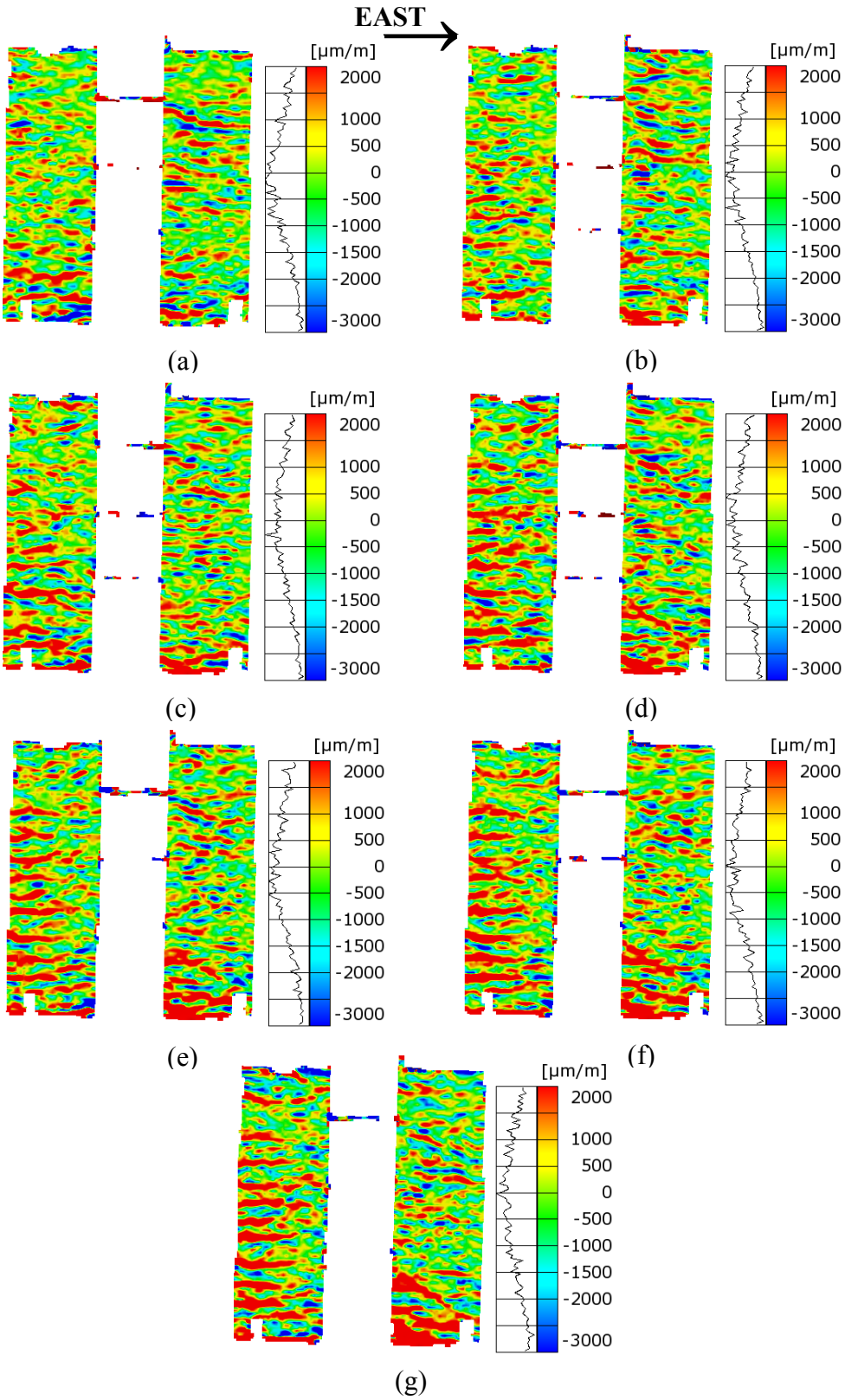

Figure 7.16: Phase II Strain Maps (Looking North): (a) 10k; (b) 20k; (c) 30k; (d) 40k; (e) 50k; (f) 60k; (g) 65k (max load)

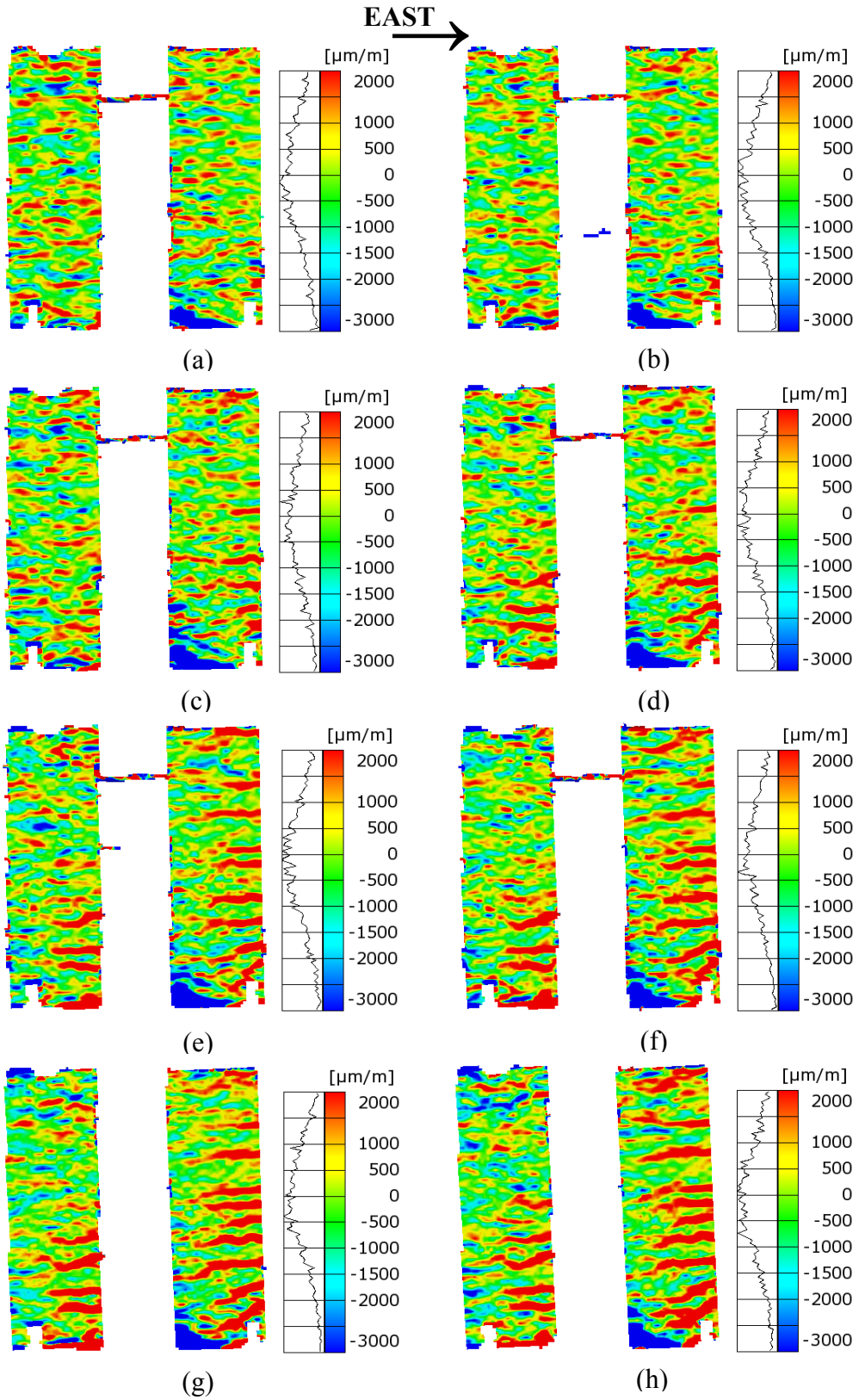

Figure 7.17: Phase III Strain Maps (Looking North): (a) 10k; (b) 20k; (c) 30k; (d) 40k; (e) 50k; (f) 60k; (g) 70k; (h) 75k (max load)

Figure 7.18 shows the comparison between the phase I 65k (max load) lateral applied load strain map and the strain map produced for 65k in ABAQUS (model discussed in Chapter 8). The comparison does not reflect an accurate representation of the actual stresses in that no cracking is shown, this is a result of the assumptions made relating to the elastic-perfectly plastic material property used for the ABAQUS model; see Section 8.1 for a detailed model description. If the ABAQUS model experienced a tension force greater than the 6000 psi strength it would show yielding in that material. Figure 7.19 shows maximum tension stress experienced in the ABAQUS model versus the drift (%) the system experienced. Even at large drifts, the system sees less than a maximum of 2500 psi; therefore the ABAQUS model should not show cracks based on our material property assumptions. Otherwise, the model is an appropriate representation.

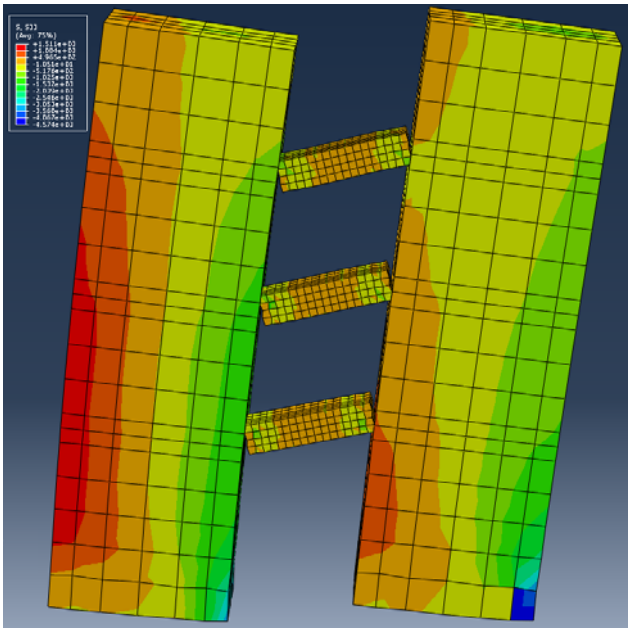

(a)

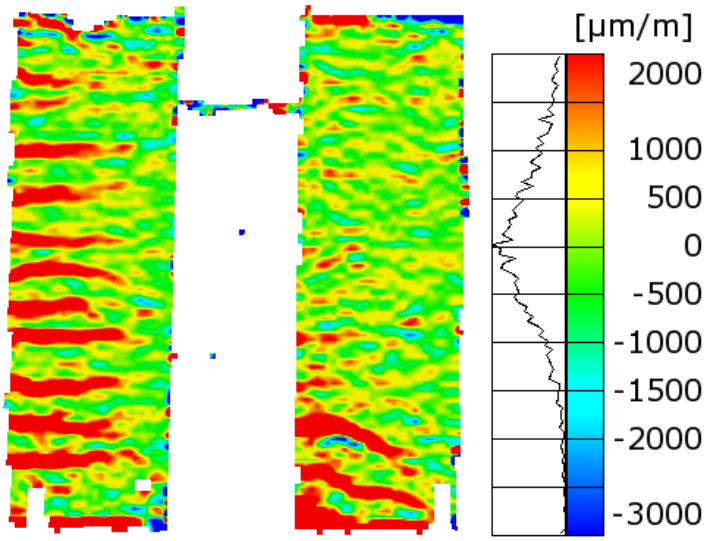

(b)

Figure 7.18: Strain Map Comparison: (a) ABAQUS; (b) DIC

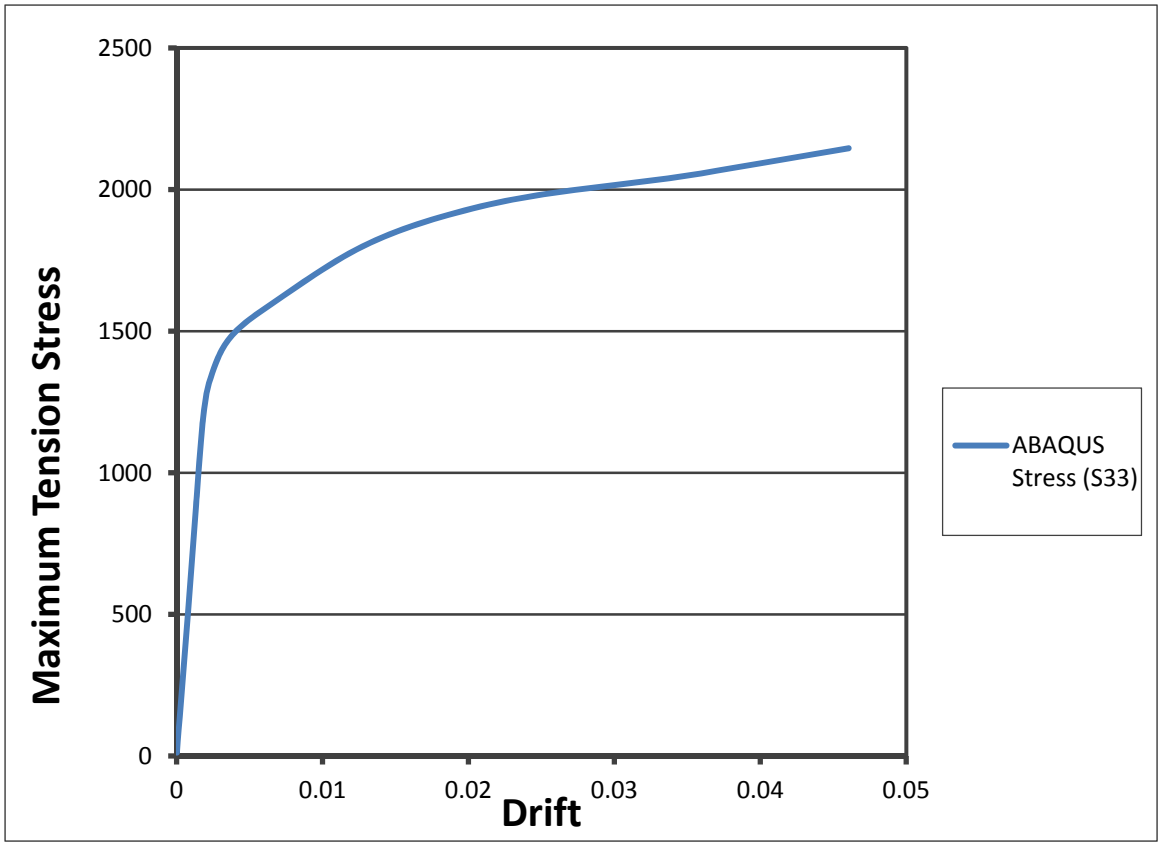

Figure 7.19: ABAQUS Maximum Tension Stress vs. Drift

7.4.1.3 Out of Plane Pier Movement (Δ_z)

The DIC system used for the global FOV is a 3D-DIC; therefore the out of plane displacements are captured during the test. Torque and twisting were not a part of the design or planned in the testing of the specimen. To verify that these did not occur during testing, the out of plane pier movements at the maximum applied load for each phase is reported in Figure 7.20. The maximum out of plane movement is approximately 5 mm. This is acceptable for the purposes of this test.

Also, because the systems used to monitor the base pier behavior, Systems 2 and 3, are 2D-DIC, large errors can occur if the specimen has large out of plane movement in the FOV – see Section 2.2.4. The out of plane displacements near the base are extremely low, therefore, the 2D-DIC systems will not experience magnification issues.

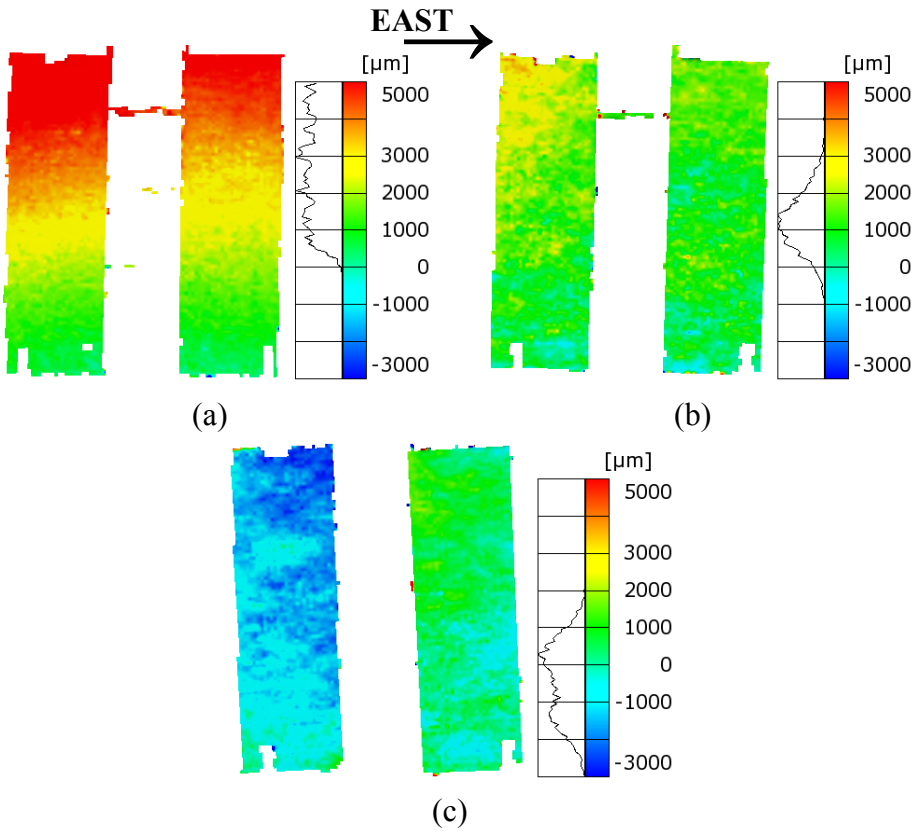

Figure 7.20: Δ_z Displacement Maps (Looking North): (a) Phase I; (b) Phase II; (c) Phase III

7.4.1.4 Global Strain Maps (ε_x)

The ε_x strain maps provided in Figure 7.21 are for the maximum load in each phase. Although the beam toes should introduce compression in the piers in this direction at the beam heights, this behavior is not shown. In Figure 7.22(a), the ABAQUS model results for a load of 70k are shown. The model does not appear to depict the appropriate stresses. However, the model does show the induced compression in Figure 7.22(b). The pier face is simply too far away from the beam toes to have captured this beam data.

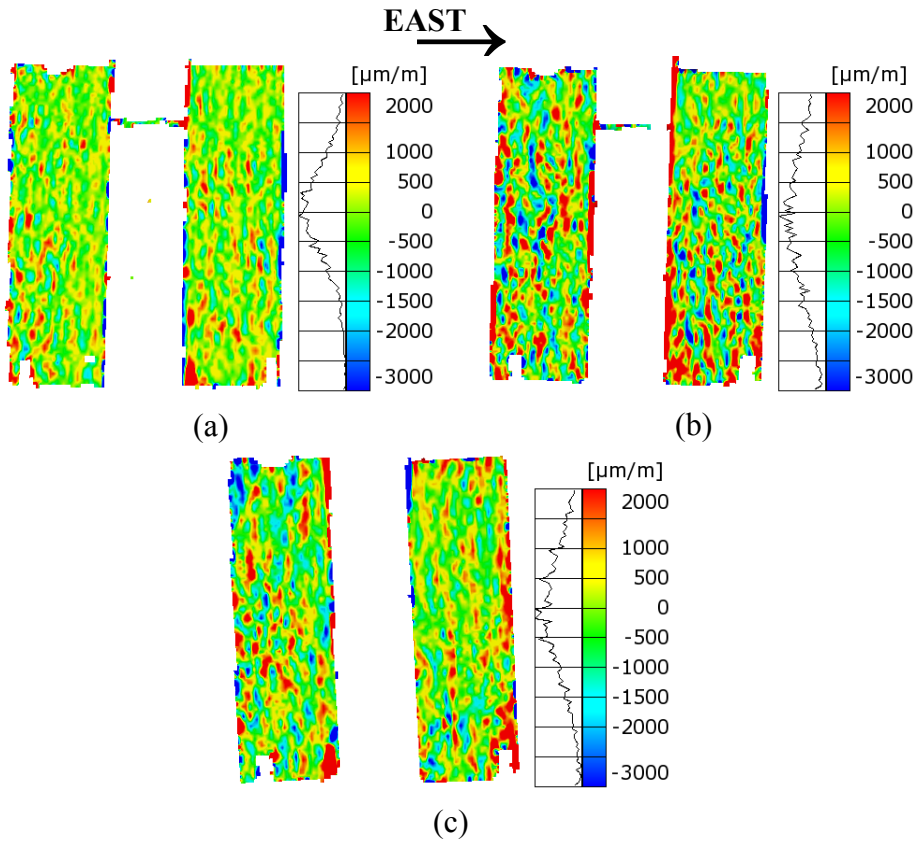

Figure 7.21: ε_x Strain Maps (Looking North): (a) Phase I; (b) Phase II; (c) Phase III

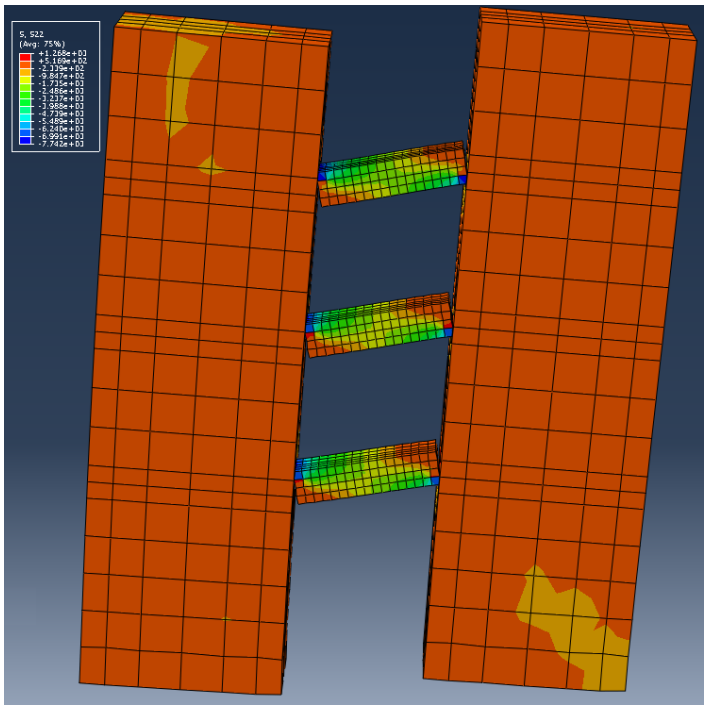

(a)

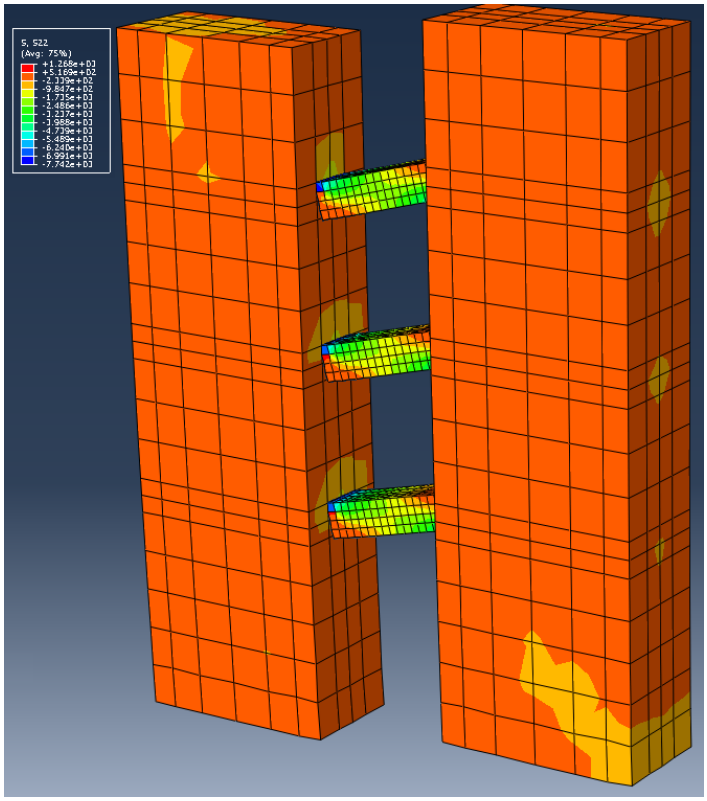

(b)

Figure 7.22: ABAQUS Strain Maps: (a) Front Face; (b) Beam End View

7.4.2 Base Pier Behavior

The base pier behavior defines the local behavior of the specimen through analysis of the base of the pier and its interaction with the foundation. In order to analyze information from both bases of the piers, the compression base and tension base FOV, defined in Figure 3.21, are utilized.

7.4.2.1 Neutral Axis Depth

The neutral axis depth is the length of the pier base that is still in contact with the foundation, also referred to as the compression toe. To calculate the neutral axis depth from the measured data, a line was taken at the base of the pier (displacement in the *y* direction) and the equation of that line was found, and the value for the *x*-intercept was calculated by assuming *y* equals zero. The *x*-intercept in this case, because of the orientation of the line, is the value of the neutral axis depth. To calculate the neutral axis depth from the ABAQUS model, the displacements along the front of the bottom face were examined and a straight line was fitted to the data. The *x*-intercept is the value of the neutral axis again. This method provided a more precise neutral axis than only reviewing the node locations where contact occurred since this method allowed interpolation between nodes. Figure 7.23 shows the neutral axis depth for both measured data from testing and the ABAQUS models. The data was only compared for drift up to 0.015 in order to adequately establish basic behavior.

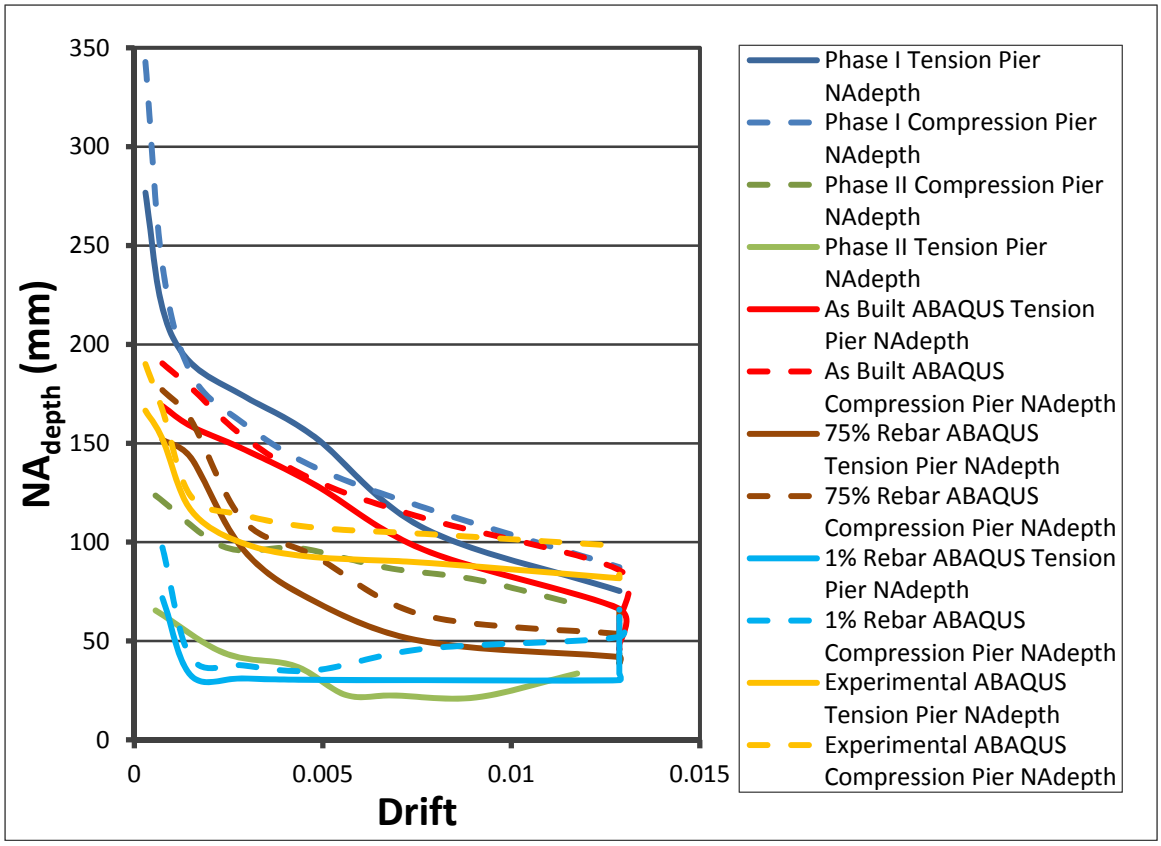

Figure 7.23: Neutral Depth vs. Drift Comparison

It is expected that the neutral axis depth should reduce as the drift of the system increases, and this is shown in Figure 7.23. It is also expected that the tension pier will have a smaller neutral axis value for the duration of testing. Although this trend is noted in the ABAQUS models, the experimental data is more variable. This may be explained by rebar pull-out at the foundation if the rebar pull-out occurred unequally or at different loads in the two wall piers. The problem of bar pull-out is discussed in Section 7.4.2.4.

7.4.2.2 Gap Opening

The gap opening at the base is the space that opens up between the base of the pier and the foundation beneath. To calculate the gap opening, a point on the corner of the pier where the gap is opening and its corresponding original contact position on the foundation (displacement in the *y* direction) were subtracted. That value reflects the

greatest gap opening for that load. Figure 7.24 shows the gap opening for both measured data collected during testing and the ABAQUS models. There is good agreement between the ABAQUS models and the measured experimental data.

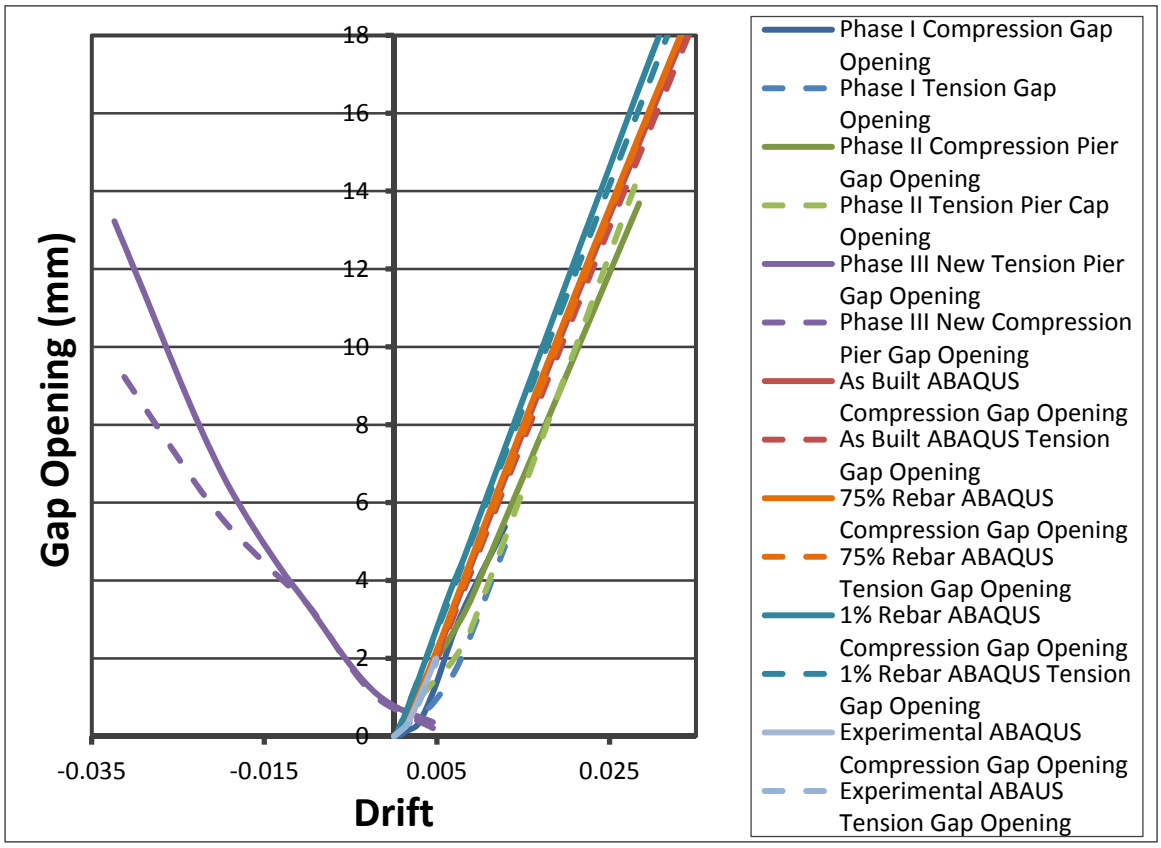

Figure 7.24: Gap Opening between Pier Base and Foundation vs. Drift Comparison

7.4.2.3 Pier Slip

Slip is the movement in the *x* direction at the base of the pier in relation to the foundation. In a perfect fixed connection, the slip is equal to zero. Because of the poor performance of the pier-foundation interface, the possibility of large slip was a concern. Figure 7.25 shows the slip of the pier bases verses drift. The maximum slip experienced during testing is less than half a millimeter. Slip at the base will not be an issue and will therefore be neglected in all further computations.

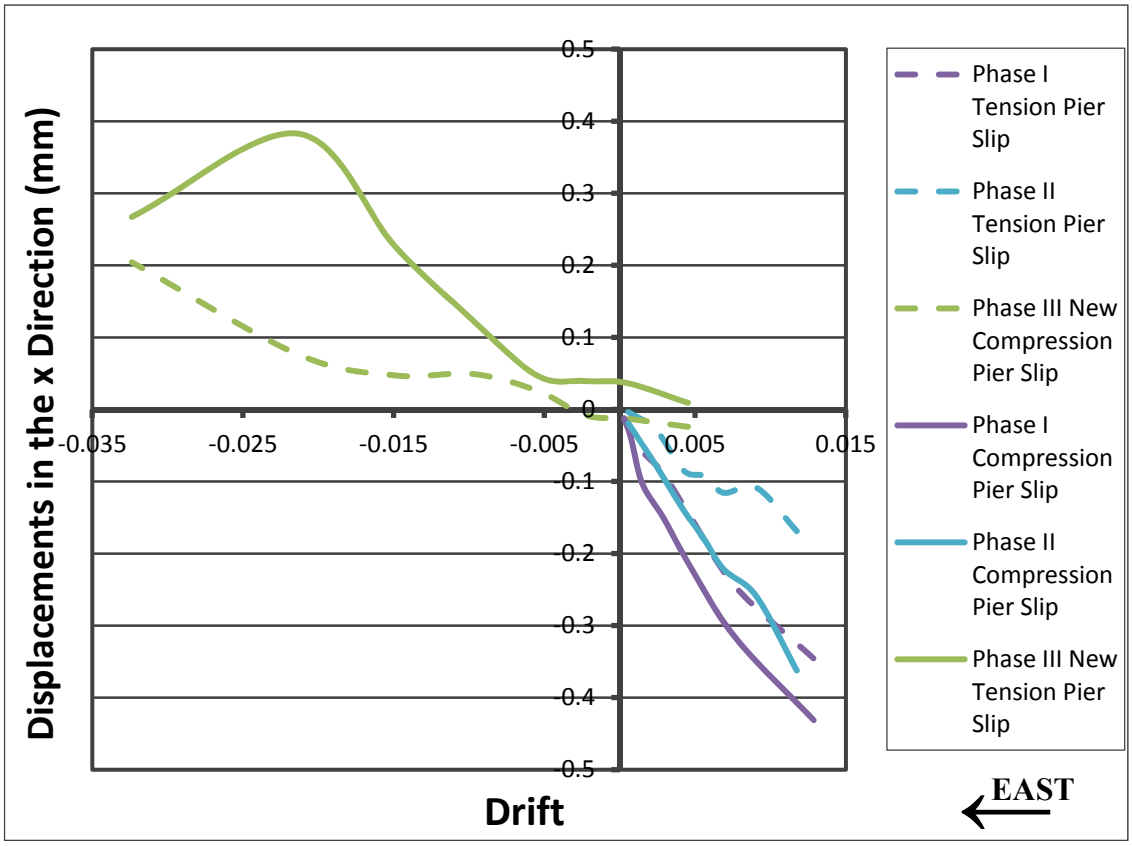

Figure 7.25: Pier Slip in the *x* Direction Pier Base and Foundation vs. Drift Comparison

7.4.2.4 Foundation and Pier Rotation

The rotation of the piers in relation to the foundation establishes an important parameter of base pier behavior. Figures 7.26 through 7.31 show the rotations of the tension and compression piers for phases I, II, and III. Figure 7.32 shows a comparison between measured rotations and rotations from the ABAQUS model based on drift, not applied lateral load (similar to Section 7.4.1.1). These figures show larger rotations of the piers than was expected for the amount of drift experienced. This is because of the rebar pull-out experienced during testing. The global behavior of the system shown in Section 7.2 reflects a much lower stiffness of the system that was expected. A parametric study was conducted to determine the source of this difference. After the conclusion of testing and completion of dismantling, the foundation was inspected to confirm or

disprove the assumption of rebar pull-out. The inspection confirmed that the rebar that should have been embedded in the foundation was pulled loose during testing. Furthermore, Figure 7.26 and 7.27 show that the compression pier rebar pulled out more severely than the tension pier, lending weight to the discussion regarding neutral aixs depth in Section 7.4.2.1. Details of the inspection results and the study conducted can be found in Section 8.2.

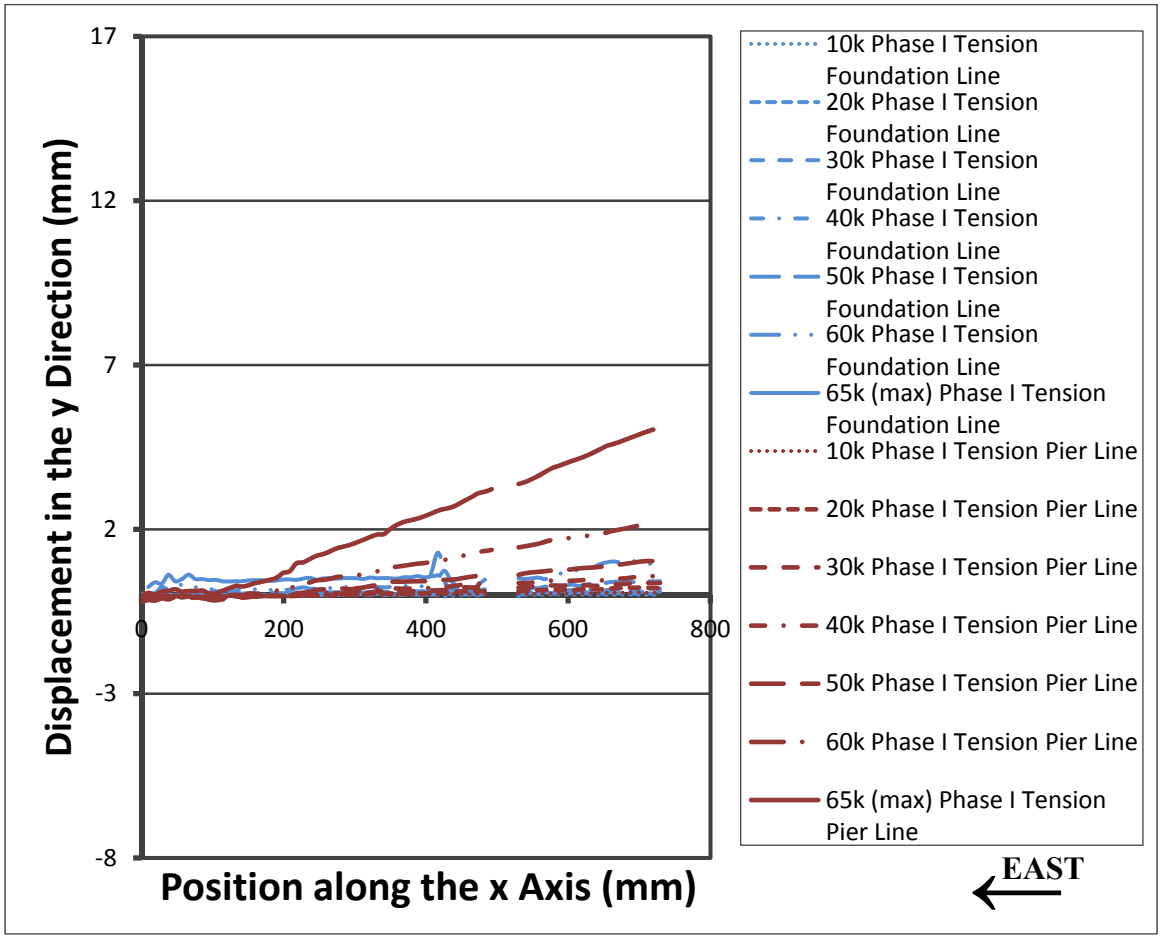

Figure 7.26: Phase I Tension (West) Pier Rotations (Looking South)

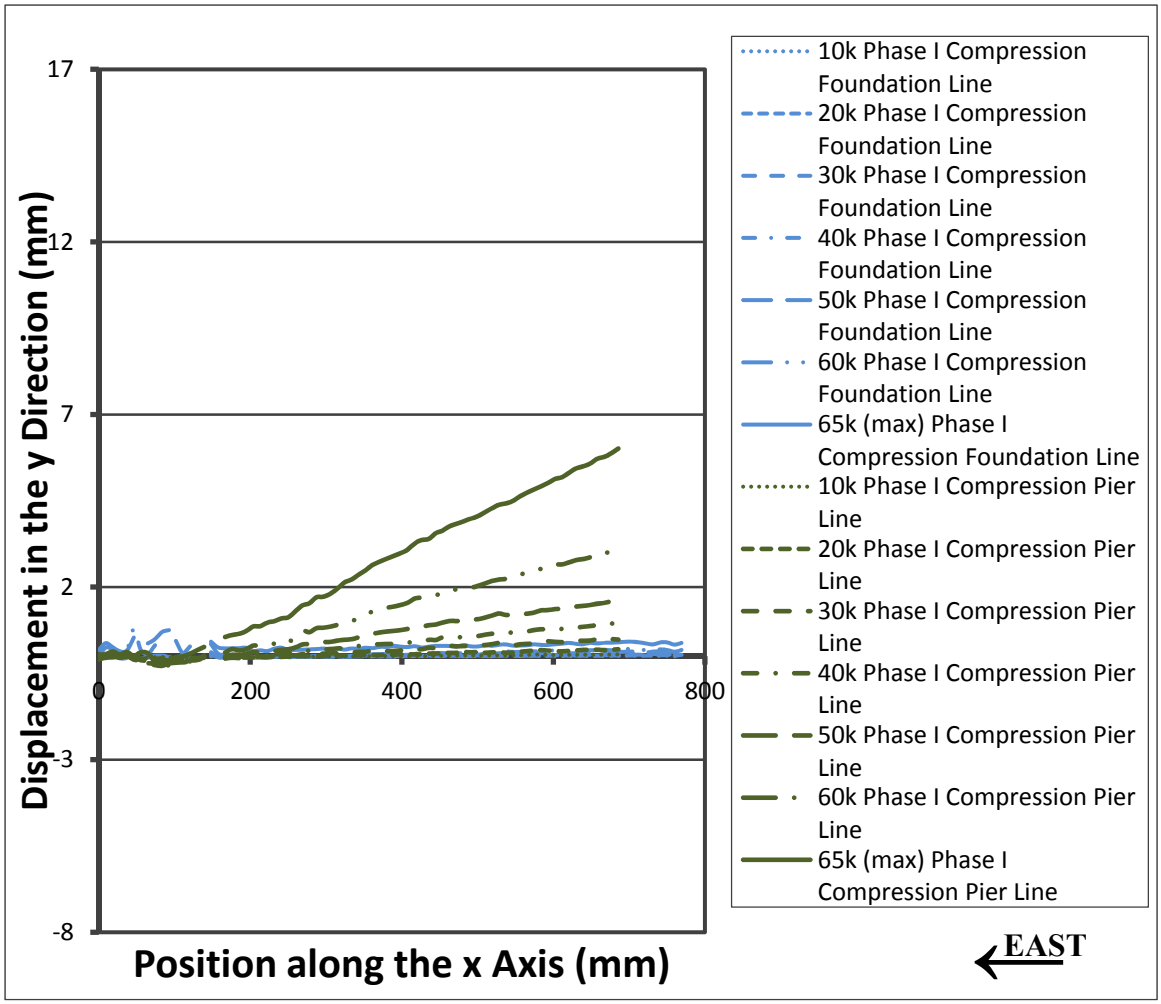

Figure 7.27: Phase I Compression (East) Pier Rotations (Looking South)

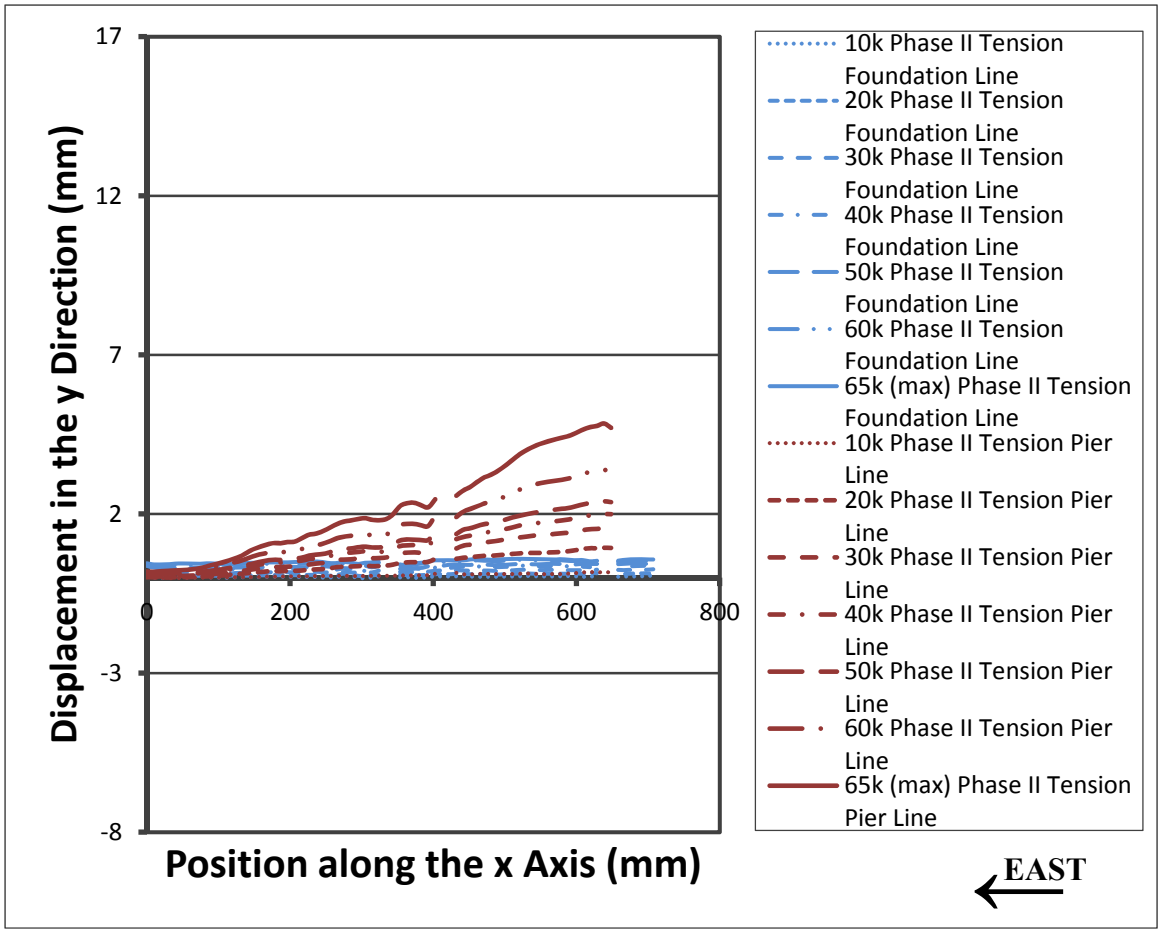

Figure 7.28: Phase II Tension (West) Pier Rotations (Looking South)

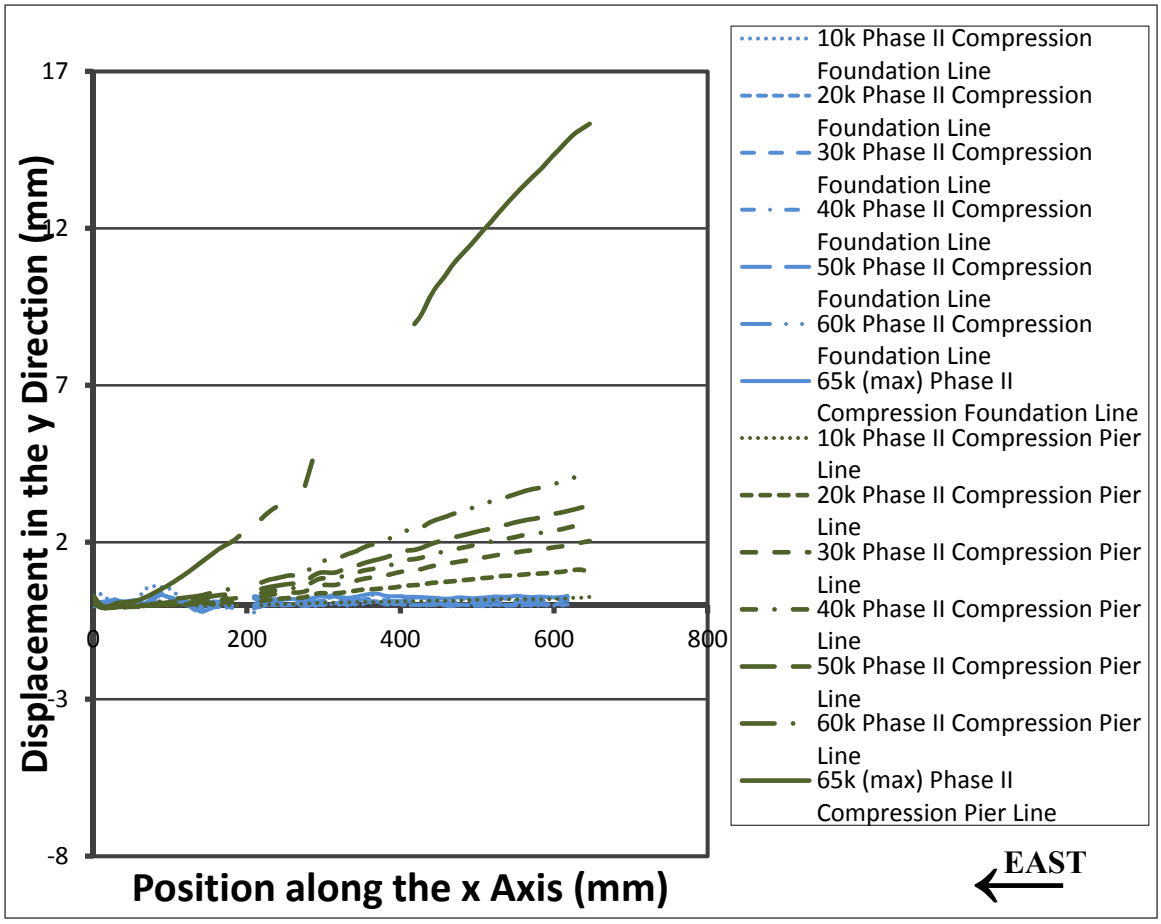

Figure 7.29: Phase II Compression (East) Pier Rotations (Looking South)

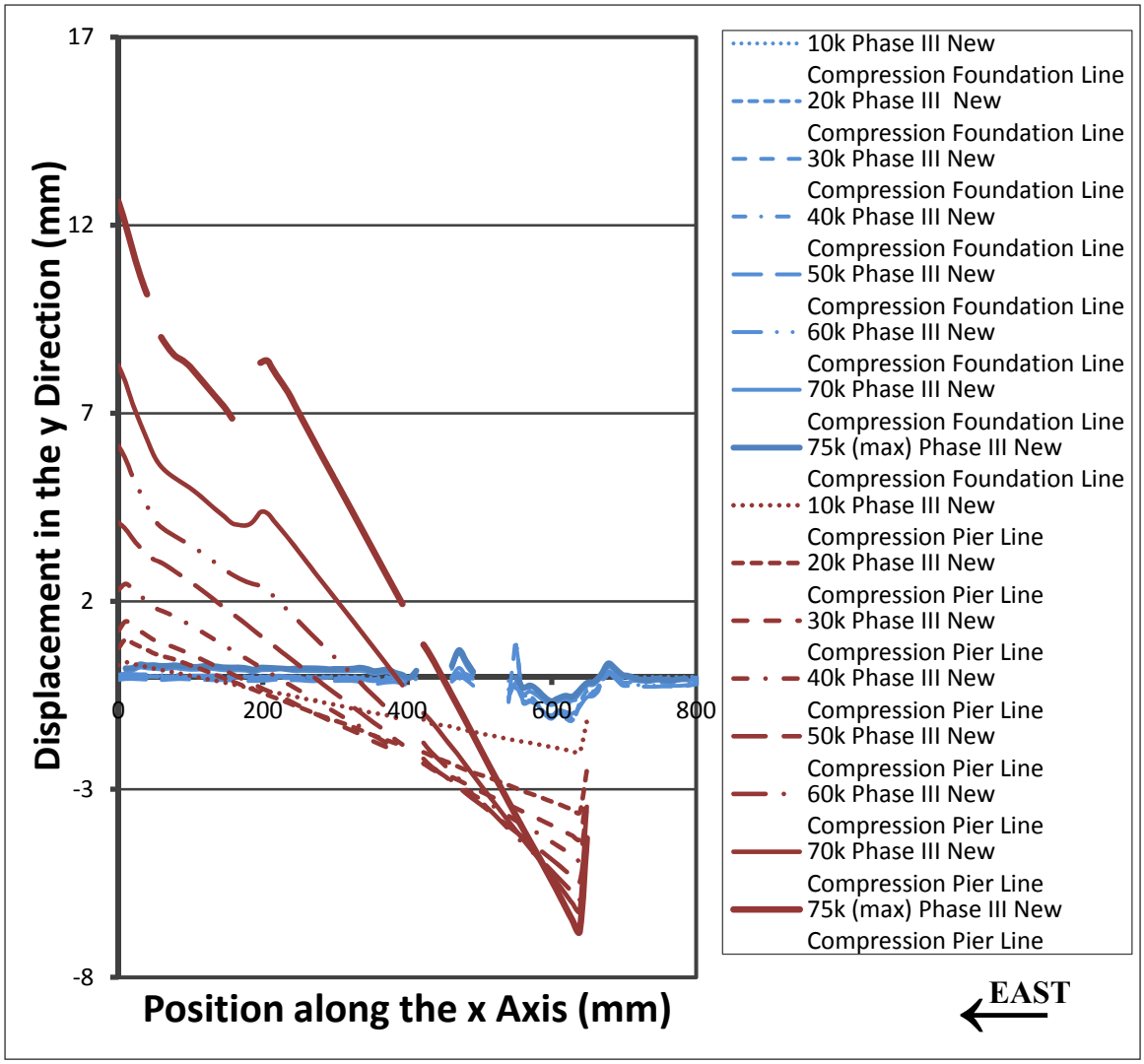

Figure 7.30: Phase III New Compression (West) Pier Rotations (Looking South)

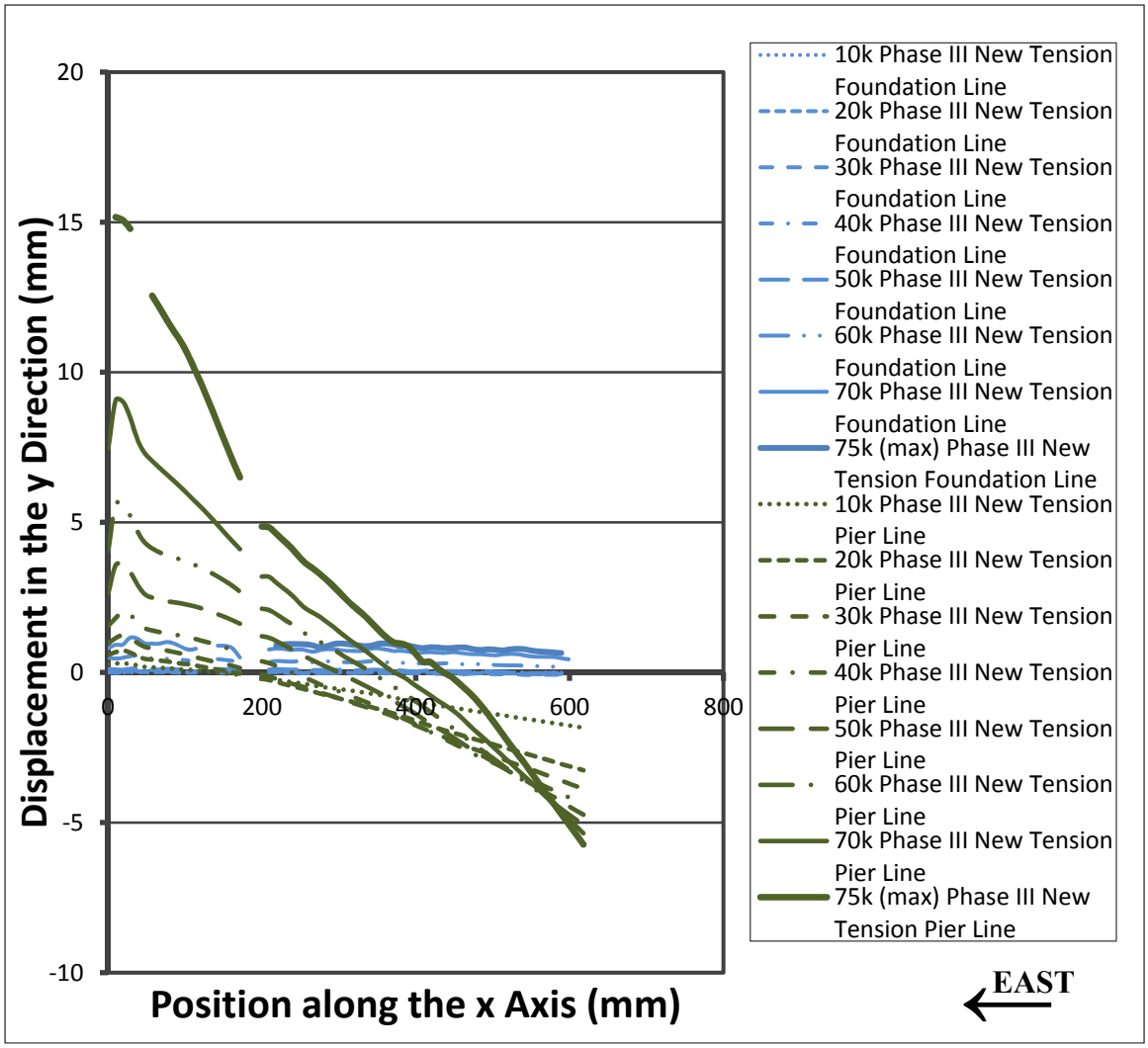

Figure 7.31: Phase III New Tension (East) Pier Rotations (Looking South)

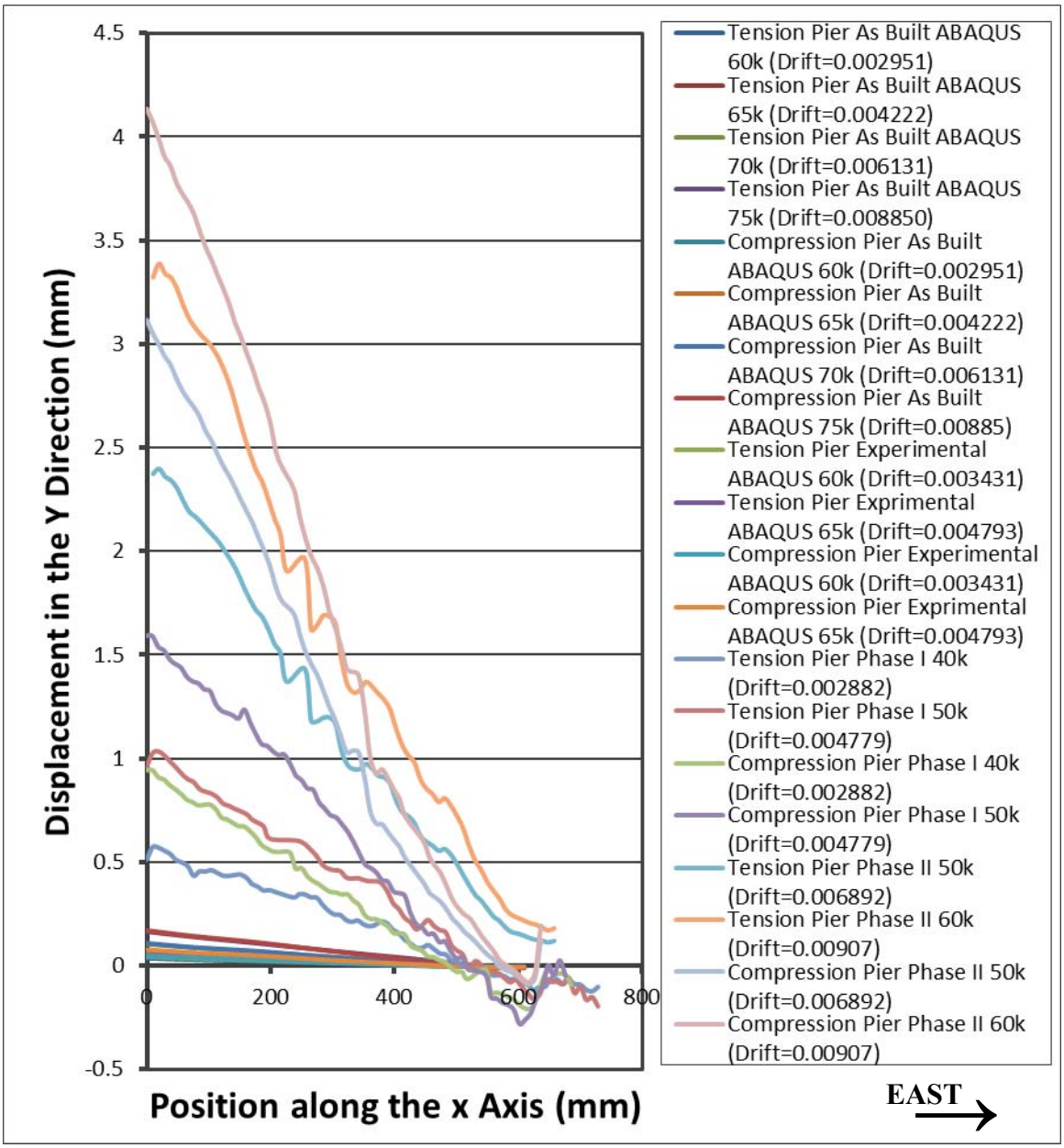

Figure 7.32: ABAQUS results and Measured Data Drift Based Comparison (Looking North)

7.4.2.5 Pier Base Strain Maps

Figures 7.33, 7.34, and 7.35 show images of the strain maps that are generated in the DIC software for the tension pier base. Figures 7.36, 7.37, and 7.38 show images of the strain maps that are generated for the compression pier base. The figures show phases I, II, and III, respectively. All figures are looking South; the direction of East is labeled in

each figure. The red areas show high tension area where cracks will begin to open. The dark blue areas show the compression zones; at the higher applied loads, the compression toes begin to develop.

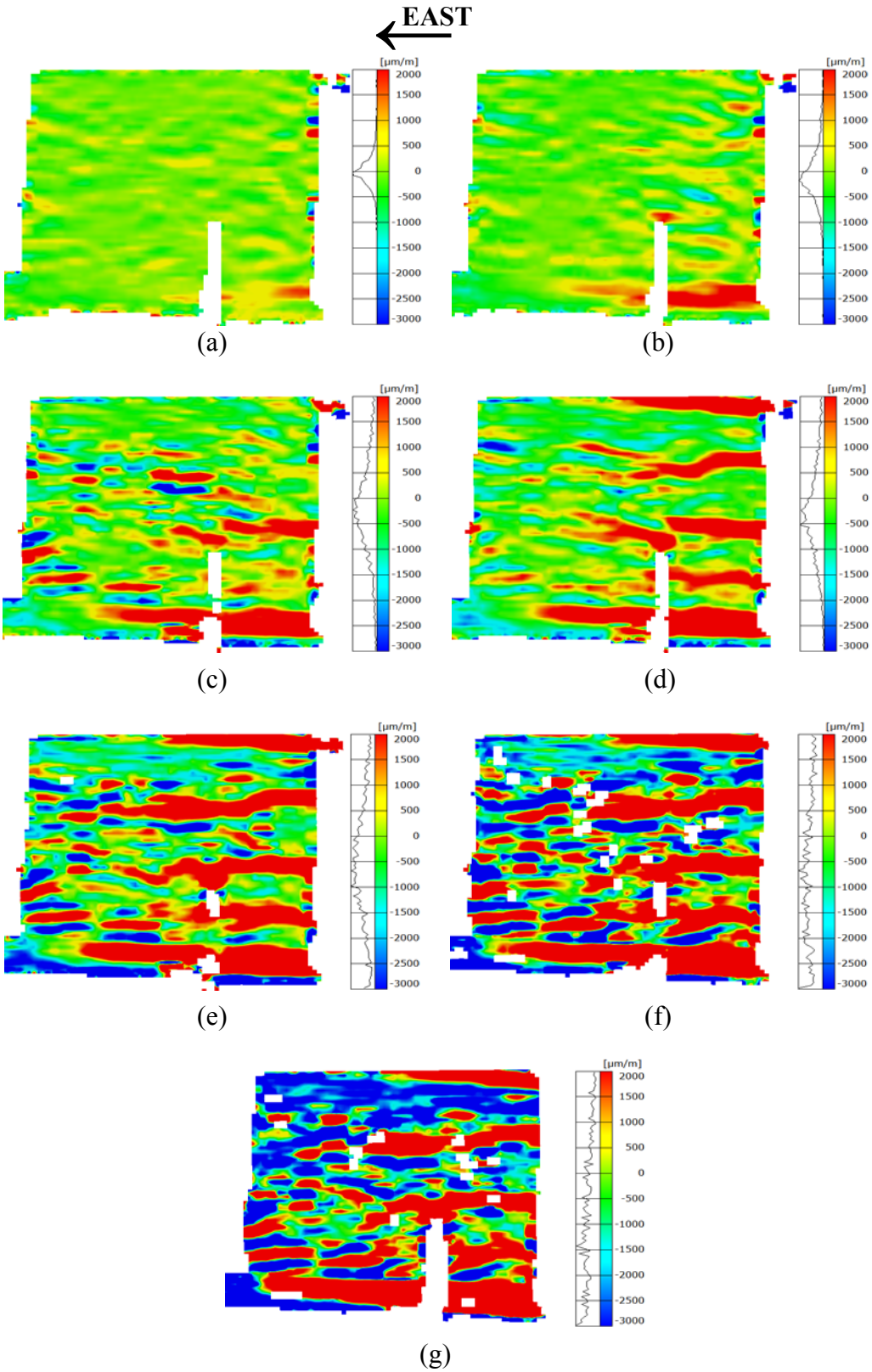

Figure 7.33: Phase I Tension (West) Pier Strain Maps (Looking South): (a) 10k; (b) 20k; (c) 30k; (d) 40k; (e) 50k; (f) 60k; (g) 65k (max load)

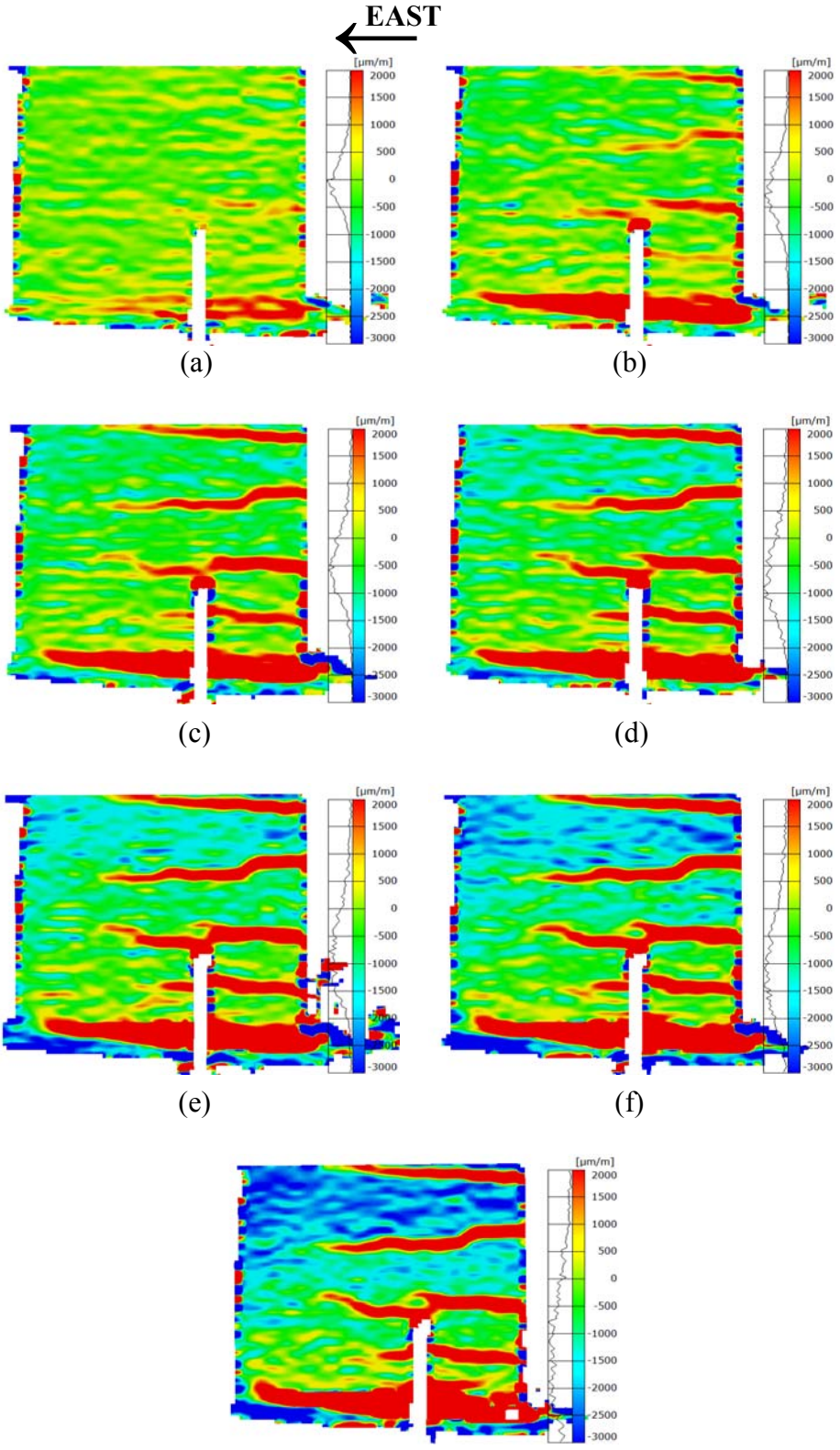

Figure 7.34: Phase II Tension (West) Pier Strain Maps (Looking South): (a) 10k; (b) 20k; (c) 30k; (d) 40k; (e) 50k; (f) 60k; (g) 65k (max load)

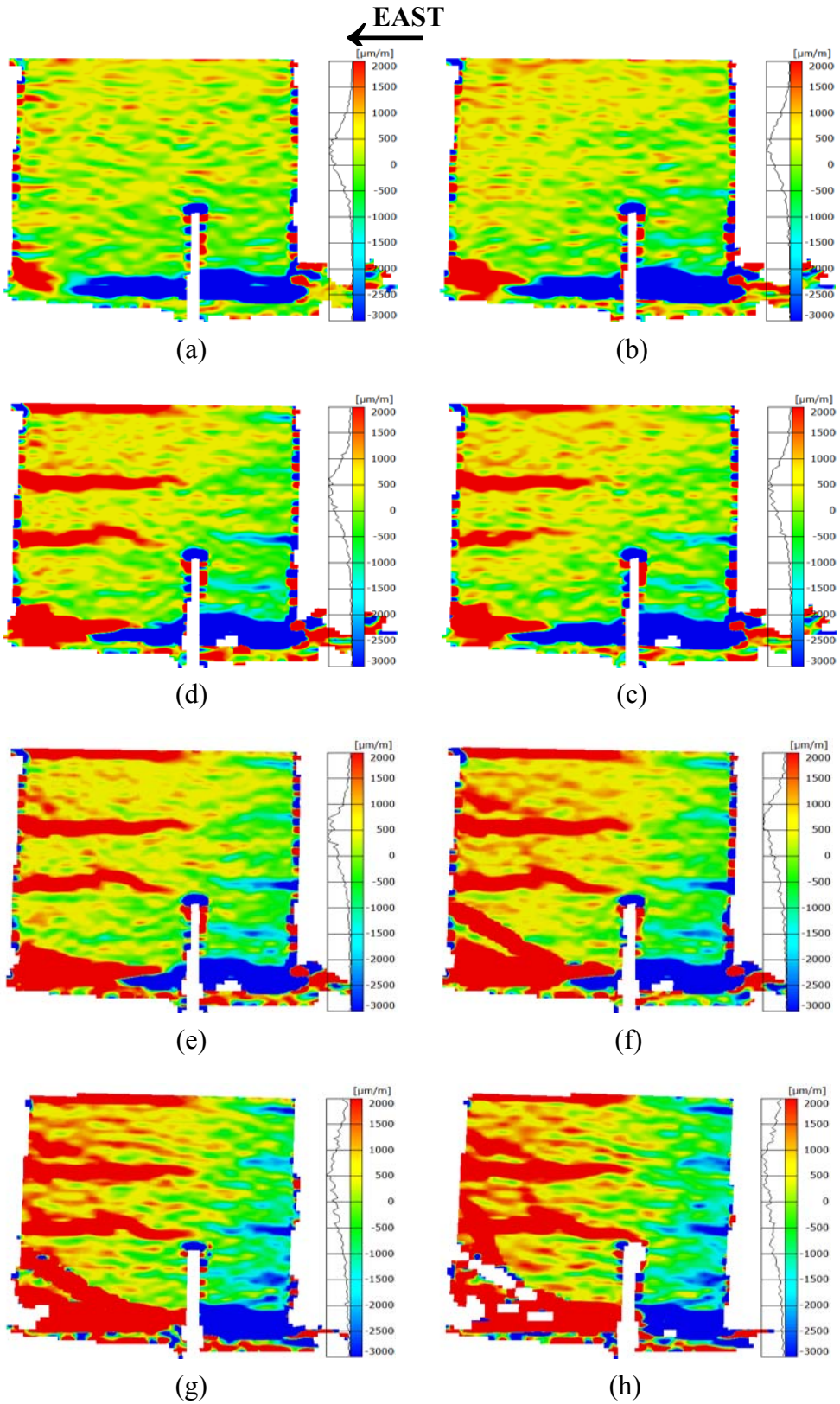

Figure 7.35: Phase III New Compression (West) Pier Strain Maps (Looking South): (a) 10k; (b) 20k; (c) 30k; (d) 40k; (e) 50k; (f) 60k; (g) 70k; (h) 75k (max load)

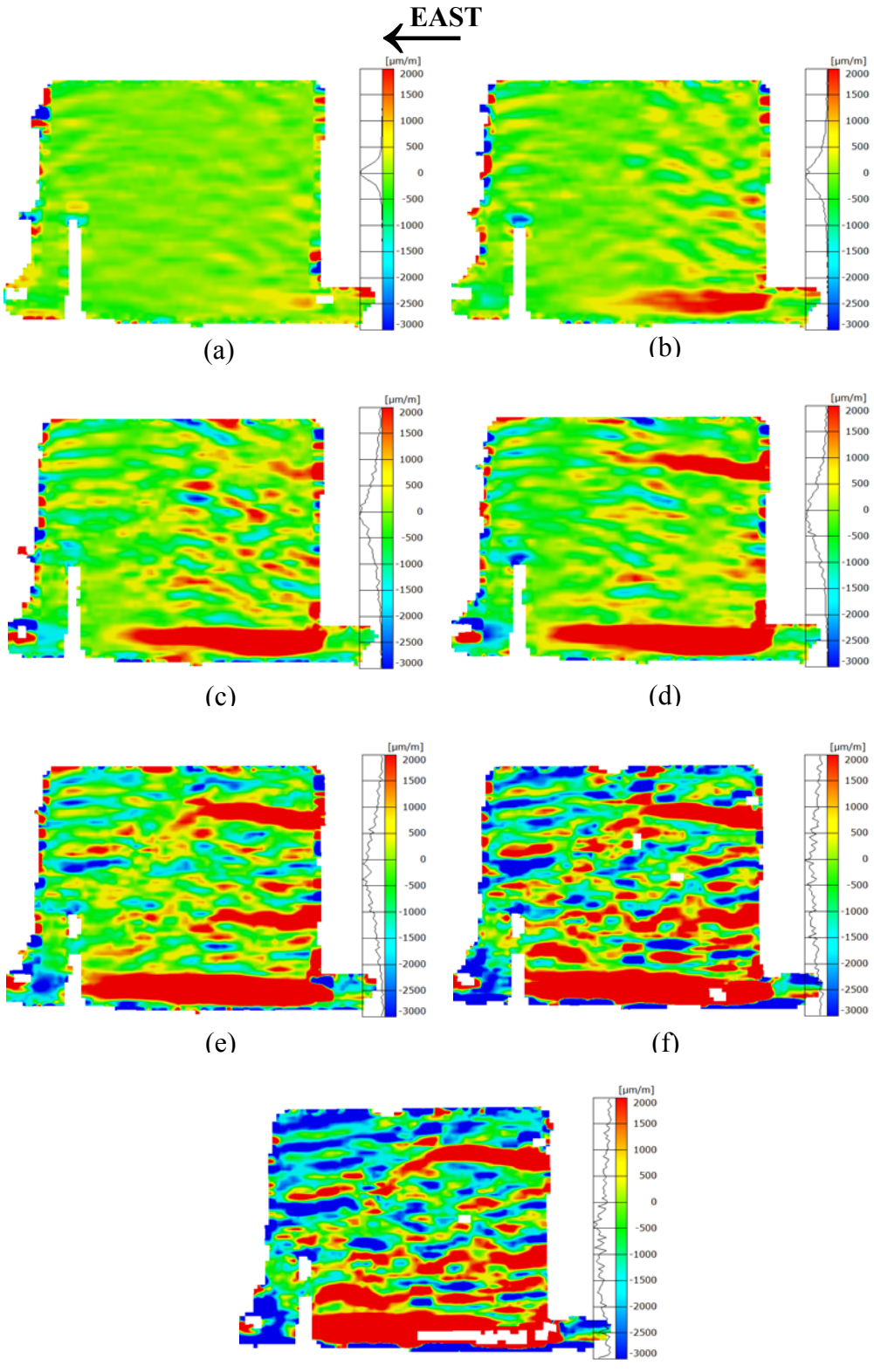

Figure 7.36: Phase I Compression (East) Pier Strain Maps (Looking South): (a) 10k; (b) 20k; (c) 30k; (d) 40k; (e) 50k; (f) 60k; (g) 65k (max load)

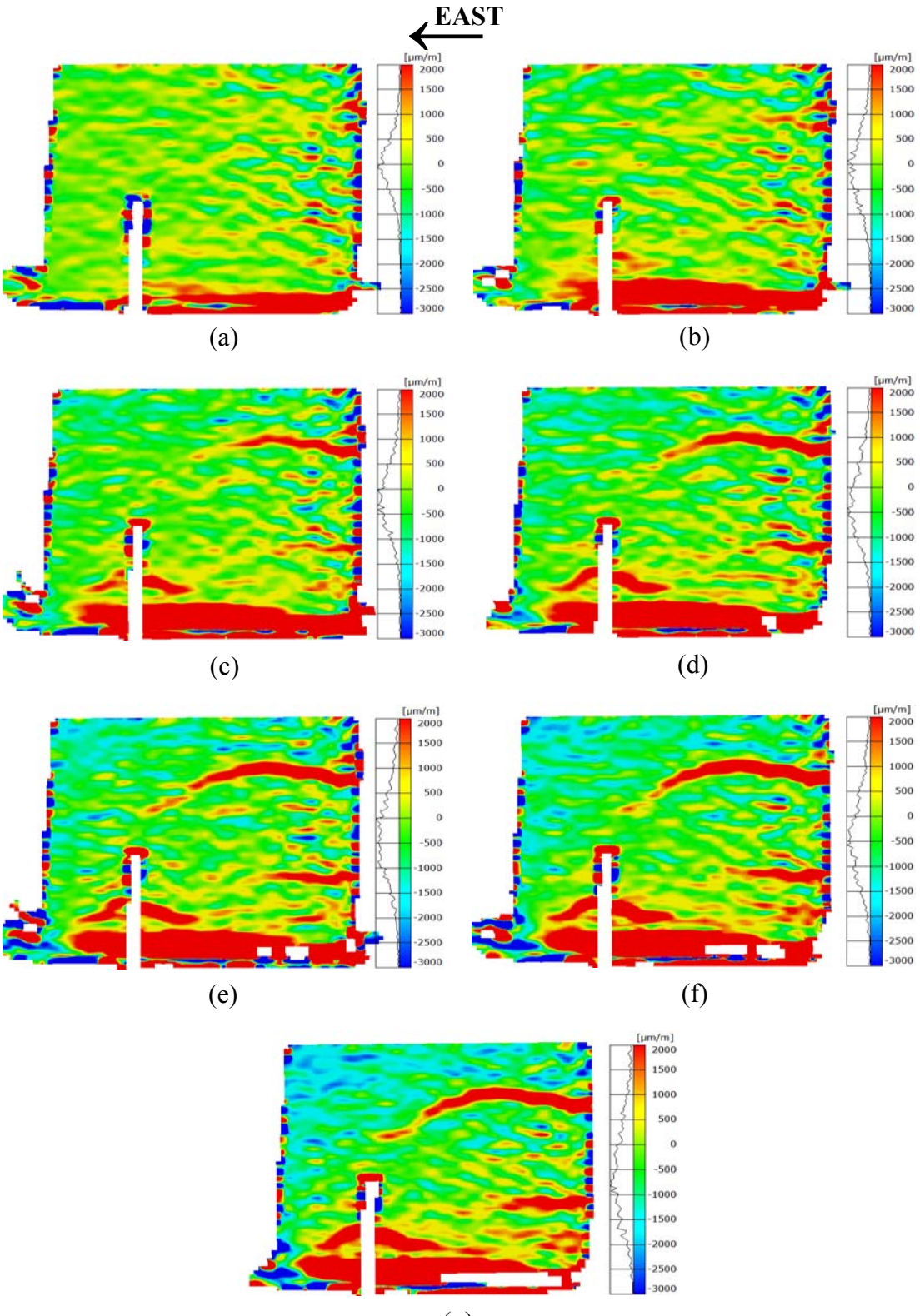

Figure 7.37: Phase II Compression (East) Pier Strain Maps (Looking South): (a) 10k; (b) 20k; (c) 30k; (d) 40k; (e) 50k; (f) 60k; (g) 65k (max load)

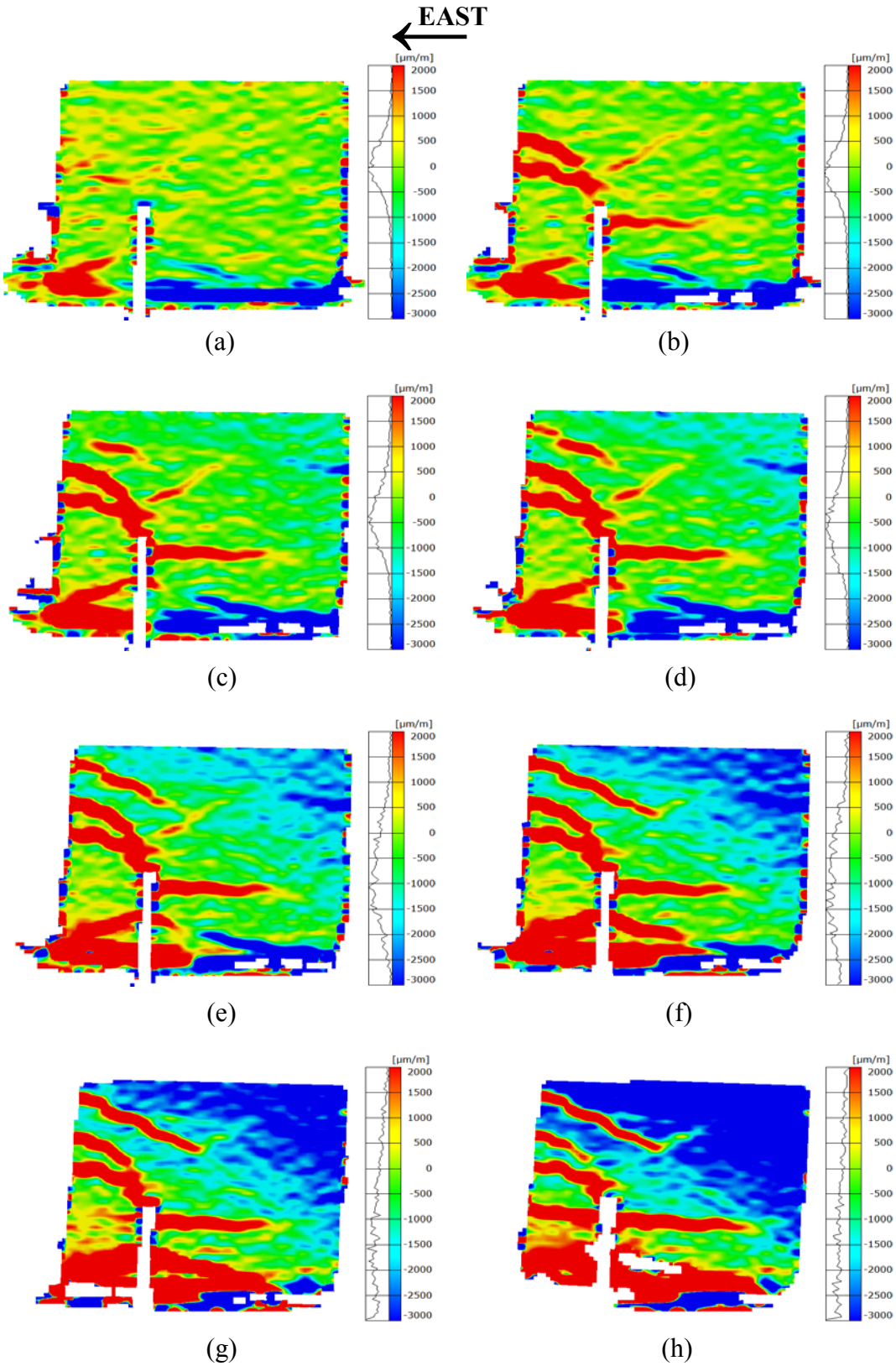

Figure 7.38: Phase III New Tension (East) Pier Strain Maps (Looking South): (a) 10k; (b) 20k; (c) 30k; (d) 40k; (e) 50k; (f) 60k; (g) 70k; (h) 75k (max load)

7.5 Beam Behavior

The behavior of the beams is a vital component in establishing the overall behavior and validity of the coupled wall system. This behavior will be established through the analysis of the elongation of the beams and the gap opening at the beam ends; cracking in the concrete will be presented in strain maps for visual aid and clarity.

7.5.1 Deflected Shape

The center line deflections from the Aramis DIC system are shown in Figures 7.39, 7.40, 7.41, 7.42, 7.43, 7.44, 7.45, 7.46, and 7.47 for Phase I, II and III at 1st story, 2nd story, and 3rd story, respectively. These graphs show the deflections from the test at increments of 10k and the maximum load for each phase. The deflections are similar for each story in each phase. The beams show little evidence of curvature, the system deflections are dominated by rigid body movement.

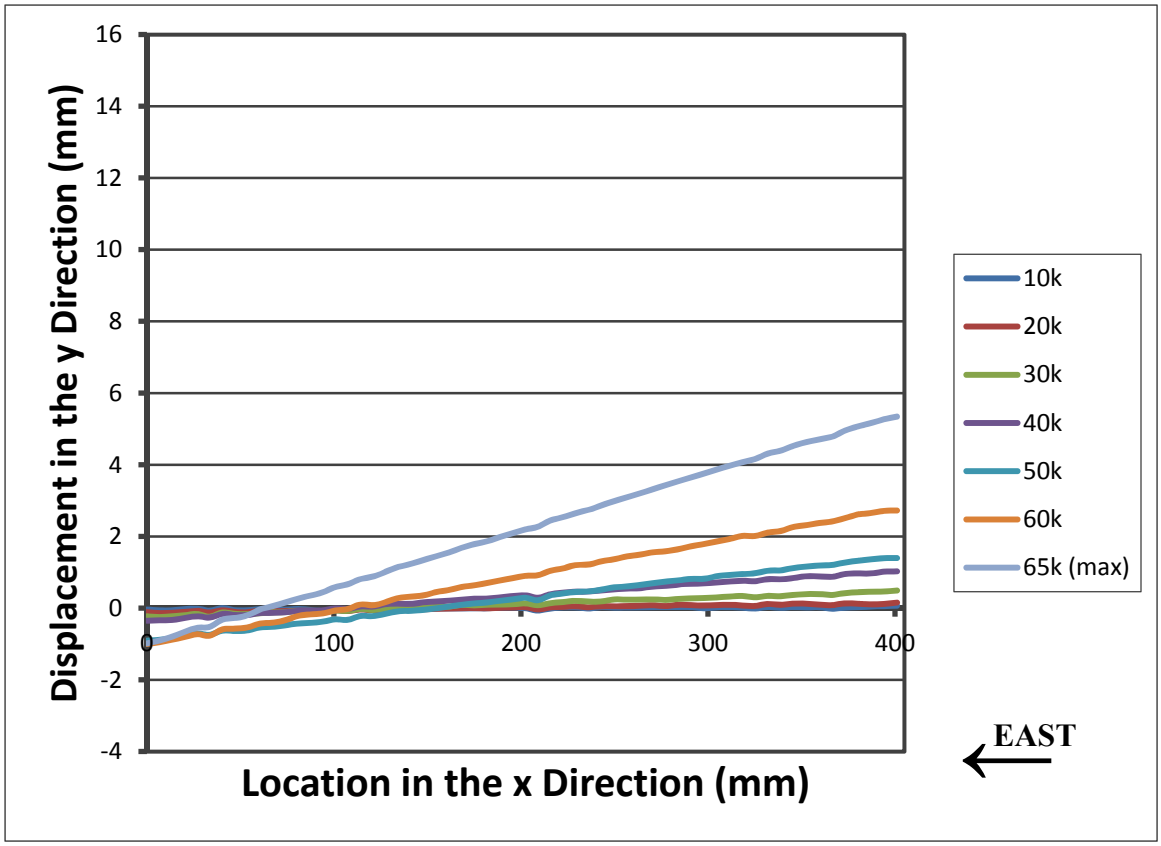

Figure 7.39: Phase I 1st Story Deflections

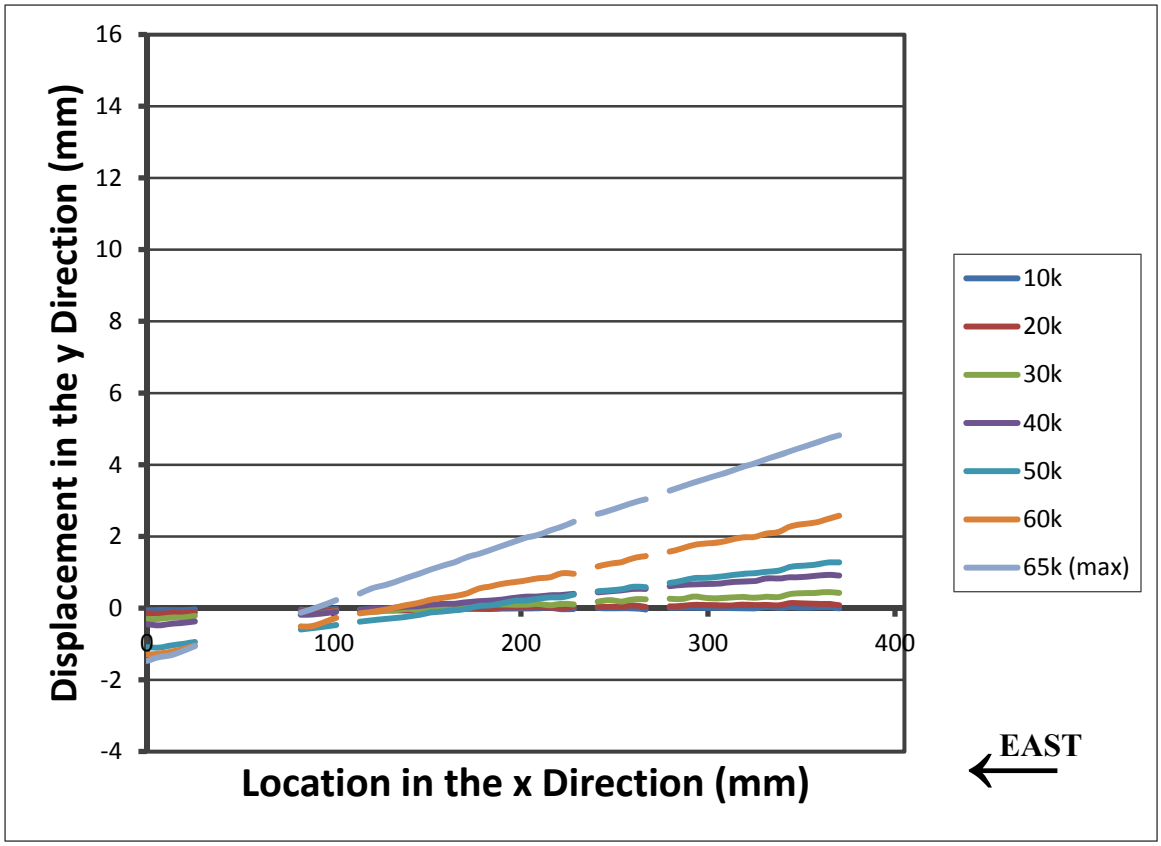

Figure 7.40: Phase I 2nd Story Deflections

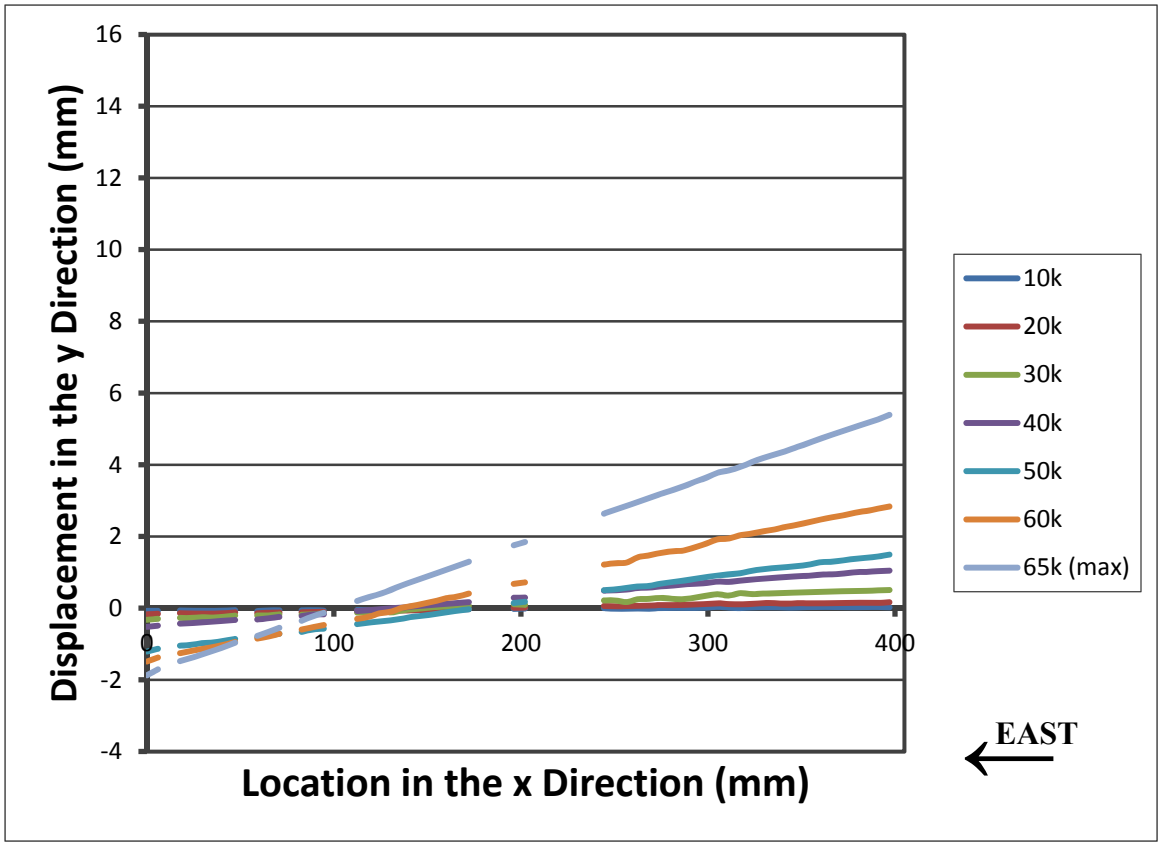

Figure 7.41: Phase I 3rd Story Deflections

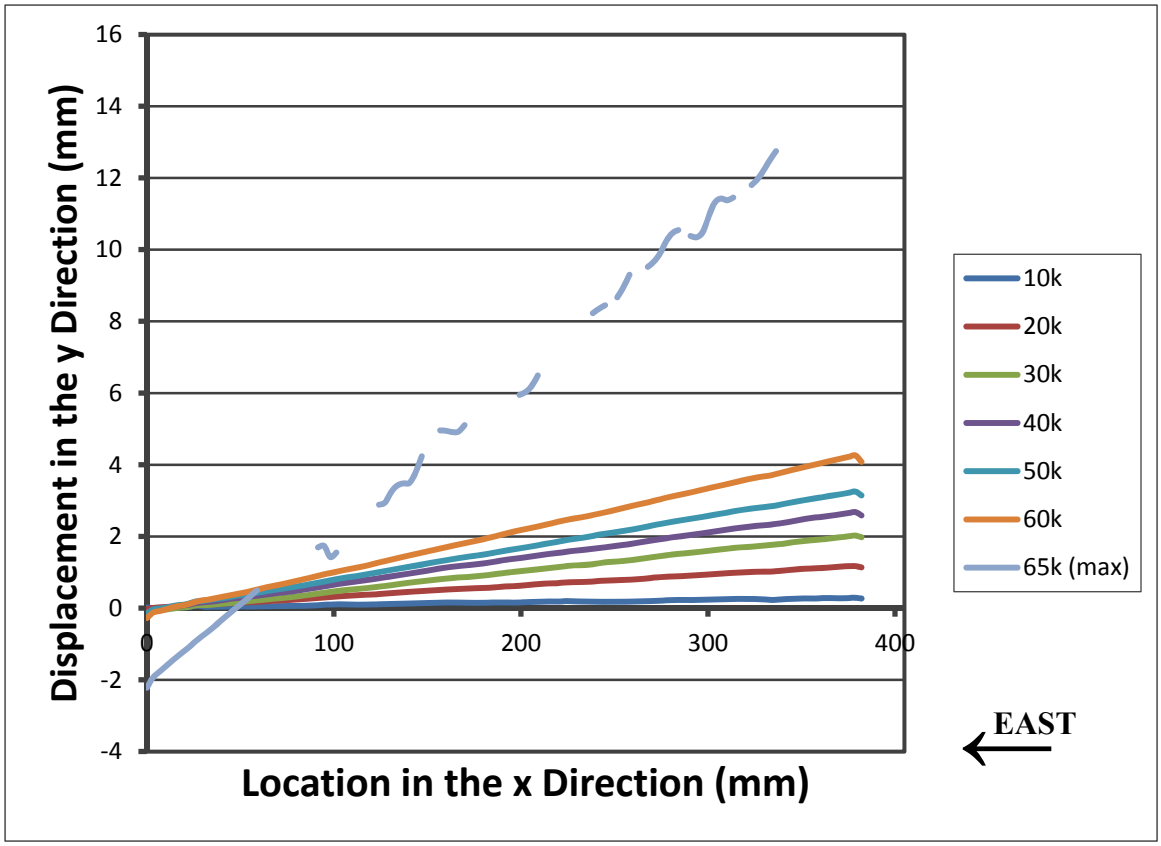

Figure 7.42: Phase II 1st Story Deflections

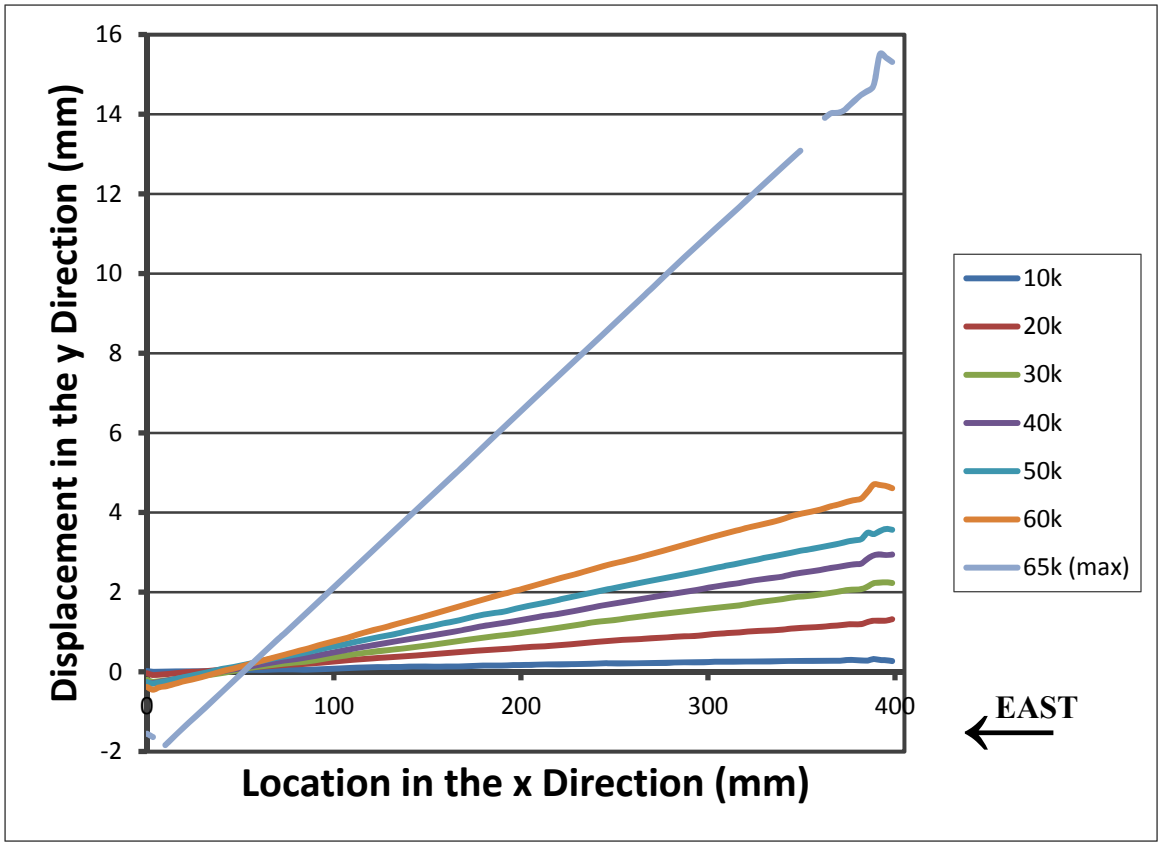

Figure 7.43: Phase II 2nd Story Deflections

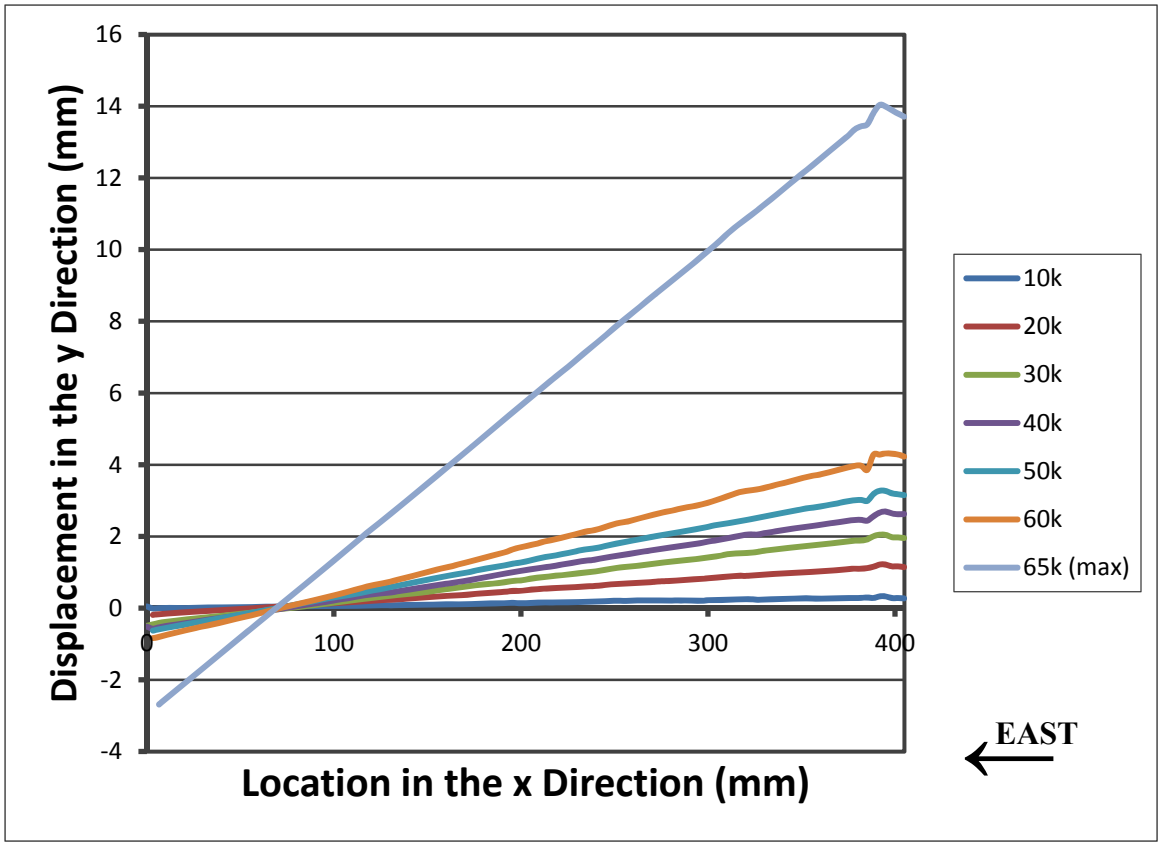

Figure 7.44: Phase II 3rd Story Deflections

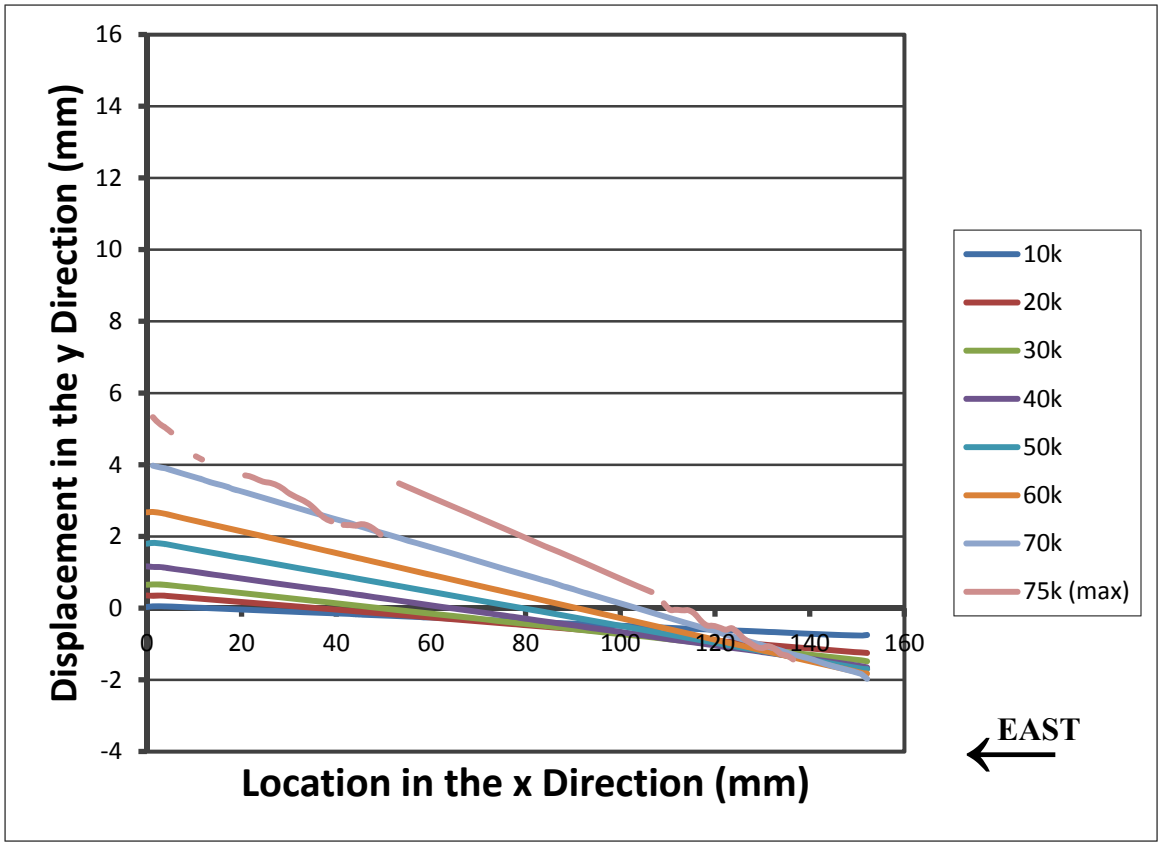

Figure 7.45: Phase III 1st Story Deflections

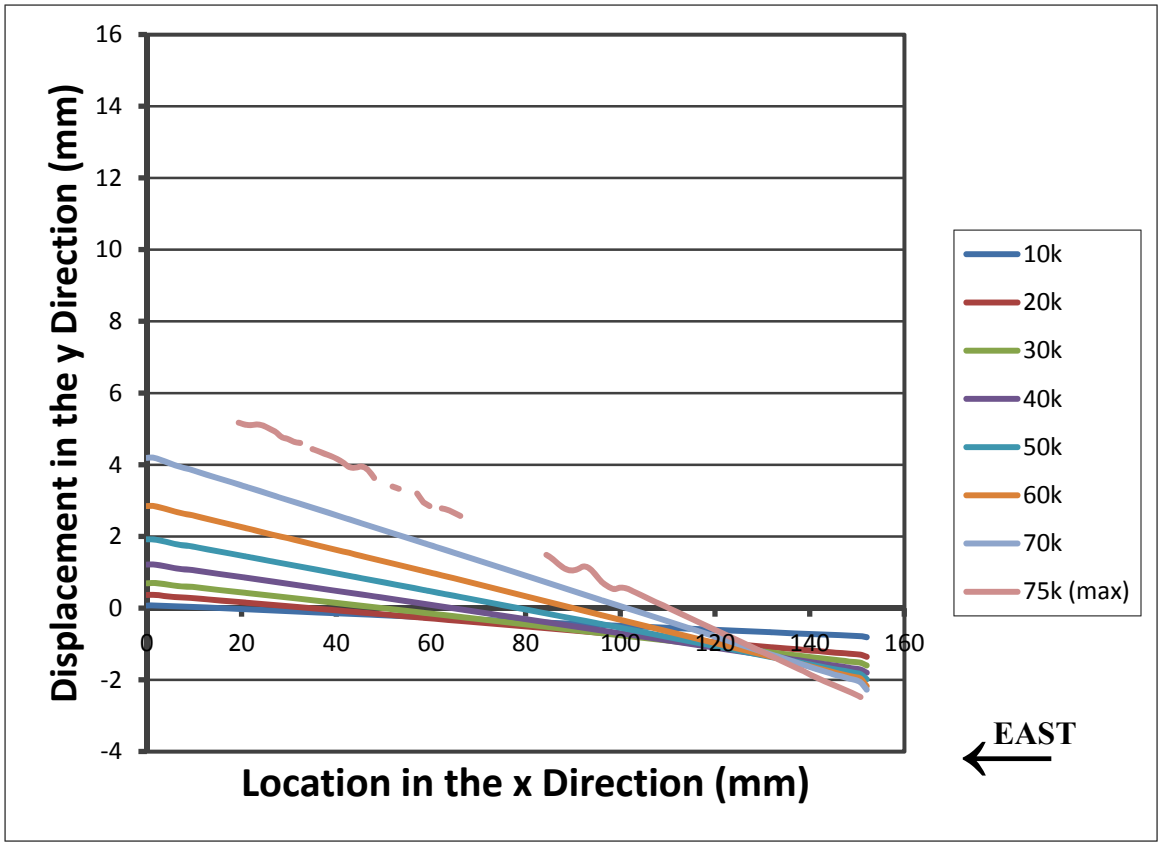

Figure 7.46: Phase III 2nd Story Deflections

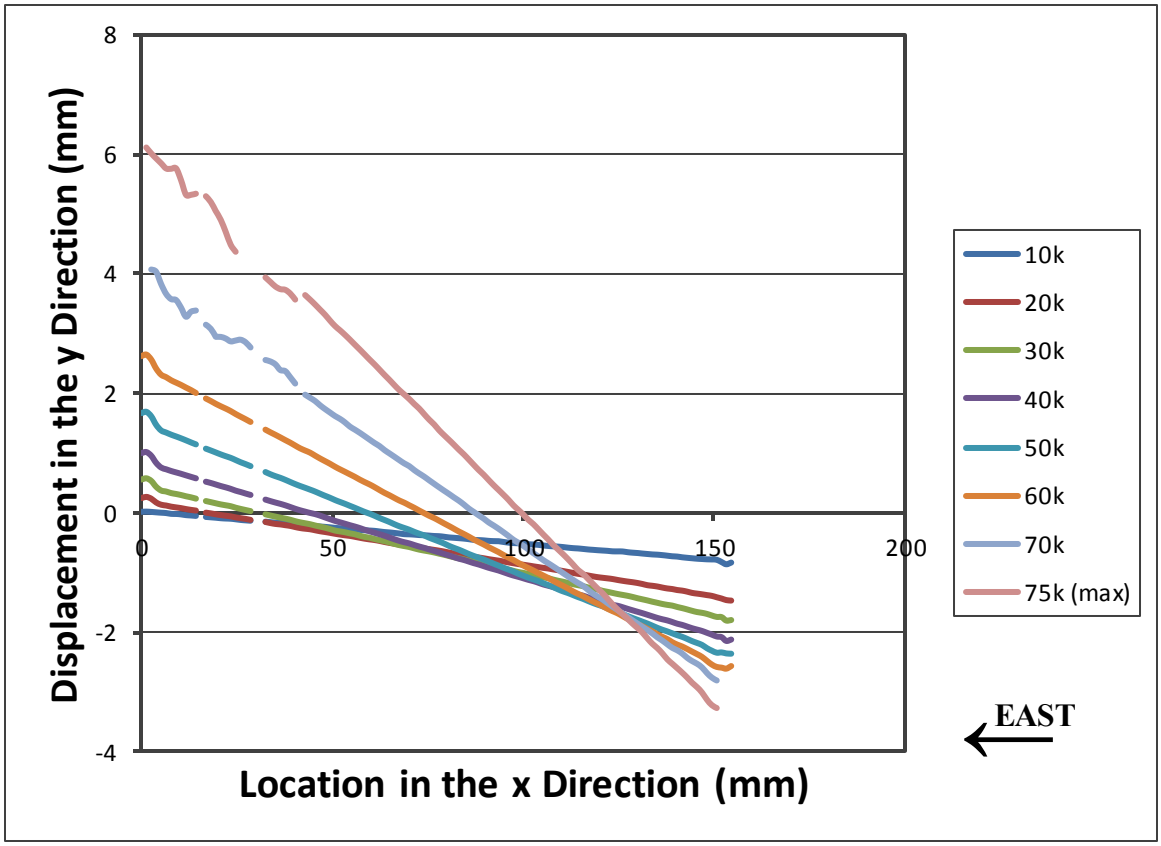

Figure 7.47: Phase III 3rd Story Deflections

As with the deflection of the full pier center lines, a comparison between the ABAQUS model results and the measured DIC data is conducted. Figure 7.48 shows the comparison between deflections for all three stories at the same load of 65 kips. Clearly the results show, as with the pier center line deflections, that the deflections are not similar based on the applied lateral loading. Instead they will be compared based on the drift produced as with the pier comparisons. Figures 7.49, 7.50, and 7.51 show the comparison of ABAQUS and measured results for the 1st, 2nd, and 3rd stories, respectively.

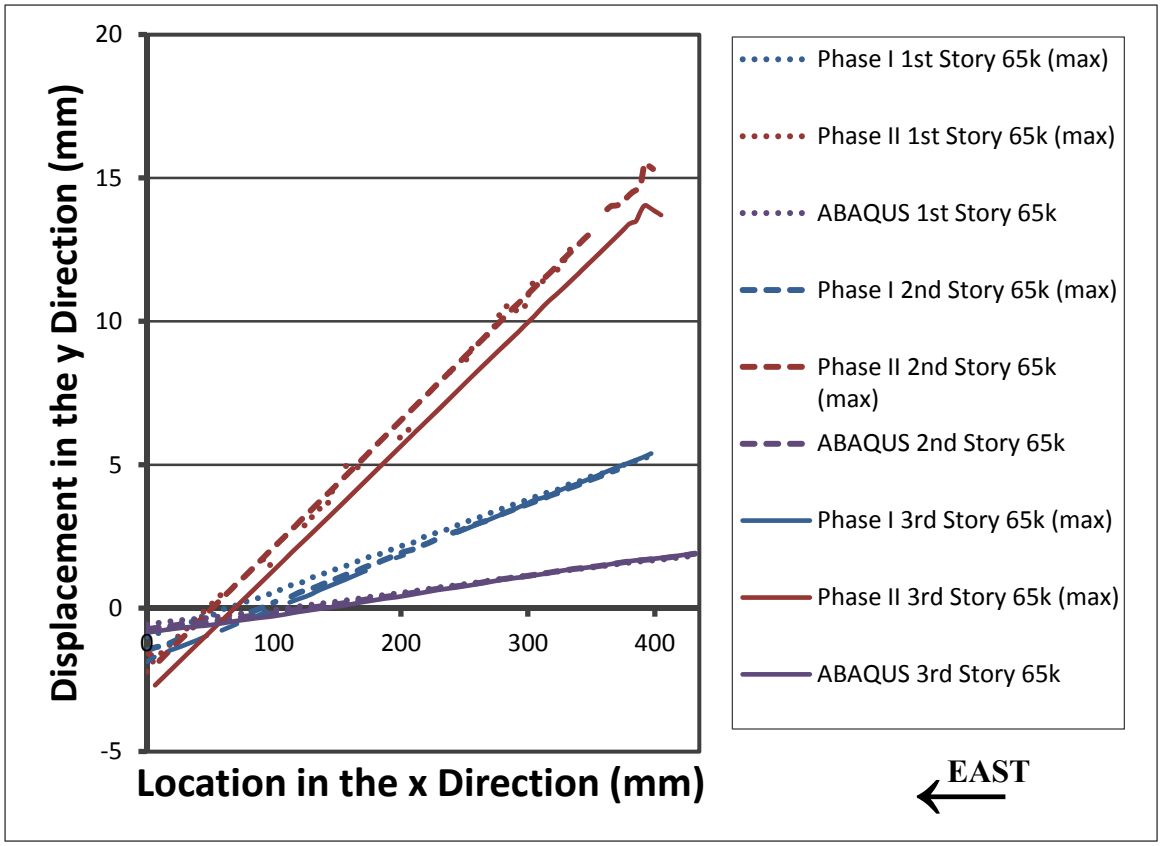

Figure 7.48: ABAQUS and Measured Results for Story Deflections

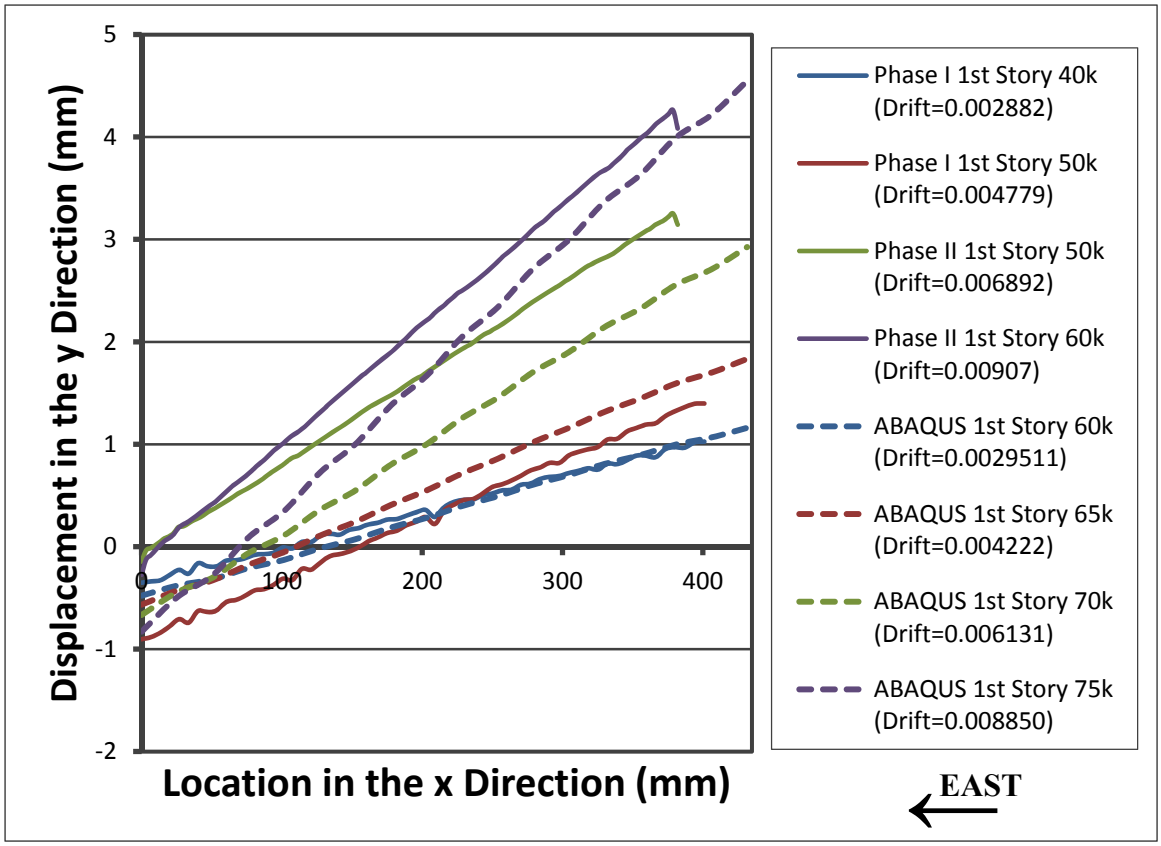

Figure 7.49: ABAQUS and Measured Results for 1st Story Deflections for Drift

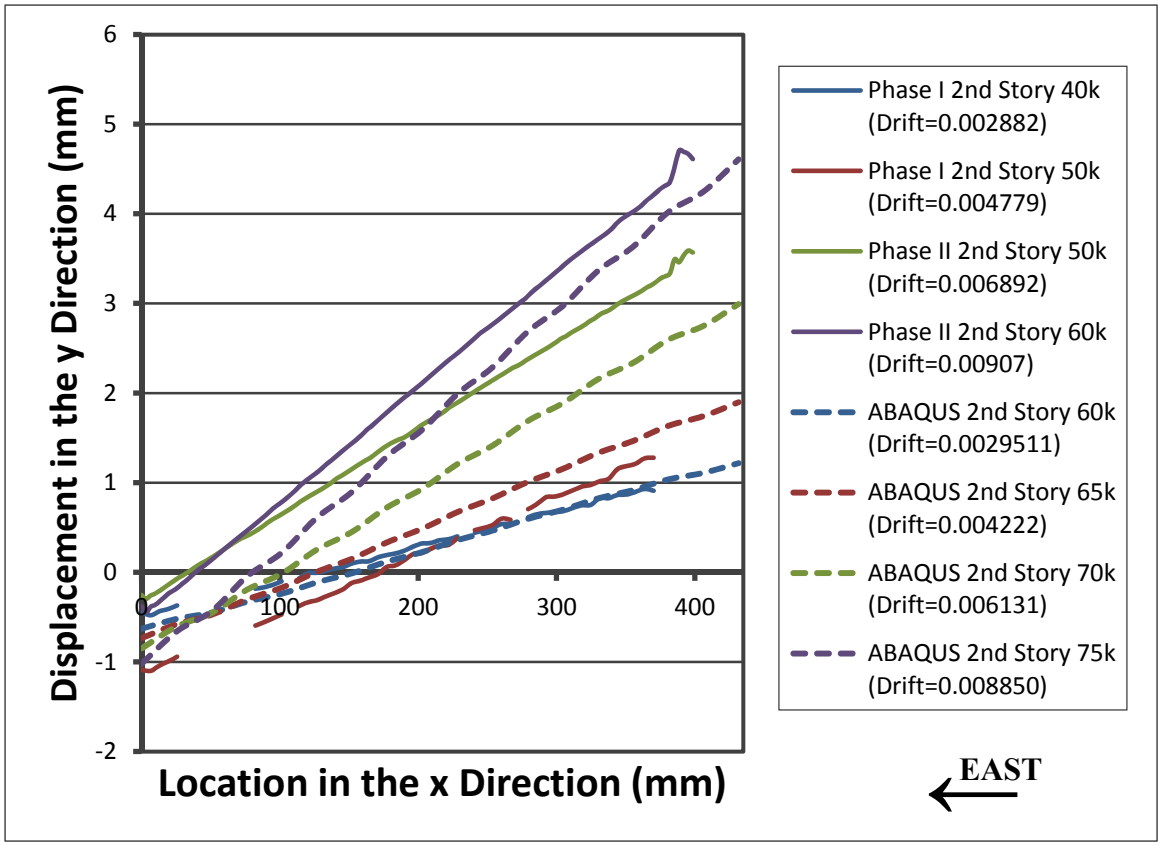

Figure 7.50: ABAQUS and Measured Results for 2nd Story Deflections for Drift

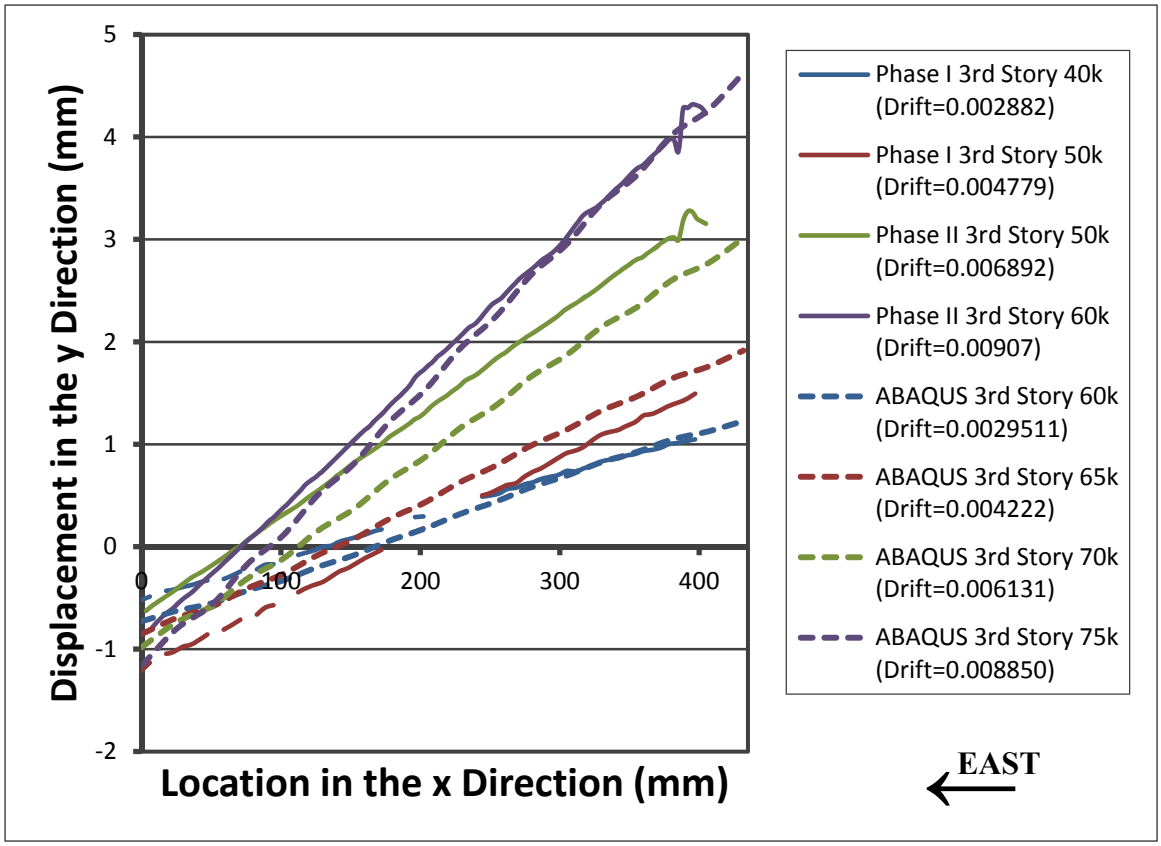

Figure 7.51: ABAQUS and Measured Results for 3rd Story Deflections for Drift

7.5.2 Axial Elongation of Beams

The axial elongation of each beam, the increase in space between the two piers, was measured in the DIC system by subtracting the displacements in the *x* direction on the center lines of the two piers, taken from the FOV global as defined in Figure 3.21, instead of subtracting the displacements in the *x* direction of the ends of the beams. The center line deflections are discussed and presented in Section 7.4.1.1. Points where data was taken and subtracted for each method can be seen in Figure 7.52.

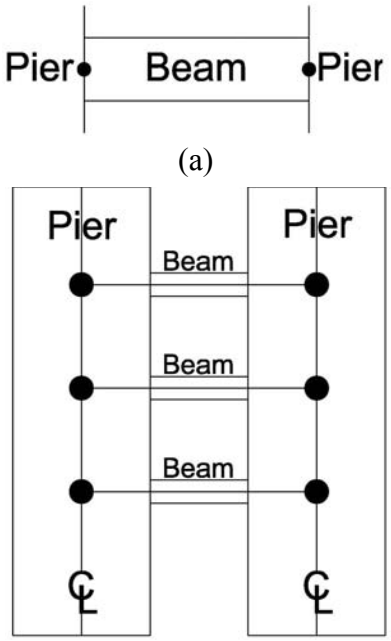

Figure 7.52: Elongation Measurement Methods: (a) Beam End Method; (b) Center Line Method

The elongation of the beams could not be measured from the DIC systems because of the data loss in the global FOV (no beam data). In order to validate measuring the beam elongation from the center lines of the piers, the ABAQUS model was used to compare the actual beam elongation with the values measured using the center line technique. The method comparison is given in Figure 7.53. Based on the measurement method comparison, the center line measurement method can be considered an accurate measurement technique.

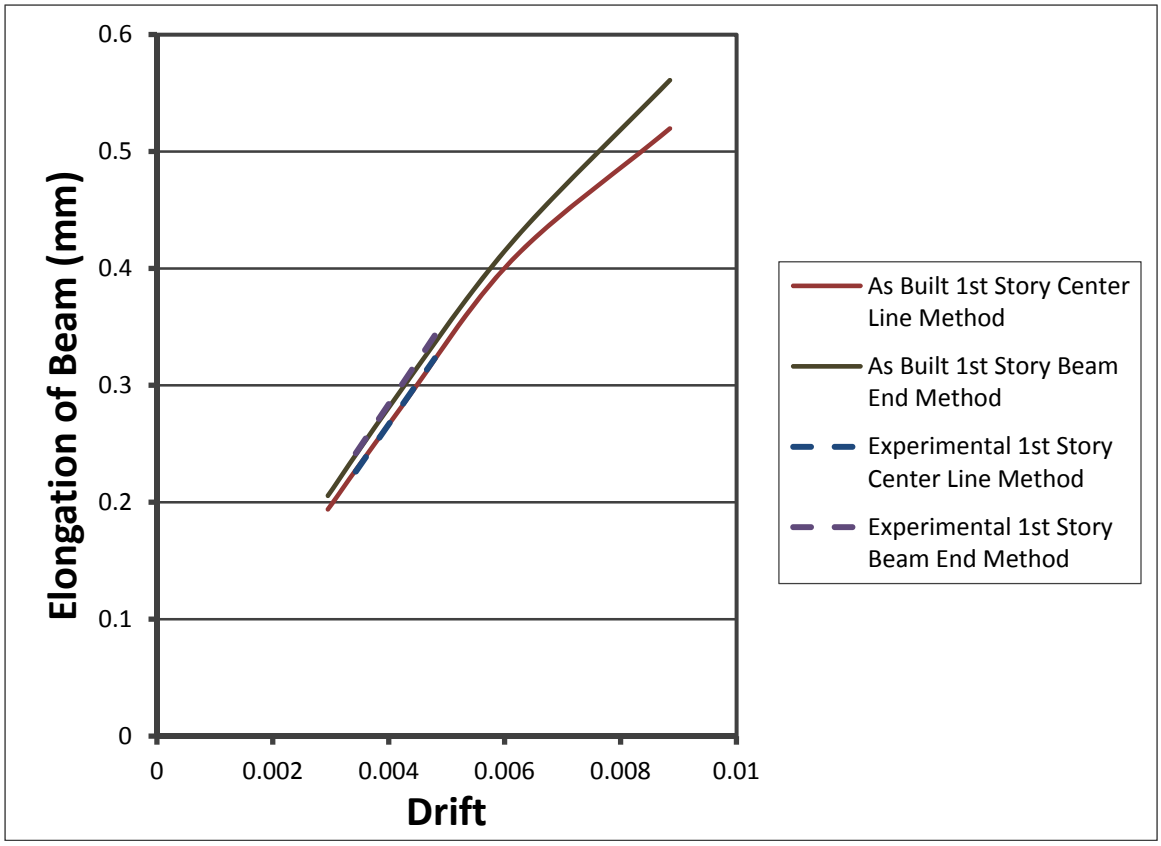

Figure 7.53: Elongation Measurement Method Comparison

The elongation of the beams is provided in Figure 7.54. The values given in Figure 7.54 were measured using the center line method validated above. The ABAQUS models show that the 1st story elongates less that the 2nd and 3rd stories. The experimental data shows that the values for the three stories are approximately equal. In phase III, the 3rd story elongated significantly less than the 1st and 2nd stories; the 3rd story should therefore have a higher compression. This can be seen in the beam strain maps in Section 7.5.3. Although the results are not identical, the comparison in results from the DIC system and the ABAQUS models shows that the ABAQUS models provide an accurate representation of the tested specimen.

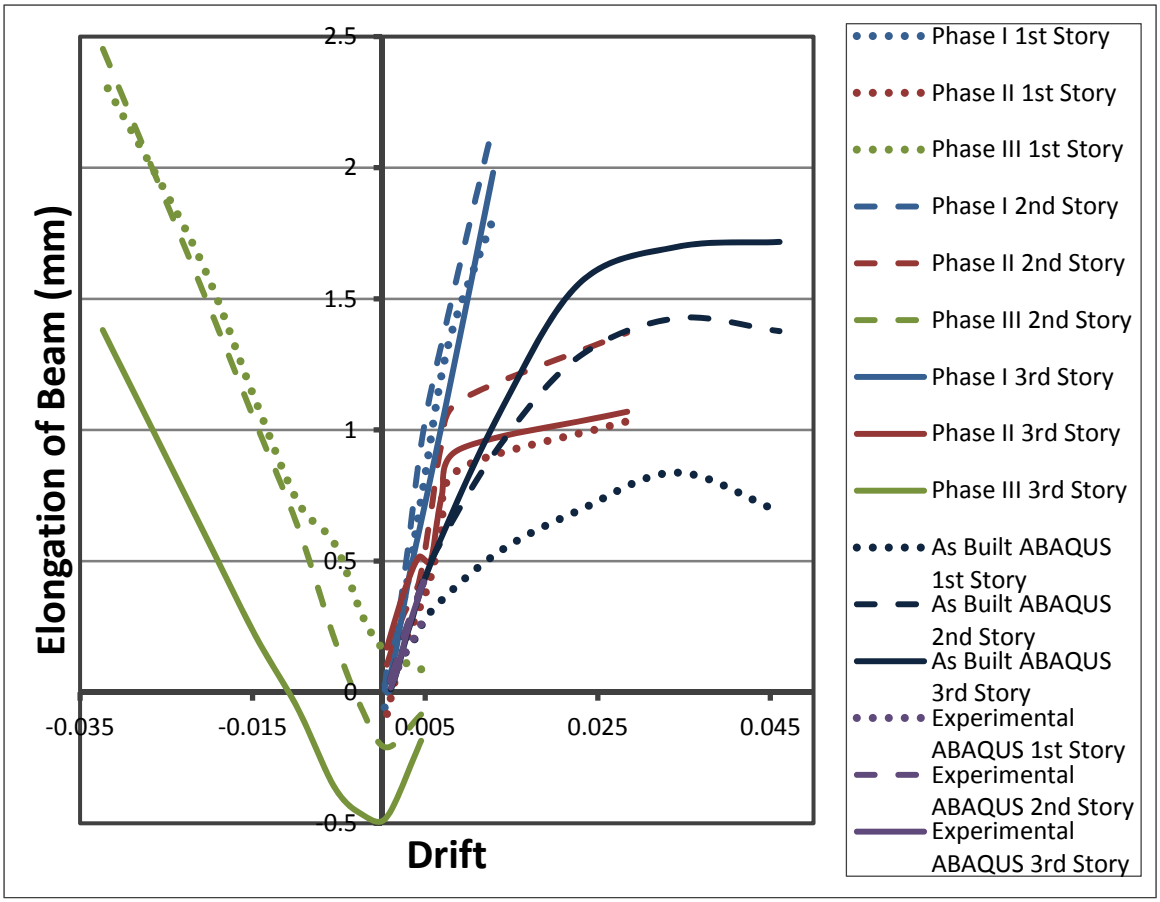

Figure 7.54: Axial Elongation of Beams, Measured and ABAQUS Results

7.5.3 Angular Opening of Beam Ends

The angular openings of the beam ends were found by calculating alpha (α) and beta (β) and summing them as described below. Alpha was found by plotting a vertical line on each beam close to the end (displacement in the *x* direction) and finding the slope of that line. The slope of the beam line produces angle alpha in radians. Beta was found by plotting a line on the pier close to the edge (displacement in the *x* direction) and finding the slope of that line. Again the slope of the pier is the angle, beta, in radians. These angles were added together to find the total angle of gap opening at the end of the beams. The information for the beam slopes was measured from local DIC data with a view of the back of the specimen; Figure 7.55 illustrates the locations and layout of the

beam-pier interface and is of the same view. The information for the Pier slopes was measured from global DIC data.

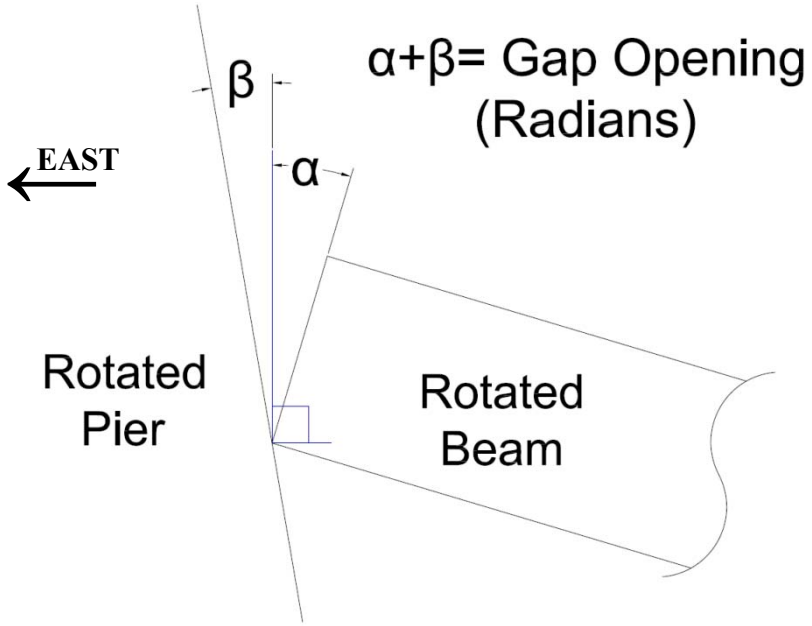

Figure 7.55: Beam Angular Gap Opening Location and Layout for Calculation

The beam angular gap opening for phases I, II and III, as well as those from the ABAQUS models are given in Figure 7.56. The angular opening at the beam ends is similar at all three stories. Again, the behavior shown during testing is reflected in the ABAQUS models.

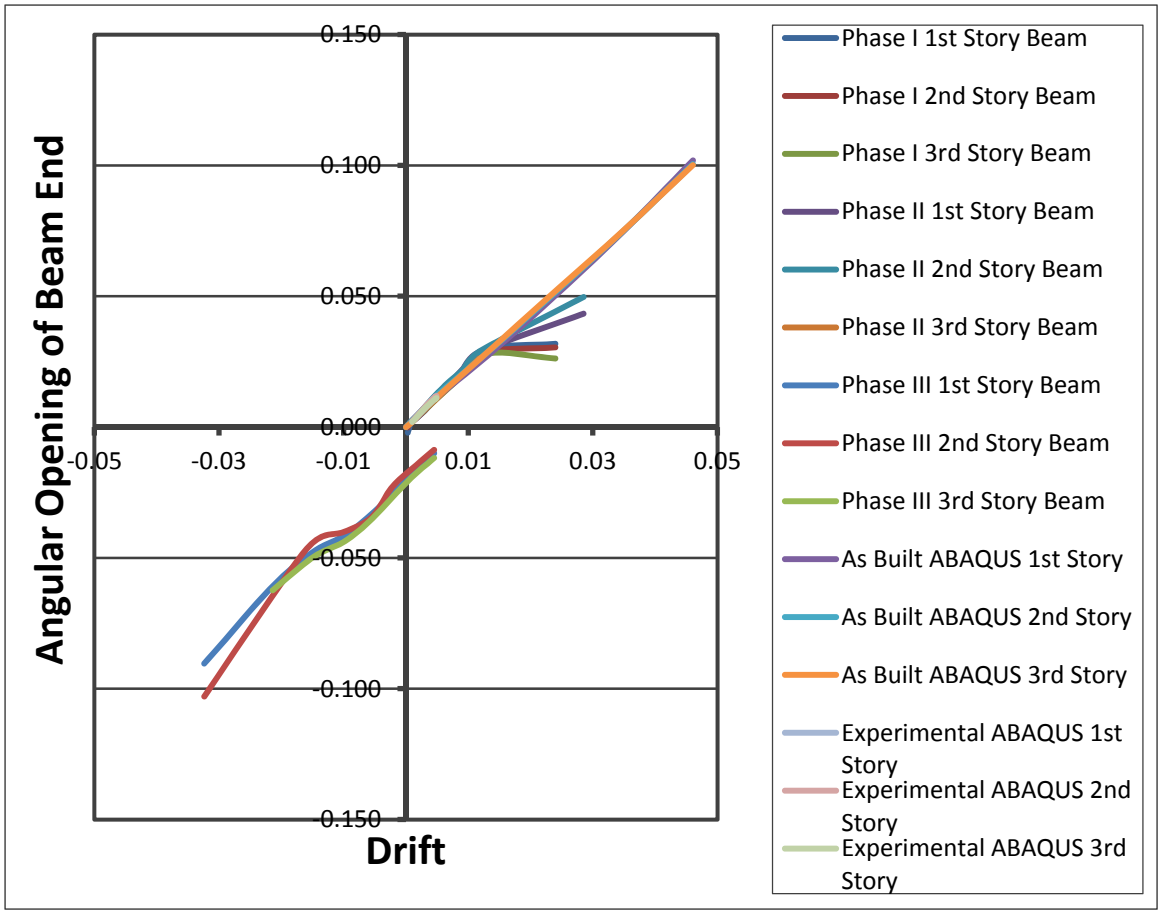

Figure 7.56: Angular Opening of Beam Ends (Radians)

7.5.4 Beam Strain Maps

Figure 7.57, 7.58, and 7.59 show the images of the strain maps that are generated in the DIC software for the three stories of beams for phases I, II, and III, respectively. The red areas are the tension areas where gap opening occurs in the diagonal corners. The dark blue areas are the compression areas where the deflected and rotated beams have forced the diagonal corners into compression.

In Phase III, the 3rd story beam has significantly more compression than the other two stories. This is also supported by the beam elongation data – see Section 7.5.1.

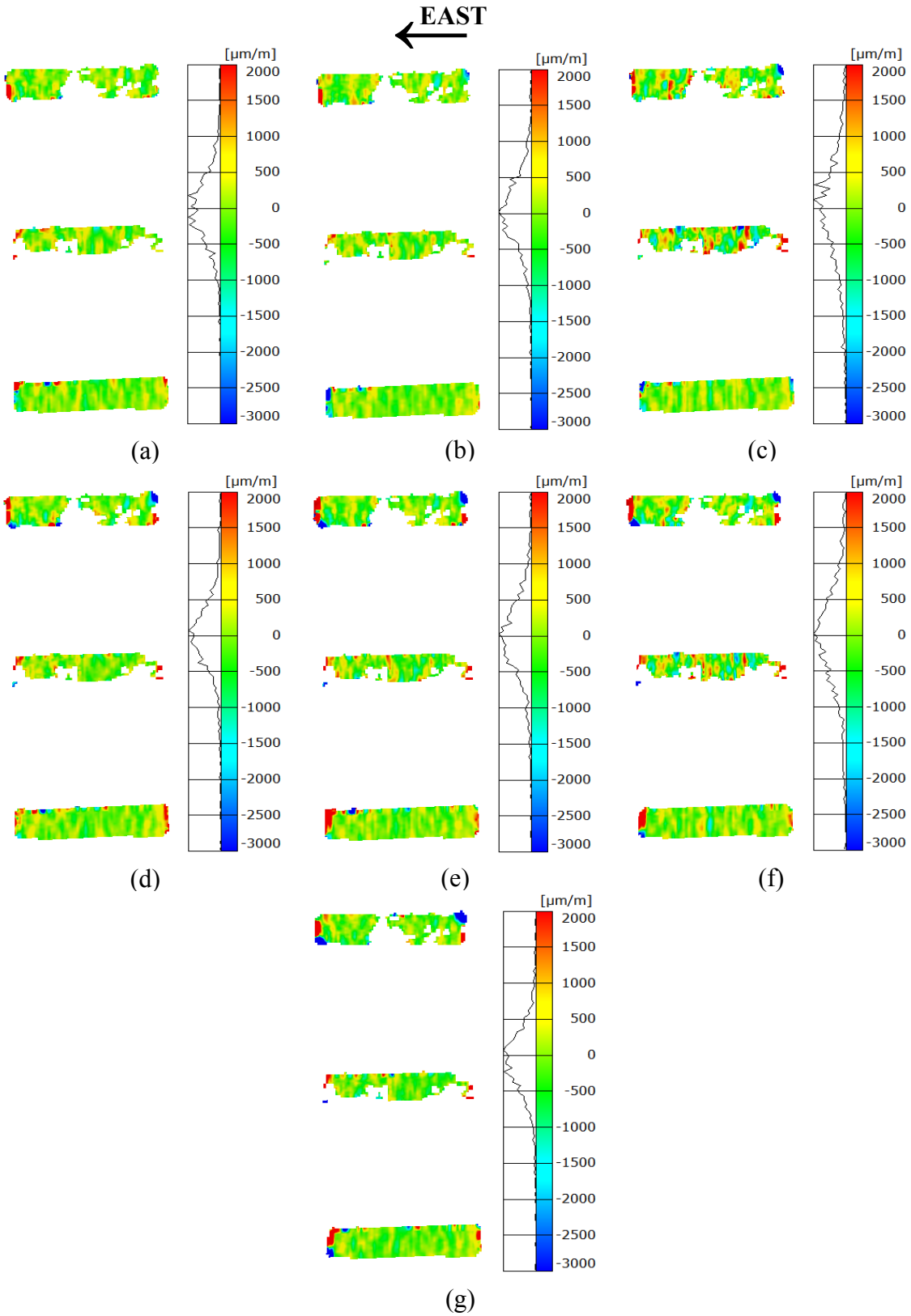

Figure 7.57: Phase I Beam Strain Maps (Looking South): (a) 10k; (b) 20k; (c) 30k; (d) 40k; (e) 50k; (f) 60k; (g) 65k (max load)

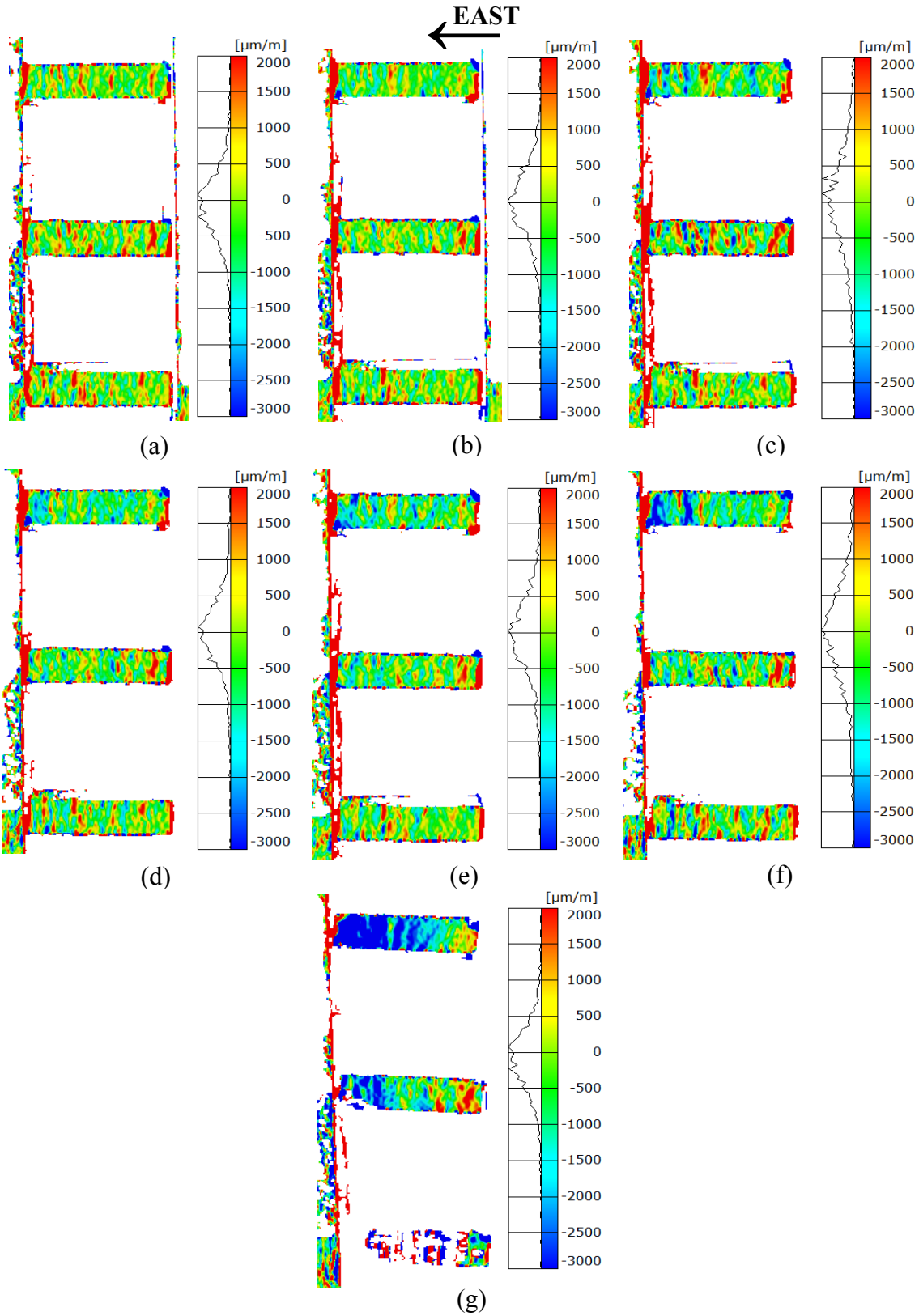

Figure 7.58: Phase II Beam Strain Maps (Looking South): (a) 10k; (b) 20k; (c) 30k; (d) 40k; (e) 50k; (f) 60k; (g) 65k (max load)

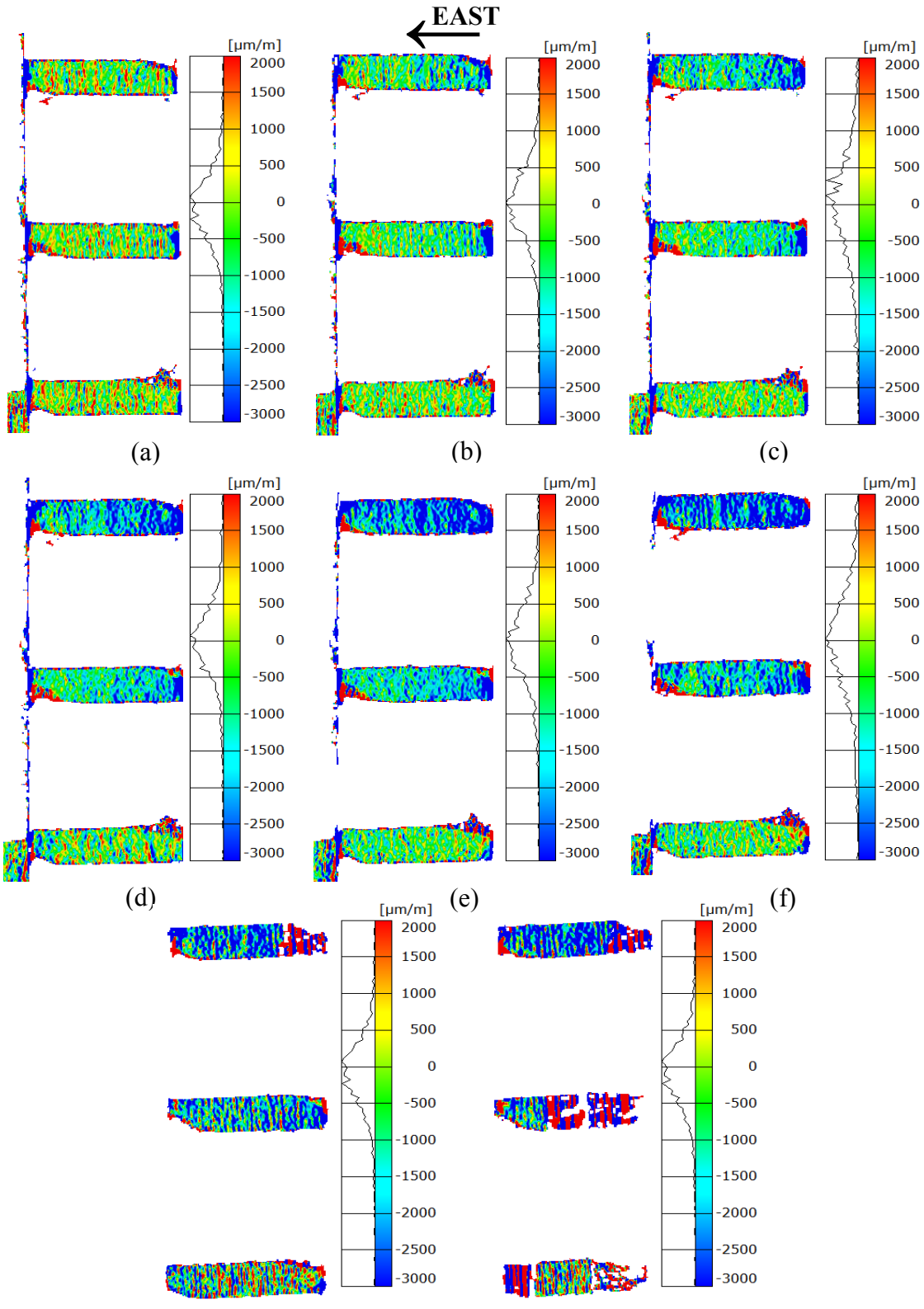

Figure 7.59: Phase III Beam Strain Maps (Looking South): (a) 10k; (b) 20k; (c) 30k; (d) 40k; (e) 50k; (f) 60k; (g) 60k; (h) 75k (max load)

7.6 Post Test Condition

The structure exhibited behavior consistent with some of the potential benefits of a post-tensioned coupled wall system, with some self-centering capability, and damage limited mostly to the toes of the coupling beams. Figure 7.59 shows the specimen after loading in both directions. The damage is clearly confined to the compression toes of the beams and piers.

Figure 7.60: Specimen Damage After Testing (Looking North): (a) Global FOV; (b) Beam

7.7 Experimental Results Conclusions

This chapter validates the data measured by the digital image correlation system. The behavior of the system is established using the measured data from the four DIC systems, in some cases multiple systems were used to determine one parameter. The ABAQUS model is later validated by comparing the deformation information from both

systems. There are several limitations of the current experimental setup, the three major being: (1) scaling the specimen meant that C-shaped walls became rectangular shaped, and energy dissipation steel in the coupling beams could not be included; (2) the forces in the beam post-tensioning cables were less than as designed, and (3) the tension reinforcement necessary to resist the base moment in each of the piers pulled out of the structural couplers in the foundation at lower than the design load. Because of these limitations, the specimen did not reach the expected design load of the coupled wall system. In spite of these limitations, the simple ABAQUS model created appears to give reasonable results: it matches experimental deformation data well.

The following conclusions can be made about the behavior of this system:

- The reinforced concrete multi-story coupled wall system behaved in accordance to the predicted behavior with exceptions related to the post-tensioning in the beam story cables and the rebar pull-out at the foundation pier joint.
- The load verses displacement plot suggests some self-centering capabilities in the coupled wall system.
- The foundation did not contribute to rotation, slip or uplift during the test.
- The curvature in the piers due to axial elongation in the beams is illustrated through the deflected shape profile.
- The strain maps generated by the DIC showed that for phase I and II tension cracking occurred in the tension (West) pier while shear cracking was shown in the compression (East) pier. For phase III, the strain maps showed tension

cracking in both piers due to existing cracks in the tension pier (West) from the previous testing phase.

- The strain maps generated by the DIC were also able to validate the use of the 2D-DIC systems at the bases of the piers by establishing small out-of-plane movements.
- As expected, the neutral axis depth decreased as the drift of the system increased. However, the measured results indicate that the tension pier does not necessarily have a smaller neutral axis depth for the duration of the test. This is believed to be caused by the rebar pull-out at the foundation-pier joint which could have occurred unequally or at different loads in the two wall piers.
- When considering drift, the results for gap openings correlate well with the numerical model generated by ABAQUS.
- When considering the rotations of the pier bases during the test, it is clear that the expected rotations, even when comparing drift, are much smaller than the measured rotations. This is potentially due to the rebar in the base of the piers pulling out of the foundation during testing.
- The deflected shape of the beams at all stories show little to no curvature as the center lines of the deflected shapes are essentially straight: the system is dominated by rigid body movement.
- The center line method of measuring axial elongation of the beams is a valid technique.

- The experimental data shows that the three beams elongate approximately the same amount, while the ABAQUS model shows the 1st story elongating less. Phase II measured data shows the 3rd story beam elongated significantly less than the other two stories, which should result in a higher compression. This is visibly seen in the beam strain maps for phase III.
- The amount of angular gap opening at the beam ends was consistent with the predicted angular openings produced by the ABAQUS model.

The following conclusions regarding the DIC are made:

- The use of multiple DIC systems provides a much larger supply of information about the specimen and helps to better establish its overall behavior.
- Because the data was collected the same time for each system, the information from more than one system can be used to calculate a single parameter.
- The DIC data reflects positively the data collected by other traditional measurement tools, and the expected behavior of the coupled wall system.
- This data could not have been captured so easily or at all with traditional measurement techniques. A single DIC system could not have captured enough data to establish the behavior of the specimen. This test could only realistically have been conducted using multiple DIC systems.

CHAPTER 8 – FINITE ELEMENT ANALYSIS

This section presents a comparison of the two finite element analysis programs used to make initial design decisions and to predict the resultant forces within the 15% scale structure constructed and tested for this thesis. This section includes descriptions of the models used, as well as their predictions of structural behavior. A parametric study was conducted using the ABAQUS software to resolve differences in stiffness between expected and experimental behavior.

8.1 Model Descriptions

The model descriptions are provided for the ABAQUS and DRAIN-2DX models which were used for analytical modeling and comparison.

8.1.1 ABAQUS

The philosophy behind this model was to simulate a simplified design office approach to analysis of the post-tensioned coupled wall system. The geometry matches Figure 4.1, including application of gravity loads through post-tensioning. The post-tension cables were created in ABAQUS as a temperature truss element. The post-tension force was created by applying a negative temperature change to produce a predetermined stress. Table 8.1 provides information on the nodes and elements used in the model.

Table 8.1: Node and Element Information

Part Instance	# of Nodes	# of Elements	Type of Elements
Piers	735	480	C3D8R
Beams	540	340	C3D8R
Foundation	2052	1404	C3D8R
Cables	2	1	T3D2T
Rebar	2	1	T3D2
Total System	5284	3509	C3D8R, T3D2T, and T3D2

The elements used for the concrete portions of the model were C3D8R: 3 dimensional, 8-node linear continuum brick elements, with reduced integration and hourglass control. The post-tension cables used T3D2T elements: 3 dimensional, 2-node coupled temperature displacement truss elements, with linear displacement and temperature. The elements used for rebar in the model are similar to those used for post-tension cables except that they have no temperature input; these elements are called T3D2: 3 dimensional, 2-node linear displacement truss elements.

The interface used for all surfaces in direct contact was contact with hard friction. The rebar and post-tension cables were tied to their terminating nodes. The bottom surface of the foundation block was fixed: the surface was not allowed to rotate or deform in any direction. The ABAQUS model uses the mesh shown in Figure 8.1. The beams required a finer mesh than the piers and foundation parts. Although no mesh study was conducted, an earlier model (Figure 8.2) which used a much finer mesh and similar dimensions containing 30188 nodes and 26113 elements produced similar behavior. Because this simpler model required less computation and produced validated results, it was used for this project's analysis.

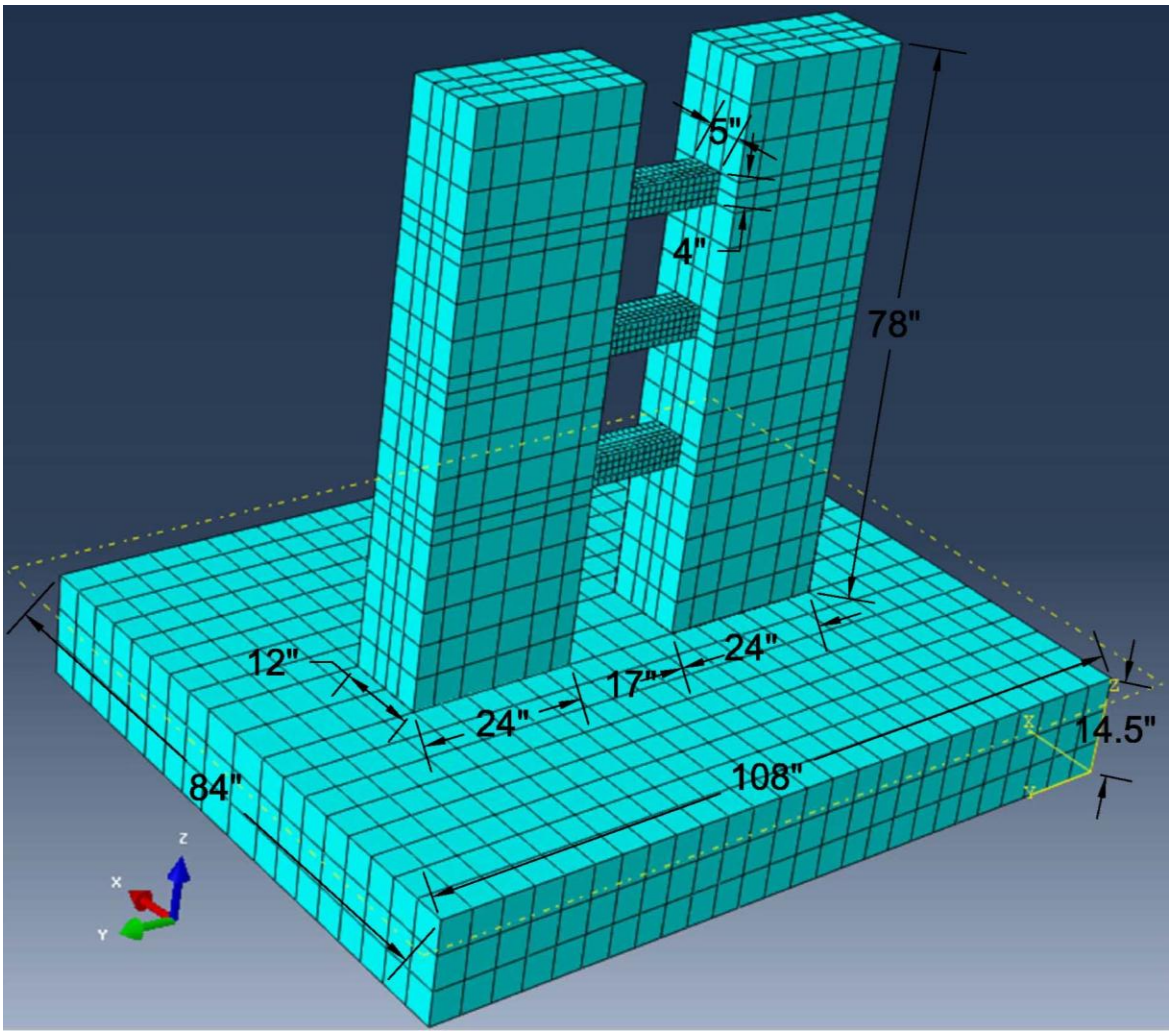

Figure 8.1: ABAQUS Model of Test Specimen

The material used for concrete in ABAQUS used some simplified properties. The ABAQUS model is elastic plastic. The density of the concrete material used was 150 pcf; Young's modulus for the concrete material was 4,200,000 psi; Poisson's ratio for the concrete material was 0.2; and the yield stress for the concrete material was 6000 psi with an elastic-perfectly plastic assumption. Because of this, the model will not predict cracking well.

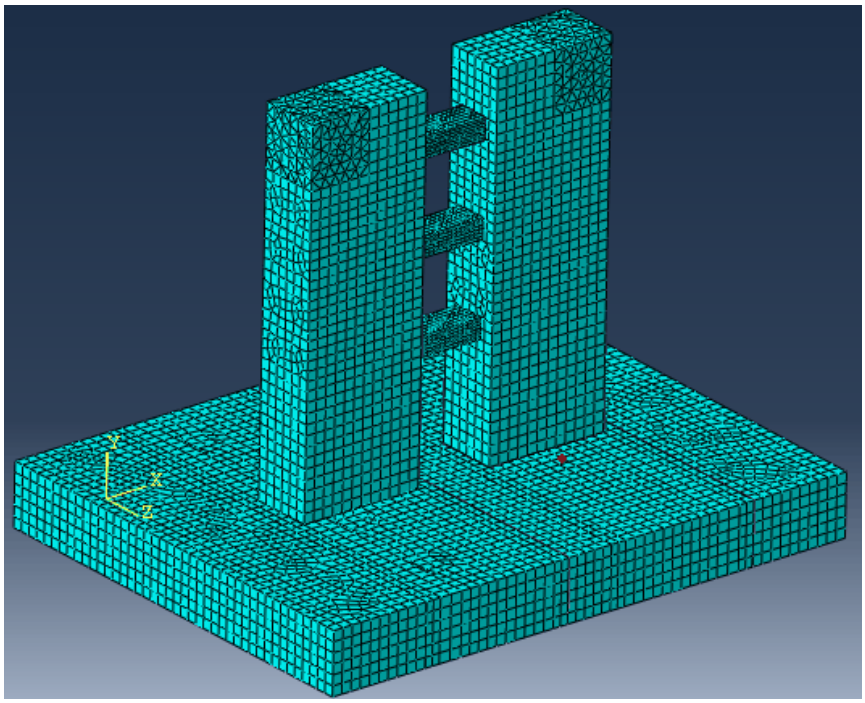

Figure 8.2: Preliminary ABAQUS Model

The loads were applied to the model using pressures in the areas where the embedded threaded rod connected the steel I-beam lever to the top of the piers and where the lateral actuator applied load– see Figure 8.3.

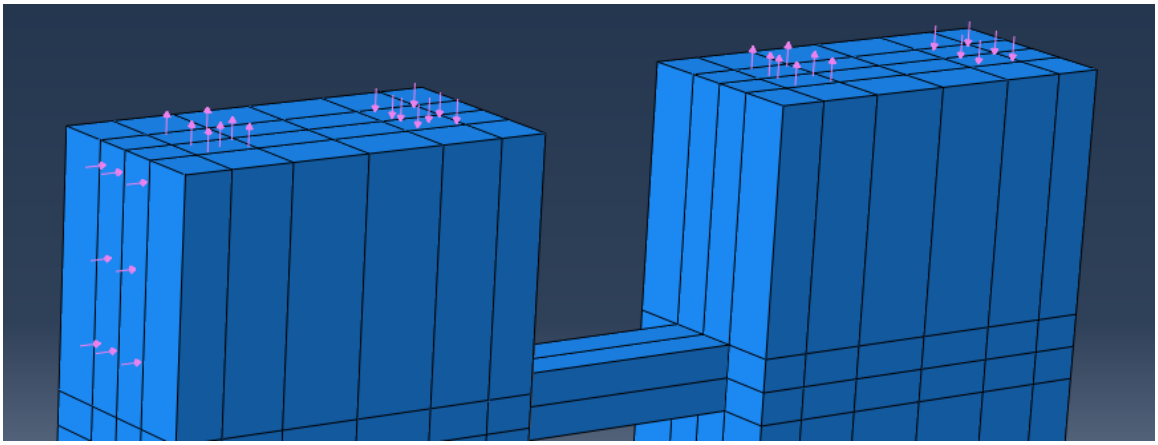

Figure 8.3: Applied Load Areas

When tensioning the cables in the experimental specimen, the relatively short length of the cables and poor construction control meant that the design initial gravity force in the gravity cables and post-tensioning force in the beam cables was not met – see

Section 5.2.4. This resulted in an as-built structure that had approximately 75% of the intended gravity load based on the tributary areas of the prototype structure (discussed in Section 8.3). The ABAQUS As-Built model reflects the As-Built forces shown in Table 8.2.

Table 8.2: As-Built Loads vs. ABAQUS Loads

	As-Built Applied Forces (lb)	ABAQUS "As-Built" (lb)
Tension Pier Gravity	37700	37700
Compression Pier Gravity	44600	44600
Beam Cable - 1st Story	454	454
Beam Cable - 2nd Story	3284	3284
Beam Cable - 3rd Story	8338	8338

8.1.2 DRAIN-2DX

The DRAIN-2DX model consists of a series of nodes connected by nonlinear beam-column elements that are discretized into fibers with areas and material properties that accurately depict the concrete and steel present in the structure (Figure 8.4). The model used the ELF procedure to determine the lateral force distribution to be applied for a displacement-controlled pushover analysis of the full 8-story structure.

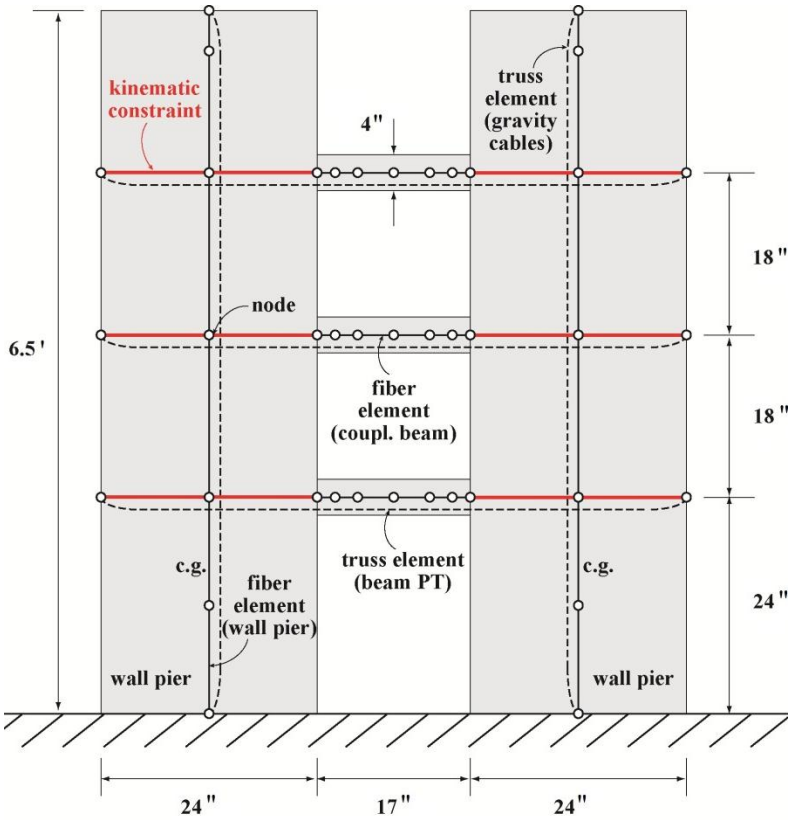

Figure 8.4: DRAIN-2DX Model

The model includes nodes (depicted using ○ markers in Figure 8.4) that are connected by nonlinear fiber beam-column elements to simulate the wall piers of the coupled wall system. The wall piers were assumed to be fixed at the base. Each fiber element cross-section was constructed by discretizing the RC wall pier cross-section into concrete and steel fibers. Each fiber was defined by its area, distance of its centroid from the element reference axis (assumed to be located at the geometrical center of the wall pier cross section), and a uniaxial material stress-strain relationship. Because of the two-dimensional analysis, the rebar layers perpendicular to the direction of loading were lumped into a single steel fiber at the same distance from the element reference axis. To simulate the overturning moment, a rigid element was created that extends from the top of each wall pier to the location of the vertical jacks where the loads are applied.

The validation of DRAIN-2DX fiber element models for RC walls can be found in Kurama and Shen (2004). The cross-sections near the base of each wall pier and the coupling beam ends included confinement reinforcement (provided by the evenly spaced hoops). A concrete confinement model developed by Mander et al. (1988) was used to simulate this effect. A reduced actual effective value of 67% was assumed for the effectiveness of the moment steel across the pier base-foundation joint based on analysis of the actual UT Tyler experimental data – see Section 8.3 for parametric study.

8.2 DRAIN-2DX vs. ABAQUS

This section compares the two models that were created for the experimental model. This is necessary to validate the behavior of the models.

8.2.1 Load Displacement Response

Figure 8.5 shows the lateral load versus displacement history for the experimental test. The ABAQUS model reflects the as-built forces. The "DRAIN" line was created through analysis of the actual UT Tyler geometry and as-built initial cable forces with the assumed effectiveness of the moment steel crossing the base joint adjusted to the actual effective value of 67%. In contrast with the target model, this model used a force-controlled analysis with the prescribed loading history that was applied during the Tyler experiment in the three jacks.

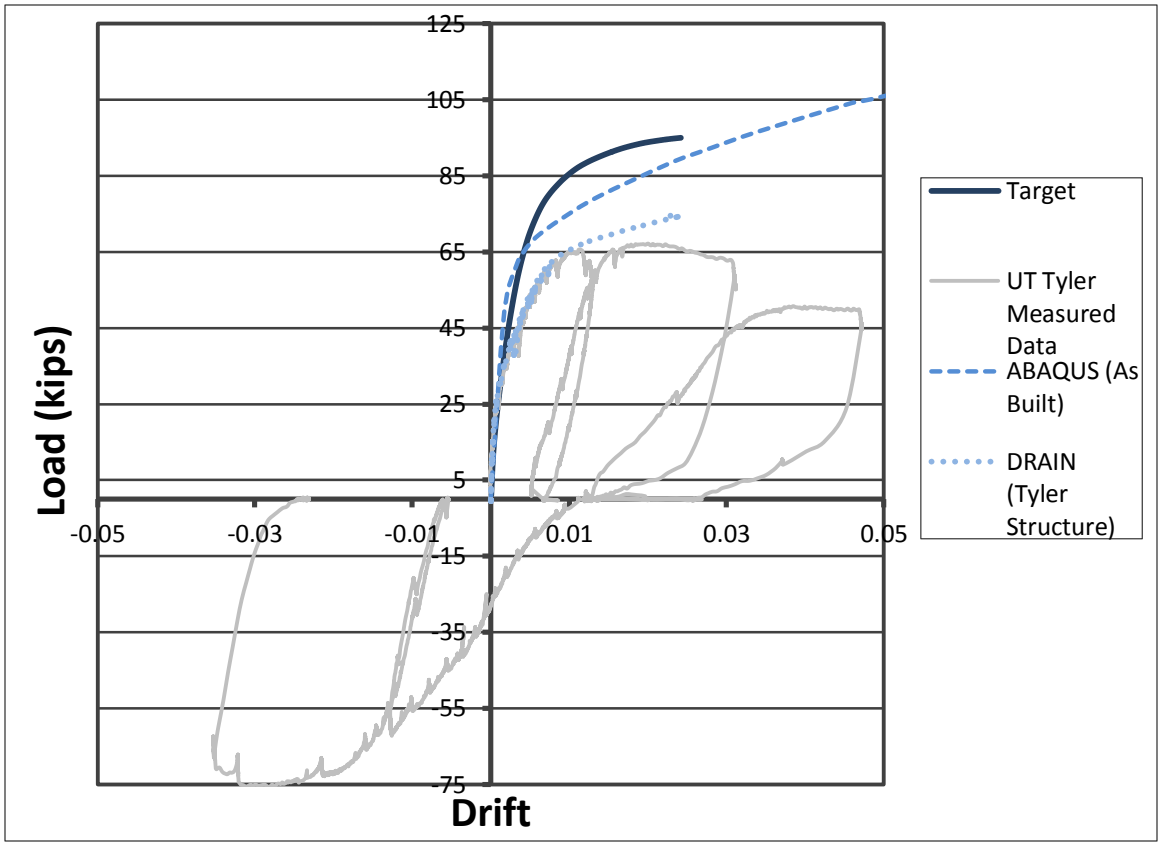

Figure 8.5: Load Displacement Response

8.2.2 Resultant Forces

Chapter 7 clearly demonstrates that the displacement behavior of the specimen is well predicted by the ABAQUS models. This section will show design quantities such as shear, moment, and axial forces of the various components of the system based on the validated ABAQUS models and the targeted values generated by DRAIN-2DX. First, values for the pier will be reviewed, and then the beams will also be considered. Forces in ABAQUS were calculated using the appropriate stresses from ABAQUS and multiplying them by element areas.

8.2.2.1 Piers

This section gives the moments generated by the applied lateral load as well as the shear and net axial forces at the tension and compression pier bases.

8.2.2.1.1 Base Moments

Figure 8.6 shows the tension pier base moment and Figure 8.7 gives the Compression pier base moment. The ABAQUS models and the target models show similar behavior in the moments. The As Built ABAQUS model has already been described. The Experimental ABAQUS model is similar except: the gravity forces are applied as pressures, and the lateral forces are those actually applied during testing. The 75% effective rebar model shows a closer performance to the DRAIN-2DX UT Tyler model because it only uses a 67% effective rebar. Details pertaining to the decision to use 75% rebar can be seen in the parametric study located in Section 8.3. The reduction in effective rebar also reduced the moment carried by the compression pier. Overall the tension pier appears to have a lower base moment than the compression pier.

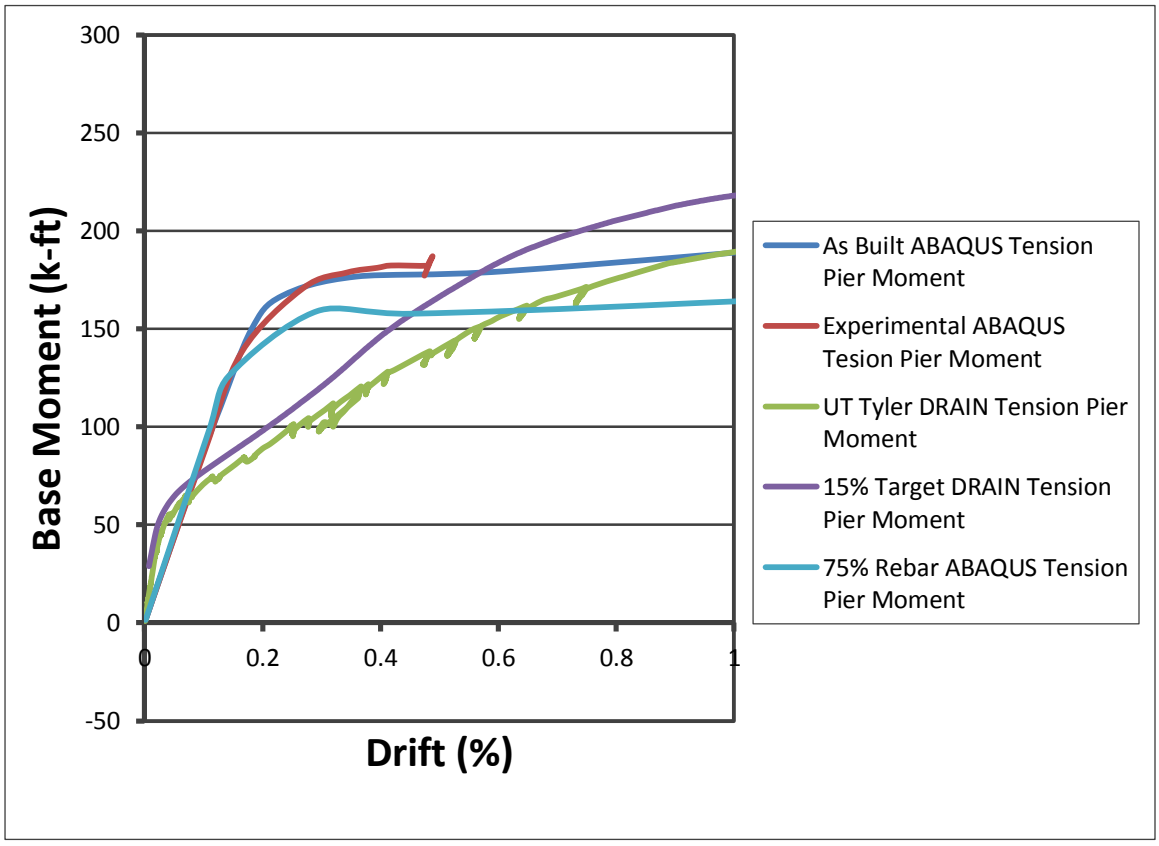

Figure 8.6: Tension Pier Moment ABAQUS DRAIN-2DX Comparison

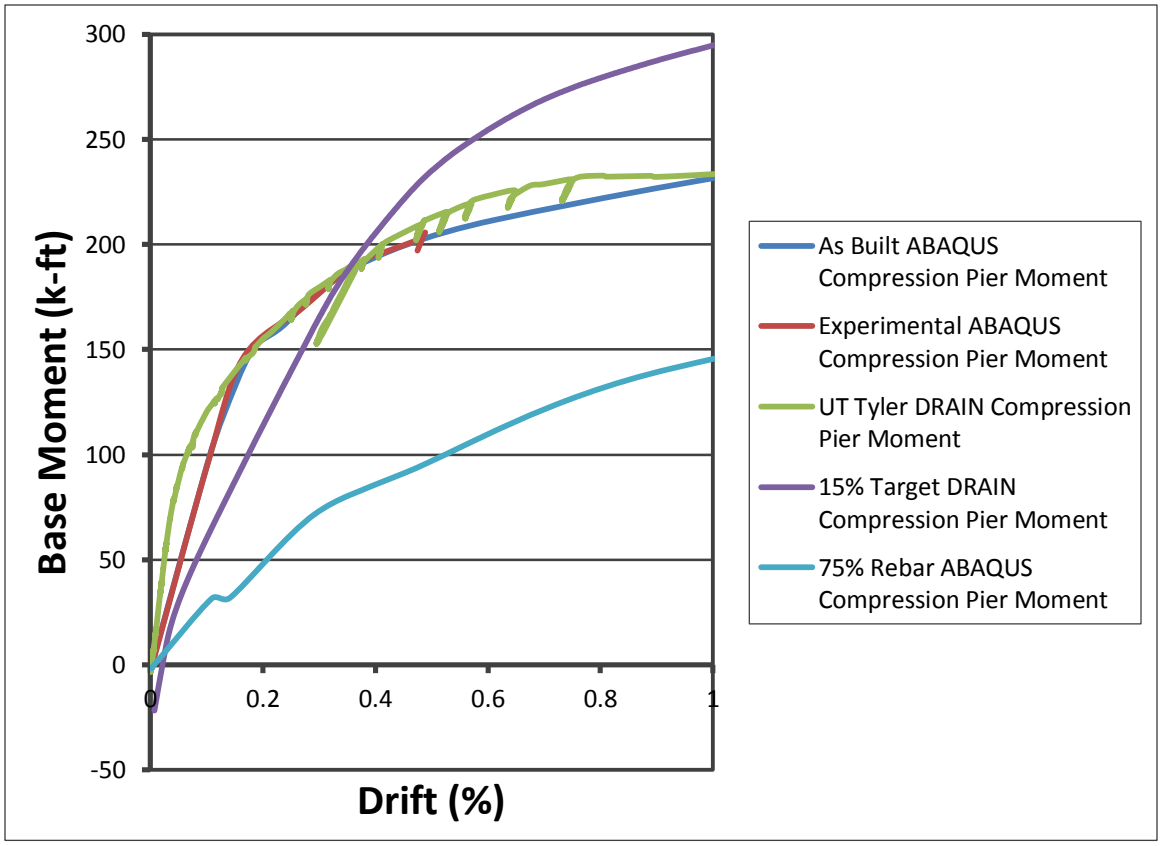

Figure 8.7: Compression Pier Moment ABAQUS DRAIN-2DX Comparison

8.2.2.1.2 Base Shear Forces

Figure 8.8 shows the base shear of the tension pier base and Figure 8.9 gives the base shear of the compression pier base. There is good agreement between the different models. Overall the compression pier resists most of the overall shear in the system.

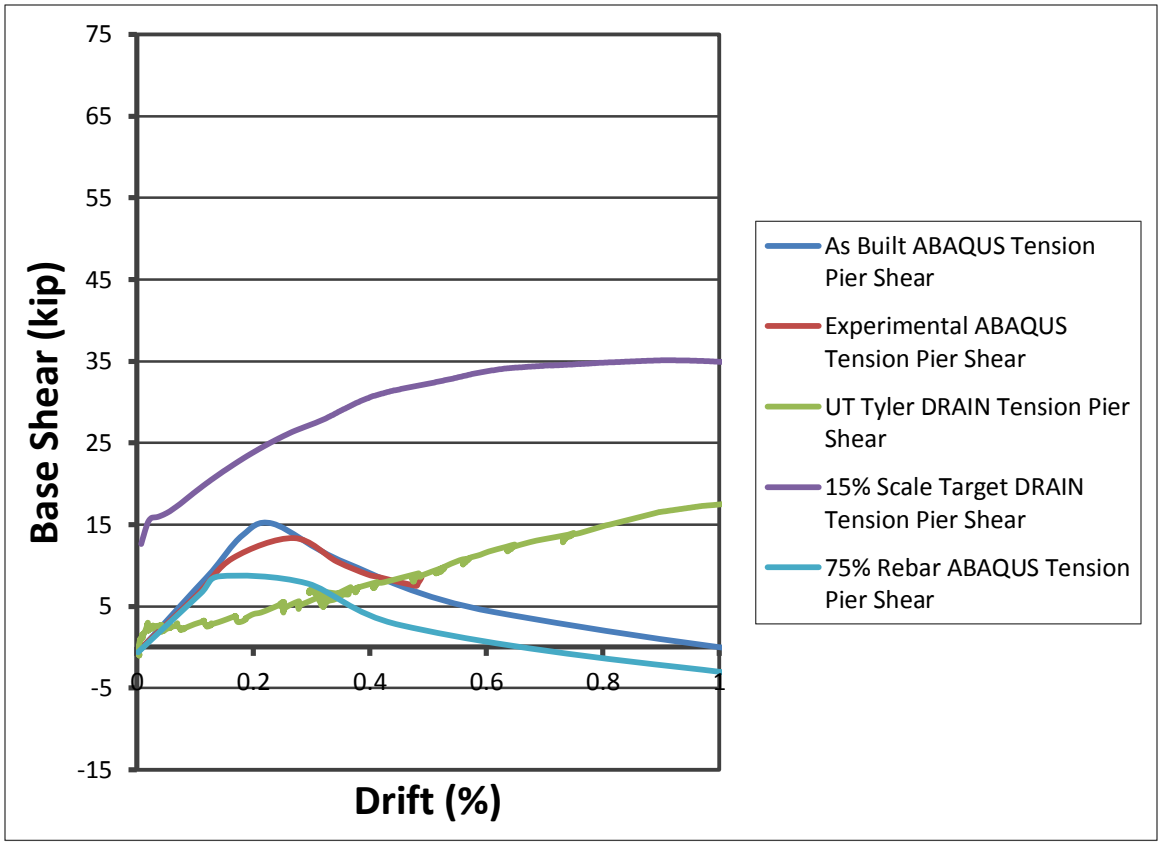

Figure 8.8: Tension Pier Shear ABAQUS DRAIN-2DX Comparison

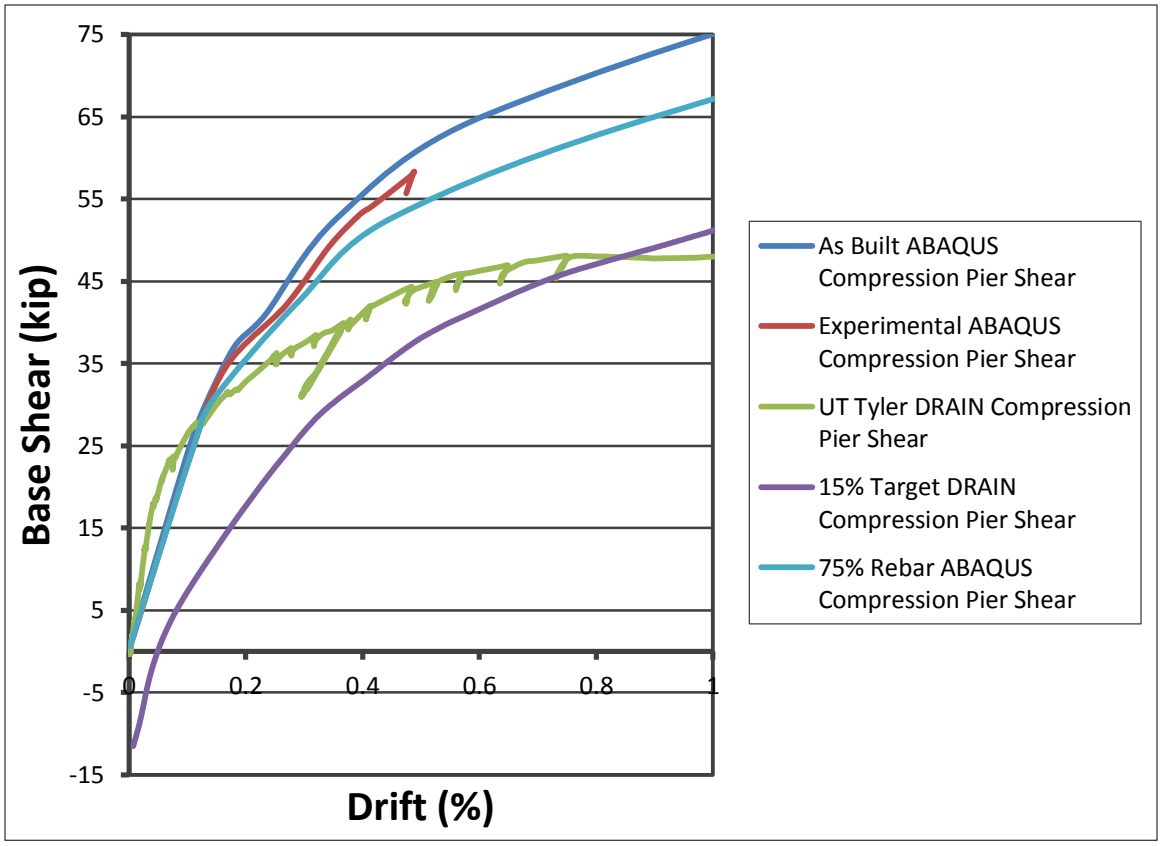

Figure 8.9: Compression Pier Shear ABAQUS DRAIN-2DX Comparison

8.2.2.1.3 Axial Forces

Figure 8.10 shows the axial forces in the tension pier base and Figure 8.11 gives the axial forces in the compression pier base. Trends in the results are similar for both pier bases. Overall the compression pier axial forces have much more significant compressive force.

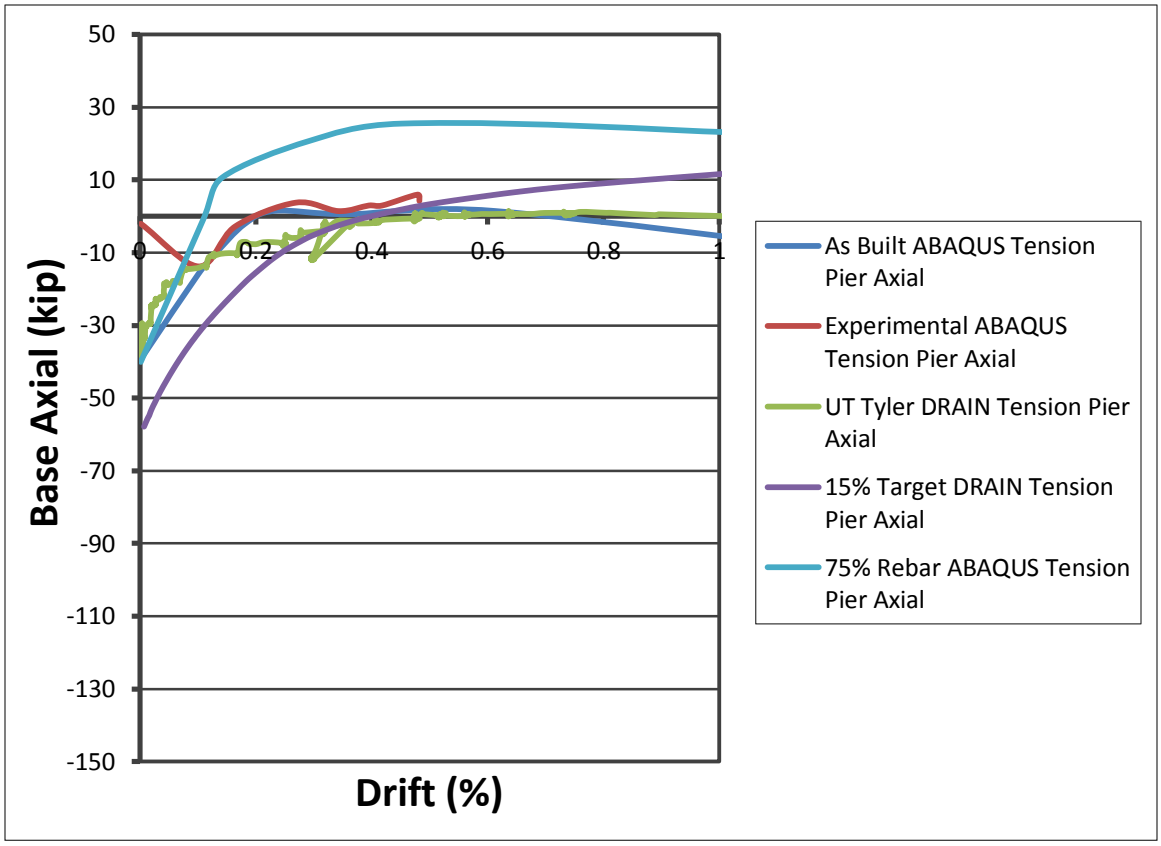

Figure 8.10: Tension Pier Axial ABAQUS DRAIN-2DX Comparison

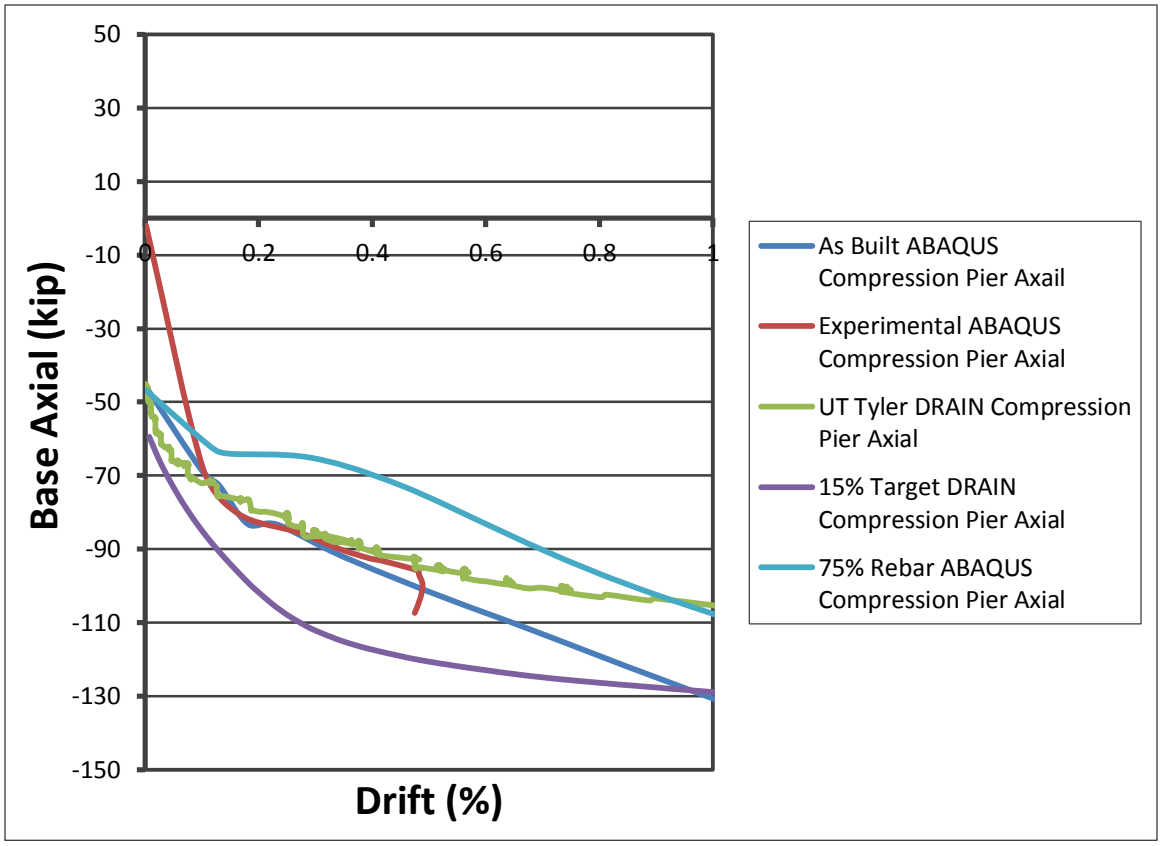

Figure 8.11: Compression Pier Moment ABAQUS DRAIN-2DX Comparison

8.2.2.2 Beams

This section gives the moments generated by the deflection in the piers as well as the shear and net axial forces in the 1st, 2nd, and 3rd story beams.

8.2.2.2.1 Moments

Figures 8.12, 8.13, and 8.14 show the beam end moments for the 1st, 2nd, and 3rd, beam stories, respectively. The predicted behavior in the moments is similar. The DRAIN-2DX model predicts that the 3rd story has the highest moment demand. The ABAQUS model shows that the three stories are very similar.

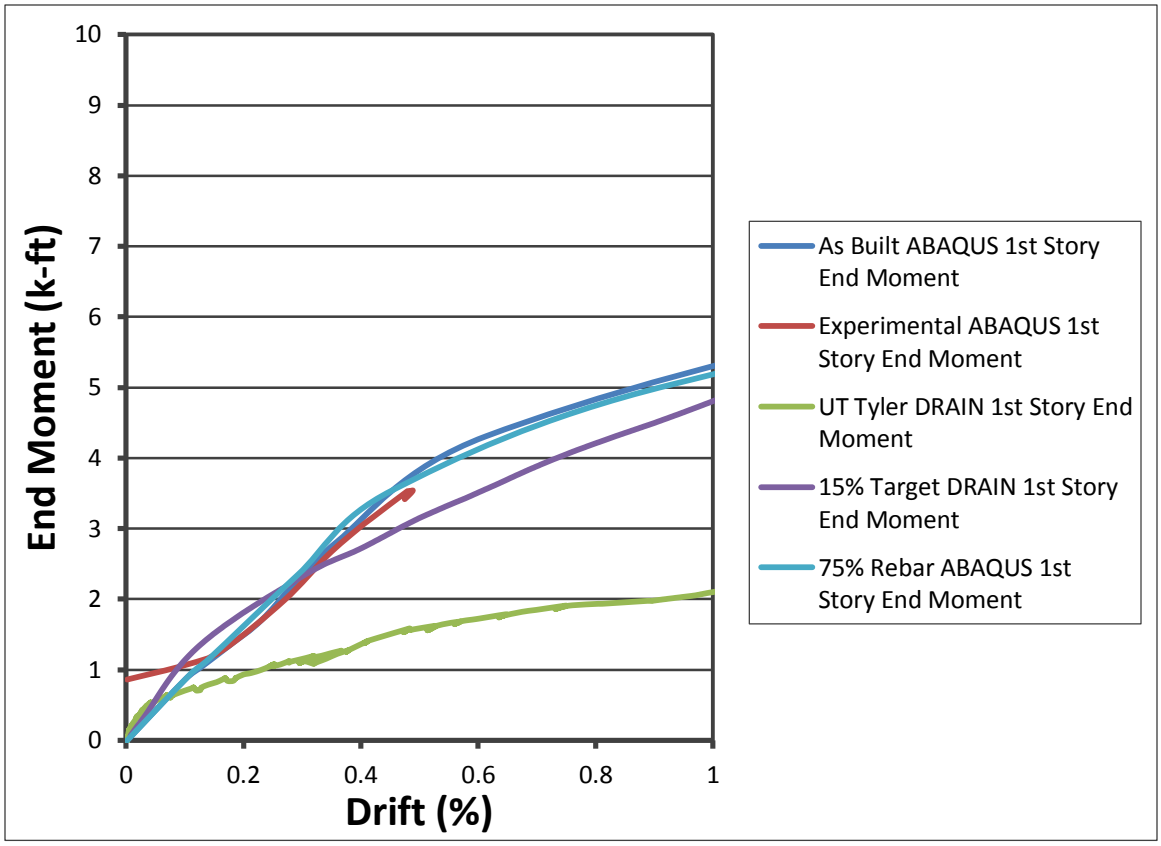

Figure 8.12: 1st Story End Moment ABAQUS DRAIN-2DX Comparison

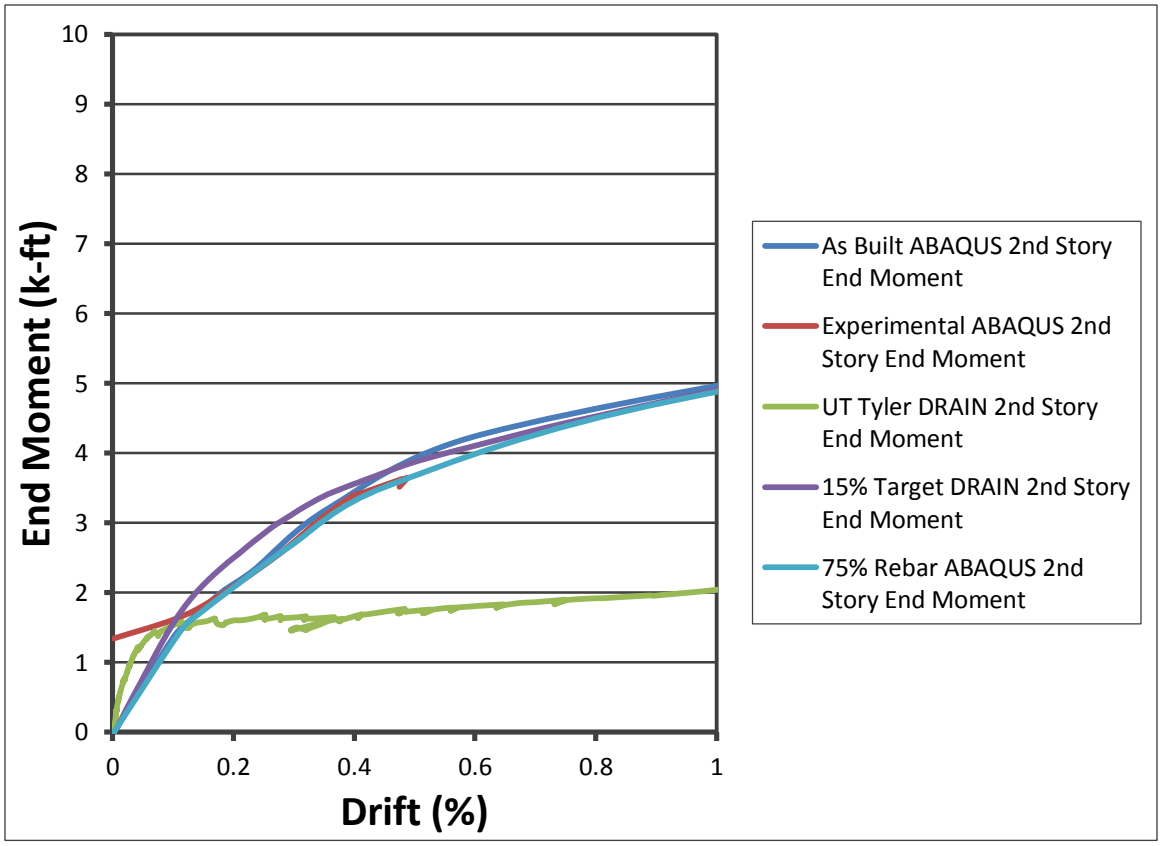

Figure 8.13: 2nd Story End Moment ABAQUS DRAIN-2DX Comparison

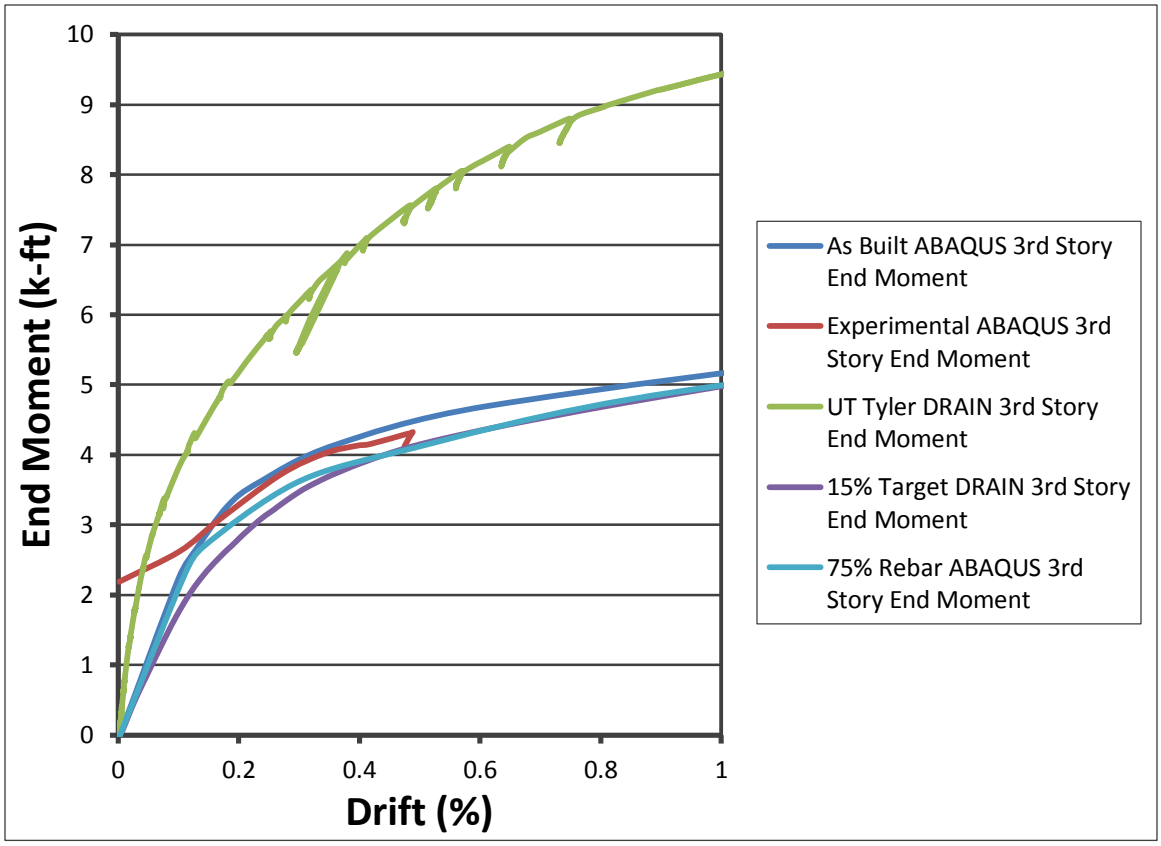

Figure 8.14: 3rd Story End Moment ABAQUS DRAIN-2DX Comparison

8.2.2.2.2 Shear Forces

Figures 8.15, 8.16, and 8.17 show the beam end shear forces for the 1st, 2nd, and 3rd, beam stories, respectively. The predicted behavior in the shear forces is similar. The DRAIN-2DX model predicts that the 3rd story resists the highest shear forces. The ABAQUS model shows that the three stories are very similar.

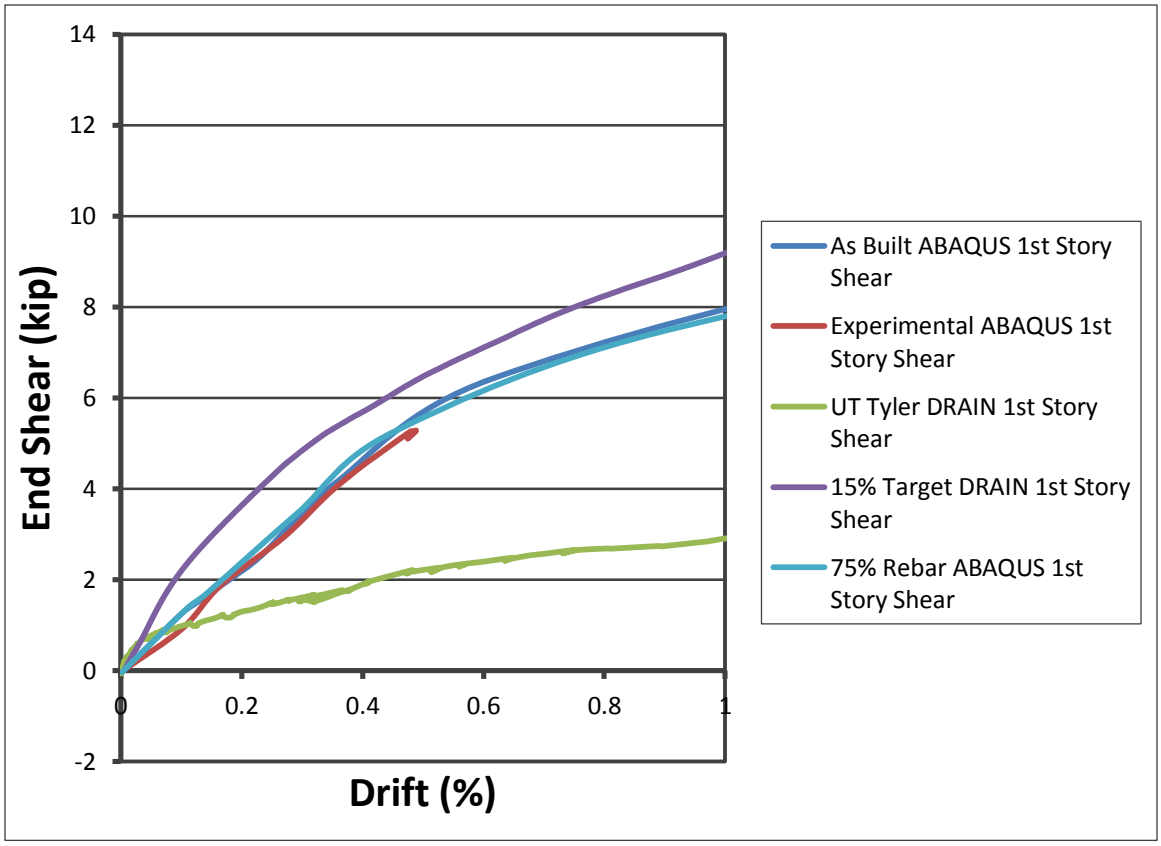

Figure 8.15: 1st Story End Shear ABAQUS DRAIN-2DX Comparison

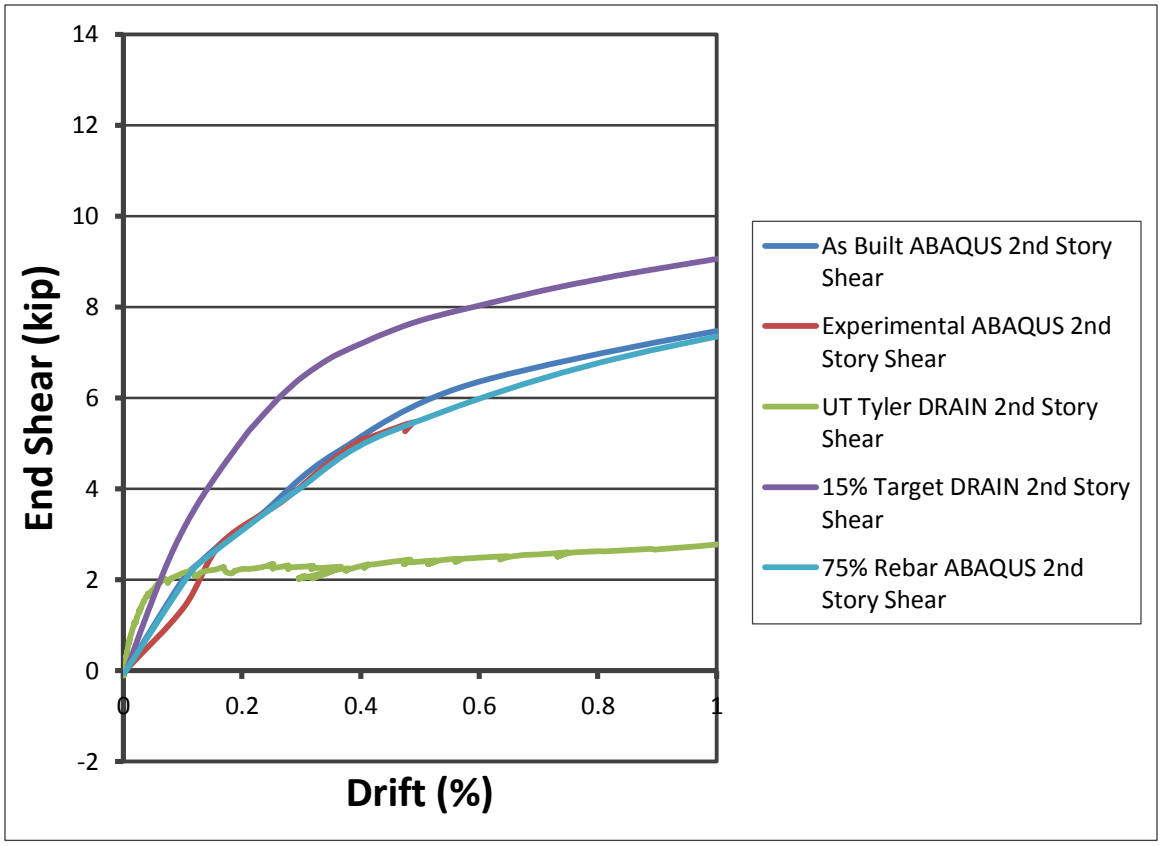

Figure 8.16: 2nd Story End Shear ABAQUS DRAIN-2DX Comparison

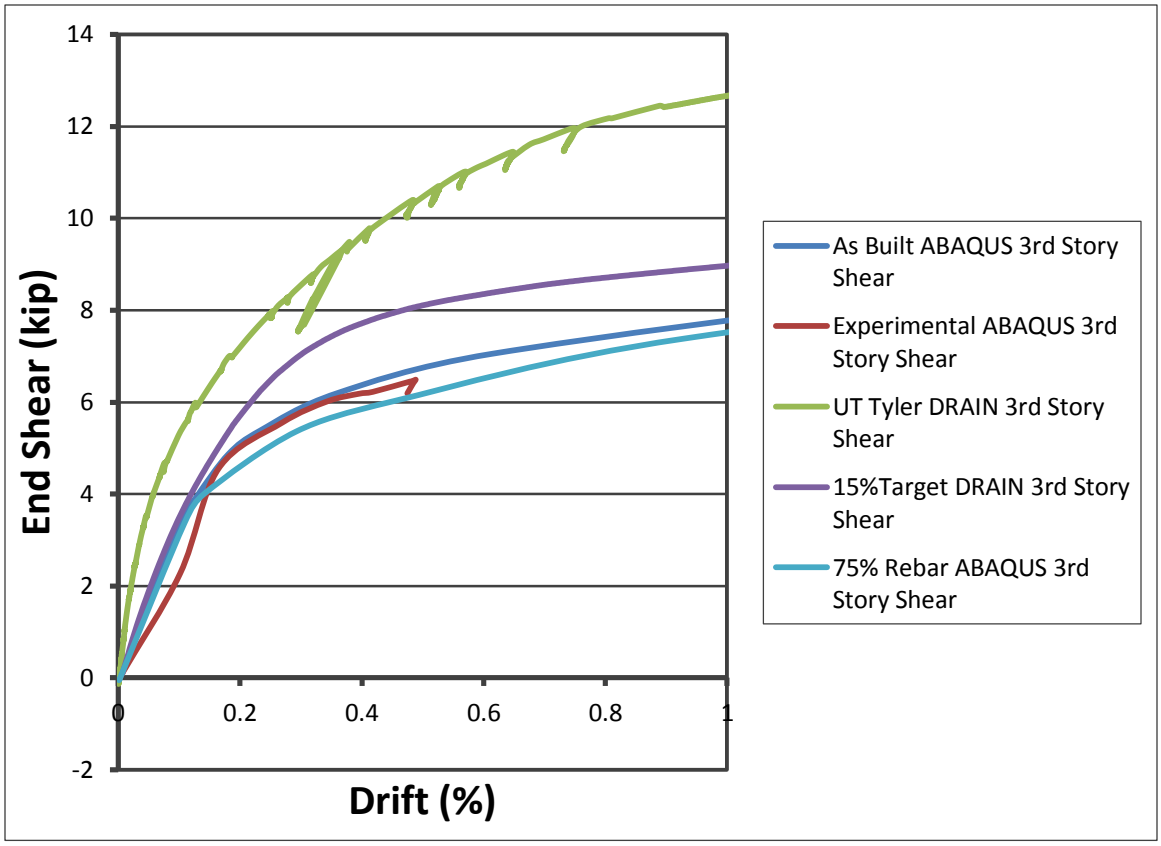

Figure 8.17: 3rd Story End Shear ABAQUS DRAIN-2DX Comparison

8.2.2.2.3 Axial Forces

The ABAQUS models were used to consider the axial forces in the beams at all three stories. Figure 8.18 shows the axial forces in each of the beam stories. The 3rd story has the greatest axial demand. This is consistent with the results reflected in Figure 7.59 (strain maps) and Figure 7.54 (axial elongation). Figure 8.19 shows the forces in the post-tensioned cables verses drift for each beam story according the ABAQUS As Built model.

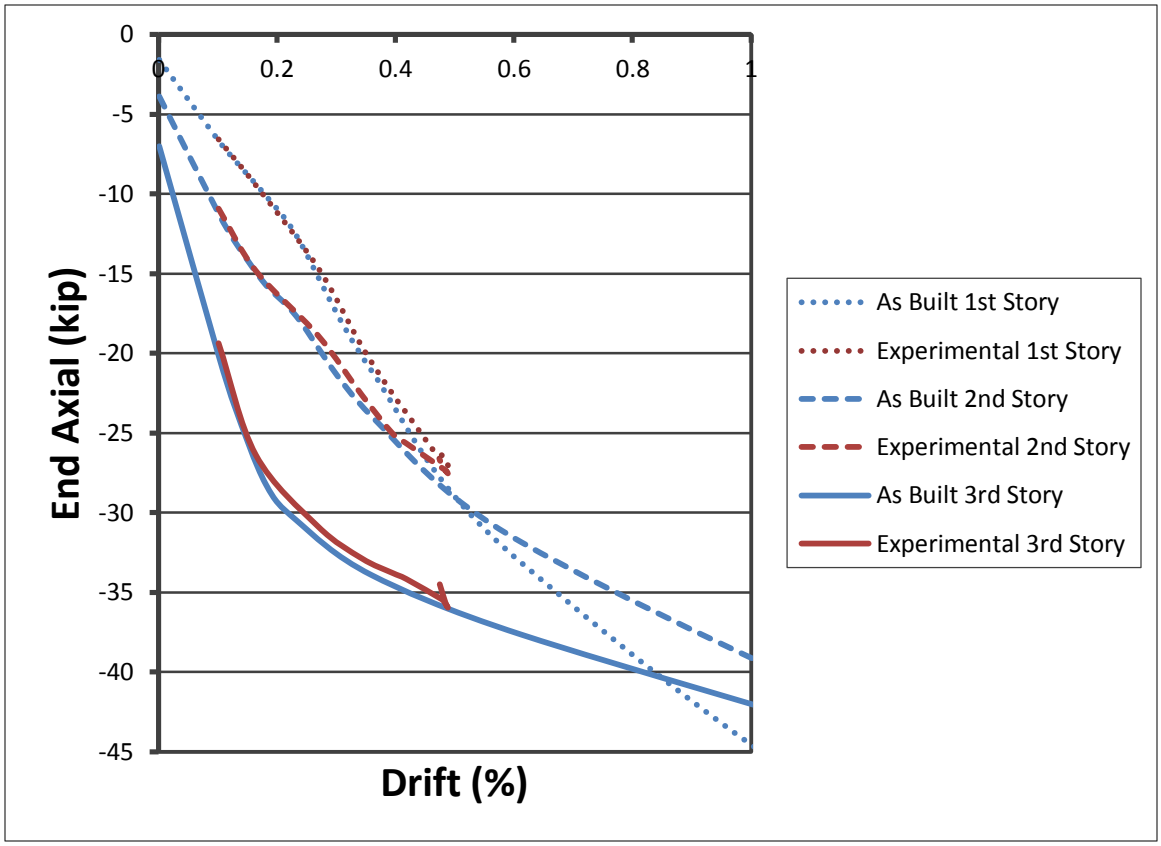

Figure 8.18: Axial Forces in Beams

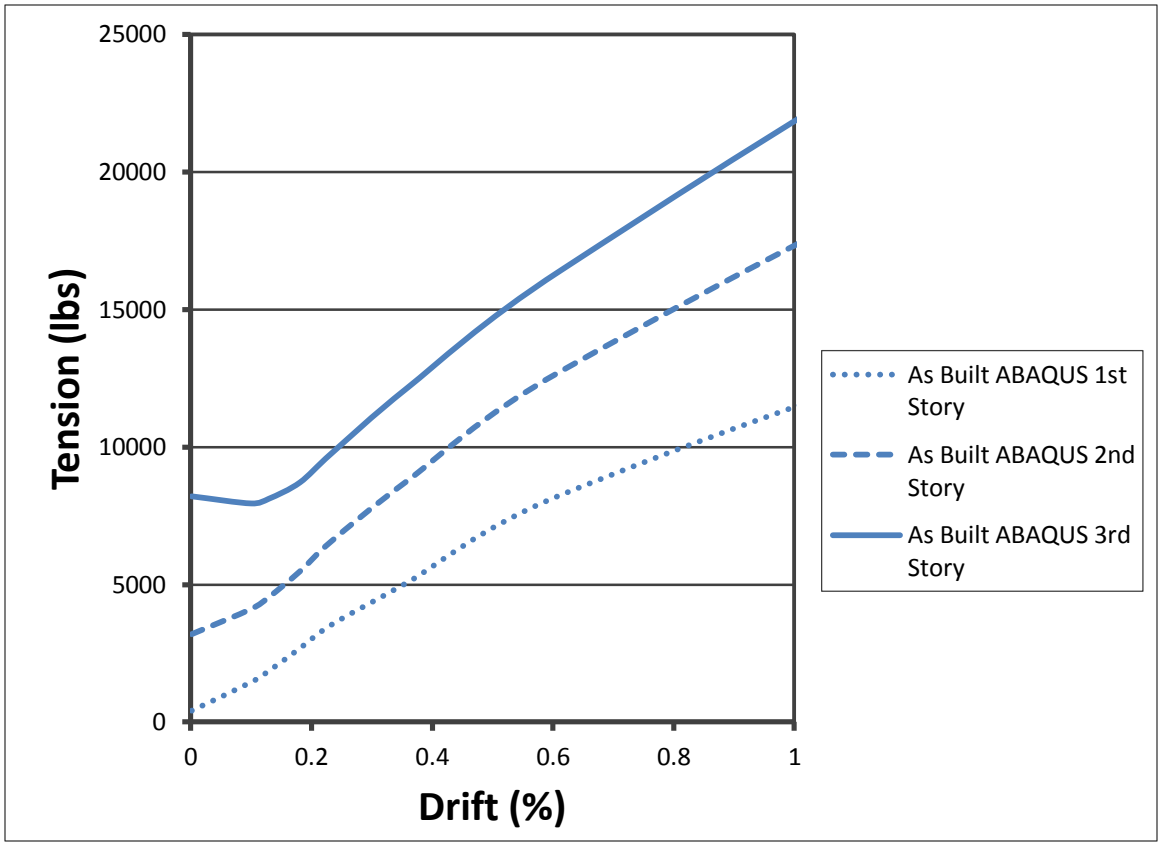

Figure 8.19: Tension Forces in Post-Tensioned Cables

8.3 Parametric Study (ABAQUS)

After a preliminary comparison of the deformation behavior of the 15% scale model to the target behavior, the initial stiffness of the test structure matches predictions, but the tested structure did not achieve the strength predicted in the target and ABAQUS lines. The disagreement in the values was greater than was realistic error. In order to determine if the behavior could be explained by some difference in the target building and what was actually constructed, a parametric study was conducted by altering one variable by different percentages. The parameters that were analyzed were: force in the post-tensioned cables that run through the center of each beam, force in the gravity cables that were anchored to the foundation, and the strength of the rebar cast in the piers and embedded in the grout sleeves which were cast in the foundation. Each parameter was

reduced to 75%, 50%, 10% and 1% in the ABAQUS model for comparison purposes. The comparison can be seen in the following sections.

8.3.1 Post-Tension Beam Force Variation

For this variation, the force in the prestress cables that support the coupling beams at the floor levels was varied to 75%, 50%, 10%, and 1% in the ABAQUS model. The graphical comparison can be seen in Figure 8.20. Based on the specimen's displacement behavior in the varied ABAQUS models, the force that is applied in the prestress cables does not greatly affect the results. The maximum % difference in the force necessary to achieve 0.05% drift is 2%. Because of this, the difference in the as built and designed models' applied forces cannot account for the disagreement in the strength predictions.

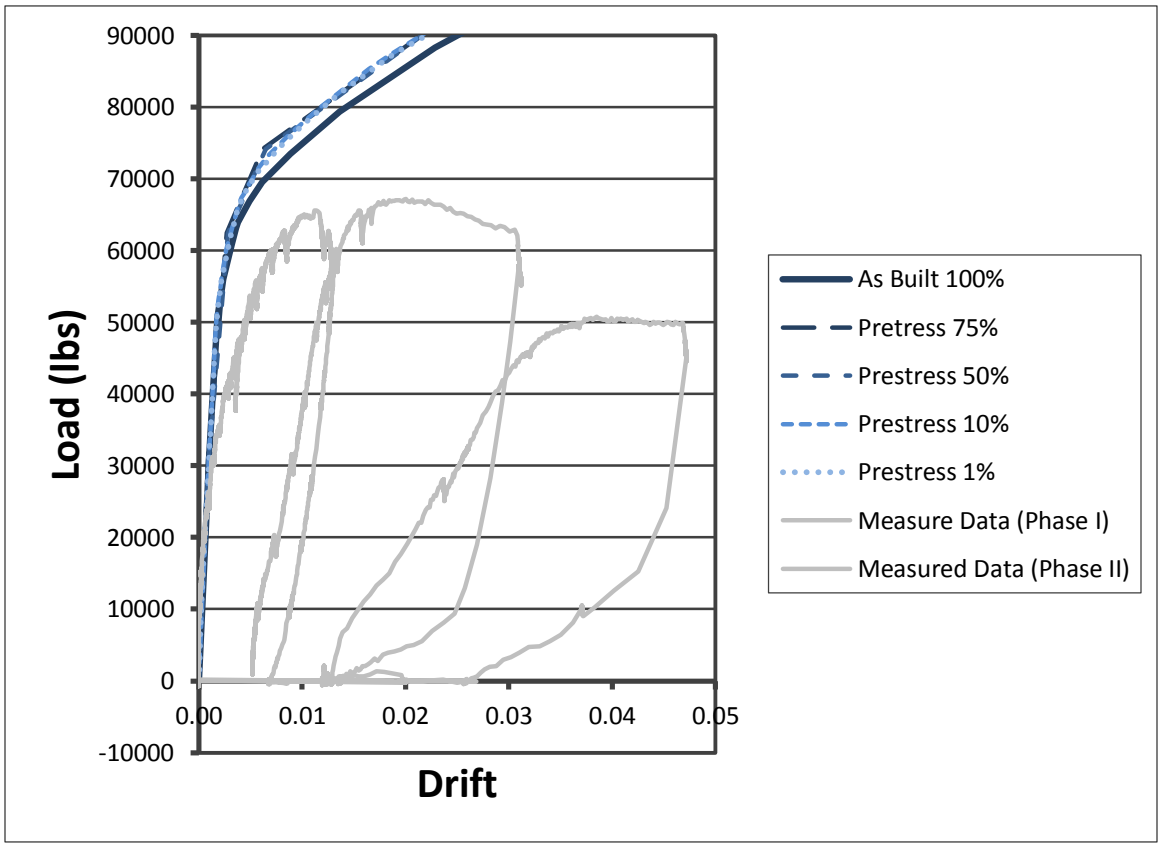

Figure 8.20: Post-Tension Beam Force Variation

8.3.2 Gravity Force Variation

For this variation, the force in the prestress cables that simulate the gravity forces from the upper stories on the bottom three stories was varied to 75%, 50%, 10%, and 1% in the ABAQUS model. The graphical comparison can be seen below in Figure 8.21. Based on the specimen's displacement behavior in the varied ABAQUS models, although the force that is applied in the gravity prestress cables has more significant affect that the variation of the prestress cables that support the coupling beams at the floor levels, it also does not affect the results to the degree that would account for the disagreement in the strength predictions. The maximum % difference in the force necessary to achieve 0.05% drift is 7%.

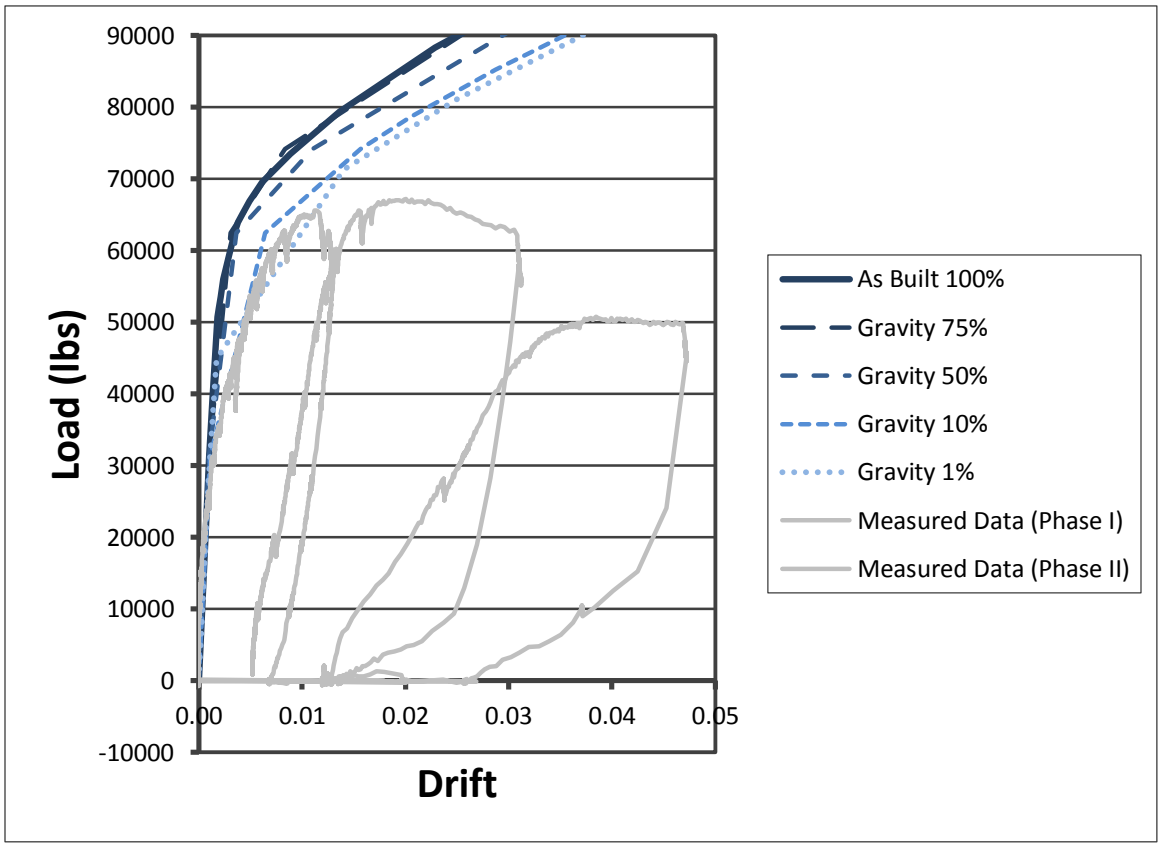

Figure 8.21: Post-Tension Gravity Force Variation

8.3.3 Rebar Embedding Variation

Figure 8.22 shows ABAQUS results varying the assumed effectiveness of the moment steel crossing the base joint by 75%, 50%, 10%, and 1%. The initial slopes and strengths of the 75% curve match portions of the measured results, indicating that this is the most likely explanation for the low strength of the test structure. The percent difference at 0.05 drift can be seen in Table 8.3.

Table 8.3: % Change in Force Necessary to achieve 0.05 Drift

% Variation in Rebar	100%	75%	50%	10%	1%
Force to achieve 0.05 drift	106222.5	96198.75	88572.50	76232.50	71001.25
Difference (lbs)	0	10023.75	17650.00	29990.00	35221.25
% Change	0	9%	17%	28%	33%

It is believed that the bars grouted into the anchors in the foundation pulled out at a relatively low load, although these couplers were Type II seismically rated. Detailed inspection of these joints shows that this conclusion is accurate, one of the #6 inside edge embedded rebar and one of the #7 outside edge embedded rebar were hand loose and two more #7 outside edge embedded rebar were able to be pulled out under stronger loading. The #6 bar was easily removed from the tension pier (Phase I and II) and the two loose #7 bars were also in the tension pier (Phase I and II). There was one loose #7 bar in the compression pier (Phase I and II).

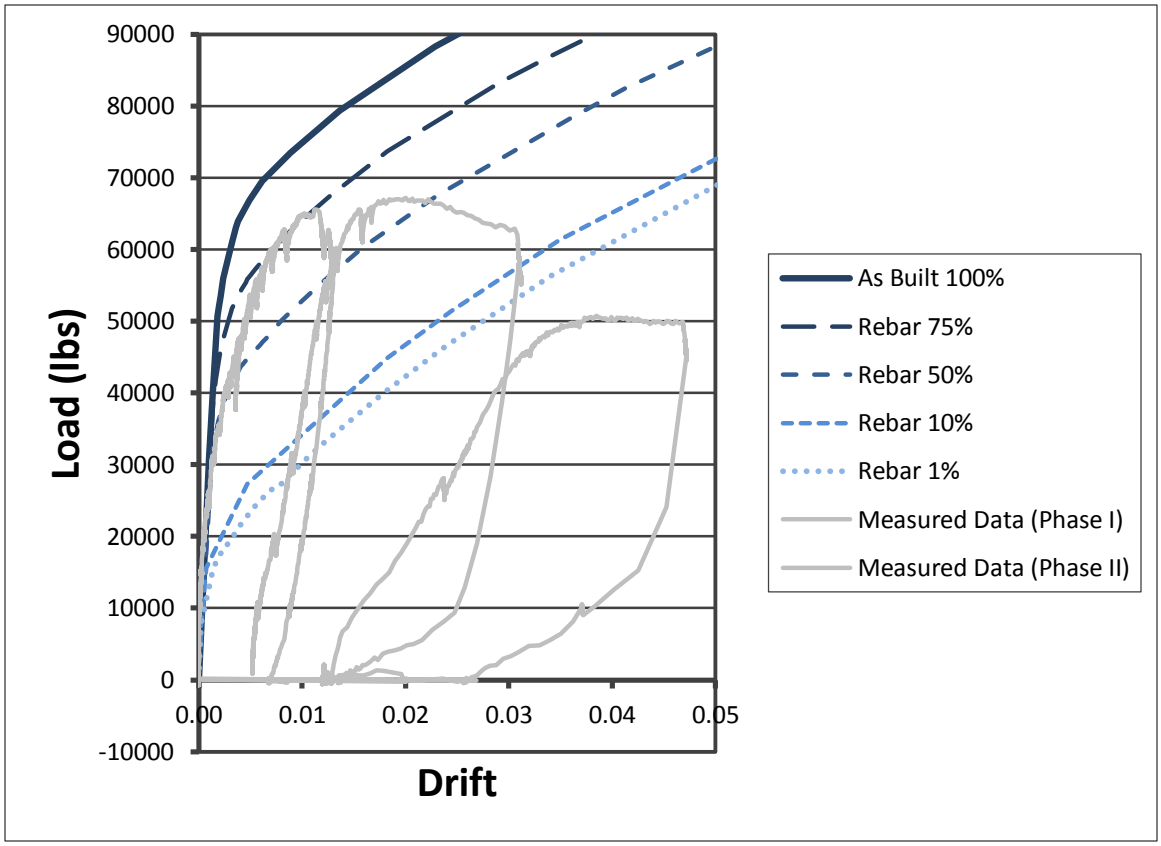

Figure 8.22: Rebar Embedding Variation

8.4 Finite Element Analysis Conclusions

The design procedure for the post-tensioned coupled wall system yielded a structure that performed as expected, and the analytical models yielded predictions in good agreement with measured behavior. Notwithstanding the limitations of the constructed specimen, the structure was scaled appropriately.

The following conclusions about the ABAQUS model are made:

- The deformations presented in Chapter 7 correlate well between the measured DIC data and the ABAQUS model results.
- The ABAQUS model and DRAIN-2DX model response quantities (pier base moment, base shear, and axial forces, beam end moment, end shear, and axial forces) match reasonably well, given the simplicity of the ABAQUS model,

especially considering the elastic-plastic behavior of the concrete material properties.

- The ABAQUS model appears to provide a reasonable alternative for preliminary design and behavior characterization, given its relative simplicity. This data set is now available for calibrating more complex coupled wall system models.
- Error in the pretensioning of the gravity cables and the beam story cables likely had little effect on the structure's response.
- The effectiveness of the moment steel crossing the foundation pier joint greatly affects the behavior of the coupled wall system. This is the greatest contributing factor to the difference between measured and expected results.

CHAPTER 9: CONCLUSIONS AND RECOMMENDATIONS

9.1 Summary

A 15% scale structure, based on a prototype coupled wall system using post-tensioning was designed and constructed. The scale structure was then tested to determine the structural behavior of the specimen. During testing, four DIC systems were simultaneously deployed to monitor the specimen, collecting the greatest amount of data possible from every iteration of the test. It is believed that this test represents the first instance of four DIC systems being deployed simultaneously as part of a building structure test. The data collected from the DIC systems and other traditional data collection systems were compared to validate the data. Furthermore, the data was further validated using finite element analysis, corroborating results and structural behavior.

This thesis presents the first ever physical model testing of a multi-story reinforced concrete coupled wall system that is coupled with post-tensioned beams. A significant advantage to this technology is the simpler detailing of the coupling beams used in this system. There are many positive consequences of the simplified detailing of the beams; the major four being:

- An improved constructability when compared to the traditional reinforced concrete coupling wall system.
- A decrease in overall cost to design and construct coupling beams for the system.

- Less material is required in the detailing of the coupling beams with adequate resistance and strength for resisting seismic loading.
- An additional result of less material use is a decrease in the environmental impacts of the construction of the coupling beams.

Some other advantages of the system discussed in this thesis are: the technology of post-tensioning cables is already used in construction and has previously been explored; this type of coupling is embedded in the shear walls and therefore can be used for retro fitting existing buildings; the damage can be contained to the toes of the beams which may allow for the preservation of buildings; and the system has self-centering capabilities that can be beneficial after a seismic event.

The structural behavior of the coupled wall system is documented in Chapter 7. Section 9.2 dictates some best practices for DIC learned from testing multiple DIC systems. Section 9.3 provides conclusions and recommendations. Section 9.4 describes future work to be conducted at Lehigh University.

9.2 DIC Best Practices

Although DIC is a very useful measurement technique, many practical aspects and complications only arise through experience. Through the experimentation and data collection conducted during this test, three effective practices emerged. Along with these practices, a basic checklist was developed for consideration of deployment of multiple DIC systems.

The DIC data from the test was not extremely clear for the beams from any FOV because of the size of the beams and the relative size of the FOVs that included the beams. In order to gather more detailed data for the beams, a FOV that only includes one

beam, or portions of one beam, depending on the size of the beam, is suggested for future monitoring of coupled wall systems.

Though it was not a major issue during this test, manually commanding each DIC system to capture an image from each of the computer systems can be cumbersome in combination with monitoring other traditional methods of measurement. In order to simplify the collection of information in the DIC systems, it is suggested that a program be created to control all DIC systems in order to capture an image in one command.

The 2D-DIC systems (Systems 2 and 3) were able to be verified as having little out-of-plane error based on the 3D-DIC system (System 1) out-of-plane movement at the base. It is strongly suggested that any area being considered for 2D-DIC systems have the out-of-plane movements be investigated prior to testing. If the predicted out-of-plane movements are large, then it is recommended that either a 3D-DIC system be used to monitor that area, or a different area with small out-of-plane movements be used to collect the data of interest. Since unintended out-of-plane movements may arise in testing of all but the simplest structures, a way to monitor these motions (with string potentiometer, LVDT, 3D-DIC system, etc.) should be included in the data acquisition plan if a 2D-DIC system is to be used.

The DIC checklist can be broken into three basic categories: planning, metadata, and other considerations. The planning portion includes some of the aspects of the experiment that should be considered while planning the layout and set up of an experiment with multiple DICs. The metadata section includes the information that should be collected which describes or pertains to the measured data, its collection system, or organization of data. This type of metadata is more specifically defined as

structural metadata: information about the design and specification of data structures, sometimes called data about the containers of data. This information is imperative to the interpretation of the collected data. The post-processing section includes the considerations of organizing the data from testing for optimal use.

PLANNING

- Camera Locations should be considered.
    - Location of cameras must not allow for a walkable path between the camera system and the object of interest. This prevents a person from walking in front of a camera while an image is being taken.
    - System must remain stationary: no contact after calibration is optimal.
        - Attaching the camera system to a stationary object, such as a column in a lab, is recommended.
        - All cords attached to the camera system must be secure and away from any walkable path.
        - If using a sensor that has an image capture on the camera, do not touch the camera during testing, use a control cord instead.
- Conduct calibration procedure after the camera system has been placed with the calibration tool located at the specimen.
- Pattern sizes should be considered.

    - Different sensors produce different precisions. This can cause an issue with the size of pattern used. Check a test pattern size using a temporary pattern on the object of interest or on a removable slip on the surface of the object.
    - The field of view being used can also cause problems with the size of pattern; again, a test pattern size should be checked before the final pattern is applied to the object.
- Lighting is a crucial part of DIC data collection. If the images are too dark or bright, areas of data can be lost. Each camera system should be checked for lighting. After each system has lighting, they should all be checked again because of the possible interaction between lighting. Although natural light is the best for little glare with good light, its variability can cause loss of data during testing.
- Camera control (computer) locations are particularly important if manual command of each system is used. They must be easy to access in order to collect data from all locations at approximately the same time.
- If an area has been determined to be appropriate for a 2D system, a secondary verification system must be present in order to confirm that the data collected by the 2D system is not skewed by out-of-plane movements.

METADATA

- The field of view for each system, as well as the calibration outputs for each system needs to be recorded.

- A photograph of each camera set up in relation to the structure should be taken and retained for later review.
- Detailed descriptions of each stage taken are essential. These descriptions should include any loads applied, any unpredicted behavior, and any other information that could help identify a specific stage.
- Camera type and pixel density should be recorded in order to determine strain gage lengths used in strain calculations conducted by the software.
- The type of system, 3D or 2D, is key to interpreting data.
- If a 2D system is used, its calibration information should be recorded, or a gauge length must be defined in the calibrated area and the measured length recorded for later calibration.
- File organization is crucial. A system should be created in a logical manner in which any project is easily accessed. The names of files should clearly describe the information contained within, and updated or copied files should be labeled as such.

POST-PROCESSING

- In order for the data collected to be clear in its presentation, all systems should be translated to the same coordinate system. By doing this, the data can be easily compared, irrelevant of its source.

9.3 Conclusions and Recommendations

The following major conclusions are made based on the results presented herein:

- The 15% scaled model behaved as expected and showed some of the anticipated benefits of a coupled wall system (in particular some self-centering, and damage limited primarily to beam and pier toes).
- It is possible to coordinate multiple digital image correlation systems simultaneously, and use data collected from multiple systems interactively.
- The relatively simple modeling tools that were employed appear to capture the system behavior well.
- There are several limitations of the current experimental setup, the three major being:

  (1) Scaling the specimen meant that C-shaped walls became rectangular shaped, the slabs at the floor levels and energy dissipation steel in the coupling beams could not be included;

  (2) The forces in the beam post-tensioning cables were less than as designed, and

  (3) The tension reinforcement necessary to resist the base moment in each of the piers pulled out of the structural couplers in the foundation at lower than the design load.
- A detailed data set characterizing the deformations of all the elements of a multi-story coupled wall system has been presented and is available for use in calibrating more complex models.

In each of these areas, the following additional conclusions are noted:

SYSTEM BEHAVIOR

- The design procedure for the post-tensioned coupled wall system yielded a structure that performed as expected, and the analytical models yielded predictions in good agreement with measured behavior.
- As expected, the neutral axis depth decreased as the drift of the system increased. However, the measured results indicate that the tension pier does not necessarily have a smaller neutral axis depth for the duration of the test. This is believed to be caused by the rebar pull-out at the foundation-pier joint which could have occurred unequally or at different loads in the two wall piers.
- The curvature in the piers due to axial elongation in the beams is illustrated through the deflected shape profile.
- The strain maps generated by the DIC showed that for phases I and II tension cracking occurred in the tension (West) pier while shear cracking was shown in the compression (East) pier. For phase III, the strain maps showed tension cracking in both piers due to existing cracks in the tension pier (West) from the previous testing phase.
- The strain maps generated by the DIC were also able to validate the use of the 2D-DIC systems at the bases of the piers by establishing small out-of-plane movements.
- When considering drift, the results for gap openings correlate well with the numerical model generated by ABAQUS.

- The deflected shape of the beams at all stories show little to no curvature; the system is dominated by rigid body movement.
- In the experiments, the axial elongation of the beams was similar in phase I and phase II for all three stories. In phase III, the 3rd story beam elongated significantly less than the other stories.
- The foundation did not contribute to rotation, slip or uplift during the test.

MULTIPLE DIGITAL IMAGE CORRELATION

- The use of multiple DIC systems provides a much larger supply of information about the specimen and helps to better establish its overall behavior.
- Because the data was collected the same time for each system, the information from more than one system can be used to calculate a single parameter.
- This data could not have been captured so easily or at all with traditional measurement techniques. A single DIC system could not have captured enough data to establish the behavior of the specimen. This test could only realistically have been conducted using multiple DIC systems.

ANALYTICAL MODELING

- The simple ABAQUS model created appears to provide reasonable results as it matches the experimental deformation data well; matches the more complex DRAIN-2DX model reasonably.
- The amount of angular gap opening at the beam ends was consistent with the predicted angular openings produced by the ABAQUS model.

- The deformations presented in Chapter 7 correlate well between the measured DIC data and the ABAQUS model results.
- The ABAQUS model and DRAIN-2DX model response quantities (pier base moment, base shear, and axial forces, beam end moment, end shear, and axial forces) match reasonably well, given the simplicity of the ABAQUS model, especially considering the elastic-plastic behavior of the concrete material properties.
- The ABAQUS model appears to provide a reasonable alternative for preliminary design and behavior characterization, given its relative simplicity. This data set is now available for calibrating more complex coupled wall system models.
- The ABAQUS deflected shape of the beams at all stories also show little curvature; the center lines of the deflected shapes are essentially straight. As with the pier deflections, the values did not correlate well with the ABAQUS model at similar applied lateral loads, but when compared according to drift, the behaviors were comparable.
- Error in the pretensioning of the gravity cables and the beam story cables likely had little effect on the structure's response.
- The effectiveness of the moment steel crossing the foundation pier joint greatly affects the behavior of the coupled wall system. This is the greatest contributing factor to the difference between measured and expected results.

SYSTEM LIMITATIONS

- Because of the limitations, the specimen did not reach expected design load of coupled wall system. Notwithstanding, the structure was scaled appropriately.
- When considering the rotations of the pier bases during the test, it is clear that the expected rotations, even when comparing drift, are much smaller than the measured rotations. This is potentially due to the rebar in the base of the piers pulling out of the foundation during testing.
- The issue of rebar pull-out can be avoided completely by casting the entire system at the same time rather than casting separately and grouting the wall piers into place.
- While post-tensioning the cables in the system, the cables in the beams were post-tensioned consecutively and therefore the force in the cables that were post-tensioned first decreased as the others were put into tension. To address the first problem, depending on the type of machine used for post-tensioning, it is recommended that a pressure measurement device be applied to the machine so that the tension applied can be monitored during application.

9.4 Future Work

Construction of the first of two 40%-scale physical laboratory specimens is currently underway at Lehigh University. These laboratory specimens will include the first three floors, tributary slabs, and foundations of the prototype coupled core wall, representing the most critical regions of the structures. The other (less critical) regions of

the structures will be simulated in the computer, resulting in a hybrid physical-computational research platform. The term hybrid has come to mean many things in engineering; in the case it refers to the combination of computer simulation and physical testing. The forces and displacements from the computer model will be applied to the physical structure using a total of 7 actuators and 4 gravity jacks, simulating the behavior of the upper 5 stories of the 8-story building. Figure 9.1(a) shows a three-dimensional rendering of the 40%-scale experimental setup in the laboratory, while Figure 9.1(b) illustrates the construction progress on the first specimen.

The 40% scale specimen will be monitored at multiple locations with two- and three-dimensional digital image correlation (DIC) on selected faces of the walls, beams, and floors to gather full-field surface deformation data during the tests (McGinnis et al. 2011). Ultimately, the results of the 15% and 40% studies are expected to lead to the development of validated design procedures and modeling/prediction tools for the new system.

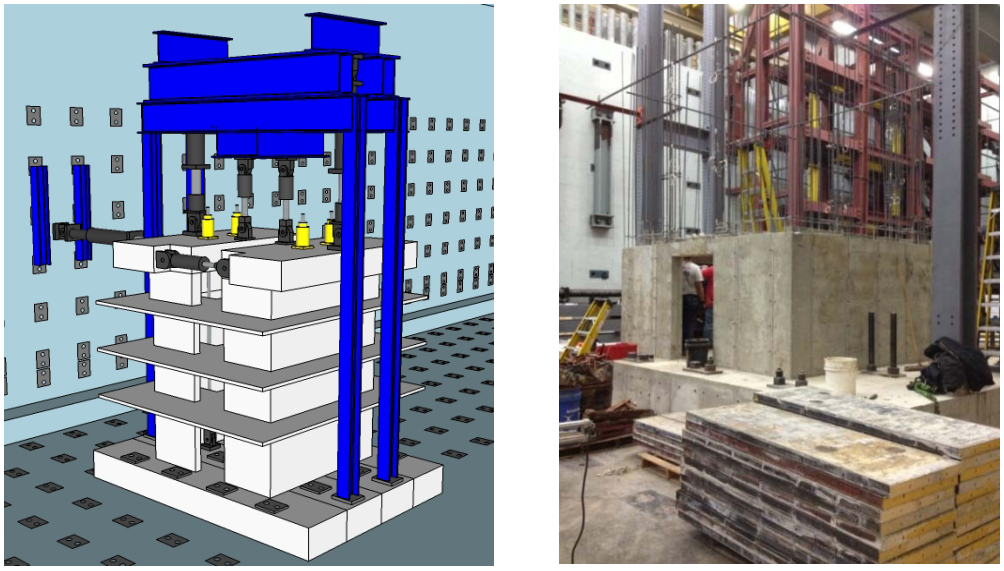

(a) (b)

Figure 9.1: 40% Scale Experimental Setup: (a) 3D Rendering; (b) Construction

REFERENCES

Barney, G., Shiu, K., Rabbat, B., Fiorato, A., Russell, H., and Corley, W., (1978) "Earthquake Resistant Structural Walls – Tests of Coupling Beams," Construction Technology Laboratories Report, Portland Cement Association.

Beghini, M. (2000). "Analytical Expression of the Influence Functions for Accuracy and Versatility Improvement in the Hole-Drilling Method," *Journal of Strain Analysis*, 35, (2), 125-135.

Bing, P., Hui-min, X., Bo-qin, X., Fu-long, D. (2006). "Performance of Sub-pixel Registration Algorithms in Digital Image Correlation," Measurement Science and Technology, 17, (6), 1615-1621.

Bristowe, S., (2000) "Seismic Response of Normal and High Strength Concrete Members," Ph.D. Dissertation. Civil Engineering and Applied Mechanics, McGill U., Montreal, Canada.

Canbolat, B., Parra-Montesinos, G., and Wight, J., (2005) "Experimental Study on Seismic Behavior of High-Performance Fiber-Reinforced Cement Composite Coupling Beams," *ACI Structural J.*, 102, (1), 159-166.

El-Tawil, S., and Kuenzli, C. (2002). "Pushover of hybrid coupled walls. II: Analysis and behavior." *J. Struct. Eng.,* 128, (10), 1282–1289.

El-Tawil, S., Kuenzli, C., and Hassan, M. (2002). "Pushover of hybrid coupled walls. I: Design and modeling." *J. Struct. Eng.,* 128, (10), 1272–1281.

Faugeras, O. and Devernay, F. (1994). "Computing Defferential Properties of 3D shapes from Stereoscopic Images without 3D models." Technical Report 2304, INRIA (France).

Galano, L. and Vignoli, A., (2000) "Seismic Behavior of Short Coupling Beams with Different Reinforcement Layouts," *ACI Structural Journal*, American Concrete Institute, 97, (6), 876-885.

Harries, K. (2001). "Ductility and deformability of coupling beams in reinforced concrete coupled walls." *Earthquake Spectra,* 17, (3), 457– 478.

Harries, K., Gong, B., and Shahrooz, B. (2000). ‘‘Behavior and design of reinforced concrete, steel, and steel-concrete coupling beams.’’ *Earthquake Spectra,* 16, (40), 775–799.

Harries, K., Mitchell, D., Cook, W., and Redwood, R. (1993). ‘‘Seismic response of steel beams coupling concrete walls.’’ *J. Struct. Eng.,* 119, (12), 3611–3629.

Helm, J. D., Sutton, M. A., and McNeill, S. R. (2003). "Deformations in wide, center-notched, thin panels, part I: Three-dimensional shape and deformation measurements by computer vision." *Optical Engineering*, 42, (5), 1293-1305.

Koldnik, O. and Stüwe, H. P., (1985) "The Stereophotogrammetric determination of the critical crack tip opening displacement." *Engineering Fracture Mechanics,* 21, (1), 145-155.

Kurama, Y. and Farrow, K., (2003). "Ground motion scaling methods for different site conditions and structure characteristics," *Earthquake Engineering & Structural Dynamics*, 32, (15), 2425-2450.

Lu, H., Zhang, X., and Knauss, W. G., (1997) "Uniaxial, shear, and poisson relaxation and their conversion to bulk relaxation: Studies on poly(methyl methacrylate)." *Polymer Composites,* 18, (2), 211-222.

Luo, P. F., Chao, Y. J., and Sutton, M. A., (1994) "Application of stereo vision to three-dimensional deformation analyses in fracture experiments." *Optical Engineering,* 33, (3), 981-990.

Luo, P. F., Chao, Y. J., Sutton, M. A., and Peters, W. H., (1993) "Accurate measurement of three-dimensional deformations in deformations in deformable and rigid bodies using computer vision." *Experimental Mechanics,* 33, (2), 123-132.

Martinez-Rueda, J., (1998). "Scaling procedure for natural accelerograms based on a system of spectrum intensity scales," *Earthquake Spectra*, 14, 135-152.

McGinnis, M. J., Barbachyn, S., Holloman, M. R., and Kurama, Y. C. (2013), "Experimental Evaluation of a Multi-Story Post-Tensioned Coupled Shear Wall Structure." Proceedings of the ASCE Structures Congress, Pittsburgh, PA.

McGinnis, M. J., Mueller, K. A., Kurama, Y. C., Graham, K. P. (2011) "RC Bearing Walls Subjected to Elevated Temperatures." Proceedings of the ASCE Structures Congress, Las Vegas, NV.

McGinnis, M. J., Pessiki, S., (2006). "Experimental and Numerical Development of the Core-Drilling Method for the Nondestructive Evaluation of In-situ Stresses in Concrete Structures," Rpt No. 05-05, Center for Advanced Technology for Large Structural Systems (ATLSS), Lehigh University.

McGowan, D. M., Ambur, D. R., Glen Hanna, T., and McNeill, S. R., (2001) "Evaluating the compressive response of notched Composite panels using full-filed desplacements." *Journal of Aircraft*, 38, (1), 122-129.

Morimoto, Y. and Fujigaki, M., (2007) "Automated analysis of #-D shape and surface strain distributions of a moving object using stereo vision." *Optics and Lasers Engineering*, 31, (4), 29-36.

Orteu, J., "3-D Computer Vision in Experimental Mechanics," (2009). *Optics and Lasers in Engineering*, 47, (3-4), 282-291.

Shahrooz, B., Remmetter, M., and Qin, F. (1993). "Seismic design and performance of composite coupled walls." *J. Struct. Eng.,* 119, (11), 3291–3309.

Shen, Q., and Kurama, Y. (2002). "Nonlinear behavior of post-tensioned hybrid coupled wall subassemblages." *J. Struct. Eng.,* 128, (10), 1290– 1300.

Shen, Q., Kurama, Y., and Weldon, B. (2004). "Seismic analysis, behavior, and design of unbonded post tensioned hybrid coupled walls." *Structural Engineering Research Rep. No. NDSE-04-01*, Dept. of Civil Engineering and Geological Sciences, Univ. of Notre Dame, Notre Dame, Ind.

Shome, N., Cornell, C., Bazzurro, P., and Carballo, J., (1998). "Earthquakes, records, and nonlinear responses," *Earthquake Spectra*, 14, 469-500.

Smith, B., Kurama, Y., and McGinnis, M. (2011a). "Comparison of Hybrid and Emulative Precast Concrete Shear Walls for Seismic Regions." *Proceeding of the ASCE Structures Congress*, Las Vegas, NV.

Smith, B., Kurama, Y., and McGinnis, M. (2011b). "Design and Measured Behavior of a Hybrid Precast Concrete Wall Specimen for Seismic Regions." *Journal of Structural Engineering*, 137, (10), 1052-1062.

Sutton, M. A. and Chao, Y. J., (1993) "Computer vision in fracture mechanics." *Experimental Techniques in Fracture*, 59-94.

Sutton, M. A., Chao, Y. J., and Lyons, L. S., (1993) "Computer vision methods for surface deformation measurements in fracture mechanics." *ASME-AMD Novel Experimental Methods in Fracture*, 176, 123-133.

Tassios, T., Moretti, M., and Bezas, A., (1996) "On the Behavior and Ductility of Reinforced Concrete Coupling Beams of Shear Walls," *ACI Structural Journal*, American Concrete Institute, 93, (6), 711-720.

Trautner, C., McGinnis, M., Pessiki, S., (2008). "Development of the Incremental Core-drilling Method for Non-Destructive Investigation of Stresses in Concrete Structures," Rpt. No. 08-10, ATLSS Center, Lehigh University.

Turker, H., Pessiki, S. (2003). "Theoretical Development of the Core-Drilling Method for Nondestructive Evaluation of Stresses in Concrete Structures," Report No. 03-07, ATLSS Center, Lehigh University, 300 pp.

Vogel, J. H. and Lee, D., (1989) "An automated two-view method for determining strain distributions on deformed surfaces." *Journal of Material Shaping Technology,* 6, (4), 205-216.

Weldon, B. and Kurama, Y., (2010) "Experimental Evaluation of Post-Tensioned Precast Concrete Coupling Beams," *Journal of Structural Engineering*, American Society of Civil Engineers, 136, (9), 1066-1077.

Weldon, B. and Kurama, Y., (2009) "Experimental Evaluation of Post-Tensioned Precast Concrete Coupling Beams," *ASCE Structures Congress*, American Society of Civil Engineers, Austin, Texas.

Weldon, B. and Kurama, Y., (2007) "Unbonded Post-Tensioned Precast Concrete Coupling Beams: An Experimental Evaluation," *ASCE Structures Congress*, American Society of Civil Engineers, Long Beach, CA.